UCGE Reports

Number 20172

Department of Geomatics Engineering

An Analysis of the Combination and Downward Continuation of Satellite, Airborne and Terrestrial Gravity Data

(URL: http://www.geomatics.ucalgary.ca/links/GradTheses.html)

by

Michael Kern

April 2003

THE UNIVERSITY OF CALGARY

An Analysis of the Combination and Downward Continuation of Satellite, Airborne and Terrestrial Gravity Data

by

Michael Kern

A DISSERTATION

SUBMITTED TO THE FACULTY OF GRADUATE STUDIES

IN PARTIAL FULFILLMENT OF THE REQUIREMENTS

FOR THE DEGREE OF DOCTOR OF PHILOSOPHY

DEPARTMENT OF GEOMATICS ENGINEERING

CALGARY, ALBERTA, CANADA

APRIL, 2003

© Michael Kern 2003

Abstract

An analysis of the combination and downward continuation of satellite, airborne and terrestrial gravity data is presented. The thesis encompasses theoretical investigations of the underlying model problems and a numerical study using simulated and real data.

The downward continuation of gravity data is inherently unstable and requires regularization, iteration or filtering methods to obtain a stable solution. This research scrutinizes several regularization methods for the downward continuation of airborne and terrestrial gravity data. All of them can be considered as filtered least-squares solutions. Additionally, an alternative numerical method is developed and compared to the other methods. It provides a considerable improvement in terms of numerical efficiency and accuracy when the assumptions for the method are satisfied.

With newly available satellite gravity data, additional low-frequency information about the gravity field can be obtained. Since applications such as geoid determination and resource exploration demand a much higher resolution than resolved by satellite-only models, the combination with data collected closer to the Earth's surface is essential. In this research, local airborne and terrestrial gravity data have been used. Several combination strategies are proposed and implemented.

The feasibility of the combination strategies is demonstrated for a local data area close to Ottawa, Canada. The results indicate that a combination of satellite, airborne and terrestrial gravity is beneficial both in terms of accuracy and resolution. A combined local geoid and a high-degree spherical harmonic model up to degree and order 900 are developed. The results show a geoid accuracy in the cm-range for the test area.

Acknowledgements

I would like to express my sincere gratitude to my distinguished supervisor Dr. Klaus-Peter Schwarz for his continuous inspiration, encouragement, advice and support throughout my graduate studies. He manages to strike the perfect balance between providing direction and encouraging independence.

I would like to extend my gratitude to my Ph.D. defense members, colleagues and teachers, namely Drs. B. Heck, P. Holota, J. Kusche, P. Novák, M. G. Sideris, N. Sneeuw and P. Wu. They are thanked for their invaluable advice, cooperation and help on many occasions.

I would like to thank my friends and fellow students for their daily help and support. In particular, I thank my dear friends Cameron Ellum, Lynn Raaflaub and Sandy Kennedy for their friendship and for making my stay in Canada a wonderful experience.

My final and most heartfelt appreciation goes to my family for their love, encouragement and understanding.

Contents

Approval Page ii

Abstract iii

Acknowledgements iv

Contents v

List of Tables viii

List of Figures xi

List of Symbols xii

List of Acronyms xvii

1 Introduction 1

2 The Remove-Restore Technique 7
- 2.1 The Meissl Scheme 8
- 2.2 Satellite Contributions 10
- 2.3 The Helmert Scheme 12
- 2.4 Transformations 24
- 2.5 Case Study – Stokes Integration 39
- 2.6 Limitations 45

3 Upward and Downward Continuation 46
- 3.1 Upward Continuation 46
- 3.2 Downward Continuation 51
- 3.3 Analysis of the Discrete Downward Continuation Problem 62
- 3.4 An Alternative Numerical Solution 67

3.5 Downward Continuation Results 72

4 The Combination of Heterogeneous Gravity Data 79
4.1 A Glance at the Combination Problem 79
4.2 Analysis and Synthesis 84
4.3 Combination Strategies 89
4.4 Quality of the Combination Strategies 93
4.5 Combining a Satellite Model with a Geopotential Model 96

5 From Theory to Application 102
5.1 General Considerations 102
5.2 Specific Considerations 107

6 Real Data Results 114
6.1 Individual Solutions 116
6.2 Combined Solutions 127

7 Concluding Remarks 136

Bibliography 152

A Tables and Properties 153
Quality Measures 153
A.1 Filter Window Functions 154
A.2 Degree Variance Models 155
A.3 Removing the Singularity from the Stokes Kernel 156
A.4 Abel-Poisson Kernel Modifications 158
A.5 Pellinen Mean 160
A.6 Covariance Functions and Least-Squares Collocation 161
Geodetic Reference Systems 166
Legendre Polynomials and Legendre Functions 166

B Additional Results 166
B.1 First Helmert versus Second Helmert Condensation Method 166
B.2 Stokes Integration and Continuation Results 167
B.3 Satellite Models and Geopotential Models 171
B.4 Geoid Determination Based on Satellite and Terrestrial Gravity Data . 171

Index 173

List of Tables

2.1 Operators, singular systems and upward continuation (uc) degree . . . 9
2.2 Direct and indirect effect 16
2.3 Condensation schemes 17
2.4 Helmert scheme – direct effect 19
2.5 Helmert scheme – indirect effect 19
2.6 Error analysis 32
2.7 Deterministic kernel modifications 38
2.8 Simulated data statistics 39
2.9 Remove-restore technique versus local data method [m] 44
2.10 Kernel function comparison (○ – small; ◐ – medium; ● – large) 44

3.1 Filter factors 62
3.2 Simulated data statistics for the downward continuation problem 73
3.3 Determination of the regularization parameter 75

4.1 Spectrals weights p_l for the satellite data 90
4.2 Input data statistics for the combination 94

5.1 Spectral sensitivity 103
5.2 Measures for spectral sensitivity 104
5.3 Link between spatial and spectral resolution 105
5.4 Satellite and geopotential models 113

6.1 Statistics of the geoid based on ground gravity data 118
6.2 Statistics of the geoid based on airborne gravity data 122
6.3 Statistics of the high-degree model TM900g 124
6.4 Statistics of the high-degree model GM900sgl 125
6.5 Statistics for the geoid determination of satellite data and a local gravity data set 129
6.6 Statistics of the first combination – satellite and airborne data 131

6.7 Statistics for the geoid determination based on satellite, airborne and terrestrial gravity data . . . 132
6.8 Statistics of the high-degree model based on satellite, airborne and terrestial gravity data . . . 133

A.1 Quality measures for $x \in \mathbb{R}^n$ . . . 153
A.2 Filter window functions . . . 154
A.3 Degree variance models (Wenzel, 1985, pg. 147) . . . 155
A.4 Stokes kernel functions ($L_{\mathrm{MD}} \leq L_{\mathrm{S}}$) . . . 157
A.5 Abel-Poisson kernel functions ($L_{\mathrm{MD}} \leq L_{\mathrm{S}}$) . . . 159
A.6 Pellinen mean formulas . . . 160
A.7 Covariance functions . . . 162
A.8 Summary of least-squares collocation (Moritz, 1989) . . . 163
A.9 Geodetic reference systems . . . 164
A.10 Legendre polynomials and Legendre functions . . . 165

B.1 First Helmert versus second Helmert condensation method . . . 166
B.2 Stokes integration – noise-free data . . . 167
B.3 Stokes integration – noisy data . . . 168
B.4 Continuation results [mGal] . . . 169
B.5 Continuation results [mGal] – cont. . . . 170
B.6 Undulation differences between the CGG2000, satellite and geopotential models [m] . . . 171
B.7 Statistics for the geoid determination of satellite data and a local gravity data set . . . 171

List of Figures

1.1 Gravity field from EGM96 (gravity anomalies exaggerated) 2

2.1 Singular values in the Meissl scheme 10
2.2 Geometry of the problem 15
2.3 Helmert values for the direct and indirect effects 23
2.4 Geometry and two divisions 27
2.5 Combinations using satellite data and one local gravity data set (de Min, 1996) 29
2.6 Computation of truncation errors using a geopotential model 35
2.7 Kernel functions and truncation coefficients with $\psi_c = 1^\circ$ and $L_S = 120$, $L_{MD} = 120$ 37
2.8 Geoid error with different kernel modifications. First bar is the geoid rms error with noise-free data, second bar the geoid rms error with noisy data [cm] 41
2.9 Influence of different modification degrees using the FEO kernel. $L_S = 120$ and $\psi_c = 1^\circ$ fixed 42

3.1 Sparsity pattern of the design matrix $\boldsymbol{A}$ with $m = 2304$ and $n = 864$. 335452 non-zero elements 50
3.2 Mean square error functions, example taken from Bouman (2000) . . . 55
3.3 Filter factors 61
3.4 Singular values and condition numbers 65
3.5 Picard condition for simulated airborne data 67
3.6 Approximate condition numbers for different continuation heights and spatial resolutions 72
3.7 RMS error of the continuation solutions. INV, LAI, TIK, DSVD, TSVD, CG, A 74
3.8 Reference solution versus A, TIK, and CG using gravity disturbances at 2 km [mGal] 76

3.9 Frequency spectra of the least-squares solution (LSQ), the conjugate gradient solution (CG) and the alternative approximation (A) 77

4.1 Degree variances of simulated global and local gravity data 80
4.2 Iteration scheme 88
4.3 Iteration scheme for the combination of satellite and geopotential models 89
4.4 Development of a high-degree spherical harmonic model 91
4.5 Geoid determination using satellite and a local gravity data set 93
4.6 Geoid determination using satellite, airborne and terrestrial gravity data 94
4.7 Undulation differences compared to GPM98a [cm]; first bar stands for mean difference, second bar is standard deviation 96
4.8 Differences between the EGM96 and CSM360 98
4.9 Differences between the EGM96 and EGM96e 99
4.10 Differences between the EGM96 and CSM360w 101

5.1 Attenuation and amplification 106
5.2 Geophysical effects in periods, wavelengths and magnitude (from Verhagen (2000); NRC (1997)) 107
5.3 Signal and error anomaly degree variances of some global models [mGal^2] 109
5.4 Location of the test area 110
5.5 Ground gravity anomalies and airborne field test [mGal] 111

6.1 Separation between the reference ellipsoid and an adopted reference equipotential 115
6.2 Undulation differences between the CGG2000, satellite models and geopotential models [cm]; first bar stands for mean difference, second bar is the standard deviation 116
6.3 Differences between CGG2000 and two models [m] 117
6.4 Determination of a local geoid based on ground gravity anomalies . . . 119
6.5 Effect of different Stokes kernel modifications 120
6.6 Determination of a local geoid based on airborne gravity disturbances . 123
6.7 High-degree spherical harmonic model based on ground gravity data . . 124
6.8 High-degree spherical harmonic model based on airborne data 126
6.9 Performance of individual solutions. First bar stands for mean difference, second bar is standard deviation 127
6.10 Undulation differences [m] 130
6.11 Geoid based on a combination of satellite, airborne and terrestrial gravity data 132

6.12 High-degree spherical harmonic model based on satellite, airborne and terrestrial gravity data 134
6.13 Performance of combined solutions. Standard deviation to CGG2000 after removing a systematic trend 135

A.1 Degree variance models 155
A.2 Pellinen curves β_l for $\psi_\mathrm{c} = 1^\circ,\ 2^\circ,\ 3^\circ$ 160
A.3 Covariance function and degree variances 162

B.1 Geoid determination based on satellite and terrestrial gravity data . . . 172

List of Symbols

a	major semi-axis of the geocentric reference ellipsoid
b	minor semi-axis of the geocentric reference ellipsoid / bandwidth
c_l	degree variances
e	first numerical eccentricity of the geocentric reference ellipsoid / noise
e_l^{G}	errors by degree of the local gravity data G
e_l^{S}	errors by degree of the satellite data S
f	polar flattening of the geocentric reference ellipsoid / frequency band
$\hat{f}$	functional of the disturbing potential ($= \mathcal{B}T$)
f_k	solution in the k-th step of the iteration
$\hat{f}_{lm}$	Fourier coefficients of $\hat{f}$
$\hat{\boldsymbol{f}}_\alpha$	regularized solution
g	magnitude of gravity
$\bar{g}$	noisy gravity data
$\boldsymbol{g}$	gravity boundary function (scalar, vector or tensor) reduced by a reference value
g_l	surface spherical harmonics of g
$\bar{g}_l^{\mathrm{S}}$	noisy data by degree of the satellite data S
g_{lm}	Fourier coefficients of $\boldsymbol{g}(P)$
h	geodetic height
k	iteration step
k_{max}	maximum number of iteration steps
l	degree of harmonic series expansion
$\boldsymbol{l}$	observation vector
m	order of the harmonic series expansion / geodetic parameter
n	degree of the harmonic series expansion
$\boldsymbol{n}$	noise vector
r	geocentric radius in spherical coordinates

r_{B}	geocentric radius of the Bouguer shell
r_n	modification coefficients to the Stokes function
$r_n(H,\psi_{\mathrm{c}})$	modification coefficients to the Abel-Poisson function
$\boldsymbol{s}$	signal vector
$\boldsymbol{s'}$	vector of to be predicted signals
t	time variability
$\boldsymbol{t}$	vector containing signals and to be predicted signals
t_l	surface spherical harmonics of T
t_l^{M}	surface spherical harmonics of T from a geopotential model M
t_{lm}	Fourier coefficients of T
u_l	left singular functions
$\boldsymbol{u}_i$	left singular vector
$\boldsymbol{u}_i^T$	left singular vector transposed
v_l	right singular functions
$\boldsymbol{v}_i$	right singular vector
x	first Cartesian coordinate / spatial resolution
$\boldsymbol{x}$	solution vector / parameter vector
$\boldsymbol{x}_0$	initial solution vector
$\hat{\boldsymbol{x}}_\alpha$	regularized solution vector
y	second Cartesian coordinate
$\tilde{\boldsymbol{y}}$	noisy measurements
z	third Cartesian coordinate / integration variable
$\boldsymbol{A}$	design matrix in the downward continuation
$\boldsymbol{A}_\alpha^+$	regularized inverse of matrix $\boldsymbol{A}$
$\boldsymbol{C}$	covariance function
$\bar{C}_{lm}$	fully normalized potential coefficient
E	error of the combination
$\bar{\boldsymbol{E}}(\cdot,\cdot)$	expectation operator
$\boldsymbol{E}$	error covariance matrix
G	universal gravitational constant
H	orthometric height
H'	orthometric height of the integration point
J_2	dynamic form factor of the Earth
K	kernel function
$\bar{K}_{lm}$	fully normalized potential coefficient
L	maximum degree / differential operator
L_{E}	selected maximum degree of the satellite model
L_{M}	maximum degree of the geopotential model

L_{MD}	maximum modification degree
L_{S}	maximum degree of the satellite model
M	meridian radius of curvature of the geocentric reference ellipsoid / mass of the Earth
M_0	mass of the reference ellipsoid
N	prime vertical radius of curvature of the geocentric reference ellipsoid / geoidal height / number of data
P	known point with r, θ, λ
$\boldsymbol{P}^{-1}$	variance-covariance matrix
P_l	Legendre's polynomial of the first kind
P_{lm}	associated Legendre's function of the first kind
$\bar{P}_{lm}$	fully normalized associated Legendre functions
Q	known point with R, θ, λ
Q_l	truncation coefficients
R	radius of the geocentric reference sphere
R	mean equatorial radius
R_{lm}	Paul's coefficients
$\bar{S}_{lm}$	fully normalized potential coefficient
T	disturbing potential
$T_x,\ T_y,\ T_z$	derivative of the disturbing potential with respect to x, y or z
U	normal gravity potential
U_{l0}	potential coefficients from a normal field
V	gravitational potential
V^{B}	potential of the Bouguer shell
V^{H}	Helmert potential
V_{ct}	gravitational potential of condensed topographic masses
V_{t}	gravitational potential of topographic masses
W	gravity potential
$\boldsymbol{X}_{lm}$	vector spherical harmonics
Y_{lm}	surface spherical harmonics
$\bar{Y}_{lm}$	fully normalized surface spherical harmonics
$\boldsymbol{X}_{lm}$	vector spherical harmonics
$\boldsymbol{Z}_{lm}$	tensor spherical harmonics
$\mathcal{A}$	linear operator
$\mathcal{A}^*$	adjoint operator
$\mathcal{A}_\alpha^+$	regularized inverse of $\mathcal{A}$
$\mathcal{A}T$	functional of the disturbing potential
$\mathcal{A}T'$	residual functional of the disturbing potential
$\mathcal{A}T^{\mathrm{S}}$	functional of the disturbing potential from satellite data

$\mathcal{A}\delta V^{\mathrm{H}}$	topographic and atmospheric effects
$\mathcal{B}$	linear operator
$\mathcal{B}T$	functional of the disturbing potential
$\mathcal{B}\hat{T}$	estimated functional of the disturbing potential
$\mathcal{B}\hat{T}'$	residual functional of the disturbing potential
$\mathcal{B}T^{\mathrm{S}}$	functional of the disturbing potential from a satellite model
$\mathcal{B}\delta V^{\mathrm{H}}$	indirect topographic and atmospheric effects
$\mathcal{F}_\alpha$	Tikhonov regularization functional
$\mathcal{N}(\boldsymbol{A})$	nullspace of matrix $\boldsymbol{A}$
$\mathcal{O}$	order of approximation (Landau's symbol)
$\mathcal{R}(\boldsymbol{A})$	range of matrix $\boldsymbol{A}$
$\mathbb{E}^n$	n-dimensional Euclidean space
$\mathbb{N}^n$	n-dimensional space of integer numbers
$\mathbb{R}^n$	n-dimensional space of real numbers
$\partial_x,\ \partial_y,\ \partial_z$	partial derivative with respect to x, y or z
α	azimuth / regularization parameter
β	relaxation parameter
β_l	Pellinen smoothing coefficients
γ	magnitude of normal gravity / constant value
γ_e	magnitude of normal gravity at the equator
γ_{E}	magnitude of normal gravity at the reference ellipsoid
γ_p	magnitude of normal gravity at the pole
δ_α	filter factor
δA^{TOP}	topographic attraction
δA^{ATM}	atmospheric attraction
δg	magnitude of gravity disturbance
$\delta g'$	residual gravity disturbance
δg^{H}	Helmert gravity disturbance
δg^{S}	gravity disturbance from a satellite model
δV	residual gravitational potential
δV^{H}	residual gravitational potential in the Helmert Scheme
ε_l	error degree variances
$\varepsilon_l^{\mathrm{c}}$	commission variance
$\varepsilon_l^{\mathrm{o}}$	omission variance
ζ^i	condensation density model
θ	co-latitude / block size
θ_j^p	p Ritz values, i.e. eigenvalues of $\mathcal{A}^*\mathcal{A}$
κ	condition number

λ	longitude
λ_l	eigenvalue
μ	Newtonian universal constant times the mean density ($G\rho_0$)
ρ_0	mean density of the topographic masses
σ_l	singular value
ϕ	geodetic latitude
φ	geocentric latitude
ψ	spherical distance
ψ_{c}	spherical cap radius
ω	unit sphere
ω_{c}	integration domain of the spherical cap
Δg	magnitude of gravity anomaly
$\Delta g'$	residual gravity anomaly
$\Delta\omega_j$	area of the trapezoidal cell centred at the j-node ω_j
$\Delta\bar{C}_{lm}$	fully normalized potential coefficient after substracting the reference field
$\Delta\delta\bar{C}_{lm}$	fully normalized residual potential coefficients
$\Delta\bar{K}_{lm}$	fully normalized potential coefficients after substracting the reference field
$\Delta K_{lm}^{\mathrm{S}}$	residual potential coefficient from a satellite model
$\Delta\bar{S}_{lm}$	fully normalized potential coefficient after substracting the reference field
$\Delta\delta\bar{S}_{lm}$	fully normalized residual potential coefficients
ΔT	Laplace operator applied on T
ΔV^{ATM}	residual atmospheric potential
ΔV^{TOP}	residual topographic potential
ΔW_0	reference potential anomaly
$\Lambda_l^{(k)}$	Helmert scheme value

Vectors and Matrices in $\mathbb{R}^n$ or $\mathbb{R}^n \times \mathbb{R}^m$ are shown in bold letters such as $\boldsymbol{x}$, $\boldsymbol{y}$, $\boldsymbol{A}$. Operators are given in calligraphic letters, e.g. $\mathcal{A}$, $\mathcal{B}$.

List of Acronyms

BVP	Boundary value problem
CG	Conjugate gradient method
CGG2000	Canadian gravimetric geoid model of 2000
CSM360	EGM96 combined with EIGEN-2 data for a large regional area
CSM360w	EGM96 combined with EIGEN-2 data for a large regional area with spectral weights
CHAMP	Challenging minisatellite payload
DAE	Direct atmospheric effect
DSVD	Damped singular value decomposition
DTE	Direct topographic effect
EGM96	Earth geopotential model 1996
EGM96e	Earth geopotential model 1996 combined with EIGEN-2 data
EVA	Eigenvalue analysis
FEO	Featherstone & Evans & Olliver kernel modification
FFT	Fast Fourier transformation
GOCE	Gravity field and steady-state ocean circulation mission
GPM98A	Geopotential model 1998a (Wenzel, 1998b)
GPS	Global positioning system
GRACE	Gravity recovery and climate experiment
GRS67	Geodetic reference system of 1967
GRS80	Geodetic reference system of 1980
GSD	Geodetic survey division Canada
HG	Heck & Grüninger kernel modification
INTERMAP	Intermap Technologies Corporation
IAG	International Association of Geodesy
IAG75	Geodetic reference system of 1975
IAG83	Geodetic reference system of 1983
JK	Meissl modified Molodenskij kernel modification (Jekeli, 1980)
LAI	Landweber iteration method
LSC	Least-squares collocation

LSQ	Least-squares
M	Meissl kernel modification
MIMO	Multiple-input/multiple output method
MO	Molodenskij kernel modification
MSE	Mean square error
PAE	Indirect atmospheric effect
PSD	Power spectral density
PTE	Indirect topographic effect
RMS	Root mean square
S	Spheroidal kernel modification
SGM	Synthetic gravity model
SGL	Sander Geophysics Ltd.
STD	Standard deviation
SVD	Singular value decomposition
TIK	Tikhonov regularization
TSVD	Truncated singular value decomposition
UofC	The University of Calgary
VK	Vaníček & Kleusberg kernel modification
WG	Wong & Gore kernel modification
WGD2000	World geodetic datum 2000

1 Introduction

"The intention and the result of a scientific inquiry is to obtain an understanding and a control of some part of the universe. No substantial part of the universe is so simple that it can be grasped and controlled without abstraction. Abstraction consists in replacing the part of the universe under consideration by a model of similar, but simpler structure. Models, formal or intellectual on the one hand, or material on the other, are thus a central necessity of scientific procedure."

Rosenblueth and Wiener, 1945

Background

Satellite geodesy has been an important part of geodesy for about 30 years and determining the Earth's gravity field is one of its major tasks (Seeber, 1993). Almost immediately after the launch of Sputnik-1 in 1957, ground-based tracking of (artificial) satellites has been used to obtain information about the global gravity field. Free-falling satellites have been considered as probes in the gravity field. Observation techniques such as Doppler and satellite laser ranging have been used and have led to first global gravity models in the 1960s. Since then, an increased number of satellites and tracking stations, technology enhancements and methodology changes have remarkably improved the knowledge of the low-degree gravity field. Combinations of satellite and other gravimetric data have increased the resolution of these models yielding combined geopotential models; see Figure 1.1 for a recent example. Yet still, the spatial distribution is inhomogeneous; the derived models are low frequency in nature and the quality is often too poor for applications in geodesy and geophysics. Characteristics of the time-variable field and the global stationary gravity field are not available in sufficient detail. It is expected that all this will change once the data of the three satellite missions CHAMP, GRACE and GOCE and their successors become available. In close collaboration with other geosciences, satellite geodesy will then move into a new phase.

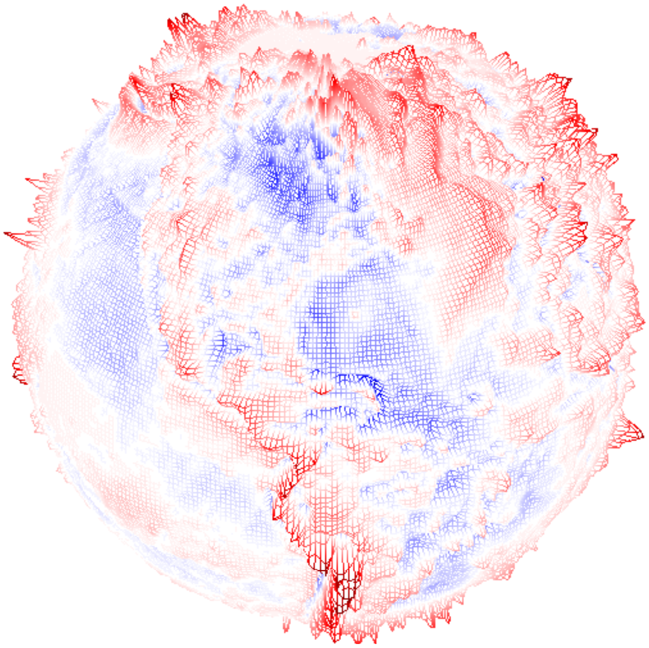

Figure 1.1: Gravity field from EGM96 (gravity anomalies exaggerated)

Two of the three satellite gravity missions have already been launched, leaving one mission under development (GOCE). Measurement techniques such as satellite gradiometry and satellite-to-satellite tracking will be used. As indicated above, the main mission objectives are to determine the stationary gravity field with an unprecedented accuracy (GOCE) and to map its variability in time in an efficient and cost-effective way (GRACE). Models will be derived that provide information down to spatial scales of about 100 km. In particular, the goals are centimeter accuracy in terms of geoid heights and less than 1-2 mGal ($1\,\mathrm{mGal}=10^{-5}\,\mathrm{m/s^2}$) in terms of gravity (ESA, 1999) for the part of the spectrum that can be resolved. If the missions are successful, they will provide state-of-the-art information for the lower frequencies since their quality will be unmatched. Undoubtedly, many global applications can greatly benefit from these missions.

Setting the Stage – Problem Statement

Typically, applications such as geoid determination and resource exploration demand a much higher resolution than that obtained by satellite-only models (expected 100 km). Since the gravity field is damped at satellite altitude and only large-scale features are visible, other means have to be found to resolve the higher frequencies. Measurements collected closer to the Earth's surface, such as airborne and terrestrial gravity data, represent attractive alternatives because the high-frequency part of the signal is more pronounced. These measurements, albeit often burdened by systematic errors and limited in spatial extent, can contribute to the determination of the medium to high frequencies of the gravity field. Airborne gravimetry is a particularly interesting candidate to resolve these frequencies since it provides gravity measurements in a cost-effective and economic way. In addition, it can be used in remote areas that are not easily accessible. For further details on airborne gravimetry and its characteristics refer to Schwarz & Li (1997, 1996); Glennie (1999); Bruton (2000). By means of data combination, the satellite spectrum could be widened and enhanced. As a result, a unified estimate of the gravity field could be obtained that satisfies requirements of many applications and is less encumbered by specific mission objectives. Hence, a detailed analysis of the combination problem of satellite, airborne and terrestrial gravity data, and its solution strategies, is one of the objectives of this dissertation.

The second problem to be discussed is the downward continuation problem. Measurements collected or derived at satellite altitude, airborne flight path or at the surface of the Earth have to be downward continued to a different surface. This process belongs to the class of improperly posed problems (Moritz, 1966; Schwarz, 1971). Numerical instabilities occur in the form of drastically amplified noise. The higher the continuation height and the finer the data spacing, the more severe is the problem. The instabilities can be overcome by adding a-priori information to the solution (Schwarz, 1979). However, a stable solution comes at the cost of a biased solution, which is equally problematic (at least in some applications). Many stabilization concepts have been developed over the years, see for instance Tikhonov & Arsenin (1977); Rummel et al. (1979); Bouman (1998); Kusche (2002). Recently, their performances have been studied for the satellite case (Bouman, 2000; Kusche, 2002). Hence, it is of interest to apply and compare these methods to the less severe case of airborne and terrestrial measurements. This has not been studied in sufficient detail. Furthermore, stability investigations on the downward continuation problem of airborne and terrestrial gravity data could enhance the understanding of the problem and lead to alternative solution concepts for specific applications.

Objectives

The main objective of this thesis is a detailed analysis of the combination and downward continuation of satellite, airborne and terrestrial gravity data. The analysis encompasses a theoretical investigation of the underlying model problems and a numerical study using simulated and real data. Furthermore, the concept of tailoring (improving a global model by local or regional gravity data) is revisited and its quality is evaluated with respect to traditional geoid modelling by integration.

Outline

The thesis is structured in the following way:

- The second chapter investigates, generalizes and analyzes the remove-restore technique, i.e., a combination strategy for the combination of satellite and one local or regional gravity data set. Further insights are provided into the second Helmert condensation scheme as well as the impact of kernel modifications.
- Chapter three delves into the continuation problem. Theoretical and numerical challenges of the downward continuation problem are discussed. After a theoretical analysis of the degree of ill-posedness of the downward continuation of airborne and terrestrial gravity data, an alternative solution concept is developed. A numerical comparison of regularization/stabilization concepts for the downward continuation

problem of airborne gravity data concludes the chapter.

- Chapter four revisits the concept of tailoring as a possible candidate for the combination of satellite and multiple local gravity data. A brief analysis of the combination model problem is followed by outlining the principle of the combination method and some refinements made by the author.
- The fifth chapter analyses gravity data from a conceptual point of view. It also includes a first glance at the real satellite, airborne and terrestrial gravity data used in Chapter six.
- Chapter six presents combination solutions using satellite, airborne and terrestrial gravity data over a local test area. A high-degree spherical harmonic model is developed and a local geoid is determined based on all available gravity data in the area. The results are compared to the official geoid in Canada.
- Conclusions are drawn in chapter seven. Future work and recommendations conclude the thesis.

Limitations

- This investigation is confined to local and regional combinations rather than optimal global solutions. This has been decided upon since airborne and terrestrial measurements are often limited in their spatial extent. In addition, they are usually not of homogeneous quality. Since a global solution would suffer from an unbalanced distribution, regional or local solutions are favoured in this study.
- Satellite information is used here in form of low-degree spherical harmonic models. Although combinations using satellite, airborne and terrestrial data could take place at the observation or normal equation level, this possibility is not investigated here.
- Throughout the thesis, it is assumed that the gravity data are of good quality, i.e. calibrated and validated.
- Spherical approximation is used throughout the thesis. This represents a clear approximation of the physical situation. Ellipsoidal formulation or ellipsoidal cor-

rection terms would be required to enhance the solutions. As only local and regional solutions are developed, however, the error remains relatively small (on the order of the ellipsoidal flatting). Whenever it seems convenient, the geoid is approximated by a reference sphere R.

- A constant density is used for the computation of the topographic effects. This assumption has been made since no specific knowledge of the actual mass density variations was available.
- Temporal variations of the gravity field are neglected in the computations.

2 The Remove-Restore Technique

Outlined in this chapter is the combination of satellite data with one local gravity data set. This is the typical case that has been discussed by numerous authors. The chapter is structured around the *remove-restore technique* that will be used for the combination of satellite and local gravity data (Rapp & Rummel, 1975; Forsberg & Tscherning, 1981). The remove-restore technique can be summarized as follows:

$$\begin{aligned} \text{Remove}: & \qquad \mathcal{A}T' = \mathcal{A}T - \mathcal{A}T^{\mathrm{S}} - \mathcal{A}\delta V^{\mathrm{H}} \\ \text{Transformation}: & \qquad \downarrow \\ \text{Restore}: \; \mathcal{B}\hat{T} = & \qquad \mathcal{B}\hat{T}' + \mathcal{B}T^{\mathrm{S}} + \mathcal{B}\delta V^{\mathrm{H}} \end{aligned} \tag{2.1}$$

where $\mathcal{A}$ and $\mathcal{B}$ are operators applied on the disturbing potential T, the residual disturbing potential T', the disturbing potential computed from a satellite model T^{S} and the residual (Helmert) gravitational potential δV^{H}.

The remove-restore technique involves three steps, see Eq. (2.1). The first step is the remove step. The local gravity data are reduced by the satellite model $\mathcal{A}T^{\mathrm{S}}$ and by the topographic and atmospheric effects $\mathcal{A}\delta V^{\mathrm{H}}$. The result of the remove step is residual gravity data ($\mathcal{A}T'$) that is input to the transformation step. The transformation step maps the residual observable to the output function ($\mathcal{B}\hat{T}'$). In the restore step, the low-frequency information of the satellite data is added back to the data in the output unit, namely $\mathcal{B}T^{\mathrm{S}}$. Furthermore, the topographic and atmospheric indirect effects ($\mathcal{B}\delta V^{\mathrm{H}}$) are restored to obtain the final output $\mathcal{B}\hat{T}$. The tools for the remove-restore technique are described in the following sections.

2.1 The Meissl Scheme

The Meissl scheme is extensively used in the following. Therefore, it will be briefly reviewed and the connection to the remove-restore technique will be established.

Every gravity observation can be expressed as a functional of (or an operator applied on) the disturbing potential $T \in X$ (Meissl, 1971b; Rummel & van Gelderen, 1995)

$$\boldsymbol{g} = \mathcal{A}T \;\longleftrightarrow\; \boldsymbol{g} = \sum_{l} \sigma_l \left(T, v_l\right)_X u_l \tag{2.2}$$

where

$\boldsymbol{g}$	is the gravity function/operator (scalar, vector or tensor) reduced by a reference value (computed from a reference ellipsoid), $\boldsymbol{g} \in Y$
$\mathcal{A}$	is an operator that maps the Hilbert space X (domain) into the Hilbert space Y (range), $\mathcal{A} : X \to Y$
T	is the disturbing potential at a known point Q ($T(Q) = W(Q) - U(Q)$)
σ_l	are singular values ($\sigma_l = \sqrt{\lambda_l}$, λ_l is the eigenvalue)
$u_l,\ v_l$	are the left and the right singular functions, respectively ($u_l = \sigma_l^{-1} \mathcal{A} v_l$)
$(T, v_l)_X$	is the scalar product of T and v_l in X
l	is the (spherical harmonic) degree ($l \in \mathbb{N}$)

Eq. (2.2) shows a link between gravity functions/operators and the disturbing potential in the space domain as well as the spectral domain. Let $\mathcal{A}^* : Y \to X$ be the *adjoint* operator of $\mathcal{A}$, i.e., $(g, \mathcal{A}T)_Y = (\mathcal{A}^* g, T)_X$. Then $\mathcal{A} : X \to X$ is called *self-adjoint* with respect to the scalar product $(\cdot, \cdot)_X$ if $\mathcal{A} = \mathcal{A}^*$ holds or, equivalently, $(g, \mathcal{A}T)_Y = (\mathcal{A}g, T)_X$. Eqn. (2.2) is an *eigenvalue analysis* (EVA) for self-adjoint cases ($u_l = v_l$) and a *singular value decomposition* (SVD) for non self-adjoint operators.

Meissl (1971b) lists the most commonly used singular values in tabularized form. The resulting *Meissl scheme* is a list of singular systems $\{\sigma_l, u_l, v_l\}$ for idealized observables continuously given on a reference sphere. The extension to non self-adjoint operators and the upward and downward continuation is treated in Rummel & van Gelderen

(1995) and Grafarend (2001). Following Meissl (1971b), van Gelderen & Rummel (2001) and Kusche (2002), Table 2.1 can be obtained. $x,\ y,\ z$ form a local coordinate system with x pointing to north, y pointing east and z normal to the sphere pointing outside. The upward continuation degree uc is used in $(R/r)^{\mathrm{uc}}$; R being the mean Earth radius, and $r = R + H$ the radius at height H. $\mathcal{I}$ stands for the identity operator.

Table 2.1: Operators, singular systems and upward continuation (uc) degree

$\mathcal{A}$	$\mathcal{A}T$	σ_l	u_l	v_l	uc
$\mathcal{I}$	T	1	$\bar{Y}_{lm}$	$\bar{Y}_{lm}$	$l+1$
∂_z	T_z	$-\frac{(l+1)}{R}$	$\bar{Y}_{lm}$	$\bar{Y}_{lm}$	$l+2$
∂_x, ∂_y	T_x, T_y	$-\frac{\sqrt{l(l+1)}}{R}$	Y_{lm}	$\bar{\boldsymbol{X}}^1_{lm}, \bar{\boldsymbol{X}}^2_{lm}$	$l+2$
∂_{zz}	T_{zz}	$\frac{(l+1)(l+2)}{R^2}$	$\bar{Y}_{lm}$	$\bar{Y}_{lm}$	$l+3$
$\partial_{xz}, \partial_{yz}$	T_{xz}, T_{yz}	$-\frac{(l+2)\sqrt{l(l+1)}}{R^2}$	$\bar{Y}_{lm}$	$\bar{\boldsymbol{Z}}^{13(1)}_{lm}, \bar{\boldsymbol{Z}}^{23(1)}_{lm}$	$l+3$
$\partial_{xx} - \partial_{yy}, 2\partial_{xy}$	$T_{xx} - T_{yy}, 2T_{xy}$	$\frac{\sqrt{(l-1)l(l+1)(l+2)}}{R^2}$	$\bar{Y}_{lm}$	$\bar{\boldsymbol{Z}}^{11(2)}_{lm}, \bar{\boldsymbol{Z}}^{12(2)}_{lm}$	$l+3$

In Table 2.1, $\bar{Y}_{lm}$, $\bar{\boldsymbol{X}}_{lm}$ and $\bar{\boldsymbol{Z}}_{lm}$ are the fully normalized scalar, vector and tensor spherical harmonics, respectively. For a thorough discussion on vector and tensor spherical harmonics reference is made to Rummel & van Gelderen (1992) or Freeden et al. (1994).

Singular values from the Meissl scheme will be used in every step of the remove-restore technique. Depending on the observable, the singular values can be taken directly from Table 2.1 (for disturbance quantities) or be derived (for anomalous quantities). For $l \to \infty$, however, disturbance and anomalous quantities have a similar behaviour. Figure 2.1 visualizes the singular values listed in Table 2.1. While the singular values of the first derivatives increase on the order of $\mathcal{O}(l)$, those of the second derivative increase as $\mathcal{O}(l^2)$.

Remark 2.1 *The singular values in Table 2.1 are not dimensionless; yet they correspond to the notation commonly used in geodesy. The scheme is commutative.*

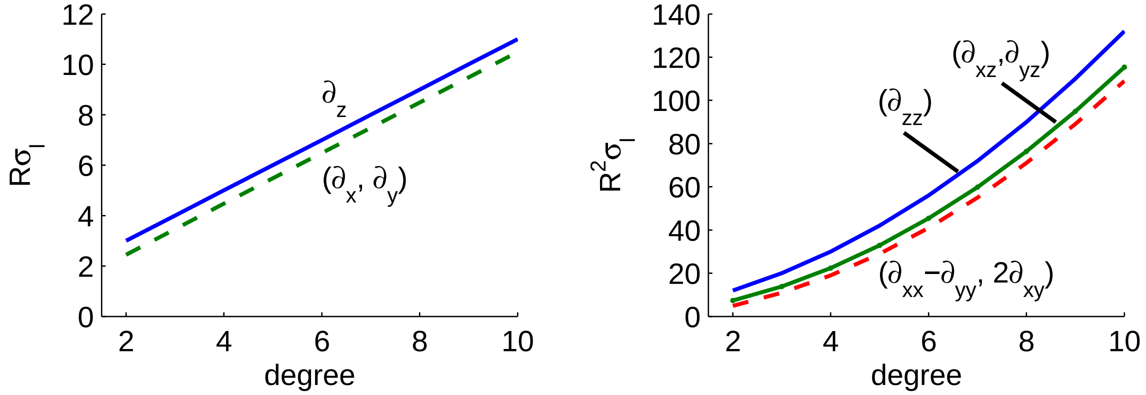

(a) first-order derivatives

(b) second-order derivatives

Figure 2.1: Singular values in the Meissl scheme

2.2 Satellite Contributions

The second terms in the remove-restore technique, $\mathcal{A}T^{\mathrm{S}}$ and $\mathcal{B}T^{\mathrm{S}}$, are contributions of the satellite data. Satellite information is usually provided in spherical harmonics. The spherical harmonic representation is advantageous since it provides global support, orthogonality and harmonicity. On the other hand, spherical harmonics do not show space localization. Thus, local problems are difficult to treat with spherical harmonics only. Non-uniformly distributed data sets may cause problems as well. Nevertheless, the satellite data are assumed to be given in spherical harmonic representation throughout the thesis. The gravitational potential is computed as (Heiskanen & Moritz, 1967),

$$V(r,\theta,\lambda) = \frac{GM}{R} \sum_{l=0}^{\infty} \left(\frac{R}{r}\right)^{l+1} \sum_{m=-l}^{l} \bar{K}_{lm} \bar{Y}_{lm}(\theta,\lambda) \tag{2.3}$$

where

$$\bar{K}_{lm} = \begin{cases} \bar{C}_{lm} \\ \bar{S}_{l|m|} \end{cases} \quad \text{and} \quad \bar{Y}_{lm}(\theta,\lambda) = \begin{cases} \cos m\lambda \bar{P}_{lm}(\cos\theta) & , m \geq 0 \\ \sin |m| \lambda \bar{P}_{l|m|}(\cos\theta) & , m < 0 \end{cases} \tag{2.4}$$

and

r, θ, λ	is the geocentric radius, co-latitude and longitude of point P
GM	is the universal gravitational constant times the mass of the Earth
R	is the mean equatorial radius
$\bar{K}_{lm}$	are the fully normalized potential coefficients
$\bar{Y}_{lm}$	are the fully normalized surface spherical harmonics
$\bar{P}_{lm}$	are the fully normalized associated Legendre functions

Proving uniform convergence of the series inside the Brillouin sphere (a sphere enclosing all masses) is an open problem. While a number of publications indicate that the series might be divergent (Bäschlin, 1948; Moritz, 1961), most of the newer publications assume that the series is also convergent for a point inside the Brillouin sphere (Krarup, 1969; Arnold, 1969, 1978; Moritz, 1989). Even if the series for V would be divergent, however, Runge's theorem ensures that an arbitrarily close V' exists that is convergent (Moritz, 1989, pg. 67). Furthermore, as the series over l is usually truncated to a maximum degree L_S, the potential can always be continued.

Disturbing Potential in Spherical Harmonics

As mentioned before, the disturbing potential is the difference between the gravity potential and a potential generated by a reference ellipsoid, i.e., $T(P) = W(P) - U(P)$. The expansion of T can then be computed as (Heiskanen & Moritz, 1967)

$$T(r, \theta, \lambda) = \frac{GM}{R} \sum_{l=2}^{\infty} \left(\frac{R}{r}\right)^{l+1} \sum_{m=-l}^{l} \Delta\bar{K}_{lm} \bar{Y}_{lm}(\theta, \lambda) \tag{2.5}$$

where

$$\Delta\bar{K}_{lm} = \begin{cases} \bar{C}_{l0} - \bar{U}_{l0} & , \ m = 0, \ l \text{ even} \\ \bar{K}_{lm} & , \ \text{else} \end{cases} \tag{2.6}$$

with $\bar{U}_{l0} = \bar{U}_{2n,0}$ given as

$$\bar{U}_{2n,0} = \frac{(-1)^n \, 3 \, (e^2)^n}{\sqrt{4n+1}(2n+1)(2n+3)} \left[1 - n + 5n\left(\frac{1}{3} - \frac{2}{45}\frac{me'}{q_0}\right)\right] \qquad n = 1, \ldots, \ 5 \tag{2.7}$$

$\bar{U}_{l0}$ are the fully normalized potential coefficients from a Somigliana-Pizzetti reference field. GRS80 is used as the reference field in this thesis. The computational formulas for m, e^2, e' and q_0 are provided in Moritz (1980a) and Chen (1981). Numerical values for $\bar{U}_{l0}$ are summarized in Table A.9. The difference $GM - GM_0$ is assumed to be sufficiently small and the center of mass of the ellipsoid coincides with the center of mass of the Earth ($\bar{C}_{10} = \bar{C}_{11} = \bar{S}_{11} = 0$).

Other Functionals in Spherical Harmonics

When functionals of the disturbing potential have to be computed, the Meissl scheme can be applied. The corresponding singular value can be taken from Table 2.1 and simply inserted into the disturbing potential series as

$$\mathcal{A}T(r,\theta,\lambda) = \frac{GM}{R}\sum_{l=2}^{\infty}\sigma_l \sum_{m=-l}^{l}\Delta\bar{K}_{lm}\bar{Y}_{lm}(\theta,\lambda) \tag{2.8}$$

Example. Gravity disturbances have to be computed from a satellite model at a known position $P = (r,\theta,\lambda)$. The singular value is known to be $\frac{l+1}{r}\left(\frac{R}{r}\right)^{l+1}$ ($\delta g = -\frac{\partial T}{\partial r} = -\frac{\partial T}{\partial z}$). Let the minimum degree of the satellite model be $l = 2$, the maximum degree L_{S} and $GM = GM_0$. The gravity disturbances from the satellite model S are then computed as

$$\delta g^{\mathrm{S}}(P) = \frac{GM}{R}\sum_{l=2}^{L_{\mathrm{S}}}\frac{l+1}{r}\left(\frac{R}{r}\right)^{l+1}\sum_{m=-l}^{l}\Delta\bar{K}^{\mathrm{S}}_{lm}\bar{Y}_{lm}(\theta,\lambda)$$

2.3 The Helmert Scheme

To obtain a solution of the classical geodetic boundary value problems, the disturbing potential has to be a harmonic function. The (twice continuously differentiable) disturbing potential $T : D \rightarrow \mathbb{R}$ ($D \subset \mathbb{R}^3$) is called *harmonic* if it satisfies Laplace's equation, $\Delta T = 0$, in D. Hence, masses between the geoid and the Earth's surface are inadmissible. A reduction process, removing the masses outside the geoid, is necessary ($\mathcal{A}\delta V^{\mathrm{H}}$). The residual field is assumed to be harmonic and the transformation step can be applied. Eventually, the effect of the topographic and atmospheric masses ($\mathcal{B}\delta V^{\mathrm{H}}$) is added back in the restore step. It should be noted that any reduction technique suffers from the insufficient knowledge of the density of the removed masses. A constant density distribution is frequently used ($2.67\,{}^{\mathrm{g}}/_{\mathrm{cm}^3}$), causing an error in the solution.

The Helmert condensation method is a widely used reduction technique, see for instance Helmert (1884); Wichiencharoen (1982); Vaníček & Kleusberg (1987); Wang & Rapp (1990); Sideris & Forsberg (1991); Heck (1992); Martinec (1998); Sjöberg (2000); Kuhn (2000); Huang (2002) to name only a few. Helmert's idea is to compress the topographic and atmospheric masses on a condensation layer that is either 'parallel' to the geoid (1st Helmert condensation with a condensation depth of 21 km below the geoid) or situated at or just below the geoid (2nd Helmert condensation).

In this thesis, the second Helmert condensation method will be used. Since the spatial forms of the Helmert condensation are extensively described in the literature, see for instance Martinec (1998); Novák (2000) and Novák et al. (2003a), only the spectral forms will be discussed. Furthermore, the derivations are confined to the topographic effects. The atmospheric effects, in turn, may be applied in the standard fashion (Ecker & Mittermayer, 1969; Moritz, 1980a). The spectral formulation highlights the concept of the reduction technique, the effect of different condensation schemes and could be used for airborne data due to their band-limited character. Similar investigations using isostatic models such as the Airy-Heiskanen model or the Pratt-Hayford model are reported in Rummel et al. (1988); Sünkel (1985, 1986); Tsoulis (2001).

The residual gravitational potential is the difference between the actual potential of the topography and the corresponding potential of the condensation layer. For a point

P on and outside the Earth's surface $S = \partial D$, it becomes (Heck, 2002)

$$\begin{aligned} \delta V^{\mathrm{H}}(P) &= V_{\mathrm{t}}(P) - V_{\mathrm{ct}}(P) = \\ &= \underbrace{\mu \int\limits_{\omega} \int\limits_{z=R}^{R+H'} \frac{z^2}{K}\, dz\, d\omega}_{\text{topography}} \;-\; \underbrace{GR^2 \int\limits_{\omega} \frac{\varsigma^i}{K}\, d\omega}_{\text{condensed topography}} \end{aligned} \tag{2.9}$$

where

P	is a known point (r, θ, λ)
$V_{\mathrm{t}}(P)$	is the gravitational potential of the topographic masses
$V_{\mathrm{ct}}(P)$	is the gravitational potential of the condensed masses
μ	is the Newtonian universal constant times the mean density $(\mu = G\rho_0)$
K	is the Newtonian integration kernel, see Table 2.2
ς^i	is a condensation density model, see Table 2.3 for different forms of condensation surface layers
z	is the integration variable in radial direction, $R \le z \le R + H'$
$\int_\omega \, d\omega$	is the integration over the unit sphere $(\omega = \{\boldsymbol{x} \mid x_1^2 + x_2^2 + x_3^2 = 1\})$ with $d\omega = \sin\theta \; d\theta d\lambda$ denoting the surface element of the unit sphere.

The *direct* and the *indirect* effect have to be separated. The direct effect $(\mathcal{A}\delta V^{\mathrm{H}})$ is computed at the computation point location P, while the indirect effect $(\mathcal{B}\delta V^{\mathrm{H}})$ is either computed at the computation point (for $\mathcal{B} = \mathcal{A}$) or at the reference sphere Q. The geometry of the problem is shown in Figure 2.2. F, B and S denote the flight path, Bouguer shell and surface of the Earth, respectively.

The integration kernel can be expanded into a series of Legendre polynomials as (Lense, 1954, pg. 14)

$$\begin{aligned} \frac{1}{K} &= \left(r^2 - 2rz\cos\psi + z^2\right)^{-\frac{1}{2}} = \frac{1}{r}\left(1 - 2\frac{z}{r}\cos\psi + \left(\frac{z}{r}\right)^2\right)^{-\frac{1}{2}} \\ &= \frac{1}{r}\sum_{l=0}^{\infty}\left(\frac{z}{r}\right)^l P_l(\cos\psi) \qquad (r > z) \end{aligned} \tag{2.10}$$

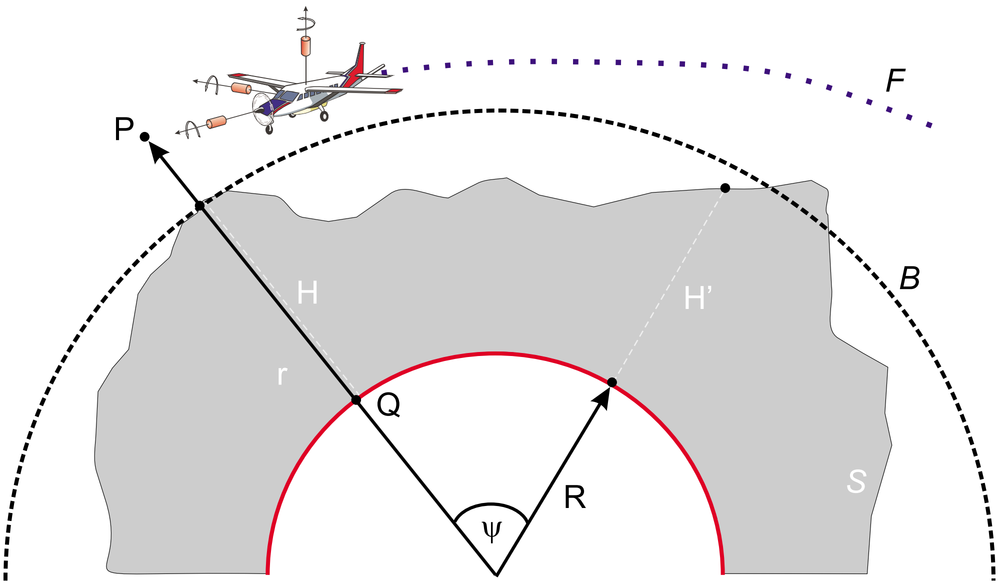

Figure 2.2: Geometry of the problem

where P_l stands for the l-th degree Legendre polynomial and $\psi\angle(P, P')$ is the spherical distance between the computation point (θ, λ) and the integration point (θ', λ')

$$\cos\psi = \cos\theta\cos\theta' + \sin\theta\sin\theta'\cos(\lambda' - \lambda) \tag{2.11}$$

Unfortunately, the series is not convergent everywhere (Grafarend & Engels, 1994). To ensure a convergent series expansion in the following derivations, the computation point P is assumed to be *outside* the Brillouin sphere. This can safely be assumed for measurements taken at airborne or satellite altitude. The indirect effect will be computed at the reference sphere R that sufficiently approximates the geoid. Table 2.2 summarizes the chosen parameters for the direct and the indirect effect and explicitly shows the integration kernel K. The case $\psi = 0$ (singularity) may require special treatment.

One has to distinguish between the *topography* and the *terrain*. The topography, shown in grey in Figure 2.2, includes all masses above the geoid (except the atmosphere). When subtracting the Bouguer shell ($V_{\mathrm{B}}(P) = \frac{4\pi\mu}{3r}(r_{\mathrm{B}}^3 - R^3)$) from the potential of

Table 2.2: Direct and indirect effect

Effect	Height	Operator	$\frac{1}{K}$	Convergence	Remark
Direct	r	$\mathcal{A}$	$\frac{1}{r}\sum_{l=0}^{\infty}\left(\frac{z}{r}\right)^l P_l(\cos\psi)$	$r > z$	$z = R$ for V_{ct}
Indirect	R	$\mathcal{B}$	$\frac{1}{z}\sum_{l=0}^{\infty}\left(\frac{R}{z}\right)^l P_l(\cos\psi)$	$z > R$	$z = R$ for V_{ct}

the topographical masses, however, the potential of the terrain (sometimes also called topographic roughness or irregular part of the topography) remains. Thus, the terrain is the deviation between the actual topographical radius $r' = R + H'$ and the constant radius $r_{\mathrm{B}} = R + H$. The Bouguer shell is mainly introduced for computational reasons; the effect of the terrain is considerably smaller than the effect of the topography.

Gravitational Potential of the Topography V_{t}

Inserting the integration kernel into Eqn. (2.9) results in the gravitational potential of the topographic masses as

$$\begin{aligned} V_{\mathrm{t}}(P) &= \mu \int\limits_{\omega} \int\limits_{z=R}^{R+H'} \frac{z^2}{K}\, dz\, d\omega \\ &= \mu \int\limits_{\omega} \int\limits_{z=R}^{R+H'} \frac{1}{r}\sum_{l=0}^{\infty}\left(\frac{z}{r}\right)^l P_l(\cos\psi) z^2\, dz\, d\omega \\ &= \mu \sum_{l=0}^{\infty}\left(\frac{1}{r}\right)^{l+1} \int\limits_{\omega} \int\limits_{z=R}^{R+H'} z^{l+2} P_l(\cos\psi)\, dz\, d\omega \end{aligned} \tag{2.12}$$

Interchanging the summation and integration is permitted due to a uniformly convergent kernel. Following Rummel et al. (1988), the integral term $\int z^{l+2}\, dz$ can be derived as

$$\int\limits_{z=R}^{R+H'} z^{l+2}\, dz = \frac{R^{l+3}}{l+3}\left[\left(1+\frac{H'}{R}\right)^{l+3} - 1\right] = \frac{R^{l+3}}{l+3}\sum_{k=1}^{l+3}\begin{pmatrix} l+3 \\ k \end{pmatrix}\left(\frac{H'}{R}\right)^k \tag{2.13}$$

Eqn. (2.12) then becomes (Vaníček et al., 1995)

$$V_{\mathrm{t}}(P) = \mu R^2 \sum_{l=0}^{\infty} \left(\frac{R}{r}\right)^{l+1} \frac{1}{l+3} \sum_{k=1}^{l+3} \begin{pmatrix} l+3 \\ k \end{pmatrix} \int_{\omega} \left(\frac{H'}{R}\right)^{k} P_l(\cos\psi)\, d\omega \quad (2.14)$$

Gravitational Potential of the Condensed Topography $V_{\mathbf{ct}}$

The derivation of the condensed topographic effects is easier than the derivation of the topography; only the integration kernel and a condensation scheme have to be inserted into the integral. The most commonly used condensation methods are listed in Table 2.3. They are extensively discussed in Wichiencharoen (1982). Selecting the mean density condensation scheme, for instance, V_{ct} becomes

$$\begin{aligned} V_{\mathrm{ct}}(P) &= GR^2 \int_{\omega} \frac{\varsigma^i}{K}\, d\omega \\ &= \mu R^2 \sum_{l=0}^{\infty} \left(\frac{R}{r}\right)^{l+1} \int_{\omega} \left(\frac{H'}{R}\right) P_l(\cos\psi)\, d\omega \qquad (2.15) \end{aligned}$$

Note that z is equal to R in the integration kernel as required for the second Helmert condensation, see Table 2.2. Using the first Helmert condensation, z would be equal to $z = R - 21\,\mathrm{km}$. In addition, the density is assumed to be constant.

Table 2.3: Condensation schemes

ς^i	Condensation name	Remarks
$\varsigma^1 = \rho_0 H$	Mean density	
$\varsigma^2 = \rho_0 H \left[1 + \frac{H}{R} + \frac{H^2}{3R^2}\right]$	Mass conservation	no $l = 0$ term
$\varsigma^3 = \rho_0 H \left[1 + \frac{3H}{2R} + \frac{H^2}{R^2} + \frac{H^3}{4R^3}\right]$	Mass-centre conservation	no $l = 1$ term

Residual Topographical Potential $\delta V^{\mathbf{H}}$

The derived expressions in Eqn. (2.14) and (2.15) are subtracted to yield the residual potential. Thus, Eqn. (2.9) becomes for the mean density condensation scheme

$$\begin{aligned}
\delta V^{\mathrm{H}}(P) &= \mu R^2 \sum_{l=0}^{\infty} \left(\frac{R}{r}\right)^{l+1} \left\{ \frac{1}{l+3} \sum_{k=1}^{l+3} \begin{pmatrix} l+3 \\ k \end{pmatrix} \int\limits_{\omega} \left(\frac{H'}{R}\right)^{k} P_l(\cos\psi)\ d\omega - \right. \\
&\qquad \left. - \int\limits_{\omega} \left(\frac{H'}{R}\right) P_l(\cos\psi)\ d\omega \right\} \\
&= \mu R^2 \sum_{l=0}^{\infty} \left(\frac{R}{r}\right)^{l+1} \frac{1}{l+3} \sum_{k=2}^{l+3} \begin{pmatrix} l+3 \\ k \end{pmatrix} \int\limits_{\omega} \left(\frac{H'}{R}\right)^{k} P_l(\cos\psi)\ d\omega \qquad (2.16)
\end{aligned}$$

The residual potential for the indirect effect takes a very similar form as the direct effect. Omitting the intermediate steps, the indirect effect becomes

$$\begin{aligned}
\delta V^{\mathrm{H}}(Q) &= \mu R^2 \sum_{l=0}^{\infty} \left\{ \frac{1}{2-l} \sum_{k=1}^{2-l} \begin{pmatrix} 2-l \\ k \end{pmatrix} \int\limits_{\omega} \left(\frac{H'}{R}\right)^{k} P_l(\cos\psi)\ d\omega \right. \\
&\qquad \left. - \int\limits_{\omega} \left(\frac{H'}{R}\right) P_l(\cos\psi)\ d\omega \right\} \\
&= \mu R^2 \sum_{l=0}^{\infty} \frac{1}{2-l} \sum_{k=2}^{2-l} \begin{pmatrix} 2-l \\ k \end{pmatrix} \int\limits_{\omega} \left(\frac{H'}{R}\right)^{k} P_l(\cos\psi)\ d\omega \qquad (2.17)
\end{aligned}$$

There are two main differences between the direct and the indirect effect formulas, compare Eqn. (2.16) and (2.17). The first difference is the binomial series and the summation over k. This is due to the different kernel functions. The second difference is that the upward continuation term is required for the direct effect to accommodate for the different computation height.

Analogous derivations can be performed for the other condensation schemes. Recognizing the conceptual similarities, one obtains the residual potential for the direct and the indirect effect as

$$\delta V^{\mathrm{H}}(\cdot) = \mu R^2 \int\limits_{\omega} \sum_{l=0}^{\infty} \sigma_l \sum_{k=1}^{\mathrm{DG}} \Lambda_l^{(k)} \left(\frac{H'}{R}\right)^k P_l(\cdot,\cdot)\, d\omega \tag{2.18}$$

where DG stands for the maximum summation degree; $\mathrm{DG} = l + 3$ for the direct effect and $\mathrm{DG} = 2 - l$ for the indirect effect. The computation point $(\cdot)$ is either P or Q. $\sigma_l = \left(\frac{R}{r}\right)^{l+1}$ for the direct effect and $\sigma_l = 1$ in the indirect effect. $\Lambda_l^{(k)}$ will be denoted as the *Helmert values*. The Helmert values for all three condensation schemes are listed in tables 2.4 and 2.5. They constitute the *Helmert scheme*.

Table 2.4: Helmert scheme – direct effect

ς^i	$\Lambda_l^{(1)}$	$\Lambda_l^{(2)}$	$\Lambda_l^{(3)}$	$\Lambda_l^{(4)}$	$\Lambda_l^{(k)},\ k > 4$
ς^1	0	$\frac{l+2}{2}$	$\frac{(l+1)(l+2)}{6}$	$\frac{l(l+1)(l+2)}{24}$	$\frac{1}{l+3}\binom{l+3}{k}$
ς^2	0	$\frac{l}{2}$	$\frac{l(l+3)}{6}$	$\frac{l(l+1)(l+2)}{24}$	$\frac{1}{l+3}\binom{l+3}{k}$
ς^3	0	$\frac{l-1}{2}$	$\frac{l^2+3l-4}{6}$	$\frac{l^3+3l^2+2l-6}{24}$	$\frac{1}{l+3}\binom{l+3}{k}$

Table 2.5: Helmert scheme – indirect effect

ς^i	$\Lambda_l^{(1)}$	$\Lambda_l^{(2)}$	$\Lambda_l^{(3)}$	$\Lambda_l^{(4)}$	$\Lambda_l^{(k)},\ k > 4$
ς^1	0	$-\frac{l-1}{2}$	$\frac{l^2-l}{6}$	$\frac{-l^3+l}{24}$	$\frac{1}{2-l}\binom{2-l}{k}$
ς^2	0	$-\frac{l+1}{2}$	$\frac{l^2-l-2}{6}$	$\frac{-l^3+l}{24}$	$\frac{1}{2-l}\binom{2-l}{k}$
ς^3	0	$-\frac{l+2}{2}$	$\frac{l^2-l-6}{6}$	$\frac{-l^3+l-6}{24}$	$\frac{1}{2-l}\binom{2-l}{k}$

For the numerical evaluation of the residual potential, Eqn. (2.18) is often arranged in an alternative form

$$\delta V^{\mathrm{H}}(\cdot) = \mu R^2 \int\limits_{\omega} \sum_{k=1}^{\mathrm{DG}} K^{(k)}(\cdot,\cdot) \left(\frac{H'}{R}\right)^k \, d\omega \tag{2.19}$$

where the kernel functions are

$$K^{(k)}(P,P') = \sum_{l=0}^{\infty} \left(\frac{R}{r}\right)^{l+1} \Lambda_l^{(k)} P_l(\cos\psi) \text{ or } K^{(k)}(Q,Q') = \sum_{l=0}^{\infty} \Lambda_l^{(k)} P_l(\cos\psi) \tag{2.20}$$

Expanding both the integration kernel and the topographical heights leads to the final results for the residual potential

$$\delta V^{\mathrm{H}}(\cdot) = \mu R^2 \sum_{l=0}^{\infty} \frac{4\pi}{2l+1} \sigma_l \sum_{k=1}^{\mathrm{DG}} \Lambda_l^{(k)} H_l^k(\theta,\lambda) \tag{2.21}$$

where the Laplace surface harmonics of topographical heights are defined as, e.g. Heck (2001)

$$H_l^k = H_l^k(\theta,\lambda) = \frac{2l+1}{4\pi} \int\limits_{\omega} \left(\frac{H'}{R}\right)^k P_l(\cos\psi) \, d\omega \tag{2.22}$$

Remark 2.2 *The series over k is converging very fast. Therefore, it is often truncated after the third term $k = 3$; see Vaníček et al. (1995), Novák et al. (2003a) or Nahavandchi & Sjöberg (1998).*

Remark 2.3 *When splitting the integration into Bouguer shell and terrain, conceptually the same formulas are obtained. The only difference is the term $\left(\frac{H'}{R}\right)^k - \left(\frac{H}{R}\right)^k$ instead of $\left(\frac{H'}{R}\right)^k$. The former is derived in Heck (2002) for the mass conservation scheme.*

Other Functionals in the Helmert Scheme

Using singular values (only self-adjoint operators are considered here) from the Meissl scheme, other functionals than the residual potential can be computed as well. Thus, a link between the Meissl scheme and the Helmert scheme is established. Omitting the intermediate steps, the direct and the indirect effect for functionals of the gravitational potential can be obtained as

$$\left.\begin{array}{l}\mathcal{A}\delta V^{\mathrm{H}}(P)\\ \mathcal{B}\delta V^{\mathrm{H}}(Q)\end{array}\right\} = \mu R^2 \int\limits_{\omega} \sum_{l=0}^{\infty} \sigma_l \sum_{k=1}^{\mathrm{DG}} \Lambda_l^{(k)} \left(\frac{H'}{R}\right)^k P_l(\cos\psi)\; d\omega \tag{2.23}$$

Note the similarity of Eqn. (2.23) to Eqn. (2.18). Depending on the functionals involved, the only difference may be the singular value σ_l. Alternatively, Eqn. (2.23) can be written as

$$\left.\begin{array}{l}\mathcal{A}\delta V^{\mathrm{H}}(P)\\ \mathcal{B}\delta V^{\mathrm{H}}(Q)\end{array}\right\} = \mu R^2 \int\limits_{\omega} \begin{cases} \displaystyle\sum_{k=1}^{l+3} K^{(k)}(P,P') \left(\frac{H'}{R}\right)^k & d\omega \\ \displaystyle\sum_{k=1}^{2-l} K^{(k)}(Q,Q') \left(\frac{H'}{R}\right)^k & d\omega \end{cases} \tag{2.24}$$

where

$$K^{(k)}(P,P') = \sum_{l=0}^{\infty} \sigma_l \Lambda_l^{(k)} P_l \quad \text{and} \quad K^{(k)}(Q,Q') = \sum_{l=0}^{\infty} \sigma_l \Lambda_l^{(k)} P_l \tag{2.25}$$

Finally, one obtains the result

$$\left.\begin{array}{l}\mathcal{A}\delta V^{\mathrm{H}}(P)\\ \mathcal{B}\delta V^{\mathrm{H}}(Q)\end{array}\right\} = \mu R^2 \sum_{l=0}^{\infty} \begin{cases} \dfrac{4\pi}{2l+1}\sigma_l \displaystyle\sum_{k=1}^{l+3} \Lambda_l^{(k)} H_l^k(\theta,\lambda) & \text{direct effect} \\ \dfrac{4\pi}{2l+1}\sigma_l \displaystyle\sum_{k=1}^{2-l} \Lambda_l^{(k)} H_l^k(\theta,\lambda) & \text{indirect effect} \end{cases} \tag{2.26}$$

Remark 2.4 *In the usual notation, the direct and the indirect effects on gravity (= attraction) are defined as the* positive *radial derivatives of the residual potential, see for instance Martinec & Vaníček (1994a,b).*

Comparison of Condensation Schemes

An advantage of the Helmert scheme is that condensation methods can be compared. For that purpose only the Helmert values have to be analyzed. Although they *cannot* be identified as singular values as in the Meissl scheme, they completely characterize the problem. The Helmert values $\Lambda_l^{(2)}$ and $\Lambda_l^{(3)}$ for the direct and the indirect effect are shown in Figure 2.3. The direct effect, shown in the subfigures (a) and (b), will be discussed first. They are essentially parallel lines, which means that the condensation schemes generate solutions that are offset with respect to one another. While the second Helmert values increase as $\mathcal{O}(l)$, the third Helmert values increase with $\mathcal{O}(l^2)$. The Helmert values of the indirect effect show an interesting behaviour. For $\Lambda_l^{(2)}$, the values are linearly decreasing with increasing degree, see Figure 2.3 (c). The Helmert values $\Lambda_l^{(3)}$ in turn are quadratically increasing, see Figure 2.3 (d). The dominant term is, however, $\Lambda_l^{(2)}$ since $(H/R)^k,\ k > 2$ is very small. Hence, comparing the direct and the indirect Helmert values, it can be concluded that the indirect effect *compensates* the direct effect. This is well-known and expected. However, this phenomenon becomes immediately obvious when examining the Helmert values.

The remarks for Table 2.3 can be explained by inspecting Figure 2.3. Both Helmert values are zero for degree $l = 0$ in the mass conservation scheme and are zero for $l = 1$ in the mass-centre conservation scheme. This has been also shown in a completely different way in Wichiencharoen (1982). Yet the analysis in the spectral domain provides a more transparent insight into the problem.

Example. The computational formulas for the *direct effect* of band-limited airborne gravity disturbances at flight height and the corresponding *indirect effect* of the residual potential on the geoid are sought. The *mass-centre conservation* scheme shall be used. Let the squared (H_l^2) and the cubed (H_l^3) Laplace surface harmonics of the topographical heights be given ($k = 3$). The singular value for gravity disturbances at flight height can be obtained from the Meissl scheme as $\sigma_l = \frac{l+1}{r}\left(\frac{R}{r}\right)^{l+1}$. The direct effect on gravity (topographic attraction would be $\delta A^{\mathrm{TOP}} = -\delta g^{\mathrm{H}}$) is then computed as ($\Lambda_l^{(2)} = [l-1]/2$ and $\Lambda_l^{(3)} = [l^2+3l-4]/6$)

$$\begin{aligned}\delta g^{\mathrm{H}}(P) &= \mu R^2 \sum_{l=n_1}^{n_2} \frac{4\pi}{2l+1}\left(\frac{l+1}{r}\right)\left(\frac{R}{r}\right)^{l+1} \sum_{k=1}^{l+3} \Lambda_l^{(k)} H_l^k(\theta,\lambda) \\ &= 2\pi\mu R \sum_{l=n_1}^{n_2} \frac{l+1}{2l+1}\left(\frac{R}{r}\right)^{l+2}\left[(l-1)H_l^2 + \frac{(l^2+3l-4)}{3}H_l^3\right]\end{aligned}$$

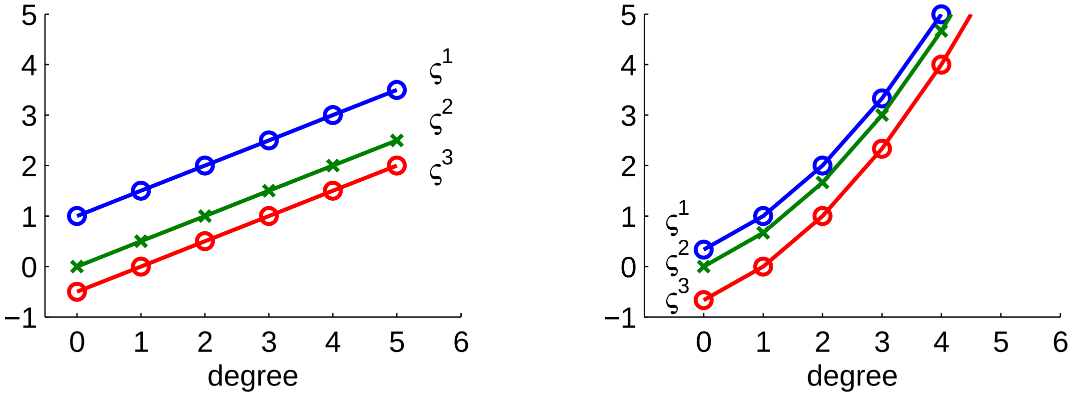

(a) $\Lambda_l^{(2)}$ terms for the direct effect (b) $\Lambda_l^{(3)}$ terms for the direct effect

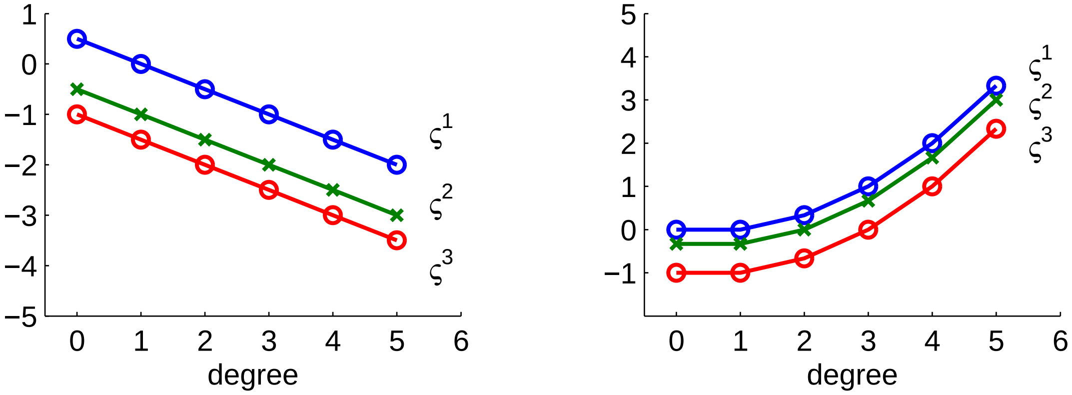

(c) $\Lambda_l^{(2)}$ terms for the indirect effect (d) $\Lambda_l^{(3)}$ terms for the indirect effect

Figure 2.3: Helmert values for the direct and indirect effects

where $n_1 \leq l \leq n_2$ is the resolved frequency band of the airborne data. The indirect effect on the potential at the geoid is ($\sigma_l = 1$, $\Lambda_l^{(2)} = -\left[l+2\right]/2$ and $\Lambda_l^{(3)} = \left[l^2 - l - 6\right]/6$)

$$\begin{aligned} \mathcal{B}\delta V^{\mathrm{H}} = \delta V^{\mathrm{H}}(R,\theta,\lambda) &= \mu R^2 \sum_{l=n_1}^{n_2} \frac{4\pi}{2l+1}\left[-\frac{l+2}{2}H_l^2 + \frac{-l^2+l-6}{6}H_l^3\right] \\ &= 2\pi\mu R^2 \sum_{l=n_1}^{n_2} \frac{1}{2l+1}\left[-(l+2)H_l^2 + \frac{l^2-l-6}{3}H_l^3\right] \end{aligned}$$

The indirect effect is the vertical separation between the co-geoid (geoid in Helmert's space) and the geoid.

Remark 2.5 *Note that all anomalous quantities require the calculation of a* secondary indirect effect*. This is due to the fact that anomalous quantities involve an unknown position (free boundary value problem).*

2.4 Transformations

The process $\mathcal{A}T \rightarrow \mathcal{B}\hat{T}$ may be defined as a *tranformation* or *mapping* from the input functional $\mathcal{A}T$ to the estimated output functional $\mathcal{B}\hat{T}$ (Note that the prime has been neglected). T is the disturbing potential. There are three common transformations in gravity field modeling besides the trivial case. For mixed problems refer to Holota (1995). In the following, only the self-adjoint case will be discussed. The three common transformations are all of convolution type. They are:

i) $\mathcal{A}T(R,\theta,\lambda) \rightarrow \mathcal{B}\hat{T}(r,\theta,\lambda)$, where $\mathcal{A} = \mathcal{B}$: The input functional is the same as the output functional. This transformation involves a height (or height level) change. It is described by the first boundary value problem; more specifically, the exterior Dirichlet problem. The upward continuation is the direct problem. The downward continuation in turn is an inverse problem for which no continuous solution exists. Chapter 3 describes and analyzes this case in detail.

ii) $\mathcal{A}T(R,\theta,\lambda) \rightarrow \mathcal{B}\hat{T}(R,\theta,\lambda)$, where $\mathcal{A} \neq \mathcal{B}$: The input functional is different from the output functional. Usually, this also includes a unit change. A well-known example is the transformation of gravity anomalies to the potential at the geoid. This involves an integration with the Stokes integral, i.e. Δg [mGal] $\rightarrow T$ [$\mathrm{m}^2/\mathrm{s}^2$]. It is the solution of the third boundary-value problem. The second boundary value problem can be described in an analogous way.

iii) $\mathcal{A}T(R,\theta,\lambda) \rightarrow \mathcal{B}\hat{T}(r,\theta,\lambda)$, where $\mathcal{A} \neq \mathcal{B}$: In this case, the transformation includes two steps at once, the upward continuation and the conversion into the desired output functional. One may denote this mapping as one-step approach (Novák & Heck, 2002). Using band-limited data, the downward continuation can also be formulated in one step.

All three transformations are based on the same solution strategy. The gravity data are transformed to the disturbing potential in the first step. The second step, in turn, maps the disturbing potential into the desired functional of the disturbing potential. These mappings may be performed in the space domain or in the spectral domain:

$$\begin{tikzcd}
\text{space domain} & g = \mathcal{A}T \arrow[r, leftrightarrow] \arrow[d, leftrightarrow] & T = \mathcal{A}^{-1}g \arrow[r, leftrightarrow] \arrow[d, leftrightarrow] & \mathcal{B}\hat{T} = \hat{f} \arrow[d, leftrightarrow] \\
\text{spectral domain} & g_{lm} = \sigma_l t_{lm} \arrow[r, leftrightarrow] & t_{lm} = \dfrac{g_{lm}}{\sigma_l} \arrow[r, leftrightarrow] & \hat{f}_{lm} = \lambda_l t_{lm} = \dfrac{\lambda_l}{\sigma_l} g_{lm}
\end{tikzcd} \tag{2.27}$$

where λ_l and $\sigma_l \neq 0$ are the singular values linking the disturbing potential and the output functionals. Eqn. (2.27) is commutative, i.e., path independent. t_{lm}, g_{lm} and $\hat{f}_{lm}$ are the Fourier coefficients of t, g and $\hat{f}$, e.g.

$$g(Q) = \sum_{l=0}^{\infty} \sum_{m=-l}^{l} g_{lm} \bar{Y}_{lm}(Q) \qquad \text{with} \qquad g_{lm} = (g, \bar{Y}_{lm})_X \tag{2.28}$$

Example. Gravity disturbances at flight height are given and the disturbing potential is the sought function. The singular value for the gravity disturbance at flight height is $\sigma_l = \frac{l+1}{r} \left(\frac{R}{r}\right)^{l+1}$ and $\lambda_l = 1$. The spectral solution is then $\hat{f}_{lm} = \hat{t}_{lm} = \frac{r}{l+1} \left(\frac{r}{R}\right)^{l+1} \delta g_{lm}$.

Integral Representation

The integral representation is an often used representation of the disturbing potential. Other parametrizations are described and discussed in Kusche (2002). Let the continuously given gravity observable (on a sphere with radius R) be decomposed into (Heiskanen & Moritz, 1967, pg. 30)

$$\sum_{m=-l}^{l} g_{lm} \bar{Y}_{lm}(\theta, \lambda) = \frac{2l+1}{4\pi} \int\limits_{\omega} g(\theta, \lambda) P_l(\cos\psi) \; d\omega \tag{2.29}$$

Then, using Eqn. (2.27), the output functional $\mathcal{B}\hat{T}(P)$ can be derived as

$$\mathcal{B}\hat{T}(P) = \frac{1}{4\pi} \int\limits_{\omega} K(\psi)\mathcal{A}T(Q)\ d\omega(Q) \tag{2.30}$$

where the (isotropic) kernel function is ($\sigma_l \neq 0$)

$$K(\psi) = K(P,Q) = \sum_{l=0}^{\infty} (2l+1)\frac{\lambda_l}{\sigma_l} P_l(\cos\psi) \tag{2.31}$$

Note that Eqn. (2.31) may include the upward continuation term. The point $P(r,\theta,\lambda)$, $r \geq R$ is on or outside a sphere of radius R and f is harmonic and regular at infinity. Depending on the functionals involved, the summation over degree l may be truncated at a finite value and start from a value different than zero.

Example. The computation of T from Δg, i.e. the Stokes integration, shall be performed. The singular values can be derived as $\sigma_l = (l-1)/R$ ($\Delta g = -\frac{\partial T}{\partial r} - \frac{2}{r}T$) and $\lambda_l = 1$. Thus, the Stokes integral becomes (Heiskanen & Moritz, 1967, pg. 97)

$$\hat{T} = \frac{R}{4\pi} \int\limits_{\omega} K(\cdot, Q')\Delta g(Q')\ d\omega(Q')$$

with the (singular) Stokes kernel function

$$K(\psi) = K(\cdot, Q') = \sum_{l=2}^{\infty} \frac{2l+1}{l-1} P_l(\cos\psi)$$

Note that the summation starts at two, since $\sigma_l = 0$ is inadmissible for $l = 1$. The $l = 0$ term can be neglected if the reference ellipsoid has the same potential as the geoid and has the same mass as the Earth (Heiskanen & Moritz, 1967, pg. 101). This problem will be treated in more detail in Chapter 6.

Discretization, Frequency Division and Integration Domain Division

In practice, the integral representation in Eqn. (2.30) has to be *discretized*, the integral is replaced by discrete summations or convolutions. Furthermore, mean values are frequently used in the integration process. They are averages of point data in a certain area. For an area of extent $2\pi(1-\cos\psi_{\mathrm{c}})$, i.e. point data inside a spherical cap of radius ψ_{c}, the mean values $\bar{g}(Q)$ can be obtained by (Meissl, 1971a)

$$\bar{g}(Q) = \frac{1}{2\pi(1-\cos\psi_{\mathrm{c}})} \int\limits_{\omega_{\mathrm{c}}} g(Q')\ d\omega(Q') \tag{2.32}$$

Due to the lack of global gravity data, two further modifications are frequently employed – the *data frequency division* and the *integration domain division*. This is shown in Figure 2.4 (b). The graphical representation of the two divisions closely follows de Min (1996). The data frequency division is shown along the horizontal axis, while the integration domain division is performed along the vertical axis of the plot. The frequency division divides the gravity spectrum into the low-frequency part and the medium to high-frequency part. The integration domain in turn, divides the spectrum spatially. One usually distinguishes between the *near zone* and the *far* or *distant zone*. The near zone is the area, where local or regional data are available. The far zone is the region over the remainder of the sphere.

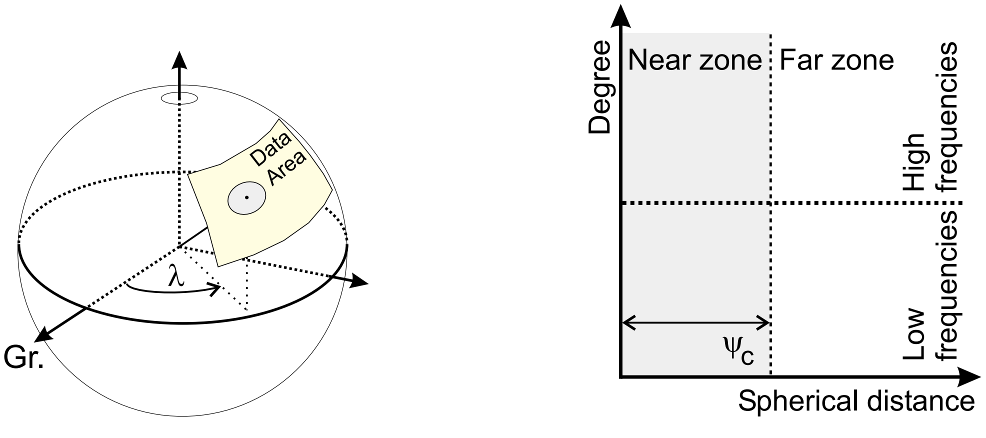

(a) Geometry of the data area and the spherical cap

(b) Two divisions (de Min, 1996)

Figure 2.4: Geometry and two divisions

In practice, the remove-restore technique represents the frequency division model.

The low-frequencies in the near-zone are replaced by the satellite or geopotential data. The integration is only performed in the near zone. The far zone may be approximated by the information from a satellite or geopotential models (Molodenskij, 1958).

Putting it alltogether, the spatial solution of the remove-restore technique is given by (Rapp & Rummel, 1975)

$$\mathcal{B}\hat{T} = \mathcal{B}T^{\mathrm{S}} + \frac{1}{4\pi} \int\limits_{\omega_{\mathrm{c}}} K(\cdot, Q)\mathcal{A}T'(Q)\; d\omega(Q) \tag{2.33}$$

where $\mathcal{A}T'(Q)$ are the residual (mean) gravity data $\mathcal{A}T'(Q) = \mathcal{A}T(Q) - \mathcal{A}T^{\mathrm{S}}(Q)$. The integral over ω_{c} stands for the near-zone integration, i.e.

$$\int\limits_{\omega_{\mathrm{c}}} d\omega(Q) = \int\limits_{\alpha=0}^{2\pi} \int\limits_{\psi=0}^{\psi_{\mathrm{c}}} \sin\psi\; d\psi\; d\alpha \tag{2.34}$$

α is the azimuth and ψ_{c} is the spherical cap radius. In the following, $\mathcal{B}\hat{T}(Q)$ is abbreviated by $\mathcal{B}\hat{T}$.

Spectral Solutions

The remove-restore technique can also be derived in the spectral domain. This illustrates the main characteristics of the method and allows for an error analysis. Let the disturbing potential be represented by surface spherical harmonics as

$$T = T(\theta, \lambda) = \sum_{l=0}^{\infty} t_l(\theta, \lambda) = \sum_{l=0}^{\infty} t_l \tag{2.35}$$

Then, the spectral solution of Eqn. (2.33) is given as

$$\begin{aligned} \mathcal{B}\hat{T} &= \sum_{l=0}^{L_{\mathrm{S}}} \lambda_l t_l^{\mathrm{S}} + \frac{1}{2} \sum_{l=0}^{L_{\mathrm{S}}} S_l (g_l - g_l^{\mathrm{S}}) + \frac{1}{2} \sum_{l=L_{\mathrm{S}}+1}^{\infty} S_l g_l \\ &= \frac{1}{2} \sum_{l=0}^{L_{\mathrm{S}}} Q_l g_l^{\mathrm{S}} + \frac{1}{2} \sum_{l=0}^{\infty} S_l g_l \end{aligned} \tag{2.36}$$

where t_l^{S} and $g_l^{\mathrm{S}} = \sigma_l t_l^{\mathrm{S}}$ are the l-th degree (estimates of the) disturbing potential and disturbing potential functionals derived from satellite potential coefficients, respectively. The first equation on the right side of Eqn. (2.36) is the spectral representation of the remove-restore technique. The second equation is the spectral representation of the *local data solution* (Method B in Rapp & Rummel (1975)). Eqn. (2.36) shows the equivalence between the remove-restore technique and the local data solution in the spectral domain. The two solutions are shown in figures 2.5 (a) and (b).

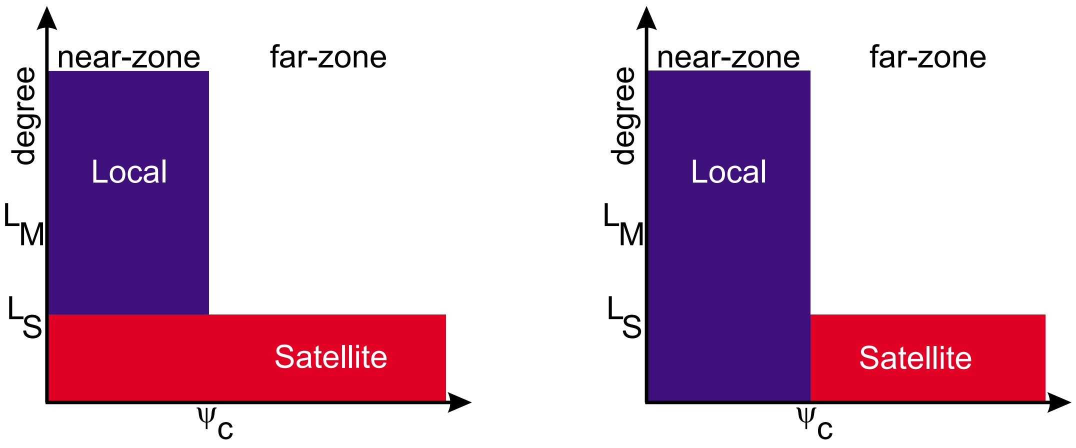

(a) Remove-restore technique (b) Local data solution

Figure 2.5: Combinations using satellite data and one local gravity data set (de Min, 1996)

The coefficients S_l are

$$S_l = \int_0^\pi K(\psi) P_l(\cos\psi) \sin\psi \; d\psi - \int_{\psi_c}^\pi K(\psi) P_l(\cos\psi) \sin\psi \; d\psi = 2\frac{\lambda_l}{\sigma_l} - Q_l \qquad (2.37)$$

due to the orthogonality relations of the Legendre polynomials $\int_0^\pi P_l P_n \sin\psi \; d\psi = \frac{2}{2l+1}\delta_{ln}$. The coefficients Q_l are usually denoted as *truncation coefficients* and can be written as (Heiskanen & Moritz, 1967, pg. 260)

$$Q_l = \int_{\psi_c}^{\pi} K(\psi) P_l(\cos\psi) \sin\psi \; d\psi = \int_{0}^{\pi} \bar{K}(\psi) P_l(\cos\psi) \sin\psi \; d\psi \tag{2.38}$$

Note that the truncation coefficients here may contain a unit while the original truncation coefficients in Heiskanen & Moritz (1967) are dimensionless. Q_l can be numerically computed using recursive algorithms (Paul, 1973; Hagiwara, 1976). The second integral of Eqn. (2.38) is extended over the entire sphere ω. In this case, the *(truncation) error kernel* $\bar{K}(\psi)$ has to be used. For the spherical case, it is piecewise discontinuous:

$$\bar{K}(\psi) = \begin{cases} 0 & \text{for } 0 < \psi \leq \psi_c \\ K(\psi) & \text{for } \psi_c < \psi \leq \pi \end{cases} \tag{2.39}$$

Example. Let the output functional be the disturbing potential ($\mathcal{B}\hat{T} = \hat{T}$) and $g_l = \Delta g_l = \Delta g_l(R, \theta, \lambda)$ the l-th degree surface spherical harmonic of the gravity anomalies ($\sigma_l = \frac{l-1}{R}$, $\lambda_l = 1$). The spherical Stokes kernel shall be used. Using Eqn. (2.36), this results in

$$\hat{T} = \sum_{l=0}^{L_S} \frac{R}{l-1} \Delta g_l^S + \frac{1}{2} \sum_{l=0}^{L_S} S_l (\Delta g_l - \Delta g_l^S) + \frac{1}{2} \sum_{l=L_S+1}^{\infty} S_l \Delta g_l$$

where the S_l are given as, see Eqn. (2.37),

$$S_l \;\; = \;\; \int_0^{\pi} S(\psi) P_l(\cos\psi) \sin\psi \; d\psi - Q_l = 2\frac{R}{l-1} - Q_l$$

This is equivalent to Eqn. (12) in Vaníček & Featherstone (1998).

In the remove-restore technique, the low-frequency spectrum is covered by the satellite data and the medium to high frequencies are obtained from the local gravity data that are reduced by the satellite model. Clearly, the medium to high frequencies of the far-zone are missing in the solution. In the local data method, the local data are not reduced by the satellite model. The combination is then obtained by, see for instance Sjöberg & Hunegnaw (2000, pg. 233),

$$\begin{aligned}\mathcal{B}\hat{T} &= \sum_{l=0}^{L_\mathrm{S}} \frac{\lambda_l}{\sigma_l} g_l^\mathrm{S} + \frac{1}{4\pi} \int\limits_{\omega_\mathrm{c}} K(\cdot, Q) \left[\mathcal{A}T(Q) - \mathcal{A}T^\mathrm{S}(Q)\right] \, d\omega(Q) \\ &= \frac{1}{2} \sum_{l=0}^{L_\mathrm{S}} Q_l g_l^\mathrm{S} + \frac{1}{4\pi} \int\limits_{\omega_\mathrm{c}} K(\cdot, Q) \mathcal{A}T(Q) \, d\omega(Q) \end{aligned} \tag{2.40}$$

since $\int\limits_{\omega_\mathrm{c}} d\omega = \int\limits_{\omega} d\omega - \int\limits_{\omega-\omega_\mathrm{c}} d\omega$ and

$$\frac{1}{4\pi} \int\limits_{\omega} K\mathcal{A}T^\mathrm{S} \, d\omega = \sum_{l=0}^{L_\mathrm{S}} \frac{\lambda_l}{\sigma_l} g_l^\mathrm{S} \quad \text{and} \quad \frac{1}{4\pi} \int\limits_{\omega-\omega_\mathrm{c}} K\mathcal{A}T^\mathrm{S} \, d\omega = \frac{1}{2} \sum_{l=0}^{L_\mathrm{S}} Q_l g_l^\mathrm{S} \tag{2.41}$$

This shows the equivalence of the remove-restore technique and the local data method in the spatial domain. Thus, the use of Eqn. (2.33) or (2.40) is a matter of taste as long as Q_l is correctly computed.

Error Analysis

Introducing errors by degree for the satellite data (e_l^S) and the local gravity data (e_l^G), such as

$$\bar{g}_l^\mathrm{S} = g_l^\mathrm{S} + e_l^\mathrm{S} \quad \text{and} \quad \bar{g}_l^\mathrm{G} = g_l + e_l^\mathrm{G} \tag{2.42}$$

an error analysis can be performed. The true solution $\mathcal{B}T$ is then subtracted from the estimated solution $\mathcal{B}\hat{T}$ yielding an error E. Using Eqn. (2.36), this results in

$$\begin{aligned} E &= \mathcal{B}\hat{T} - \mathcal{B}T \\ &= \frac{1}{2} \left(\sum_{l=0}^{L_\mathrm{S}} Q_l e_l^\mathrm{S} + \sum_{l=0}^{\infty} S_l e_l^\mathrm{G} - \sum_{l=L_\mathrm{S}+1}^{\infty} Q_l g_l - \sum_{l=0}^{\infty} S_l \left[1 - \beta_l\right] g_l \right) \end{aligned} \tag{2.43}$$

The first two summations in Eqn. (2.43) are the *commission errors* of the local data and the satellite data. The third summation represents the *truncation* or *omission* *error*. The last summation is the *discretization error* that is due to the use of mean values instead of point values (Heck, 1979; Smeets, 1994). β_l are the Pellinen functions, see Appendix A.5.

Table 2.6: Error analysis

Error Case	Factor	Commission satellite	Commission local	Omission	Discretization
Eqn. (2.43)	$\frac{1}{2}$	$+\sum_{l=0}^{L_\mathrm{S}} Q_l e_l^\mathrm{S}$	$+\sum_{l=0}^{\infty} S_l e_l^\mathrm{G}$	$-\sum_{l=L_\mathrm{S}+1}^{\infty} Q_l g_l$	$-\sum_{l=0}^{\infty} S_l (1-\beta_l)\, g_l$
$e_l^\mathrm{S}=0$	$\frac{1}{2}$		$+\sum_{l=0}^{\infty} S_l e_l^\mathrm{G}$	$-\sum_{l=L_\mathrm{S}+1}^{\infty} Q_l g_l$	$-\sum_{l=0}^{\infty} S_l (1-\beta_l)\, g_l$
$e_l^\mathrm{G}=0$	$\frac{1}{2}$	$+\sum_{l=0}^{L_\mathrm{S}} Q_l e_l^\mathrm{S}$		$-\sum_{l=L_\mathrm{S}+1}^{\infty} Q_l g_l$	$-\sum_{l=0}^{\infty} S_l (1-\beta_l)\, g_l$
$e_l^\mathrm{S}=e_l^\mathrm{G}=0$	$\frac{1}{2}$			$-\sum_{l=L_\mathrm{S}+1}^{\infty} Q_l g_l$	$-\sum_{l=0}^{\infty} S_l (1-\beta_l)\, g_l$
$\psi_c=\pi$			$+\sum_{l=0}^{\infty} \frac{\lambda_l}{\sigma_l} e_l^\mathrm{G}$		$-\sum_{l=0}^{\infty} \frac{\lambda_l}{\sigma_l} (1-\beta_l)\, g_l$
$\psi_c=0$		$+\sum_{l=0}^{L_\mathrm{S}} \frac{\lambda_l}{\sigma_l} e_l^\mathrm{S}$		$-\sum_{l=L_\mathrm{S}+1}^{\infty} \frac{\lambda_l}{\sigma_l} g_l$	

Different error scenarios and the special cases $\psi_\mathrm{c}=\pi$ (integration over the entire sphere) and $\psi_\mathrm{c}=0$ (no integration) are summarized in Table 2.6. For completeness, Eqn. (2.43) is repeated in the first line of Table 2.6. To obtain an error estimate E for each case, the respective terms have to be multiplied with the factor and then simply added. The global mean square error (MSE) is derived by squaring the terms involved. Signal degree variances are then used instead of g_l and error degree variances instead of e_l^S and e_l^G.

Ideally, the error E (or MSE) could be reduced by

i) improving the data quality, i.e., reducing the errors e_l^S and e_l^G

ii) computing the truncation or omission errors

iii) computing the discretization error that is due to the use of mean data

iv) decreasing the magnitude of the truncation coefficients Q_l

v) improving the decay rate of Q_l

In reality, only approximations for the truncation error can be computed and the magnitude of the truncation coefficients decreased by kernel modifications.

Example. An error analysis of the Hotine integration shall be performed assuming the satellite data to be error-free. The singular values are $\sigma_l = [l+1]/R$ and $\lambda_l = 1$. Using Table 2.6, the combination error of local and global data is given by

$$E = \frac{1}{2\gamma_{\mathrm{E}}} \left(\sum_{l=1}^{L_{\mathrm{S}}} S_l e_l^{\mathrm{G}} - \sum_{l=L_{\mathrm{S}}+1}^{\infty} Q_l g_l - \sum_{l=1}^{\infty} S_l \left(1-\beta_l\right) g_l \right) \tag{2.44}$$

where γ_{E} is normal gravity evaluated at the reference ellipsoid. Even though the global data are error-free, low-frequency errors from the local data leak into the solution, see also Vaníček & Featherstone (1998). The global mean-square error of Eqn. (2.44) is then given as

$$\mathrm{MSE} = \|E\|_2^2 = \left(\frac{1}{2\gamma_{\mathrm{E}}}\right)^2 \left(\sum_{l=1}^{L_{\mathrm{S}}} \left[S_l\right]^2 \varepsilon_l^{\mathrm{G}} + \sum_{l=L_{\mathrm{S}}+1}^{\infty} \left[Q_l\right]^2 c_l + \sum_{l=1}^{\infty} \left[S_l\left(1-\beta_l\right)\right]^2 c_l \right)$$

where ε_l are the error degree variances of the local data and c_l are the degree variances of the local data, see Chapter 5.

Truncation Errors

When a geopotential model is available, the truncation errors can be approximately computed. Hence, the combination error in Eqn. (2.43) will be reduced. The distant zone data is approximated by geopotential model data as, compare Eqn. (2.8),

$$\mathcal{A}T' \approx \sum_{l=L_{\mathrm{S}}+1}^{L_{\mathrm{M}}} \sigma_l t_l^{\mathrm{M}} \tag{2.45}$$

where t_l^{M} are the l-th degree of the surface spherical harmonics of the disturbing potential computed from the geopotential model M and L_{M} is the maximum degree of the geopotential model. Clearly, the degrees $0 \leq l \leq L_{\mathrm{S}}$ will be computed in the restore step. Thus, the far-zone contribution becomes

$$\mathcal{B}\hat{T}_{\omega-\omega_{\mathrm{c}}} = \frac{1}{4\pi} \int\limits_{\omega-\omega_{\mathrm{c}}} K(\cdot, Q)\mathcal{A}T'(Q)\; d\omega \doteq \frac{1}{2} \sum_{l=L_{\mathrm{S}}+1}^{L_{\mathrm{M}}} Q_l \sigma_l t_l^{\mathrm{M}} \tag{2.46}$$

The situation of Eqn. (2.46) is shown in Figure 2.6 (a). It shows the combination of local gravity data with a satellite model and a geopotential model. Unfortunately, the far-zone effect from degree $l = L_{\mathrm{M}}+1$ to $l = \infty$ is still missing in the solution. Figure 2.6 (b) shows the combination of satellite and local data also using a geopotential model. In this case, however, the local data have more power in the lower degrees (degrees L_{E} to L_{S}). This approach may be applied when the satellite data contain errors that increase with increasing degree. The degree L_{E} may be chosen with respect to the errors of the satellite data, the expected local data errors, the data coverage or following other ideas. The far-zone contribution consists of two parts, the truncation error computed from the satellite model ($L_{\mathrm{E}} \leq l \leq L_{\mathrm{S}}$) and the truncation error from the geopotential model ($L_{\mathrm{S}} < l \leq L_{\mathrm{M}}$). In any case, a modification procedure that reduces the magnitude of the far-zone effect or improves the decay rate with increasing degree (or does both) is desirable (Evans & Featherstone, 2000).

Kernel Modifications

As indicated before, kernel modifications are performed

- to decrease the magnitude of the far-zone contribution,
- to improve the decay rate of the far-zone contribution,
- to change filtering properties of the kernel function or
- to change the smoothing behaviour of the error kernel.

There are stochastic and deterministic kernel modifications (Heck & Grüninger, 1987). The deterministic methods neglect all possible stochastic a-priori information about the

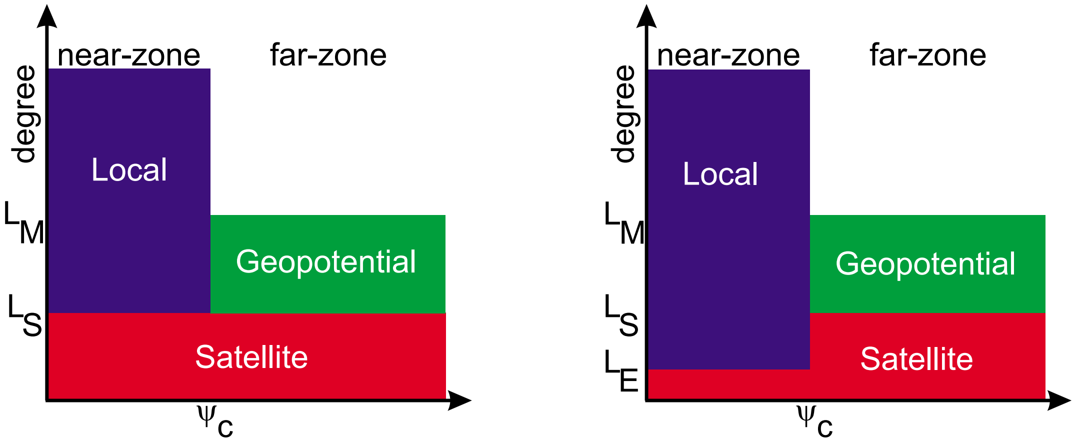

(a) Using a geopotential model for the computation of truncation errors

(b) Combination of satellite, geopotential and local data with emphasis on the local data

Figure 2.6: Computation of truncation errors using a geopotential model

data sources and might in some cases be too pessimistic. The stochastic solutions, in turn, more or less rely on the quality of the error and noise estimates. In this section, only deterministic modifications are briefly reviewed and compared.

Table 2.7 summarizes the most commonly used deterministic kernel modifications. The unmodified spherical kernel, shown in the first row of Table 2.7, is added for completeness. The kernels are given in form of Eqn. (2.39), i.e. for $0 < \psi \leq \psi_\mathrm{c}$ in the first row and $\psi_\mathrm{c} < \psi \leq \pi$ in the second row of each method discussed. The kernel function and error kernel are listed in Table 2.7. Originally, all of the modifications are introduced for the Stokes kernel, see Appendix A.3. However, other isotropic kernel functions can be modified in the same way. In Table 2.7, r_k stands for modification coefficients that are obtained from

$$\min_{r_n} \left\{ \int_{\psi_\mathrm{c}}^{\pi} \left[K(\psi)\right]^2 \sin\psi \; d\psi \right\} \tag{2.47}$$

which can be re-written as a system of linear equations, see for instance (Novák et al., 2001b) ($l = 0, 1,\ 2, \dots,\ L_{\mathrm{S}}$)

$$\sum_{n=0}^{L_{\mathrm{MD}}} \frac{2n+1}{2} R_{l,n} r_n(\psi_{\mathrm{c}}) = Q_l \tag{2.48}$$

L_{MD} is the modification degree; often $L_{\mathrm{MD}} = L_{\mathrm{S}}$ is chosen. r_n are called the Molodenskij modification coefficients. Ideally, they minimize the truncation coefficients, and thus the truncation error, in the least-squares sense. Of course, Q_l are the truncation coefficients associated with the respective kernel function in Eqn. (2.48) and R_{ln} are coefficients introduced in Paul (1973)

$$R_{ln} = R_{ln}(\psi_{\mathrm{c}}) = \int\limits_{\psi=\psi_{\mathrm{c}}}^{\pi} P_l(\cos\psi) P_n(\cos\psi) \sin\psi \; d\psi \quad n \leq l \tag{2.49}$$

Remark 2.6 *It should be noted once again that some of the functionals require the summation starting from a value other than 0 in the kernel. Furthermore, the Molodenskij modification coefficients are often computed from 1 or 2 mainly due to stability (ill-conditioning) problems (Vaníček & Sjöberg, 1991) when solving the system of linear equations.*

Figure 2.7 shows some (modified) Stokes kernel functions and (dimensionless) truncation coefficients. The kernel functions, shown on the left side of Figure 2.7, are very similar except for the spheroidal Stokes kernel. All kernel functions are decreasing with increasing spherical distance. Most of the power is close to the computation point ($\psi = 0$). Note that the Meissl (1971a) (M) kernel and the Featherstone et al. (1998) (FEO) kernel are zero for $\psi = 1°$ since $K(\psi_{\mathrm{c}})$ is subtracted. The truncation coefficients Q_l of four kernel functions are shown on the right side of Figure 2.7. The Molodenskij (MO) and the Vaníček and Kleusberg (VK) truncation coefficients are more or less zero from spherical harmonic degree 181 on. Thus, the resulting far-zone contribution will be very small for these degrees. The spheroidal and spherical coefficients on the other hand, exhibit considerable power in these degrees and the resulting far-zone contribution will be large. These kernel functions should be avoided in geoid computations. Not shown in the figures is the discontinuity of some of the error kernels listed in Table 2.7. For instance, while the Meissl error kernel is a continuous function, the spherical error kernel has a discontinuity at $\psi = \psi_c$. The discontinuity of the spherical error kernel causes oscillations in the truncation coefficients. Moreover, a smoother error kernel enjoys a much improved convergence rate (Jekeli, 1980).

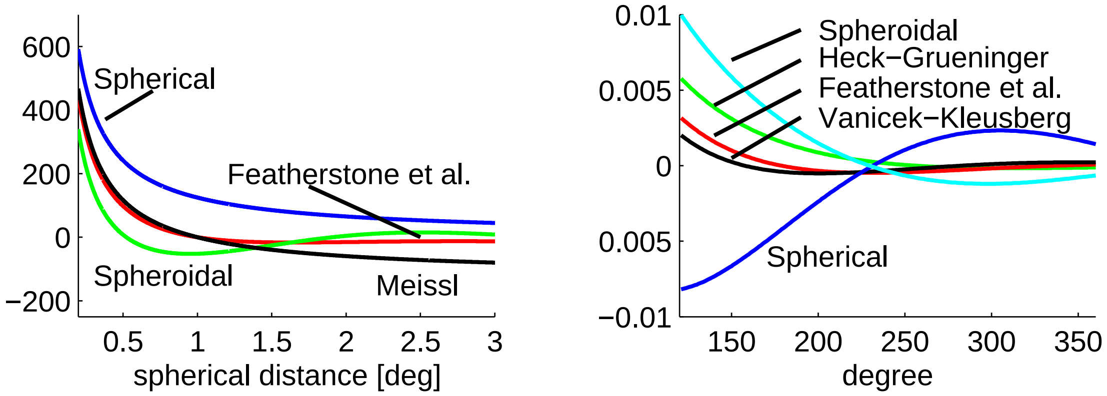

(a) Kernel functions

(b) Truncation coefficients

Figure 2.7: Kernel functions and truncation coefficients with $\psi_c = 1°$ and $L_S = 120$, $L_{MD} = 120$

Table 2.7: Deterministic kernel modifications

Source	Abbr.	Kernel	Error Kernel $\bar{K}(\psi)$
Heiskanen & Moritz (1967)	–	$K(\psi)$ 0	0 $K(\psi)$
Molodenskij (1958)	MO	$K(\psi) - \sum_{n=0}^{L_{\mathrm{MD}}} \frac{2n+1}{2} r_n(\psi_{\mathrm{c}}) P_n$ 0	0 $K_{\mathrm{MO}}(\psi)$
Wong & Gore (1969)	WG	$K(\psi) - \sum_{l=0}^{L_{\mathrm{MD}}} (2l+1) \frac{\lambda_l}{\sigma_l} P_l$ 0	0 $K(\psi) - \sum_{l=0}^{L_{\mathrm{MD}}} (2l+1) \frac{\lambda_l}{\sigma_l} P_l$
Meissl (1971a)	M	$K(\psi) - K(\psi_{\mathrm{c}})$ 0	$K(\psi_{\mathrm{c}})$ $K(\psi)$
Jekeli (1980)	JK	$K_{\mathrm{MO}}(\psi) - K_{\mathrm{MO}}(\psi_{\mathrm{c}})$ 0	$K_{\mathrm{MO}}(\psi_{\mathrm{c}})$ $K_{\mathrm{MO}}(\psi)$
Vaníček & Kleusberg (1987)	S	$K(\psi) - \sum_{l=0}^{L_{\mathrm{S}}} (2l+1) \frac{\lambda_l}{\sigma_l} P_l$ 0	0 $K(\psi) - \sum_{l}^{L_{\mathrm{S}}} (2l+1) \frac{\lambda_l}{\sigma_l} P_l$
Heck & Grüninger (1987)	HG	$K_{\mathrm{S}}(\psi) - K_{\mathrm{S}}(\psi_{\mathrm{c}})$ 0	$K_{\mathrm{S}}(\psi_{\mathrm{c}})$ $K_{\mathrm{S}}(\psi)$
Vaníček & Kleusberg (1987)	VK	$K_{\mathrm{S}}(\psi) - \sum_{n=0}^{L_{\mathrm{MD}}} \frac{2n+1}{2} r_n(\psi_{\mathrm{c}}) P_n$ 0	0 $K_{\mathrm{VK}}(\psi)$
Featherstone et al. (1998)	FEO	$K_{\mathrm{VK}}(\psi) - K_{\mathrm{VK}}(\psi_{\mathrm{c}})$ 0	$K_{\mathrm{VK}}(\psi_{\mathrm{c}})$ $K_{\mathrm{VK}}(\psi)$

2.5 Case Study – Stokes Integration

To assess the performance of different integration kernels, four tests using simulated data are conducted. The simulated data are generated using a synthetic spherical harmonic model (SGM), see Table 2.8. The model consists of the EGM96 up to degree and order 360 and a Kaula-like extension for higher degrees. The maximum degree and order of the model is 2160, corresponding to 5'×5'. The higher degrees are fitted to the GPM98B (Wenzel, 1998b) and decay slightly faster than the original Kaula rule of thumb. For more information on the model refer to Novák et al. (2001b). The simulated data represent idealized versions of the rugged gravity field over the Rocky Mountains, Canada. $L_\mathrm{S} = 120$ is used due to the data coverage of $3° \times 5°$ degrees, i.e. $49° \leq \varphi \leq 52°$ and $238° \leq \lambda \leq 243°$.

Remark 2.7 *A number of alternative synthetic models have been developed, see for instance Haagmans (2000); Pail (2000) or Featherstone (2002). Unfortunately, they were not available when the test were done and have therefore not been used.*

Table 2.8: Simulated data statistics

Type	Degree [–]	Density [']	Height [km]	Min	Max	Mean	Std	Unit
T	2-2160	5	0	−175.778	−121.175	−146.908	7.470	$\mathrm{m^2/s^2}$
T	121-2160	5	0	−6.386	7.977	−0.093	2.421	$\mathrm{m^2/s^2}$
Δg	2-2160	5	0	−31.295	54.098	4.301	11.430	mGal
Δg	121-2160	5	0	−30.896	30.903	−0.254	10.215	mGal
$\Delta g + e$	121-2160	5	0	−33.649	31.045	−0.311	10.392	mGal

The kernels are compared for the Stokes integration, see also Appendix A.3. A spherical cap radius of $\psi_\mathrm{c} = 1°$, $L_\mathrm{S} = L_\mathrm{MD} = 120$ are used in the first and second test ($L_\mathrm{S} = 21$ for Wong-Gore). Although these values may adversely affect the results for some of the kernel modifications, the values have been chosen for comparison purposes. Generally, the optimal choice of ψ_c, L_MD and L_S is a difficult matter. It will not be discussed here in detail.

The applied computational scheme for the first two tests is summarized in Eqn. (2.50). In the first test, residual gravity anomalies (spacing 5 ’× 5 ’) are input into the integration process yielding an estimate of the residual potential $\hat{T}_{121-2160}$. Comparing this estimate with the residual potential directly computed from the SGM, an error estimate of the integration process can be obtained. In the second test, noisy gravity anomalies have been used. White noise of 1.5 mGal standard deviation is applied to the gravity data. Otherwise, the computational procedure is equivalent to the first test. The potential $T_{121-2160}$ from the SGM is considered to be the true solution in both cases. Dividing the result by the normal gravity γ_{E} leads to geoidal undulations in units of m (Bruns).

$$\text{SGM}\left\{\begin{array}{lcc} \Delta g_{121-2160} & \rightarrow \text{Stokes} \rightarrow & \hat{T}_{121-2160} \\ & & \downarrow \\ T_{121-2160} & \longrightarrow & \text{Geoid error} \end{array}\right. \tag{2.50}$$

The results of the two tests are shown in Figure 2.8 (Statistics are summarized in tables B.2 and B.3 in the Appendix). The various solutions are given along the horizontal axis of the figure. The first bar in each case stands for the rms geoid error for noise-free gravity data (first test) while the second bar is the rms geoid error for noisy gravity anomalies (second test). The scale of the rms-error is shown on the left vertical axis. For easy comparisons, a line is drawn showing the 1 cm rms error. Also shown are the rms values of the far-zone contributions. In this case, the right vertical axis is the scale. Although the far-zone contribution is small for most solutions, large values are obtained for the spherical, spheroidal (S) and Heck-Grüninger (HG) kernels.

The results using noise-free gravity data are somewhat surprising. In most cases, the errors stay consistently below 1 cm. Only the spherical, the Wong-Gore (WG) and the S kernel perform worse than 1 cm rms error. The residual errors are due to remaining integration errors and model approximations. The situation is not as good when using noisy gravity anomalies. Although the Stokes convolution generally acts as a low-pass filter, the noise seems to leak into the solution. Errors larger than 1 cm are obtained and

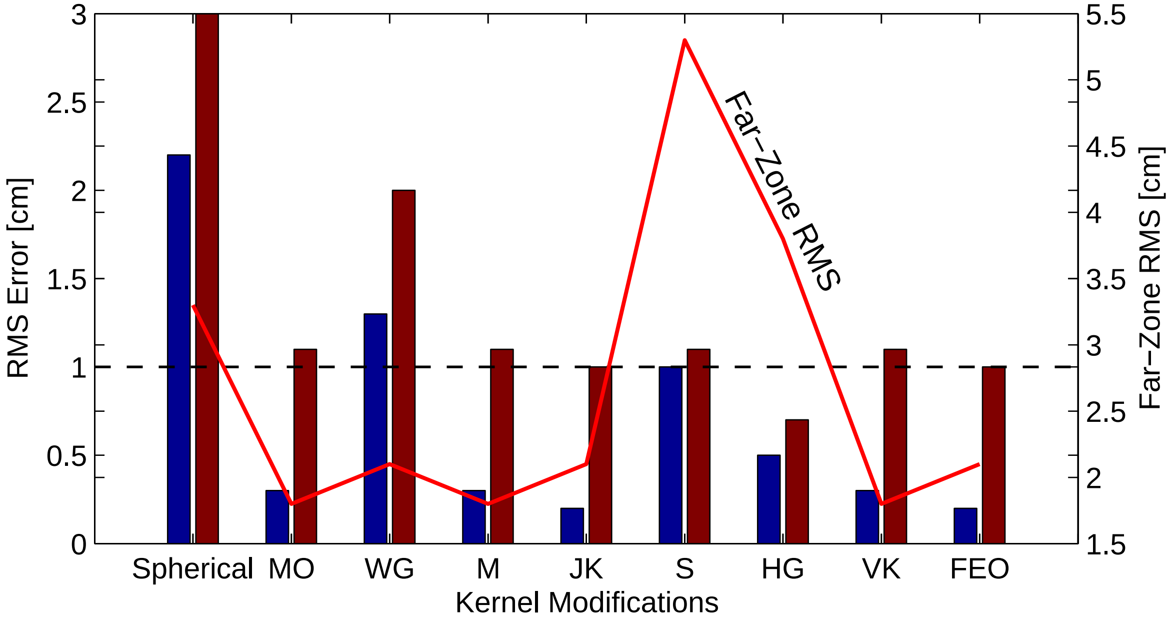

Figure 2.8: Geoid error with different kernel modifications. First bar is the geoid rms error with noise-free data, second bar the geoid rms error with noisy data [cm]

lead to the conclusion that a kernel modification should be used. Taking the far-zone results into account, the MO, JK, VK and FEO kernels successfully alleviate the effect of the far-zone contribution. Using gravity anomalies that may be burdened by low-frequency inconsistencies, one of the kernels WG, S, HG, VK or FEO should be favored. They reduce the impact of these inconsistencies since they represent an ideal high-pass filter up to degree L_S (if the integration would be extended over the entire sphere). Generally, modifications such as MO, JK, VK, FEO are computationally demanding. They add additional complexity to the problem since modification coefficients have to be computed.

A third test is performed to investigate the influence of different modification degrees. The FEO kernel is used for this test and noisy gravity anomalies, see again Table 2.8. The spherical cap ψ_c and the satellite degree L_S are fixed to the previous values of 1° and 120. Thus, only the modification degree L_{MD} varies in steps of 10 (modification) degrees. The results of this test are shown in Figure 2.9. For $L_{MD} = 0$, the FEO

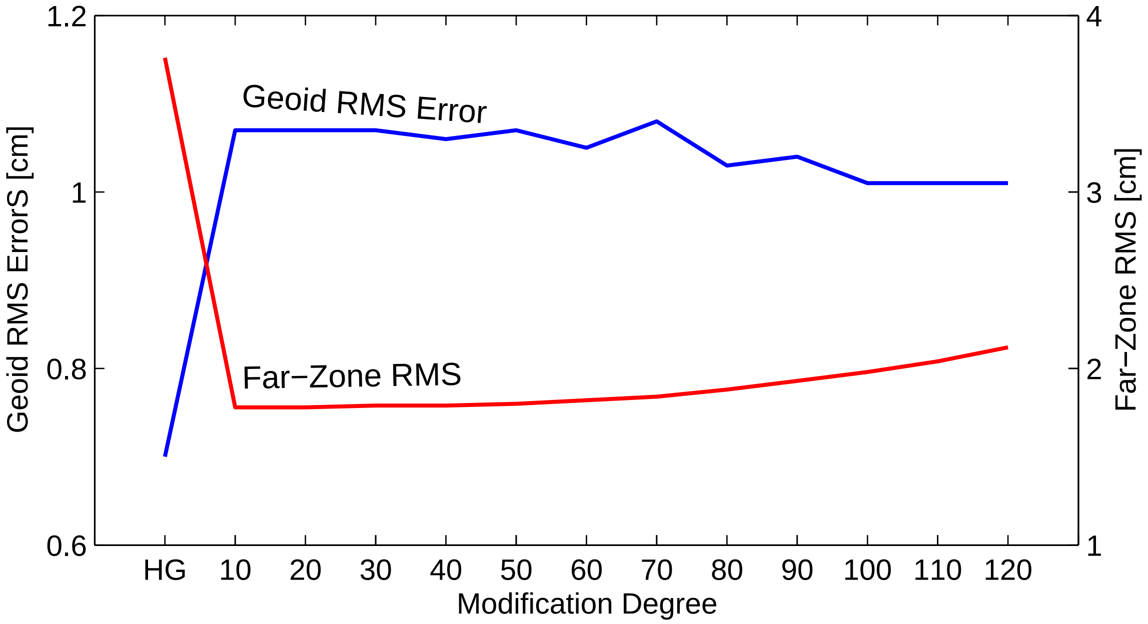

Figure 2.9: Influence of different modification degrees using the FEO kernel. $L_\mathrm{S} = 120$ and $\psi_\mathrm{c} = 1°$ fixed

kernel reduces to the HG kernel. This provides the smallest geoid error rms of 7 mm. Yet, the HG has a relatively large far-zone contribution of about 3.7 cm, compare also Figure 2.8. Selecting a larger modification degree such as $L_\mathrm{MD} = 10,\ 20, \ldots$ yields considerably smaller far-zone contributions. However, the overall geoid error rms seems to suffer from higher modifications. A choice has to be made between modifying the kernel function, and thus reducing considerably the far-zone contribution, or taking a slightly larger far-zone contribution into account but reducing the overall geoid error. This choice may depend on the quality of the available data, the data coverage size and the bandwidth of the satellite data.

The fourth test is a comparison of the remove-restore technique and the local data method. Clearly, the investigation in Section 2.4 using gravity data over the entire sphere has shown that the two models are theoretically equivalent. A similar conclusion is drawn in Sjöberg & Hunegnaw (2000); Rapp & Rummel (1975) indicating that the local data model may perform as well as the remove-restore technique. Kearsley (1988) in turn claims that the remove-restore technique is numerically superior and should be used. The following test set-up is applied to investigate the quality of the two methods:

$$\begin{array}{cccccc}
\Delta g_{121-2160} & \rightarrow \text{Stokes} \rightarrow & \hat{T}_{121-2160} & \hat{T}_{2-2160} & \leftarrow \text{Stokes} \leftarrow & \Delta g_{2-2160} \\
 & \textbf{Method A} & \downarrow & \downarrow & \textbf{Method B} & \\
T_{2-2160} & \rightarrow \text{Error A} \leftarrow & T_{2-120}+\hat{T}_{121-2160} & \text{Error B} & \longleftarrow & T_{2-2160}
\end{array}$$

In method A (remove-restore technique), residual gravity anomalies are input into the Stokes integration. The gravity anomalies are previously reduced by the low-frequency information up to degree and order 120. After the Stokes integration, which includes the calculation of the far-zone contribution from $121 \leq L_{\mathrm{S}} \leq 360$, the residual potential is obtained. Finally, an estimate of the potential is found when adding back the low-frequency information in units of potential (T_{2-120}). This, in turn, may be compared to the potential directly computed from the model yielding *error A*. In method B (local data model), the gravity data are not reduced by a model. The Stokes kernel is identical to the one in method A, yet the added low-frequencies are differently computed. They are

$$\frac{1}{2} \sum_{l=2}^{L_{\mathrm{S}}} \left(r_l + Q_l^*\right) \Delta g_l^{\mathrm{S}} \tag{2.51}$$

where a modified kernel function is used ($r_l = 0$ and $Q_l^* = Q_l$ for the spherical Stokes). The far-zone contribution is computed in the same way as in the remove-restore technique. Comparing the estimate $\hat{T}_{2-2160}$ with the potential from the model, *error B* is obtained. Table 2.9 summarizes the results of the two concepts. Error-free gravity anomalies are used to show best-case scenarios and convolved with the Molodenskij kernel (JK). The truncation radius of $\psi_{\mathrm{c}} = 1°$ and $L_{\mathrm{S}} = L_{\mathrm{MD}} = 120$ is used once again. Clearly, the methods are also numerically equivalent. Hence, the local data method can be used instead of the remove-restore technique whenever it seems more convenient (Sjöberg & Hunegnaw, 2000).

Summary. Table 2.10 summarizes the comparison of different kernel functions. The

Table 2.9: Remove-restore technique versus local data method [m]

Error	Min	Max	Mean	Std	RMS
A	−0.007	0.007	0.001	0.003	0.003
B	−0.007	0.007	0.000	0.003	0.003

HG kernel does not reduce the far-zone effect as effectively as the FEO or VK kernel. But it represents a good alternative to the sophisticated kernel functions and shows best overall performance taking the required computation time and implementation complexity into account. The FEO kernel is recommended when the data area is very small. It successfully alleviates the far-zone effect. The spherical kernel function is not recommended for local or regional geoid determinations.

Table 2.10: Kernel function comparison (○ – small; ◐ – medium; ● – large)

Name	Computation Time	Implementation Complexity	Far-zone Contribution	Inclusion of Inconsistencies (Biases)
Spherical	○	○	◐	●
MO	●	●	○	●
WG	○	◐	○	○
M	○	○	○	●
JK	●	●	○	●
S	○	◐	●	○
HG	○	◐	◐	○
VK	●	●	○	○
FEO	●	●	○	○

Remark 2.8 *The presentation and comparison of different kernel modifications is confined here to the Stokes integration. Other isotropic kernel functions have been studied as well. However, the conclusions are either equivalent or very similar and are thus not further pursued here.*

2.6 Limitations

The remove-restore technique is a proven strategy for the combination of satellite data and one local gravity data set. A unified estimate of the gravity spectrum is obtained by combining global and local data complementary in the spectral domain. However, there are a number of problems and limitations associated with the technique. Some of them are listed here:

i) New satellite and local gravity data are available that should be incorporated into the solution. Thus, an *overdetermined* situation arises where more information is available than actually needed to solve the problem. This cannot be instantly handled by the remove-restore technique.

ii) The remove-restore technique is a solution for almost ideal measurements. The basic assumption is that the signal-to-noise ratio of the data is high. Errors from the satellite and the local data can leak into the solution since no error measures are taken into account.

iii) The remove-restore technique does not provide quality measures for the output functional.

iv) Possible correlations between the two data sets are neglected. These may occur due to a calibration or regularization process of the satellite data.

v) The determination of optimal values for the spherical cap size ψ_{c} and the maximum satellite degree L_{S} are unsolved problems.

3 Upward and Downward Continuation

Gravity measurements are observed or derived at the Earth's surface, at the airborne flight path or at satellite altitude. In many instances, however, the gravity information is not required at the measurement location. Thus, an upward or downward continuation process to a different height level has to be performed. Two problems are addressed in this chapter:

i) The measurements are not taken on a regular surface such as a sphere, etc. An approximation has to be applied for the upward and downward continuation.

ii) The mathematical model is given for the upward continuation. The downward continuation problem is an ill-posed problem, which may be unstable. The downward continuation problem is analyzed and an alternative approximation formulated.

3.1 Upward Continuation

Upward Continuation of the Disturbing Potential

The *upward continuation* of the disturbing potential can be formulated as (Kellogg, 1929; MacMillan, 1930)

$$\hat{T}(P) = \frac{1}{4\pi} \int\limits_{\omega} K(P,Q)\; T(Q)\; d\omega(Q) \quad \longleftrightarrow \quad g = \mathcal{A} f \tag{3.1}$$

where

$\hat{T}(P)$	is the sought estimate of the disturbing potential (harmonic and regular at infinity) on a radius of a sphere $r = R + H$, abbreviated by $g \in G$
$T(Q)$	is the continuously given disturbing potential on the reference sphere R, abbreviated by $f \in F$
$\mathcal{A}$	is a linear operator $\mathcal{A} : F \rightarrow G$, where F and G are appropriate (Hilbert) spaces

The kernel function $K(P, Q)$ is given as (Heiskanen & Moritz, 1967, pg. 35)

$$\begin{aligned} K(P,Q) = K(r,\psi,R) &= \sum_{l=0}^{\infty} (2l+1) \left(\frac{R}{r}\right)^{l+1} P_l(P,Q) \\ &= R \frac{r^2 - R^2}{(r^2 + R^2 - 2Rr\cos\psi)^{\frac{3}{2}}} \end{aligned} \tag{3.2}$$

The upward continuation is also denoted as direct or forward continuation problem. It is the solution of the *first boundary value problem* (exterior Dirichlet problem). The kernel function is referred to as *Abel-Poisson* or *Poisson* kernel function.

Upward Continuation of Other Functionals

Linear functionals of the disturbing potential are upward continued using

$$\mathcal{A}\hat{T}(P) = \frac{1}{4\pi} \int\limits_{\omega} K(P,Q)\ \mathcal{A}T(Q)\ d\omega(Q) \quad \longleftrightarrow \quad g = \mathcal{A}f \tag{3.3}$$

where g stands now for $\mathcal{A}\hat{T}(P)$ and f for $\mathcal{A}T(Q)$, respectively.

Example. Applying Eqn. (3.3) to the (Helmert) disturbing potential (no masses above the geoid), gravity disturbances can be upward continued from the sphere R to $R + H$ as

$$-\frac{\hat{T}(r,\theta,\lambda)}{\partial r}\bigg|_r = \hat{\delta g}(P) = \frac{R}{4\pi r} \int\limits_{\omega} K(P,Q)\ \delta g(Q)\ d\omega(Q)$$

This is allowed since $r\delta g$ is a harmonic function. Note that $\delta g(Q) = \delta g(R, \theta, \lambda)$ does not depend on r (Heiskanen & Moritz, 1967, pg. 37).

Discrete Problem

The numerical evaluation of the upward continuation requires the discretization of the problem. Eqn. (3.1) is then given as

$$T(r, \theta_i, \lambda_i) = \sum_j A_{ij} T(R, \theta_j, \lambda_j) + T_{\omega-\omega_\mathrm{c}}(r, \theta_i, \lambda_i) \tag{3.4}$$

where $T_{\omega-\omega_\mathrm{c}}(r, \theta_i, \lambda_i)$ is the far-zone contribution, which can be approximately computed from a geopotential model. Eqn. (3.4) is cast into the following matrix-vector form (Novák et al., 2001a)

$$\boldsymbol{T}(r) - \boldsymbol{T}_{\omega-\omega_\mathrm{c}}(r) = \boldsymbol{A}\boldsymbol{T}(R) \quad \longleftrightarrow \quad \boldsymbol{y} = \boldsymbol{A}\boldsymbol{x} \tag{3.5}$$

where $\boldsymbol{x} \in \mathrm{I\!R}^n$ is the disturbance vector at the reference sphere R, and $\boldsymbol{y} \in \mathrm{I\!R}^m$ is the disturbance vector minus the far-zone vector at the sphere $r = R + H$. $\boldsymbol{A} \in \mathrm{I\!R}^m \times \mathrm{I\!R}^n$ is the design matrix with full rank. In the downward continuation problem, m stands for the number of measurements and n is the number of unknowns ($m \geq n$).

The entries of the matrix $\boldsymbol{A}$ are explicitly derived in Martinec (1996, 1998). The off-diagonal entries of the matrix are ($A_{ij} = 0$ for $\psi_{ij} > \psi_\mathrm{c}$)

$$A_{ij} = \frac{1}{4\pi} K(r_i, \psi_{ij}, R) \Delta\omega_j \qquad \text{for } \psi_{ij} \leq \psi_\mathrm{c} \qquad i \neq j \tag{3.6}$$

and the entries on the main diagonal become (Martinec, 1996)

$$A_{ii} = \frac{1}{4\pi} \int\limits_{\omega_\mathrm{c}} K(r, \psi, R)\, d\omega - \frac{1}{4\pi} \sum_{j=1, j\neq i}^{N} K(r_i, \psi_{ij}, R) \Delta\omega_j \tag{3.7}$$

$$= \frac{1}{2} \left[\frac{r+R}{r} \left(1 - \frac{r-R}{\sqrt{r^2 + R^2 - 2Rr\cos\psi_\mathrm{c}}} \right) \right] - \frac{1}{4\pi} \sum_{j=1, j\neq i}^{N} K(r_i, \psi_{ij}, R) \Delta\omega_j \tag{3.8}$$

where $\Delta\omega_j$ is the area of the trapezoidal cell centered at the j-th geographical node ω_j and N is the number of data within the spherical cap of radius ψ_c. Of course, band-limited kernel functions and modified kernel functions can be used instead of the original Abel-Poisson kernel. In this thesis, the VK kernel modification is used, see Appendix A.4. Similar derivation steps as described above can be performed for linear functionals of the disturbing potential.

Since the upward continuation is a direct problem, it does not pose any numerical difficulty. The process is stable and acts, due to the kernel function characteristics, as a low-pass filter. It effectively smooths the high-frequency noise or measurement errors when continuing gravity data to a different height.

Deviations from Constant Height

Actual gravity data are not provided at a constant height. For airborne data, for instance, the height deviations are typically at the level of a few meters depending on the flight conditions. This causes theoretical as well as computational problems. The theoretical problem is that the constant radius approximation is not rigorously satisfied. The computational problem is the adequate computation of the matrix $\boldsymbol{A}$. The following approximation is used: Firstly, compute matrix entries A_{ij} and A_{ii} for different height layers, such as $H_k = 200\,\mathrm{m},\ 300\,\mathrm{m},\ 400\,\mathrm{m}$ etc., corresponding to the height range of the data. Note that the kernel function has to be evaluated for only one computation point per parallel since the kernel function is isotropic for each height layer. Then, secondly, interpolate between matrix entries to obtain the matrix entry for the specific data height and spherical distance ψ_{ij}. The interpolation method of Lagrange is used. The pseudo code for setting up the matrix $\boldsymbol{A}$ becomes:

```
Algorithm (Computation of Matrix $\boldsymbol{A}$):
  set $\psi_\mathrm{c}$, set $L_\mathrm{S}$ (set $L_\mathrm{MD}$ kernel modification degree if desired)
  while number of parallels $\leq$ maximum number of parallels
  compute off-diagonal entries $A_{ij}$
      if $\psi_{ij} \leq \psi_\mathrm{c}$        integration point is inside the spherical cap
          for height layer $k \leq$ maximum number of height layers
              compute $A_{ij}$ (Eqn. (3.6)) for $\psi_{ij}$ and $r = R + H_k$
```

```
            end
        else
            set $A_{ij} = 0$ (Eqn. (3.6))
        end
    compute main diagonal matrix entries $A_{ii}$
        for height layer $k \leq$ maximum number of height layers
                compute $A_{ii}$ (Eqn. (3.8))
        end
    end
    interpolate between matrix entries
        compute final $A_{ij}$ and $A_{ii}$ entries by interpolation between the
        data height and the matrix entries of the height layers $k$
```

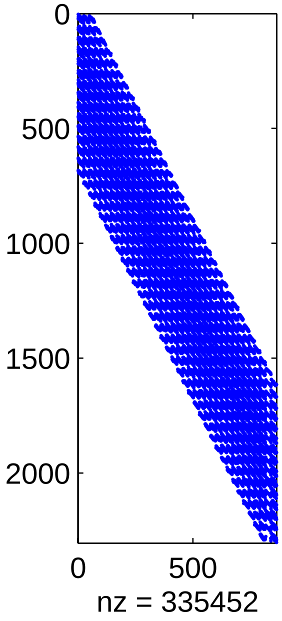

Figure 3.1: Sparsity pattern of the design matrix $\boldsymbol{A}$ with $m = 2304$ and $n = 864$. 335452 non-zero elements

A typical pattern of the design matrix is shown in Figure 3.1; only non-zero elements are shown. The matrix is predominately diagonally structured, which may be used to speed up the computation process. In the figure, the number of measurements and the number of unknowns is different. The design matrix is taken from the numerical investigation carried out in Section 3.5, i.e. gravity data are given in a 2° × 2° data area with spacing $2.5' \times 2.5'$. This yields $m = 48 \times 48 = 2304$ data points. To avoid edge effects, a smaller output area is used ($1.5° \times 1.5°$, i.e $n = 24 \times 36 = 864$ points).

3.2 Downward Continuation

The downward continuation is a problem where the unknown function f is to be determined from the given function/data g and operator $\mathcal{A}$. Eqn. (3.1) turns into a *Fredholm integral of the first kind* where $\hat{T}(P)$ is known and $T(Q)$ sought. A solution for Eqn. (3.1) only exists for $g \in \mathcal{R}(\mathcal{A}) := \{\mathcal{A}f : f \in F\}$ (range of $\mathcal{A}$). Let the operator $\mathcal{A} : F \to G$ be *compact*, i.e., the sequence $(\mathcal{A}f_n)$ contains a convergent subsequence in G for each bounded sequence (f_n) in F (Kress, 1989, pg. 18). Consequently, the inverse $\mathcal{A}^{-1}$ (if it exists at all) cannot be continuous since $\mathcal{A}$ is compact and $\dim(F) = \infty$. Hence, the downward continuation is inherently *unstable* and *ill-posed*, see also Section 3.3. The generalized inverse solution can be written as

$$\mathcal{A}^+ g = f \quad \longleftrightarrow \quad \boldsymbol{A}^+ \boldsymbol{y} = \boldsymbol{x} \tag{3.9}$$

Strategies for the solution of Fredholm integrals of the first kind have been extensively discussed in the mathematical and geodetic literature, see for instance Hoerl & Kennard (1970); Tikhonov & Arsenin (1977); Schwarz (1979); Rummel et al. (1979); Louis (1988); Rauhut (1992); Xu & Rummel (1994); Engl et al. (1996); Hansen (1998); Bouman (1998, 2000); Kern & Schwarz (2001); Huang (2002); Kusche (2002) to name a few. After a revision of the model problem, some of these strategies are described and applied.

Model Problem of Downward Continuation

Least-squares solutions aim at minimizing the norm

$$\|\mathcal{A}f - \tilde{g}\| \tag{3.10}$$

where the norm may be the L_2 norm. The measurements g usually contain measurement noise e, i.e. $\tilde{g} = g + e$ and $\|e\|_2 < \|g\|_2$ is usually assumed. The least-squares solution will provide a stable solution (small changes in the input do not cause large changes in the output) if the problem is well-posed:

$$\hat{f} = (\mathcal{A}^*\mathcal{A})^{-1}\mathcal{A}^*\tilde{g} \quad \longleftrightarrow \quad \hat{f} = \mathcal{A}^+\tilde{g} = \sum_{i=1}^{\infty} \frac{(\tilde{g}, u_i)}{\sigma_i} v_i \tag{3.11}$$

When the continuous problem is an ill-posed problem, however, the spectral form, shown on the right side of Eqn. (3.11), instantly exhibits the instability problem: Errors in the high-frequency components (large i) are amplified by large factors $1/\sigma_i$ (Schwarz, 1979; Louis, 1988). Consequently, the least-squares solution may become unbounded for $i \to \infty$ as $\sigma_i \to 0$. In this case, the main challenge is to find a stable solution. Characteristic elements of the model problem are the gravity observable (disturbance, anomaly or other functional of the potential) and its roughness, the data noise e, the continuation height H and the radius of the reference sphere R, the approximation method and choice of parametrization, the data spacing S, the dimension of the problem n, m and the solution bandwidth b. Moreover, the regularization parameters α or k are elements that influence the quality of the downward continuation, see also Kusche (2002, pg. 34). In short, the model problem is given by

$$\{g,\ e,\ R,\ R+H,\ \mathcal{A},\ S,\ n,\ m,\ b,\ \alpha \text{ or } k\} \tag{3.12}$$

Mathematically, a solution is found by first *stabilizing* (or regularizing) the continuous problem using some sort of a-priori information and, in the second step, to *discretize* the problem (Hansen, 1998). The other way (first discretizing and then regularizing) is possible and will lead to the same numerical results. However, the norm to be minimized cannot always be interpreted.

Regularization

The goal of a regularization scheme is the substitution of the unbounded operator $\mathcal{A}^+$ by a bijective (surjective and injective) bounded operator (Kress, 1989, pg. 224). The bijective operator is defined as

$$\{\mathcal{A}_\alpha^+\}_{\{\alpha>0\}} \;:\; G \to F \; . \tag{3.13}$$

where G and F are normed spaces and $\mathcal{A} : F \to G$ shall be an injective operator. The operator $\mathcal{A}_\alpha^+$ is called the *regularized inverse* (Louis, 1988) and α is the *regularization parameter*. In iteration methods, the iteration step k is used instead of α. A regularization scheme for $\mathcal{A}^+$ could consist of the following three conditions (Louis, 1988; Ilk, 1993):

i) $\mathcal{A}_\alpha^+$ should be *bounded*, i.e.

$$\|\mathcal{A}_\alpha^+\|_2 \;\leq\; d(\alpha) \tag{3.14}$$

where $d(\alpha)$ is a positive constant (Kress, 1989)

ii) The regularized solution should converge to the generalized inverse when the data do not contain errors (asymptotic condition I)

$$\lim_{\substack{\tilde{g}\to g \\ e\to 0}} \mathcal{A}_{\alpha(e,g)}^+ \tilde{g} = \mathcal{A}^+ g \qquad g \in \mathcal{D}(\mathcal{A}^+) \tag{3.15}$$

iii) The regularization parameter should converge to zero when the data errors go to zero (asymptotic condition II)

$$\lim_{\substack{\tilde{g}\to g \\ e\to 0}} \alpha(e,g) = 0 \; . \tag{3.16}$$

Unfortunately, not all regularization schemes can be described by the above conditions. A different access to regularization schemes is given by the singular value decomposition. A regularized solution can be described by

$$\hat{f}_\alpha = \mathcal{A}_\alpha^+ \tilde{g} \quad \longleftrightarrow \quad \hat{f}_\alpha = \sum_{i=1}^{\infty} \delta_\alpha \frac{(\tilde{g}, u_i)}{\sigma_i} v_i \tag{3.17}$$

where δ_α is a filter factor satisfying the properties $\lim_{\alpha\to 0}\delta_\alpha = 1$ and $|\delta_\alpha| \leq d(\alpha)\sigma_i$. $\|\mathcal{A}_\alpha^+\| \leq d(\alpha)$ is then a bounded operator with bound $d(\alpha)$ (Kress, 1989, pg. 236). The original ill-posed problem is turned into a well-posed problem. Eqn. (3.17) represents a filtered least-squares solution.

Using discrete measurements, the regularized solution vector $\hat{\boldsymbol{x}}_\alpha$ is computed from

$$\hat{\boldsymbol{x}}_\alpha = \boldsymbol{A}_\alpha^+ \tilde{\boldsymbol{y}} \quad \longleftrightarrow \quad \hat{\boldsymbol{x}}_\alpha = \sum_{i=1}^{n} \delta_\alpha \frac{\boldsymbol{u}_i^T \boldsymbol{y}}{\sigma_i} \boldsymbol{v}_i \tag{3.18}$$

where $\tilde{\mathbf{y}}$ are the noisy measurements. The solution and residual (L_2-) norms are given as

$$\|\hat{\boldsymbol{x}}_\alpha\|_2^2 = \sum_{i=1}^{n} \left(\delta_\alpha \frac{\boldsymbol{u}_i^T \tilde{\boldsymbol{y}}}{\sigma_i}\right)^2 \quad \text{and} \quad \|\boldsymbol{A}\hat{\boldsymbol{x}}_\alpha - \tilde{\boldsymbol{y}}\|_2^2 = \sum_{i=1}^{n} \Big((1-\delta_\alpha)\, \boldsymbol{u}_i^T \tilde{\boldsymbol{y}}\Big)^2 \tag{3.19}$$

Mean-Square Error Function

Comparing the regularized solution $\mathcal{A}_{\alpha(e,g)}^+\, \tilde{g}$ with the (generalized) inverse solution for the error-free solution, a *regularization error* is obtained. The difference between the solutions is given by (Bouman, 2000)

$$\hat{f}_\alpha - f = \mathcal{A}_\alpha^+(\tilde{g} - g) + (\mathcal{A}_\alpha^+ - \mathcal{A}^+)g \tag{3.20}$$

The first part of the right-hand side of Eqn. (3.20), $\mathcal{A}_\alpha^+(\tilde{g} - g)$, is frequently called *data* or *perturbation error* and the second part, $(\mathcal{A}_\alpha^+ - \mathcal{A}^+)g$, is the *regularization error* or *bias*. If f is known, the quality of the regularized solution $\hat{f}_\alpha$ can be investigated. This is often done (in simulation studies when f is known) using the mean-square error function. On the other hand, the mean-square error function can also be used to select an optimal value of α. Thus, the mean-square error function serves a dual function – to find an optimal value of α and to describe the quality of the solution.

When $\boldsymbol{P}^{-1}$ contains the variance-covariance information of the noisy data ($D(\tilde{\boldsymbol{y}}) = \boldsymbol{P}^{-1}$), the mean square error matrix can be derived using the covariance law as (Hoerl

& Kennard, 1970; Bouman, 2000)

$$\begin{aligned}\boldsymbol{MSE} &= \boldsymbol{E}\left(\left[\hat{\boldsymbol{x}}_\alpha - \boldsymbol{x}\right]\left[\hat{\boldsymbol{x}}_\alpha - \boldsymbol{x}\right]^T\right) \\ &= \underbrace{\boldsymbol{A}_\alpha^+ \boldsymbol{P}^{-1}\left(\boldsymbol{A}_\alpha^+\right)^T}_{\text{Data Error}} + \underbrace{\left[\left(\boldsymbol{A}_\alpha^+ - \boldsymbol{A}^+\right)\boldsymbol{A}\right]\boldsymbol{x}\boldsymbol{x}^T\left[\left(\boldsymbol{A}_\alpha^+ - \boldsymbol{A}^+\right)\boldsymbol{A}\right]^T}_{\text{Bias}} \qquad (3.21)\end{aligned}$$

The mean-square error function (MSE) is obtained by taking the trace of $\boldsymbol{MSE}$. Obviously, the MSE function can only be approximated in real world computations since the true solution $\boldsymbol{x}$ is unknown. Kusche (2002, pg. 41) summarizes three approximation methods for the term $\boldsymbol{x}\boldsymbol{x}^T$. They involve the use of

- $\hat{\boldsymbol{x}}_\alpha \hat{\boldsymbol{x}}_\alpha^T$ instead of $\boldsymbol{x}\boldsymbol{x}^T$, see also Xu & Rummel (1994).
- the inverse term $(1/\alpha^2)$ when the standard Tikhonov regularization is used, see also Grafarend & Schaffrin (1993, pg. 117)
- a scaled inverse (γ^2/α^2), where γ may be determined by setting $(\gamma^2/\alpha^2) = \text{trace}\{\hat{\boldsymbol{x}}_\alpha \hat{\boldsymbol{x}}_\alpha^T\}$, see Kusche (2002) for further details.

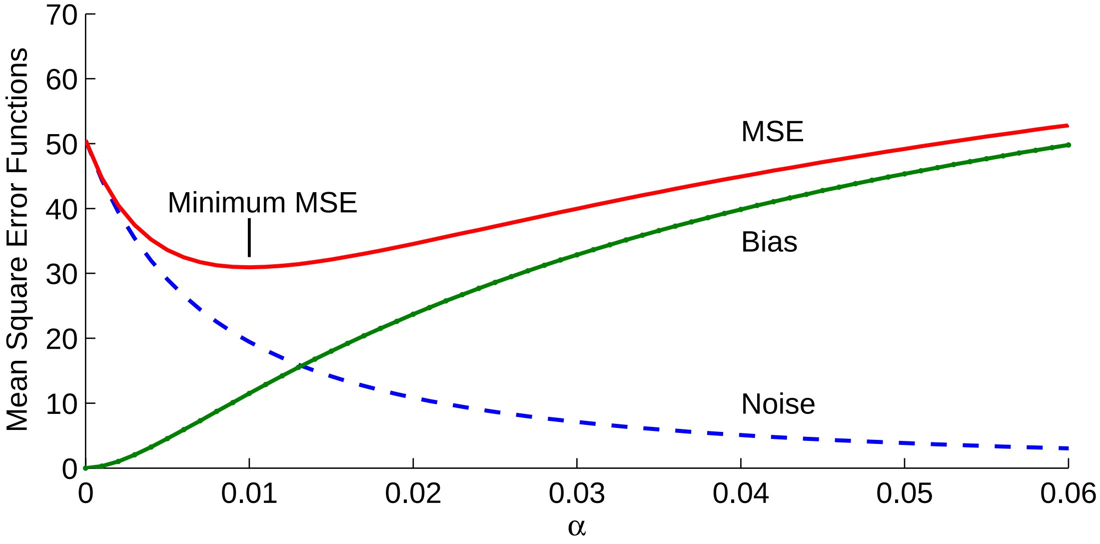

Figure 3.2: Mean square error functions, example taken from Bouman (2000)

Figure 3.2 shows the three terms together – bias, noise (data error) and mean-square error function. The example is borrowed from Bouman (2000). It demonstrates the potential of the mean-square error function to determine an optimal solution. The minimum mean square error represents a balance between an unstable solution (very small α) and an overly filtered, biased result (large α). In Figure 3.2, a regularization parameter α of about 0.01 would solve the problem.

Regularization Methods

Tikhonov Regularization (TIK). The Tikhonov regularization has been described and implemented for different purposes. Introduced independently by Phillips (1962) and Tikhonov (1963), it is the most prominent regularization method. An advantage of the Tikhonov regularization is that the method stabilizes the problem and may simultaneously incorporate information about the solution smoothness. The main idea is to extend the minimizing function $\|\mathcal{A}f - \tilde{g}\|^2$ by a stabilizing function. The Tikhonov regularization functional becomes (Tikhonov & Arsenin, 1977, pg. 72)

$$\mathcal{F}_\alpha = \|\mathcal{A}f - \tilde{g}\|^2 + \alpha^2\|\mathcal{L}f\|^2 \tag{3.22}$$

where $\|\mathcal{L}f\|^2$ is the stabilizing function, $\mathcal{L}$ a differential operator. It should be noted that the norm of the second term can be associated with a Sobolev space. The regularized solution is given as (Tikhonov & Arsenin, 1977)

$$\hat{f}_\alpha = \mathcal{A}_\alpha^+\tilde{g} \quad \text{with} \quad \mathcal{A}_\alpha^+ = (\mathcal{A}^*\mathcal{A} + \alpha^2\mathcal{L}^*\mathcal{L})^{-1}\mathcal{A}^* \tag{3.23}$$

$\mathcal{A}_\alpha^+$ is a bounded operator since $(\mathcal{A}^*\mathcal{A} + \alpha^2\mathcal{L}^*\mathcal{L})^{-1}$ is bounded and $\mathcal{A}^*\mathcal{A}$ is compact. Often, the standard form of the minimizing function is used, i.e the minimizing term becomes a signal constraint. The general case of (3.22) is simplified to

$$\mathcal{F}_\alpha = \|\mathcal{A}f - \tilde{g}\|^2 + \alpha^2\|f\|^2 \tag{3.24}$$

The solutions in space and spectral domain turn into:

$$\hat{f}_\alpha = (\mathcal{A}^*\mathcal{A} + \alpha^2\mathcal{I})^{-1}\mathcal{A}^*\tilde{g} \quad \longleftrightarrow \quad \hat{f}_\alpha = \sum_{i=1}^{\infty}\left(\frac{\sigma_i^2}{\sigma_i^2 + \alpha^2}\right)\frac{(\tilde{g}, u_i)}{\sigma_i}v_i \tag{3.25}$$

where $\mathcal{I}$ is the identity operator and

$$\delta_\alpha = \left(\frac{\sigma_i^2}{\sigma_i^2 + \alpha^2}\right) \approx \begin{cases} 1 & \text{for } \sigma_i \gg \alpha \\ \dfrac{\sigma_i^2}{\alpha^2} & \text{for } \sigma_i \ll \alpha \end{cases} \tag{3.26}$$

the filter factor. In discrete form, the Tikhonov solution becomes (assuming orthogonal base functions)

$$\hat{\boldsymbol{x}}_\alpha = \left(\boldsymbol{A}^T\boldsymbol{A} + \alpha^2\boldsymbol{I}\right)^{-1}\boldsymbol{A}^T\boldsymbol{y} \quad \longleftrightarrow \quad \hat{\boldsymbol{x}}_\alpha = \sum_{i=1}^{n} \delta_\alpha \frac{\boldsymbol{u}_i^T\boldsymbol{y}}{\sigma_i}\boldsymbol{v}_i \tag{3.27}$$

where $\boldsymbol{I}$ is the identity matrix.

Remark 3.1 *In other research areas, the terms* ridge regression *or* biased estimation *are often used, see for instance Golub & van Loan (1996); Vinod & Ullah (1981). The discrete Tikhonov regularization and the ridge estimation are formally identical (Bouman, 1998, pg. 27). Yet the solution motivation is different. The primary motivation in the development of the Tikhonov regularization is the solution of Fredholm integrals of the first kind (Tikhonov & Arsenin, 1977). Ridge estimation in turn stabilizes linear systems of equations that may originate from an arbitrary (physical or mathematical) problem.*

Methods Based on Singular Value Decomposition. Ekstrom & Rhodes (1974) introduced a variant of Tikhonov's regularization that filters the unstable solution with the filter factors

$$\delta_\alpha = \frac{\sigma_i}{\sigma_i + \alpha} \approx \begin{cases} 1 & \text{for } \sigma_i \gg \alpha \\ \dfrac{\sigma_i}{\alpha} & \text{for } \sigma_i \ll \alpha \end{cases} \tag{3.28}$$

It is often denoted as damped singular value decomposition (DSVD). The damped singular value decomposition introduces less filtering than the Tikhonov regularization (for the same α). The filter factors decay slower than the Tikhonov filter factors.

The truncated singular value decomposition (TSVD) suppresses the highest frequencies in the solution. The summation is truncated using the filter factors and thus, high-frequency errors have no impact in the solution. Unfortunately, high-frequency components of the signal are also truncated. The regularized solution of the truncated singular value decomposition is (Hansen, 1998)

$$\hat{\boldsymbol{x}}_k = \sum_{i=1}^{n} \delta_k \frac{\boldsymbol{u}_i^T \boldsymbol{y}}{\sigma_i} \mathbf{v}_i \qquad \delta_k = \begin{cases} 1 & \text{for } i \leq k \\ 0 & \text{for } i > k \end{cases} \tag{3.29}$$

The solution represents the ideal low-pass filter in the spectral domain (Oppenheim et al., 1999).

Landweber Iteration (LAI). The iteration method solves the normal equation via matrix-vector multiplications and constructs a sequence of iteration vectors that converge to the generalized inverse solution. It only has a regularization effect when it is stopped before convergence is achieved. This phenomenon is frequently referred to as *semiconvergence*, see for instance Hansen (1998). Hence, the iteration number plays the role of a regularization parameter. The solution may become unstable again when the iterations exceed an optimal value. Starting from the normal equation, here in continuous form,

$$\mathcal{A}^* \mathcal{A} f = \mathcal{A}^* \tilde{g} \tag{3.30}$$

the Landweber iteration method is formulated as (Strand, 1974)

$$f_{k+1} = f_k + \beta \left(\mathcal{A}^* \tilde{g} - \mathcal{A}^* \mathcal{A} f_k \right) \tag{3.31}$$

where

k	stands for the number of iteration steps
f_k	is the solution in the k-th step
f_{k+1}	is the solution in the $k+1$-th step
β	is the relaxation parameter, set as $0 < \beta < 2/\sigma_1$

The starting value for the solution is often $f_0 = 0$. The Landweber iteration method converges to the generalized solution when β is chosen as $0 < \beta < 2/\sigma_1$. It can be written in spectral form as (Louis, 1988; Hansen, 1998)

$$f_k = \sum_{i=1}^{\infty} \left(1 - (1 - \beta\sigma_i^2)^k\right) \frac{(\tilde{g}, u_i)}{\sigma_i} v_i \tag{3.32}$$

In pseudo-code, the method becomes

```
Algorithm (Landweber Iteration):
  set $k_{max}$, set $\beta$, $\boldsymbol{x} = 0$, $\boldsymbol{r} = \boldsymbol{y}$
    for $k = 1 : k_{max}$
        $\boldsymbol{x} = \boldsymbol{x} + \beta \boldsymbol{A}^T \boldsymbol{r}$        Solution Vector
        $\boldsymbol{r} = \boldsymbol{y} - \boldsymbol{A}\boldsymbol{x}$        Residual Vector
    end
```

Conjugate Gradients (CG). The conjugate gradient method is much more involved than the Landweber iteration method. Conjugate gradients are especially suited for the solution of large, sparse (symmetric and positive definite) systems of equations (Lanczos, 1950). It has been applied to large-size adjustment problems from satellite geodesy by several authors, see for instance Schuh (1996). The main idea of the algorithm is that the residuals $r_k = \tilde{g} - \mathcal{A} f_k$ and the iterates f_k are orthogonal to the residuals of the normal equations $\mathcal{A}^* r_k = \mathcal{A}^* \tilde{g} - \mathcal{A}^* \mathcal{A} f_k$ (Hestenes & Stiefel, 1952). The convergence rate of the method is dependent on the condition number of $\boldsymbol{A}$; often preconditioned versions are employed. Since the (non-linear) method is more complex than the preceding methods, the following pseudo-code describes the algorithm for the solution of the normal equation system $\boldsymbol{A}^T\boldsymbol{A}\boldsymbol{x} = \boldsymbol{A}^T\boldsymbol{y}$ in detail. It is often denoted as conjugate gradients by least-squares (CGLS) (Björk, 1996) and does not involve the explicit computation of $\boldsymbol{A}^T\boldsymbol{A}$. Alternative conjugate gradient algorithms can be found in Lanczos (1950), Golub & van Loan (1996, pg. 520) or Hanke (1995, pg. 17, 24).

```
Algorithm (Conjugate Gradients by Least-Squares):
  set $k_{max}$, $\boldsymbol{x} = 0$, $\boldsymbol{r} = \boldsymbol{y}$, $\boldsymbol{d} = \boldsymbol{A}^T\boldsymbol{r}$, $\rho_0 = \boldsymbol{d}^T\boldsymbol{d}$
    for $k = 1 : k_{max}$
        $\alpha_k = \rho_{k-1} / \left[(\boldsymbol{A}\boldsymbol{d})^T \boldsymbol{A}\boldsymbol{d}\right]$
```

```
        $\boldsymbol{x} = \boldsymbol{x} + \alpha_k \boldsymbol{d}$                  Solution Vector
        $\boldsymbol{r} = \boldsymbol{r} - \alpha_k \boldsymbol{A}\boldsymbol{d}$                Residual Vector
        $\rho_k = \left(\boldsymbol{A}^T\boldsymbol{r}\right)^T \boldsymbol{A}^T\boldsymbol{r}$
        $\boldsymbol{d} = \boldsymbol{A}^T\boldsymbol{r} + \rho_k/\rho_{k-1}\boldsymbol{d}$
    end
```

After k iterations, the residuals are mutually orthogonal. As before, the stop criteria for the iteration is a complicated matter if one wants to make use of the regularization properties of CGLS (Hansen, 1998, pg. 149). In this thesis, the appropriate value for k_{max} is determined experimentally. The spectral filter factors can be found again in Hansen (1998) to

$$\delta_{i,k} = 1 - \prod_{j=1}^{p} \frac{\theta_j^p - \sigma_i^2}{\theta_j^p} \qquad i = 1, \ldots,\ n \tag{3.33}$$

The (Ritz values) θ_j^p are the p eigenvalues of $\mathcal{A}^*\mathcal{A}$ of the *Krylov space* $\mathcal{K}_k$. The Krylov space, often referred to as the space of polynomials of degree k, is defined as (Hanke, 1995, pg. 7)

$$\mathcal{K}_k = \operatorname{span}(\boldsymbol{r}_0,\ \boldsymbol{A}\boldsymbol{r}_0,\ \boldsymbol{A}^2\boldsymbol{r}_0, \ldots,\ \boldsymbol{A}^{k-1}\boldsymbol{r}_0) \tag{3.34}$$

where $\boldsymbol{r}_0 = \boldsymbol{y} - \boldsymbol{A}\boldsymbol{x}_0$ is computed using an initial guess $\boldsymbol{x}_0$. The convergence rate of the CG method is given by (Golub & van Loan, 1996, pg. 530)

$$\|\boldsymbol{x} - \hat{\boldsymbol{x}}_k\|_A \leq 2\|\boldsymbol{x} - \boldsymbol{x}_0\|_A \left(\frac{\sqrt{\operatorname{cond}(\boldsymbol{A})} - 1}{\sqrt{\operatorname{cond}(\boldsymbol{A})} + 1}\right)^k \tag{3.35}$$

where $\operatorname{cond}(\boldsymbol{A})$ is the condition number of $\boldsymbol{A}$.

Summary. All discussed methods can be considered as filtered least-squares solutions. Table 3.1 summarizes the corresponding filter factors. p stands for the upper summation limit in the spectral decomposition. The inverse solution (INV), the least-squares solution (LSQ) and least-squares collocation (LSC) are added for completeness. Note the difference in matrix dimension when using the INV solution or the other solutions, the design matrix is either square or rectangular. A similar result is shown in Bouman (1998), which should also be consulted for further analyses.

Three filter factors are compared in Figure 3.3 (a). The singular value is chosen as $\sigma_l = (R/(R+4))^{l+1}$, which corresponds to a continuation height of 4 km. The singular values are sorted with respect to the spherical harmonic degree. The considered frequency band is $1 \leq l \leq 4000$. The regularization parameter $\alpha = 0.5$ is used for TIK and DSVD. The TIK corresponds to the LSC for $\alpha = 1$. As mentioned before, the DSVD filter decays slower than the Tikhonov filter, which corresponds to less filtering. Figure 3.3 (b) shows the TIK and the DSVD solution versus a varying regularization parameter, l is fixed.

As mentioned before, a numerical evaluation requires the finite dimensional discretization of the downward continuation problem. Discretization, however, always stabilizes the problem to a certain extend. Depending on the resolution, continuation height, noise level etc., further regularization may not be required. Additional regularization methods can be derived by combining several methods. Kusche (2002), for instance, derives a combination of the Tikhonov regularization and iteration methods, which shows an increased filtering effect.

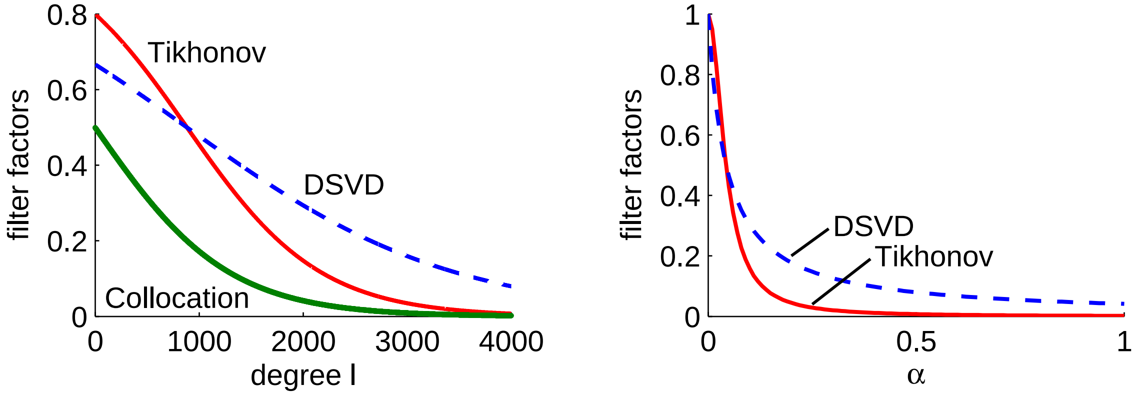

(a) Filter factors as a function of degree

(b) Filter factors as a function of the regularization parameter α

Figure 3.3: Filter factors

Table 3.1: Filter factors

Name	Abbr.	p	Filter δ
Inverse solution	INV	m	1
Least-squares solution	LSQ	n	1
Tikhonov regularization	TIK	n	$\dfrac{\sigma_i^2}{\sigma_i^2+\alpha^2}$
Least-squares collocation	LSC	n	$\dfrac{\sigma_i^2}{\sigma_i^2+1}$
Damped SVD	DSVD	n	$\dfrac{\sigma_i}{\sigma_i+\alpha}$
Truncated SVD	TSVD	n	$\begin{cases} 1, & i=1,\dots,k \\ 0, & i=k+1,\dots,n \end{cases}$
Landweber iteration	LAI	n	$1-(1-\beta\sigma_i^2)^k$
Conjugate gradient	CG	n	$1-\prod_{j=1}^{k}\dfrac{\theta_j^k-\sigma_i^2}{\theta_j^k}$

3.3 Analysis of the Discrete Downward Continuation Problem

The concept of ill-posed problems goes back to Hadamard (1923). He calls a problem *well-posed* when the solution:

- exists (surjective), the input data satisfy $g \in \mathcal{R}(\mathcal{A})$,
- is unique (injective),
- is a continuous function of the data, $\mathcal{A}^{-1} : G \rightarrow F$ is continuous.

Consequently, a problem that does not satisfy one or more of these conditions is called an *ill-posed* problem. The continuous downward continuation problem has been classified as an inverse, ill-posed problem (Schwarz, 1979); at least the last (Hadamard) condition is violated since the operator $\mathcal{A}$ is compact and $\dim(F) = \infty$.

The classification of the discrete problem has been controversially discussed. Discrete Fredholm integrals of the first kind are not ill-posed in the original Hadamard sense according to Groetsch (1984). Hansen (1990) uses the terminology of *discrete* *ill-posed problems* whenever the underlying continuous problem is ill-posed. Vaníček et al. (1996), Martinec (1996) and Wong (2000) define the discrete downward continuation problem as a well-posed problem for a 'reasonable' grid size, continuation height and computer floating point accuracy. Their classification is mainly based on the last Hadamard condition. It is argued that $\boldsymbol{A}^{-1}$ remains bounded ($\mathcal{R}(\boldsymbol{A}) \subset \mathbb{R}^n$) and discretization acts as natural filter/regularization.

The first two conditions are less studied. The first condition depends on the used data (including the noise). Basically, it is a smoothness condition and existence cannot be guaranteed for all cases. Hence, there may be cases where the n functionals are not linearly independent or $g \notin \mathcal{R}(\boldsymbol{A})$. Moreover, the discrete problem may not be injective: If a solution exists, the nullspace $\mathcal{N}(\boldsymbol{A})$ may not be empty. Hence, one can always add an arbitrary element from the nullspace to the solution $\boldsymbol{x}$. Consequently, even if the discrete solution exists and appears to be stable, it may not be unique (Kusche, 2002). Therefore, the discrete downward continuation problem is considered here as a *discrete ill-posed problem.*

Two aspects of the discrete problem may be further studied (Louis, 1988; Hansen, 1990):

- the degree of ill-posedness, condition numbers and decay rate of singular values
- the discrete Picard condition.

An analysis of the degree of ill-posedness, condition numbers and decay rate of the singular values, provides more insight into the stability problem. The Picard condition, in turn, examines the existence of the problem (linearly independent functionals) and the need for stabilization. It should be noted that an analysis of the problem does not change the numerical complexity and theoretical difficulty of the problem, but it may improve the understanding of the problem and lead to alternative solution concepts.

Degree of Ill-posedness

The degree of ill-posedness is a finer classification for ill-posed problems. According to Wahba (1990) and Hofmann (1993), the degree of ill-posedness ν is given by the decay rate of the singular values $\sigma_i \rightarrow 0$ or

$$\nu \;:=\; \sup\{\mu \;:\; \sigma_i \;=\; \mathcal{O}(i^{-\mu}) \text{ as } i \rightarrow \infty\} \tag{3.36}$$

A linear *mildly* ill-posed problem is then given by

$$\sigma_i \;\sim\; i^{-\nu}, \quad 0 \;<\; \nu \;<\; 1 \tag{3.37}$$

Similarly, a *moderately* ill-posed problem is $1 \leq \nu < \infty$ and a *severely* ill-posed problem if $\nu = \infty$. For a discrete problem, one could reformulate the conditions to $0 < \nu < 1$ for a mildly ill-posed problem, $1 \leq \nu \leq 5$ for a moderately ill-posed problem and $\nu > 5$ for a severely ill-posed problem. The values of ν are selected for a computer precision of about 10^{-16} and maximum value of $i = 2000$. Alternatively, the degree of ill-posedness could be linked to the ratio between height H and spacing S. As described in Schwarz (1973), the problem becomes problematic for a ratio $\frac{H}{S} > 1$.

Figure 3.4 shows the singular values for the downward continuation of simulated airborne data (spacing $2.5' \times 2.5'$). The continuation height is between 2 km and 6 km. The data used for Figure 3.4 are further described in Section 3.5. The singular values decay by $i^{-\nu}$, where $0 < \nu < 1$. Conservatively, ν lies between 0.01 to 0.3 while the height-to-spacing ratio is $0.4 < \frac{H}{S} < 1.3$. For the selected spacing and heights, the discrete downward of airborne and terrestrial gravity data can be classified as a *mildly ill-posed* problem. Figure 3.4 also shows the corresponding *condition numbers* that are defined as

$$\kappa = \text{cond}(\mathcal{A}) := \|\mathcal{A}^{-1}\|\|\mathcal{A}\| \geq \|\mathcal{A}^{-1}\mathcal{A}\| = 1 \tag{3.38}$$

An analysis of the condition numbers for airborne gravity data was first performed in Schwarz (1971, 1973). For the satellite case refer to Kusche (2002, pg. 37). If matrix $\boldsymbol{A}$ is symmetric and positive-definite, the condition number can be computed as

$$\kappa = \text{cond}(\boldsymbol{A}) = \frac{\sigma_1}{\sigma_{\text{rank}(\boldsymbol{A})}} \tag{3.39}$$

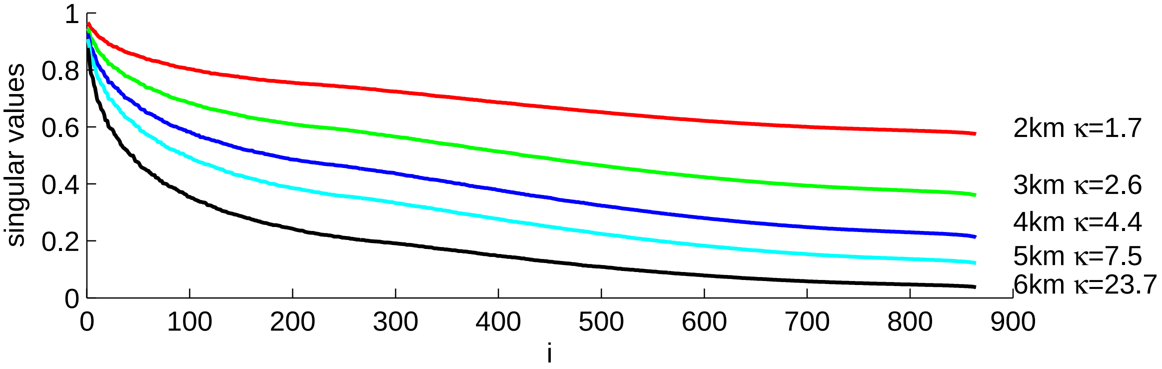

Figure 3.4: Singular values and condition numbers

where $\sigma_1 \geq \sigma_2 \geq \cdots \geq \sigma_{\mathrm{rank}(\boldsymbol{A})}$. The very small condition numbers lead to the conclusion that the problem is *well-conditioned* for the considered spacing and heights.

Note that the condition number can be used to quantify the effect of pertubations in $\mathcal{A}$ and in g. For $\|\delta\mathcal{A}\| < \frac{1}{\|\mathcal{A}^{-1}\|}$, the equation $\mathcal{A}f = g$ becomes

$$(\mathcal{A} + \delta\mathcal{A})(f + \delta f) = g + e = \tilde{g} \tag{3.40}$$

The following *stability measure* can then be derived (Kress, 1989, pg. 216)

$$\frac{\|\delta f\|}{\|f\|} \leq \frac{\mathrm{cond}(\mathcal{A})}{1 - \mathrm{cond}(A)\frac{\|\delta\mathcal{A}\|}{\|\mathcal{A}\|}} \left(\frac{\|e\|}{\|g\|} + \frac{\|\delta\mathcal{A}\|}{\|\mathcal{A}\|} \right) \tag{3.41}$$

since $\delta f = \left(\mathcal{I} + \mathcal{A}^{-1}\delta\mathcal{A}\right)^{-1} \mathcal{A}^{-1} \left(e - \delta\mathcal{A}f\right)$.

Picard Condition

A square-integrable solution of $\mathcal{A}f = g$ exists if and only if $g \in \mathcal{R}(\mathcal{A})$ and the Picard condition is satisfied (Hansen, 1990, 1994)

$$\sum_{i=1}^{\infty} \left(\frac{(u_i, g)}{\sigma_i} \right)^2 < \infty \qquad \text{for} \quad \sigma_i \neq 0 \tag{3.42}$$

This follows directly from (Kress, 1989, pg. 234)

$$\sum_{i=1}^{\infty} \left(\frac{(u_i, g)}{\sigma_i} \right)^2 = \sum_{i=1}^{\infty} (f, v_i)^2 \leq \|f\|_2^2 \tag{3.43}$$

The Picard condition states that the Fourier coefficients (u_i, g) have to decay faster than the corresponding singular values σ_i. Hence, the Picard condition is a smoothness condition for g. Using discrete data, the summation in Eqn. (3.42) is bounded although it may become large for noisy data (this is one of the reasons for Wong (2000) to call the problem well-posed). Analogously, a discrete Picard condition can be formulated, which compares the decay rate of $\boldsymbol{u}_i^T \boldsymbol{y}$ to the singular values σ_i. The decay rate of $\boldsymbol{u}_i^T \boldsymbol{y}$ does not have to be monotonic but should be on average faster than the one of the singular values (Hansen, 1990). Cases of i, where $\boldsymbol{u}_i^T \boldsymbol{y}$ or σ_i are numerically zero, should be excluded.

$\boldsymbol{u}_i^T \boldsymbol{y}$ may be varying fast when using noisy observations. Hence, a plot of $\boldsymbol{u}_i^T \boldsymbol{y}$ and σ_i is often difficult to interpret. Therefore, Hansen (1990) proposes to check the *Picard ratio*

$$\omega_i := \left(\frac{\prod_{j=i-q}^{i+q} |\boldsymbol{u}_i^T \boldsymbol{y}|}{\sigma_i} \right)^{1/(2q+1)} \qquad i = 1+q, \ldots, n-q \tag{3.44}$$

where q is a small integer ($q = 10$ is chosen here). This ratio should decay monotonically to zero to satisfy the Picard condition. It is a moving geometric mean and filters out the highest variations of $\boldsymbol{u}_i^T \boldsymbol{y}$.

Figure 3.5 shows two examples for the Picard condition. The left hand side shows the Picard ratio for the downward continuation of noise-free gravity disturbances. The data height is 2 km. The Picard condition is satisfied in Figure 3.5 (a). The Picard ratio ω_i given in Eqn. (3.44) decays monotonically (red line). Hence, a solution for $\mathcal{A}f = g$ exists. Stabilization or regularization may only be required to filter some of the high variations of $\boldsymbol{u}_i^T \boldsymbol{y}$. No regularization is required for smaller degrees i.

A different situation is shown in Figure 3.5 (b). Noisy gravity data at 6 km are

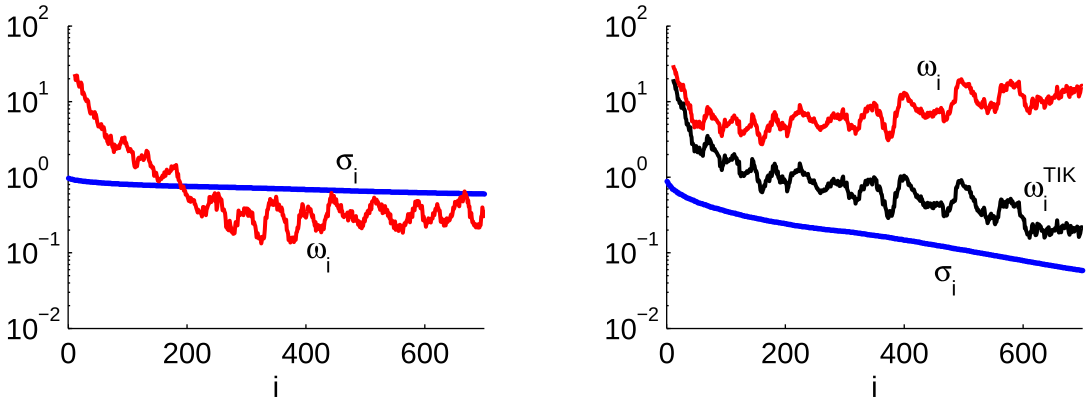

(a) Picard ratio ω_i for noise-free data at 2km, $q = 10$

(b) Picard ratio ω_i for noisy data at 6km and Tikhonov-regularized Picard ratio ω_i^{TIK} with $\alpha = 0.25$, $q = 10$

Figure 3.5: Picard condition for simulated airborne data

used. In this case, the Picard condition is *not* satisfied. The Picard ratio increases for $i \geq 200$. To solve this downward continuation problem, regularization is required. The stabilization should dampen the components for which the perturbation dominates. Using the TIK filter factor $\delta_\alpha = \sigma_i^2/(\sigma_i^2 + \alpha^2)$ for instance, the following *regularized Picard ratio* can be computed

$$\omega_i^{\mathrm{TIK}} = \left(\delta_\alpha \frac{\prod_{j=i-q}^{i+q} |\boldsymbol{u}_i^T \boldsymbol{y}|}{\sigma_i} \right)^{1/(2q+1)} \qquad i = 1 + q, \ldots, n - q \tag{3.45}$$

The regularized Picard ratio ω_i^{TIK} is also shown in Figure 3.5(b). Clearly, the ratio decays rapidly and indicates that the problem is stabilized by the Tikhonov regularization.

3.4 An Alternative Numerical Solution

The preceding continuation solutions are very involved both in terms of implementation and computational burden. Moreover, it is often not possible to solve the large system of linear equations on a standard computer even when sparse matrix computations could be performed. Other approximate solutions have to be found.

An alternative solution for the downward continuation of terrestrial gravity anomalies can be formulated as

$$\hat{\Delta g}(Q) = \frac{R+\bar{H}}{4\pi R} \int\limits_{\omega_{\mathrm{c}}} K(Q,\bar{P})\Delta g(\bar{P})\ d\omega(\bar{P}) \tag{3.46}$$

where only the critical near-zone is considered and the kernel function $K(Q,\bar{P})$ is given as

$$K(Q,\bar{P}) = \sum_{l=2}^{L_{\mathrm{Max}}} (2l+1) \left(\frac{R+\bar{H}}{R}\right)^{l+1} P_l(Q,\bar{P}) \tag{3.47}$$

In eqns. (3.46) and (3.47), $\bar{H}$ is the mean height of the gravity data inside the spherical cap ψ_{c}. $\bar{H}$ is changing from computation point to computation point. The maximum L_{Max} may be selected according to the input data or to the desired solution bandwidth. Of course, the kernel function can be modified if necessary.

Remark 3.2 *The truncated (or band-limited) summation kernel can be considered as* TSVD- *regularized since the highest frequencies are suppressed.*

Using the remove-restore technique, the input data $\Delta g(P)$ are first reduced by the satellite data (Δg^{S}) and the topographic and atmospheric effects, yielding residual gravity data $\Delta g'(r,\theta,\lambda)$. They are then upward or downward continued to a mean height $\bar{H}$, i.e. $\Delta g'(r,\theta,\lambda) \rightarrow \Delta g'(\bar{r},\theta,\lambda) = \Delta g'(\bar{P})$. This intermediate continuation step may approximately be solved by taking the first term of a Taylor series development:

$$\begin{aligned} \Delta g'(r,\theta,\lambda) &= \Delta g'(\bar{r},\theta,\lambda) + \left(\frac{\partial \Delta g'}{\partial r}\right)\Bigg|_{(\bar{r},\theta,\lambda)} (r-\bar{r}) + \cdots \\ &\approx \Delta g'(\bar{r},\theta,\lambda) + \left(\frac{\partial \Delta g'}{\partial r}\right)\Bigg|_{(\bar{r},\theta,\lambda)} (H-\bar{H}) \end{aligned} \tag{3.48}$$

Hence, the upward and downward continuation of the residual gravity data to a mean height can be performed with

$$\Delta g'(\bar{r},\theta,\lambda) = \Delta g'(r,\theta,\lambda) - \left(\frac{\partial \Delta g'}{\partial r}\right)\Bigg|_{(\bar{r},\theta,\lambda)} (H - \bar{H}) \tag{3.49}$$

The vertical gradient of gravity anomalies is computed from a high-degree spherical harmonic model as

$$\left(\frac{\partial \Delta g'}{\partial r}\right)\Bigg|_{(\bar{r},\theta,\lambda)} = \frac{GM}{R} \sum_{l=L_\mathrm{S}+1}^{L_\mathrm{M}} \frac{(l-1)(l+2)}{\bar{r}^2} \left(\frac{R}{\bar{r}}\right)^{l+1} \sum_{m=-l}^{l} \Delta \bar{K}_{lm}^{\mathrm{M}} \bar{Y}_{lm}(\theta,\lambda) \tag{3.50}$$

Similar derivations can easily be made for gravity disturbances or other functionals of the disturbing potential.

In eqns. (3.46) to (3.50), it has been assumed that

i) the gravity data are band-limited (note that mean gravity data are frequency limited) or the desired continuation result is not adversely affected by band-limiting the kernel function. Solving for the geoid, for instance, may permit such an approximation since most of the power is in the low-frequencies (the omission error is small).

ii) the data spacing is not too fine and the continuation height is not too large. A stability investigation may be required for critical cases since the kernel function is divergent for a large continuation height.

iii) the height difference between the data point H and mean height $\bar{H}$ is small.

iv) higher Taylor terms do not significantly contribute in Eqn. (3.49).

v) the vertical gradient of the gravity anomalies computed from a model (Eqn. 3.50) sufficiently represents the actual vertical gradient between H and $\bar{H}$.

After the integration yielding $\hat{\Delta g}'(Q)$, the final result $\hat{\Delta g}(Q)$ at the reference sphere is obtained by adding back the indirect topographic and atmospheric effects as well as the satellite contribution Δg^{S}, see Eqn. (2.1). Additionally, the far-zone effect $(\omega - \omega_\mathrm{c})$ may be approximately computed using a geopotential model. This approach will be denoted as the *alternative numerical solution* (A).

Remark 3.3 *A downward continuation approach based on a Taylor series development is the so-called analytical continuation (Moritz, 1989; Sideris, 1987). The approach can be used due to Runge's theorem, see for instance Moritz (1989). A numerical comparison to the Poisson downward continuation is performed in Huang (2002).*

When the geoid is sought, the downward continuation and transformation into the potential can be combined into one step. This will be called the *direct approach* (DA). The integral in Eqn. (3.46) and the kernel in Eqn. (3.47) are replaced by (employing $\frac{R+\bar{H}}{l-1}$ from the Meissl scheme)

$$\hat{T}(Q) = \frac{R+\bar{H}}{4\pi} \int\limits_{\omega_c} K(Q,\bar{P}) \Delta g(\bar{P}) \; d\omega(\bar{P}) \tag{3.51}$$

and

$$K(Q,\bar{P}) = \sum_{l=2}^{L_{\text{Max}}} \frac{2l+1}{l-1} \left(\frac{R+\bar{H}}{R}\right)^{l+1} P_l(Q,\bar{P}) \tag{3.52}$$

Using (airborne) gravity disturbances instead of anomalies, the kernel function would be given by

$$K(Q,\bar{P}) = \sum_{l=1}^{L_{\text{Max}}} \frac{2l+1}{l+1} \left(\frac{R+\bar{H}}{R}\right)^{l+1} P_l(Q,\bar{P}) \tag{3.53}$$

if no further kernel modification was used. Eqns. (3.51 - 3.53) remind of the *one-step approach* presented in Novák & Heck (2002). Indeed, the DA would be equivalent to the one-step approach if the gravity data were provided on a reference sphere $R + H$. This is, however, rarely the case in reality. Therefore, the A or DA should be preferred in practical computations. Moreover, the design matrix is *not* explicitly assembled (in constrast to the formulation in Novák & Heck (2002)). This allows for an efficient computation and reduces the memory load (no storage problem). More importantly, the solution will be less burdened with numerical instabilities, see for instance Björk (1996). Note also that the continuation process to a mean height in a first step acts implicitly as a (low-pass) filter. The following pseudo code describes the implemenation of the algorithm:

```
Algorithm (Alternative Approximation/Direct Approach):
  set $\psi_c$, set $L_M$ (set $L_{MD}$ kernel modification degree if desired)
  while computation point $\leq$ total number of computation points
    if $\psi_{ij} \leq \psi_c$          integration point is inside the spherical cap
          $\mathrm{sum} = \mathrm{sum} + H_j$          add heights in spherical cap
    end
          $\bar{H} = \frac{\mathrm{sum}}{n}$          average height over all points inside the cap
          $\bar{r} = R + \bar{H}$          average radius of the spherical cap
    compute Eqn. (3.50) for point $(\bar{r}, \theta, \lambda)$ from a high-degree model
  end
  while computation point $\leq$ total number of computation points
     if $\psi_{ij} \leq \psi_c$          integration point is inside the spherical cap
        continue to mean height of spherical cap using Eqn. (3.49)
           integrate with (modified) band-limited kernel function
        end
     end
  end
```

Stability Investigation

Before the alternative approximation is applied, a stability investigation ought to be performed since the term $\left(\frac{R+H}{R}\right)^{l+1}$ is divergent for higher degrees of l. Three main factors influence the alternative approximation – the continuation height, the solution bandwidth and the data spacing. All three components are lumped into the factor

$$\kappa \approx \left(\frac{R+H}{R}\right)^{l+1} \approx \left(\frac{R+H}{R}\right)^{R\pi/x} \tag{3.54}$$

when the upward continuation degree is associated with the data spacing and band-limitation degree. The condition number κ is increasing with increasing continuation height ($H \to \infty$), decreasing grid spacing or increasing upward continuation degree ($l + 1 \to \infty$). Figure 3.6 shows approximate condition numbers for different spatial resolutions and continuation heights. The conversion between spatial resolution x [km]

and the upward continuation degree is $l + 1 = R\pi/x$, see also Table 5.3. When the condition number is above the computer precision ($\approx 10^{16}$), the problem is said to be numerically unstable and requires stabilization.

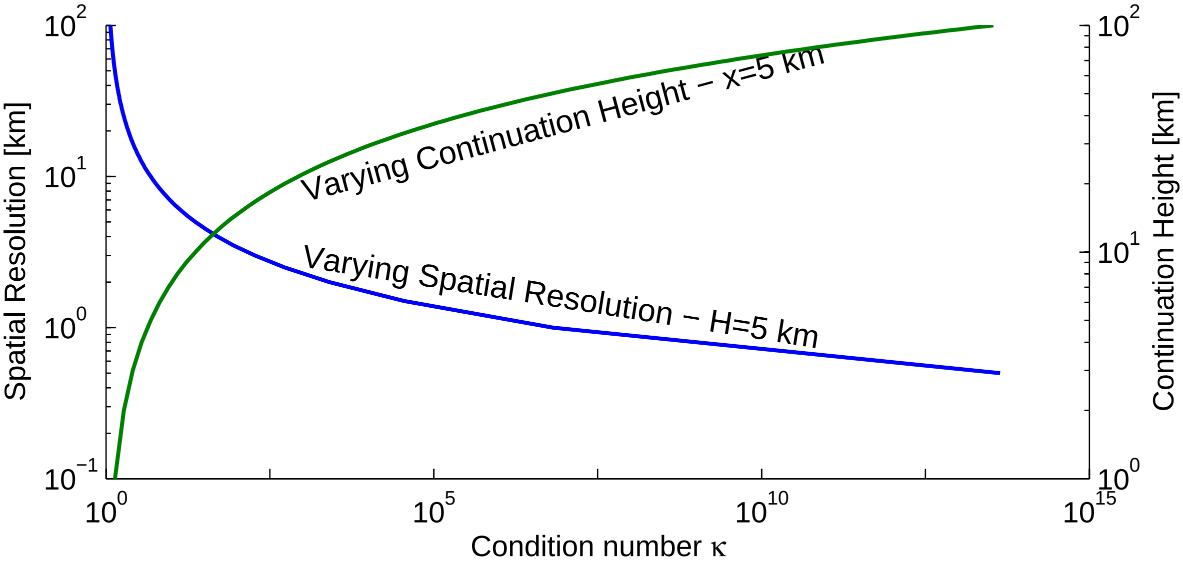

Figure 3.6: Approximate condition numbers for different continuation heights and spatial resolutions

From Figure 3.6 it can be concluded that the alternative approximation may be applied to terrestrial and airborne measurements. The downward continuation of satellite data may be only admissible for large data spacings, say 100 km, since the altitude is large. Furthermore, the alternative approximation is confined to spatial resolutions larger than 0.7 km. In reality, the quality of the alternative approximation may also suffer from errors due to the recursive computation of Legendre polynomials. Feasibility tests with satellite data will have to follow.

3.5 Downward Continuation Results

The downward continuation of airborne gravity disturbances was simulated. A spacing of $2.5' \times 2.5'$ (about 5 km half-wavelength) was selected since coarser grids did not suffer from the downward continuation problem at the specified continuation heights and the simulated gravity data, see Novák et al. (2001b). Also, the downward continuation of terrestrial gravity data did not involve additional difficulties. The statistics of the simulated data are summarized in Table 3.2. In this case, a data area of 2° × 2° was used and a spherical cap radius of $\psi_{\mathrm{c}} = 0.5°$ due to numerical difficulties with larger data areas.

Table 3.2: Simulated data statistics for the downward continuation problem

Type	Degree [–]	Density [']	Height [km]	Min	Max	Mean	Std	Unit
T	121-2160	2.5	0	-6.438	8.523	-0.093	2.422	$\mathrm{m}^2/\mathrm{s}^2$
δg	121-2160	2.5	0	-30.983	31.563	-0.261	10.278	mGal
$\delta g + e$	121-2160	2.5	2	-29.266	28.437	-0.259	9.050	mGal
$\delta g + e$	121-2160	2.5	3	-27.721	26.573	-0.258	8.498	mGal
$\delta g + e$	121-2160	2.5	4	-26.286	25.157	-0.256	8.003	mGal
$\delta g + e$	121-2160	2.5	5	-24.950	24.202	-0.254	7.556	mGal
$\delta g + e$	121-2160	2.5	6	-23.707	23.303	-0.250	7.152	mGal

Analyzing the noisy gravity disturbances at $H = 4\,\mathrm{km}$, the signal-to-noise ratio was about $\frac{\|b\|}{\|e\|} \doteq 5.3$. Together with the height-to-spacing ratio $\frac{H}{S} \doteq 0.8$, the problem can be categorized as a critical downward continuation problem (Schwarz, 1973). An unstable least-squares solution can be expected although the applied noise is highly idealized and the data are band-limited.

A computational procedure analogous to Eqn. (2.50) was used. In this case, however, the Poisson integration was performed, see Eqn. (3.55).

$$\begin{tikzcd} \delta g_{121-2160}(R+H,\theta,\lambda)+e \arrow[r, "\text{Poisson}"] & \hat{\delta g}_{121-2160}(R,\theta,\lambda) \arrow[d] \\ \delta g_{121-2160}(R,\theta,\lambda) \arrow[r] & \text{Error} \end{tikzcd} \tag{3.55}$$

The VK modification was used to alleviate the contribution of the far-zone (Huang, 2002). The results of the test are shown in Figure 3.7. Shown along the horizontal axis are the different solutions for various continuation heights. Each bar stands for the rms error of a solution compared to the data at the reference sphere R. The left vertical axis applies to the bars. The order of the solution bars is INV, LAI, LSQ, TIK, DSVD, TSVD, CG, A. For completeness, all solutions are also listed in the Appendix in tabularized form, see Table B.4 and B.5. Two immediate conclusions can be drawn by inspecting Figure 3.7. Firstly, the downward continuation provides unstable results even for simulated, band-limited, data. The different solution concepts provide significantly different results for the same continuation height. Secondly, the downward continuation problem becomes more severe for higher continuation heights when the data spacing stays constant. In particular, the error of the LSQ solution, shown in light blue as the third column, is almost exponentially increasing, reaching maximum error ranges from -73 mGal up to +83 mGal. Without a doubt, the solution has to be stabilized or the problem differently solved.

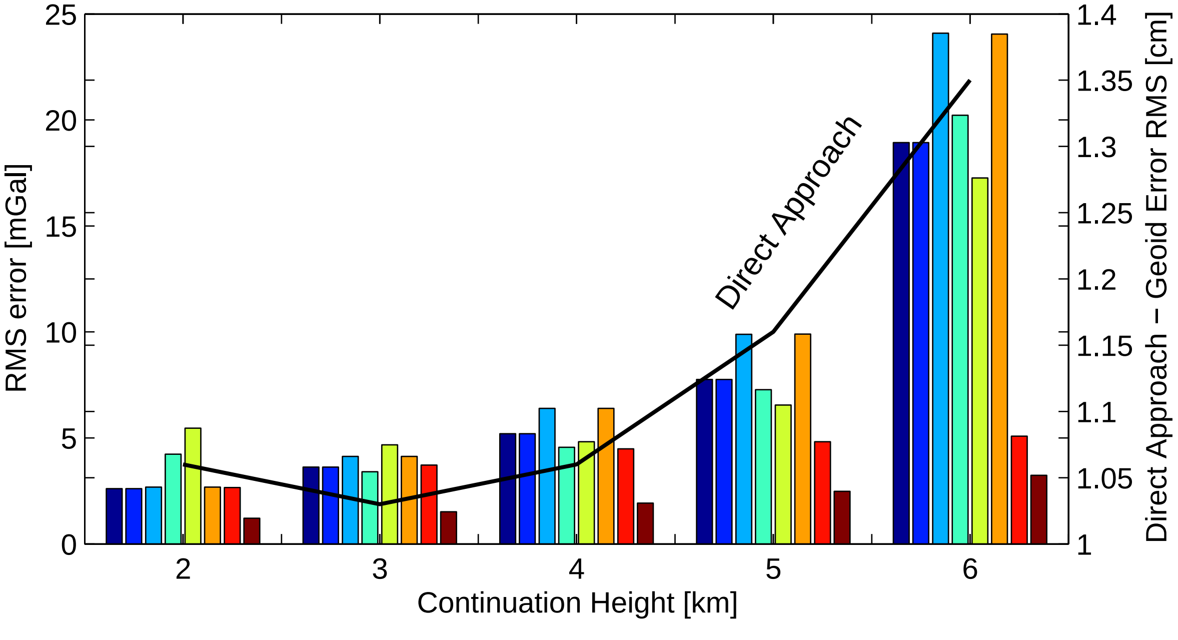

Figure 3.7: RMS error of the continuation solutions. INV, LAI, TIK, DSVD, TSVD, CG, A

Comparing the different stabilization, regularization or iteration methods, only the

CG and A seem to provide acceptable results. The noise is not overly amplified and the bias remains reasonably small. The solutions found with the TIK and DSVD are burdened with noise and have a bias. The regularization parameter α was found by the generalized cross-validation (Wahba, 1977; Golub et al., 1979) (last row in Table 3.3) and by inspecting the mean-square error function (calculating the result for several values of α). The regularization parameter α obtained from the generalized cross-validation gives an estimate for the unknown (predictive) mean square error, see for instance Kusche & Klees (2002),

$$\alpha = \arg\ \min \frac{1}{m} \|\boldsymbol{A}\hat{\boldsymbol{x}}_\alpha - \boldsymbol{A}\boldsymbol{x}\|^2 \tag{3.56}$$

where m is the number of measurements.

Table 3.3: Determination of the regularization parameter

Name	α	Remark
Optimal (MSE)	$\arg\ \min \frac{1}{n}\|\hat{\boldsymbol{x}}_\alpha - \boldsymbol{x}\|^2$	true $\boldsymbol{x}$ unknown
L-curve	$\arg\ \min \|\boldsymbol{A}\hat{\boldsymbol{x}}_\alpha - \boldsymbol{y}\|\|\hat{\boldsymbol{x}}_\alpha\|$	
GCV	$\arg\ \min \frac{m\|\boldsymbol{A}\hat{\boldsymbol{x}}_\alpha - \boldsymbol{y}\|^2}{(\mathrm{trace}(\boldsymbol{I} - \boldsymbol{Q}_\alpha))^2}$	$\boldsymbol{Q}_\alpha = \boldsymbol{A}(\boldsymbol{A}^T\boldsymbol{A} + \alpha^2\boldsymbol{I})^{-1}\boldsymbol{A}^T$

Since the problem was only mildly ill-posed for the airborne data at the considered spacing and continuation height, the mean-square error curve is relatively flat and allows a range of values for α. The results shown in Figure 3.7 represent the best set of solutions. Remarkable is the performance of the alternative approximation (A), which is the last bar in each case. It provides by far the best solution to the problem with rms error values of only 3.236 mGal. Although it clearly represents an approximation of the problem, it seems to solve the simulated downward continuation problem with the smallest rms error. It should also be noted that the alternative approximation is the most efficient solution in terms of computation time. The better performance can be attributed to the fact that the normal equation system is not set up. Furthermore, the band-limited kernel function suppresses the highest frequencies.

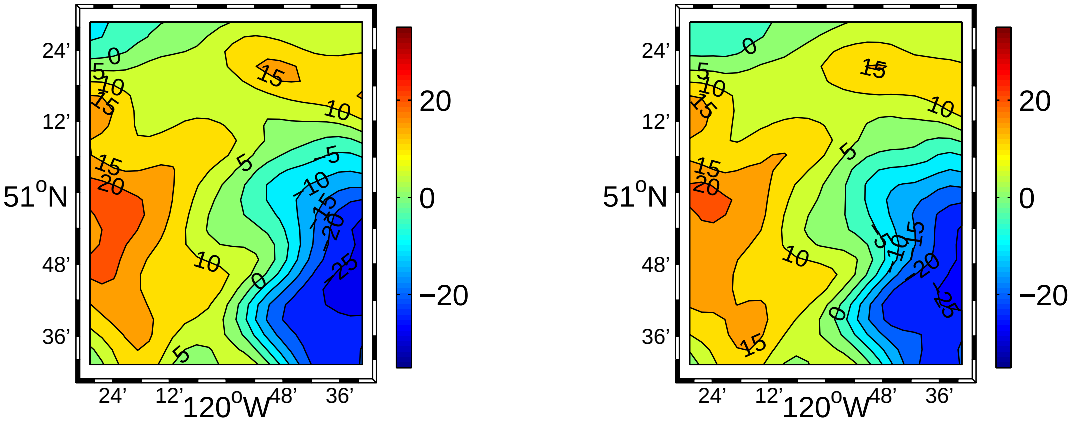

(a) Reference solution

(b) Alternative approximation solution

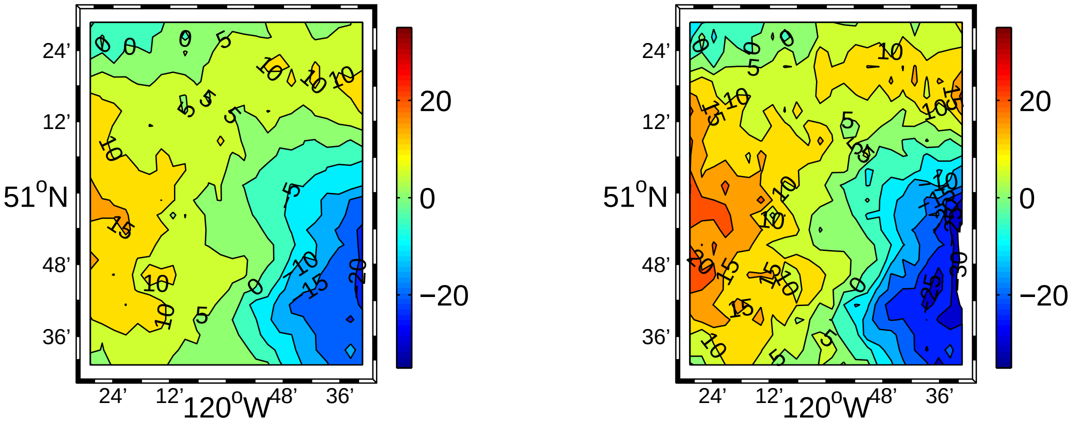

(c) Tikhonov solution

(d) Conjugate gradient solution

Figure 3.8: Reference solution versus A, TIK, and CG using gravity disturbances at 2 km [mGal]

Added to Figure 3.7 is the direct approach (DA), i.e., the direct transformation of gravity disturbances into potential as described in Section 3.4. Since the gravity data are generated at a constant height, the direct approach corresponds to the one-step approach presented in Novák & Heck (2002). The right vertical axis applies for these results. Although the error of the solution increases, it is still surprisingly accurate (less

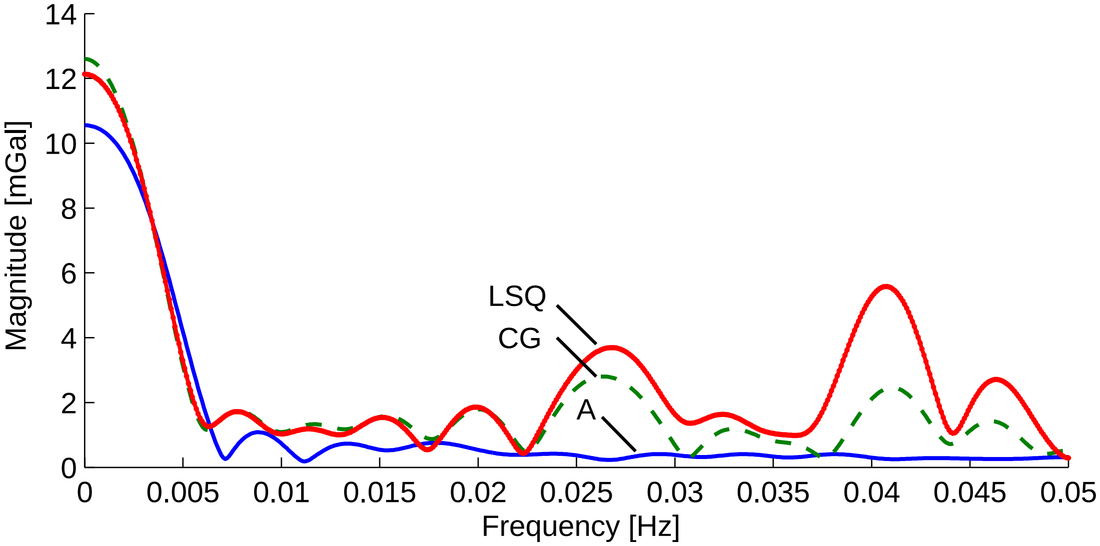

Figure 3.9: Frequency spectra of the least-squares solution (LSQ), the conjugate gradient solution (CG) and the alternative approximation (A)

than 1.5 cm for airborne data at an altitude of 6 km) taking the small computational effort into account. The direct approach is also listed in tables B.4 and B.5 in units of m.

For illustration, the A, TIK and CG solutions for a continuation height of 2 km are shown in Figure 3.8 side-by-side with the reference gravity disturbances at the reference sphere. Comparing the figures, the amplification of the noise is clearly visible in the TIK and CG solution while the A solution is very similar to the reference solution. Using a different regularization parameter in the TIK may yield a smoother solution, yet a larger bias.

Remark 3.4 *A biased solution is a problem in geoid determinations. In resource exploration, however, a biased solution would be irrelevant and a larger regularization parameter could be used.*

The error spectra, shown in Figure 3.9, visually emphasize the quality of the solutions in the frequency domain. The differences along one parallel are transformed into the frequency domain. Clearly, the LSQ amplifies the high-frequency components. The CG in turn seems to solve the inverse problem with a reasonable error compared to the reference solution. However, it follows the general trend of the LSQ. Finally, the A provides much better results. Once more, it introduces the smallest bias and does not amplify the added noise. The alternative approach is therefore recommended for the downward continuation of airborne and terrestrial gravity data. For higher resolutions and data altitudes, the conjugate gradient method is generally recommended.

4 The Combination of Heterogeneous Gravity Data

In this chapter, strategies for the combination of heterogeneous gravity data are developed. After a brief review of the underlying model problem and a discussion of alternative solutions, the formulas to be used are derived and the combination strategies are presented. Advantages and limitations of the proposed methods are discussed. Finally, a satellite model and a combined geopotential model are combined in a large regional area and a local data area.

4.1 A Glance at the Combination Problem

The combination of heterogeneous gravity data is among the most involved problems in gravity field modeling. Its solution is needed in applications such as geoid determination and resource exploration. Since a single measurement device (or measurement campaign) provides only parts of the solution, a combination with additional data enhances the quality and reliability of the solution and widens its spectrum. The remove-restore technique may be understood in this way: Satellite data and local gravity data complement each other in the frequency domain. The satellite data provides the low-frequency information of the solution and the local data covers the medium and higher frequencies. The combined solution enjoys higher quality and a wider spectrum.

Model Problem

The main problem when combining gravity data is that the data are heterogeneous. Gravity data g are functions in space (λ, φ, H) and time (t). Moreover, they have an individual noise spectrum (e) and resolve a certain frequency band (f). Hence, the following elements constitute the model problem

$$\left\{g, \varphi, \lambda, H, e, t, f, A(\mathcal{B}\hat{T})\right\} \tag{4.1}$$

where $A(\mathcal{B}\hat{T})$ stands for the used approximation method and selected representation/base functions that depends on the desired combination output. In Chapter 5, several of these characteristics are discussed in more detail.

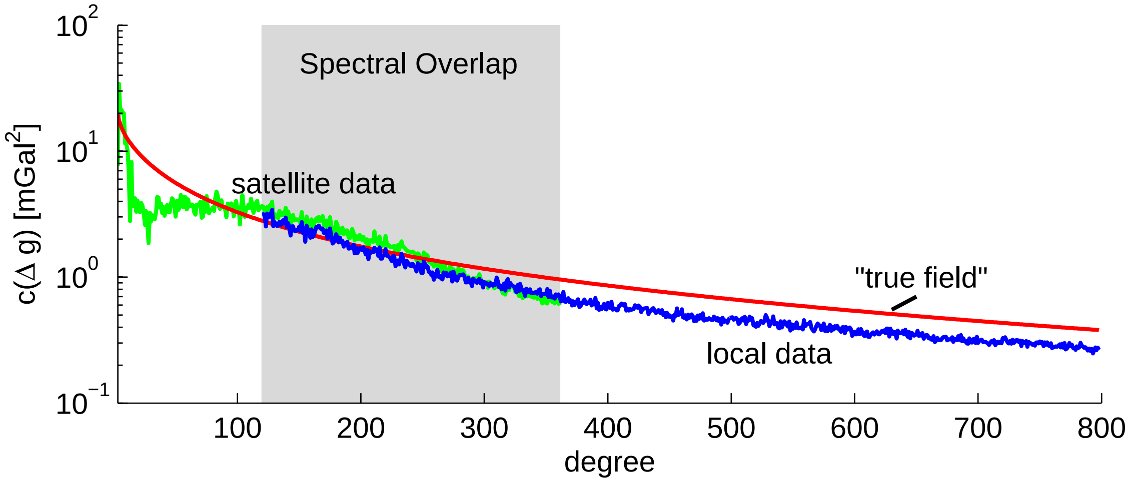

Figure 4.1: Degree variances of simulated global and local gravity data

When heterogeneous gravity data are used on the same spatial grid, the main difference (no stochastics considered) between the data is their frequency content (Schwarz, 1984). Figure 4.1 shows global and local degree variances in the spectral domain and compares them to the ’true’ solution. In this case, satellite data are the only means to recover long wavelengths of the gravity field. The extent of the medium frequency zone, shown in grey in Figure 4.1, depends on the area size of the local data and the resolution of the satellite data. Possible correlations between the local data and the global models are strongest in this overlapping zone. The high-frequency part is solely resolved from the local gravity data, representing small-scale features of the gravity field. Figure 4.1 indicates that a single data set does not resolve the entire spectrum of the gravity field. However, a unified estimate of the entire spectrum could be obtained by combining global and local gravity data in a complementary way. Additional local data would strengthen the (medium to high frequency) solution when combined in an adequate way. The maximal achievable resolution and accuracy of the combination depends on the quality of the data that are used. In this thesis, two specific local data sets are used in the combination – airborne gravity disturbances and terrestrial gravity anomalies. The global data sets include satellite data and combined geopotential models. The combination outputs are a local gravimetric geoid and a tailored high-degree spherical harmonic model.

Combination Methods

Least-squares collocation is the most commonly used model for the combination of heterogeneous gravity data. It is based on ideas in the fields of least-squares estimation, approximation theory, functional analysis, potential theory and inverse problems, see Krarup (1969); Moritz (1980b). The main elements of the model are summarized in Table A.8. In addition to the possible use of heterogeneous gravity data, the following elements describe the least-squares collocation solution (Denker, 1988, pg. 32):

i) the solution is independent of the number of signal parameters to be estimated

ii) the solution is invariant to linear transformations of the data and results

iii) the result is optimal with respect to the covariance functions used.

Least-squares collocation (LSC) is a powerful model to combine heterogeneous gravity data. Different theoretical variants (stochastic, deterministic, spatio-statistical) and various interpretations have been developed and established over the years, see for instance Moritz (1978); Sansò (1980); Moritz & Sansò (1980); Kotsakis (2000). Yet, the method has also disadvantages. The LSC solution (in physical geodesy) is usually sought in a reproducing kernel Hilbert space. The harmonic kernel function requires terms that are dependent on the choice of base functions. Typically, degree variances are used, i.e., spherical harmonics are the base functions. The choice of the base functions, and subsequently the associated norm, is somewhat arbitrary, see for instance Dermanis (1977). Furthermore, LSC may not be suited for the use of mixed gravity data problems (Svensson, 1983). This is due to the fact that the problem may not be well-posed in terms of the mean-square norm. Hence, one could argue the suitability of LSC to the current problem. A practical problem is the determination of suitable covariance functions from empirical covariance functions; see also Appendix A.6. The covariance functions are usually chosen to be invariant to rotations. As the fitting process can only be done approximately, the question arises whether the approximation leads to the correct solution. This is mainly a convergence problem as discussed in Sansò & Tscherning (1980) and cannot be proven in general. The stochastic variant of LSC suffers from the fact that it does not correspond to the physical reality – the gravity field is not a stochastic field. For a thorough discussion on this topic refer to Kotsakis (2000, pg. 46). Other valid arguments and open problems are discussed in Schwarz (1986). Although LSC will not be used in this thesis, it certainly represents an alternative for the combination of heterogeneous gravity data.

Principally, the *multiple-input/multiple-output method* (MIMO) is equivalent to least-squares collocation (Sansò & Sideris, 1997). Originally introduced in the framework of system theory, the MIMO has become a fast alternative to LSC provided that the data are given on a grid, see Bendat & Piersol (1986); Vassiliou (1986); Schwarz et al. (1990); Bendat & Piersol (1993); Sideris (1996); Li & Sideris (1997); Andritsanos et al. (2001). In addition to the efficient numerical computations, an advantage of the MIMO is the possible use of the full power spectra. While LSC requires an isotropic covariance function, the MIMO may also incorporate nonisotropic components into the solution. If they are available, their use may lead to more accurate results as pointed out in Li & Sideris (1997). Yet, a principal drawback of the method is the reliance on the observation spectra (PSD), the cross-PSD functions between different data types and noise PSD's. All these have to be determined or approximated. In particular, the non-stationarity of the noise leads to approximate solutions for the noise PSD.

A slightly different access to the combination problem offers *spectral combination*. It has been introduced as a special case of LSC by Moritz (1975). Further theoretical and practical developments are reported in Sjöberg (1980); Wenzel (1981, 1982); Wichiencharoen (1984); Wei (1986); Smeets (1994); Kern et al. (2003). Since the method involves virtually the same assumptions as LSC (stationarity is additionally assumed), interest has waned for the last decade. On the positive side, though, one could argue that the method is easier to implement and can handle an arbitrary amount of data. In addition, the method does not rely on the selection of an optimal covariance function; only the principal behaviour of the data and errors has to be modelled. A different access to the spectral combination, starting from boundary value problems and their general solution, is provided in Sacerdote & Sansò (1987) and van Gelderen & Rummel (2001).

In the following, strategies for the combination of satellite, airborne and terrestrial gravity data will be developed. Because error measures of the local gravity data at hand are insufficiently known, none of the the above combination methods will be used. An iteration method will be used that is largely immune against high-frequency noise and may filter gross errors. It is based on spherical harmonic analysis and the idea of tailoring, i.e. of improving a geopotential model by local or regional data. The original idea is revisited and further refined for the use of satellite, airborne and terrestrial gravity data. The proposed strategies solve for a combined geoid and a tailored, high-degree spherical harmonic model. The concepts of spherical harmonic analysis and synthesis are reviewed first.

4.2 Analysis and Synthesis

A square integrable function $f(\theta, \lambda)$ on the unit sphere can be expanded into a series of spherical harmonics as (Hobson, 1931)

$$f(\theta, \lambda) = \sum_{l=0}^{\infty} \sum_{m=0}^{l} \left(\bar{C}_{lm} \cos m\lambda + \bar{S}_{lm} \sin m\lambda \right) \bar{P}_{lm}(\cos\theta) \tag{4.2}$$

where $\bar{C}_{lm}$ and $\bar{S}_{lm}$ are fully normalized spherical harmonic coefficients. Due to the orthogonality relations of spherical harmonics, the spherical harmonic coefficients can be obtained as, see for instance Colombo (1981),

$$\left.\begin{matrix} \bar{C}_{lm} \\ \bar{S}_{lm} \end{matrix}\right\} = \frac{1}{4\pi} \int\limits_{\omega} f(\theta, \lambda) \left\{\begin{matrix} \cos m\lambda \\ \sin m\lambda \end{matrix}\right\} \bar{P}_{lm}(\cos\theta)\ d\omega \tag{4.3}$$

Eqn. (4.3) is usually denoted as the (continuous) *global spherical harmonic analysis*, see also Sneeuw (1994) or Jekeli (1996). The function f is given at every point and the summation in Eqn. (4.2) is performed up to infinity.

Analysis and Synthesis of the Disturbing Potential

Let the disturbing potential $T(Q)$ be the given function. Then, it can be expanded into a series of spherical harmonics as shown in Eqn. (4.2). Hence, the spherical harmonic coefficients are derived as

$$\left.\begin{matrix} \Delta\bar{C}_{lm} \\ \Delta\bar{S}_{lm} \end{matrix}\right\} = \frac{R}{GM} \frac{1}{4\pi} \int\limits_{\omega} T(Q) \left\{\begin{matrix} \cos m\lambda \\ \sin m\lambda \end{matrix}\right\} \bar{P}_{lm}(\cos\theta)\ d\omega \tag{4.4}$$

Note that $T(Q)$ is given at the reference sphere with radius R. The spherical harmonic coefficients are dimensionless due to the factor $\frac{R}{GM}$. Using cap mean values instead of point values, the spherical harmonic analysis takes the form ($\beta_l \gg 0,\ \forall\ l = 0, 1, \dots$)

$$\left.\begin{matrix} \Delta\bar{C}_{lm} \\ \Delta\bar{S}_{lm} \end{matrix}\right\} = \frac{R}{GM} \frac{1}{4\pi} \int\limits_{\omega} \frac{1}{\beta_l} \bar{T}(Q) \left\{\begin{matrix} \cos m\lambda \\ \sin m\lambda \end{matrix}\right\} \bar{P}_{lm}(\cos\theta)\ d\omega \tag{4.5}$$

Eqn. (4.5) follows from the orthogonality relations applied to

$$\bar{T}(Q) = \frac{GM}{R} \sum_{l=0}^{\infty} \beta_l \sum_{m=0}^{l} \left(\Delta\bar{C}_{lm} \cos m\lambda + \Delta\bar{S}_{lm} \sin m\lambda \right) \bar{P}_{lm}(\cos\theta) \tag{4.6}$$

where β_l are the Pellinen smoothing functions, see Appendix A.5, and $\bar{T}$ is the mean disturbing potential.

Analysis and Synthesis of Functionals of the Disturbing Potential

Since the disturbing potential is not a measurable quantity, other functionals must be used for the analysis. Equivalent to Eqn. (4.6), the synthesis step of a (mean) functional of the disturbing potential is given as

$$\mathcal{A}\bar{T}(Q) = \frac{GM}{R} \sum_{l=0}^{\infty} \beta_l \sigma_l \sum_{m=0}^{l} \left(\Delta\bar{C}_{lm} \cos m\lambda + \Delta\bar{S}_{lm} \sin m\lambda \right) \bar{P}_{lm}(\cos\theta) \tag{4.7}$$

where the spherical harmonic coefficients are

$$\left. \begin{array}{c} \Delta\bar{C}_{lm} \\ \Delta\bar{S}_{lm} \end{array} \right\} = \frac{R}{GM} \frac{1}{4\pi} \int_{\omega} \frac{1}{\sigma_l \beta_l} \mathcal{A}\bar{T}(Q) \left\{ \begin{array}{c} \cos m\lambda \\ \sin m\lambda \end{array} \right\} \bar{P}_{lm}(\cos\theta)\ d\omega \tag{4.8}$$

As before, σ_l stands for the singular value (or more precise, the eigenvalue in the self-adjoint case) in the Meissl scheme. Dividing the sphere into N data blocks, Eqn. (4.8) can be written as (Wenzel, 1985, pg. 72)

$$\left. \begin{array}{c} \Delta\bar{C}_{lm} \\ \Delta\bar{S}_{lm} \end{array} \right\} = \frac{R}{GM} \frac{1}{4\pi} \sum_{i=1}^{N} \frac{1}{\sigma_l \beta_l} \mathcal{A}\bar{T}(Q) \int_{\Delta\omega_i} \left\{ \begin{array}{c} \cos m\lambda \\ \sin m\lambda \end{array} \right\} \bar{P}_{lm}(\cos\theta)\ d\omega \tag{4.9}$$

The integrals over $\Delta\omega_i$ can be computed as

$$\int_{\Delta\omega_i} \left\{ \begin{array}{c} \cos m\lambda \\ \sin m\lambda \end{array} \right\} \bar{P}_{lm}(\cos m\lambda)\ d\omega = \int_{\lambda_{\mathrm{W}}}^{\lambda_{\mathrm{E}}} \left\{ \begin{array}{c} \cos m\lambda \\ \sin m\lambda \end{array} \right\} d\lambda \int_{\theta_{\mathrm{N}}}^{\theta_{\mathrm{S}}} \bar{P}_{lm}(\cos\theta) \sin\theta\ d\theta \tag{4.10}$$

Note that the integration of the fully normalized Legendre polynomials may become unstable for a high-degree expansion and certain values of θ. Investigations on this issue are reported in Wenzel (1985) and Holmes & Featherstone (2002). It should be noted that H.-G. Wenzel provided two subroutines for the computation of Eqn. (4.10) to the author.

Improving a Geopotential Model Using Additional Data

Improving a geopotential model using additional gravity data is often referred to as *tailoring*. Originally, the approach goes back to an investigation in Kaula (1966) and has been further studied by Rapp (1967). The basic assumption is that the additional data have not been used in the development of the geopotential model. The main idea is then to add small correction terms to the original spherical harmonic coefficients such as

$$\left.\begin{array}{c} \Delta\bar{C}_{lm}^{\mathrm{New}} \\ \Delta\bar{S}_{lm}^{\mathrm{New}} \end{array}\right\} = \left\{\begin{array}{c} \Delta\bar{C}_{lm}^{\mathrm{Old}} \\ \Delta\bar{S}_{lm}^{\mathrm{Old}} \end{array}\right\} + \left\{\begin{array}{c} \delta\Delta\bar{C}_{lm} \\ \delta\Delta\bar{S}_{lm} \end{array}\right\} \tag{4.11}$$

where the corrections terms are computed from the residual data as

$$\left\{\begin{array}{c} \delta\Delta\bar{C}_{lm} \\ \delta\Delta\bar{S}_{lm} \end{array}\right\} = \frac{R}{GM}\frac{1}{4\pi}\sum_{i=1}^{N} p_l \frac{1}{\sigma_l\beta_l}\mathcal{A}\bar{T}'(Q)\int\limits_{\Delta\omega_i}\left\{\begin{array}{c} \cos m\lambda \\ \sin m\lambda \end{array}\right\}\bar{P}_{lm}(\cos\theta)\; d\omega \tag{4.12}$$

In Eqn. (4.12), p_l are spectral weights that control the magnitude of the contributions per degree and the residual (mean) gravity data are given as

$$\mathcal{A}\bar{T}'(Q) = \mathcal{A}\bar{T}(Q) - \mathcal{A}\bar{T}^{\mathrm{Old}}(Q) \tag{4.13}$$

Note that the data have to be downward continued to the reference sphere and that topographic and atmospheric effects must be applied. This appproach was used in Li & Sideris (1994). The model was developed to degree and order 500, i.e., down to spatial scales of 40 km.

Example. Let mean gravity anomalies $\Delta\bar{g}(Q)$ be given over the entire Earth. Furthermore, let a geopotential model be given that was independently developed. Then, the correction terms in Eqn. (4.11) are computed as ($p_l = 1$)

$$\left\{ \begin{array}{c} \delta\Delta\bar{C}_{lm} \\ \delta\Delta\bar{S}_{lm} \end{array} \right\} = \frac{R}{GM}\frac{1}{4\pi}\sum_{i=1}^{N}\frac{R}{(l-1)\beta_l}\Delta\bar{g}'(Q)\int\limits_{\Delta\omega_i}\left\{ \begin{array}{c} \cos m\lambda \\ \sin m\lambda \end{array} \right\}\bar{P}_{lm}(\cos\theta)\; d\omega$$

where the residual data $\Delta\bar{g}'(Q)$ are given as

$$\Delta\bar{g}'(Q) = \Delta\bar{g}(Q) - \Delta\bar{g}^{\mathrm{Old}}(Q)$$

An Iterative Combination Approach

Typically, gravity data are not continuously provided over the entire Earth and a spherical harmonic analysis may lead to large errors in the coefficients due to the Gibbs phenomenon, aliasing and leakage problems. Also, the orthogonality relations cannot be applied. The standard approach to (numerically) alleviate the effect of this problem is to set up an iteration process, see for instance Wenzel (1985); Weber & Zomorrodian (1988); Kearsley & Forsberg (1990). The iteration scheme is shown in Figure 4.2.

In the first step, one has to provide an initial model (a computed model can be used or an initial guess) that is input to Eqn. (4.7). Residual gravity data are then obtained by subtracting the mean data $\mathcal{A}\bar{T}^{\mathrm{Old}}$ from the mean data $\mathcal{A}\bar{T}$, see Eqn. (4.13). A harmonic analysis of the residuals ($\mathcal{A}\bar{T}'$) yields correction terms that are added to the initial model coefficients. The new model is then used to compute updated $\mathcal{A}\bar{T}^{\mathrm{Old}}$ and so on. The iteration is stopped when the rms of the residual gravity data is smaller than a previously set threshold. Usually, this implies only a few iterations. The iteration scheme is advantageous since gross errors can be detected and eliminated. A smooth combined field is obtained that does not require the a-priori knowledge of data error measures. The iteration method can use a large number of data and may combine different functionals of the disturbing potential. Alternatively, a least-squares adustment may be used that optimally fits a truncated set of coefficients to the given data, see Rapp (1967); Pavlis (1988). However, this will not be studied here since large computational resources are required.

The combination of global and local data could also be done by a combined spherical harmonic and wavelet expansion, see Freeden & Windheuser (1997) or Freeden et al. (1998, pg. 272). In this way, the spherical harmonics are used for the representation of the low-frequency spectrum and spherical wavelets represent the high-frequency part.

Lastly, the spherical harmonic analysis of local data could be performed in a spherical cap (Haines, 1985; de Santis, 1991) or the base functions could be (re-)orthonormalized, see Hwang (1993); Albertella et al. (1999). While the spherical cap analysis as described in de Santis (1992) did not result in better results, further investigations on the orthonormalization could be made. This is, however, outside the scope of this study.

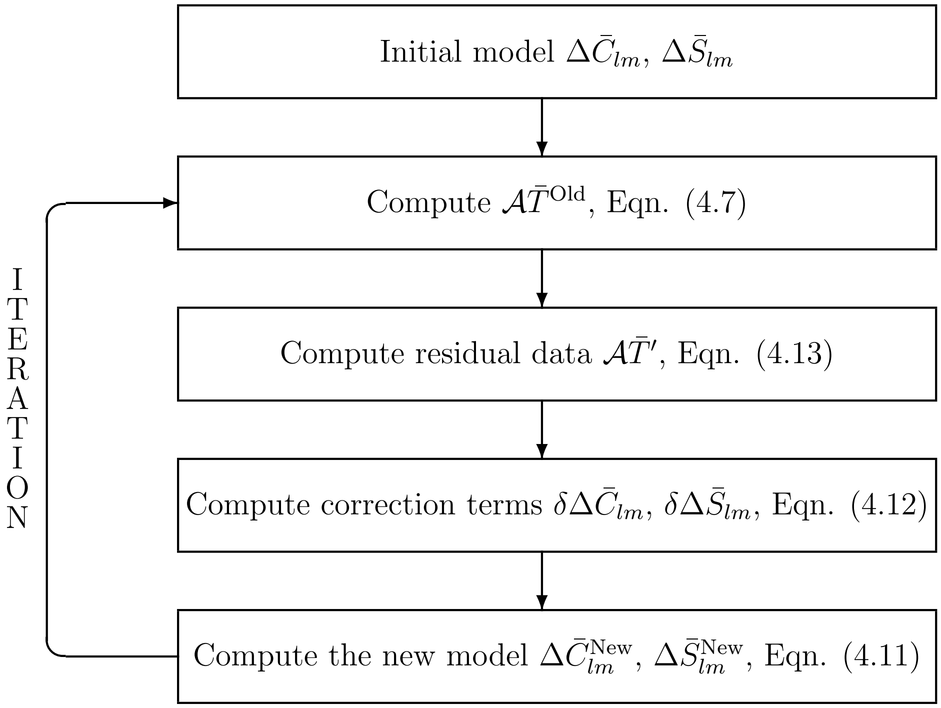

Figure 4.2: Iteration scheme

4.3 Combination Strategies

Based on the iteration method presented in the last section, several strategies for the combination of satellite, airborne and terrestrial gravity data will be developed. The first combination is a way for combining a satellite and a combined geopotential model. The second strategy aims at a high-degree spherical harmonic model and the last strategy is proposed for geoid determination.

Combination of a Satellite Model and a Geopotential Model

The combination of a satellite-only model and a geopotential model can be beneficial for many global and regional purposes. The new combined model has an increased resolution compared to the satellite-only model, or conversely, the quality of the geopotential model is enhanced in the lower frequencies. Ideally, the combination is performed globally and the original normal equation system, which was set up for the geopotential model, is enriched by the satellite data. This is problematic in practice for a number of reasons (normal equation system would have to be set up again, demanding computational load, not all data are publicly available, etc.). Hence, the combination using tailoring may be an alternative. The combination scheme is shown in Figure 4.3.

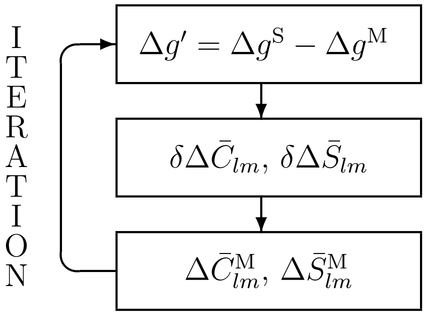

Figure 4.3: Iteration scheme for the combination of satellite and geopotential models

Mean gravity anomalies from a satellite model (Δg^{S}) are input into the iteration process. They are computed on a global or regional grid using Eqn. (4.7). After computing correction terms $\delta\Delta\bar{C}_{lm}$ and $\delta\Delta\bar{S}_{lm}$, new model coefficients can be computed.

Subsequently, the model coefficients are used to compute new values of Δg^{M} and the iteration process continues until convergence is achieved. The quality of this combination approach is investigated in Section 4.5. Of course, other functionals can also be used. The new coefficients adopt the semi-major axis a and geocentric gravitational constant GM from the combined geopotential model.

When error measures of the satellite and the geopotential model are available, they can be used to weight the individual contributions. Table 4.1 summarizes some of the possibilities for satellite degree variances c_l^{S} and error degree variances $\varepsilon_l^{\mathrm{S}}$, respectively. $\varepsilon_l^{\mathrm{M}}$ stand for the error degree variances of the geopotential model.

Table 4.1: Spectrals weights p_l for the satellite data

Linear ($l_2 > l_1$)	Least-Squares	Least-Squares Collocation
$\dfrac{l - l_2}{l_1 - l_2}$	$\dfrac{(\varepsilon_l^{\mathrm{S}})^{-1}}{(\varepsilon_l^{\mathrm{S}})^{-1} + (\varepsilon_l^{\mathrm{M}})^{-1}}$	$\dfrac{(\varepsilon_l^{\mathrm{S}})^{-1}}{(c_l^{\mathrm{S}})^{-1} + (\varepsilon_l^{\mathrm{S}})^{-1} + (\varepsilon_l^{\mathrm{M}})^{-1}}$

Development of a High-Degree Spherical Harmonic Model

Based on the previous combination approach, a spherical harmonic model can be developed that exceeds the maximum degree of the satellite or geopotential model. This is done using local or regional gravity data that may provide information about the higher frequencies. The proposed combination concept is shown in Figure 4.4.

In the first step, a satellite and a geopotential model are combined. This step is equivalent to the previously discussed combination and can take place on a global or regional grid. In the second combination step, local or regional airborne gravity disturbances (δg) are used to derive a new, high-degree, spherical harmonic model. The maximum degree of the model is theoretically limited to a degree of $l_{\max} = 180^\circ/\Delta\omega$, where $\Delta\omega$ is the grid size of the given mean gravity disturbances. In the final combination, terrestrial gravity data (Δg) are input to the iteration and yield final coefficients $\Delta\bar{C}_{lm}^{\mathrm{C}}$, $\Delta\bar{S}_{lm}^{\mathrm{C}}$.

The maximum degree and order of the model is dependent on the data grid size

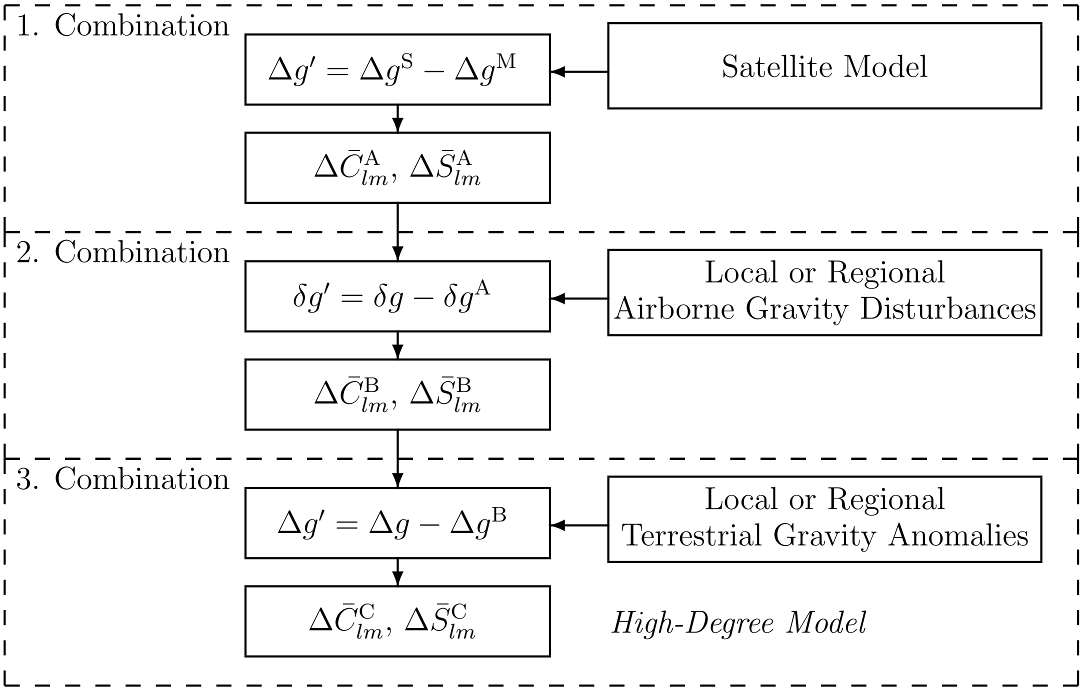

Figure 4.4: Development of a high-degree spherical harmonic model

and the data extent. Practical tests have indicated that a high-degree model based on local terrestrial and airborne data is not likely to exceed a maximum degree of $l_{\max} = 180°/(2\Delta\omega)$. Beyond that degree, errors due to the iteration process, the computation of normalized Legendre polynomials and other approximations increase. A clear distinction between numerical round-off errors and actual information cannot be made. Another limitation is due to the use of the Pellinen smoothing functions β_l. Large errors are introduced when they tend to zero. This problem can only partially be overcome by the iteration.

It is recommended that the lowest coefficients in the second and the third combination step remain unchanged. Otherwise, leakage errors may affect the solution. In addition, local gravity data cannot match the quality of the global data in the lower frequencies due to various systematic errors (Heck, 1990). The lowest degree that can be resolved from local data is $l_{\min} = 180°/\theta$, where θ stands for the data block size. Due to the good quality of satellite data, however, a minimum degree of $l_{\min} = 2 \cdot 180°/\theta$ is recommended for the second and third combination step. In this thesis, the airborne and terrrestrial gravity data are reduced by topographic and atmospheric effects. This provides a smooth residual field that is easier to combine. In addition, the gravity data are downward continued to the reference sphere before they are combined with other data.

Example. Let local terrestrial gravity data be provided on a $5' \times 5'$ grid in an area of $5^\circ \times 10^\circ$. Then the coefficients that can be resolved from this data are $l_{\text{min}} = 36 \leq l \leq 2160 = l_{\text{max}}$. However, only coefficients in the band of $l_{\text{min}} = 72 \leq l \leq 1080 = l_{\text{max}}$ will be solved for in this thesis.

Geoid Determination

Geoid determinations based on a combination of heterogeneous gravity data have been done in numerous ways. In this thesis, two strategies are proposed that are based on the concepts of tailoring and the remove-restore technique. The first strategy is shown in Figure 4.5. As before, a combined model ($\Delta\bar{C}^{\text{A}}_{lm}$, $\Delta\bar{S}^{\text{A}}_{lm}$) is computed using satellite and geopotential data. This model serves as reference model in the remove-restore technique. A combined gravimetric geoid can be obtained.

The strategy is especially advantageous for local geoid determinations. Since satellite models are low-frequency in nature, the satellite spectrum does not necessarily overlap with the local data spectrum. Hence, the remove-restore combination with local data would leave some frequencies unresolved – the geoid is spectrally incomplete. The combination of satellite data with a combined geopotential model increases the bandwith of the satellite model. The information content of the satellite data is somewhat stretched into higher frequencies. The new model is of better quality in the lower frequencies and maintains the bandwidth of the initial model. Consequently, the new model reduces to the problem of finding a proper spherical cap radius and modification degree in the (Poisson and Stokes) integrations. Hence, a refined local geoid can be expected by such a combination.

The second strategy uses two local or regional gravity data sets and satellite data. The computational steps of this combination are shown in Figure 4.6. In the first step, the satellite data and a geopotential model data are combined. This can be done

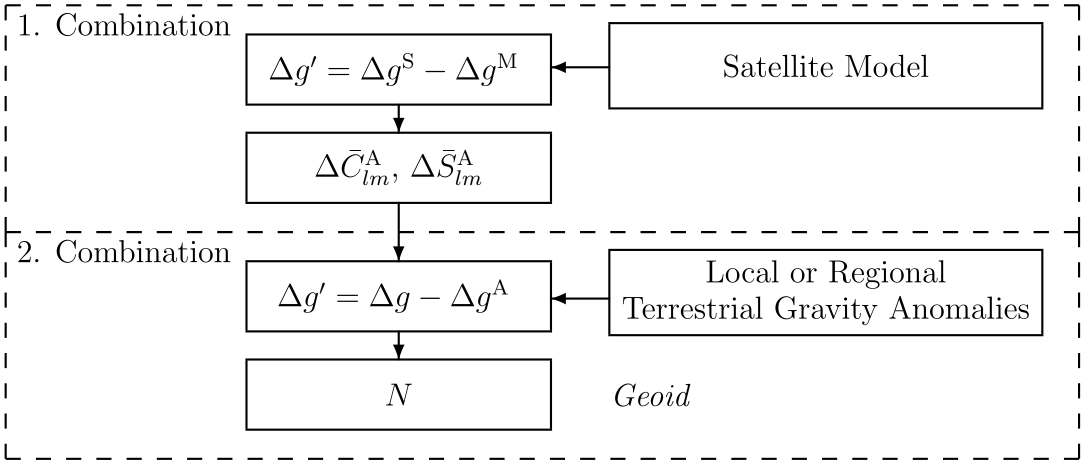

Figure 4.5: Geoid determination using satellite and a local gravity data set

using the above-mentioned iteration scheme. The new model ($\Delta\bar{C}^{\mathrm{A}}_{lm}$, $\Delta\bar{S}^{\mathrm{A}}_{lm}$) is the initial model for the combination with airborne gravity data (δg). A high-degree model $\Delta\bar{C}^{\mathrm{B}}_{lm}$ and $\Delta\bar{S}^{\mathrm{B}}_{lm}$ is obtained through iteration. It serves as a reference field for the terrestrial gravity data in the remove-restore technique and a combined geoid based on satellite, airborne and terrestrial gravity data can be computed. It should be noted that the strategy can also be used for airborne data that are given in a small area. The iteration method preserves the information content of the data as will be demonstrated in Chapter 6.

4.4 Quality of the Combination Strategies

To evaluate the quality of the combination strategies, two tests were performed. The first test aimed at the development of a high-degree model based on two local data sets and a global model. In the second test, in turn, a combined local geoid was computed using the same simulated data. Closed-loop simulations were performed.

The simulated local gravity data were gravity disturbances and gravity anomalies. They were computed from the GPM98a (Wenzel, 1998b) up to degree and order 1800 in a $10^\circ \times 5^\circ$ area. The gravity disturbances were predicted to a (flight) height of 600 m on a $5' \times 5'$ grid. Furthermore, the gravity disturbances were burdened with

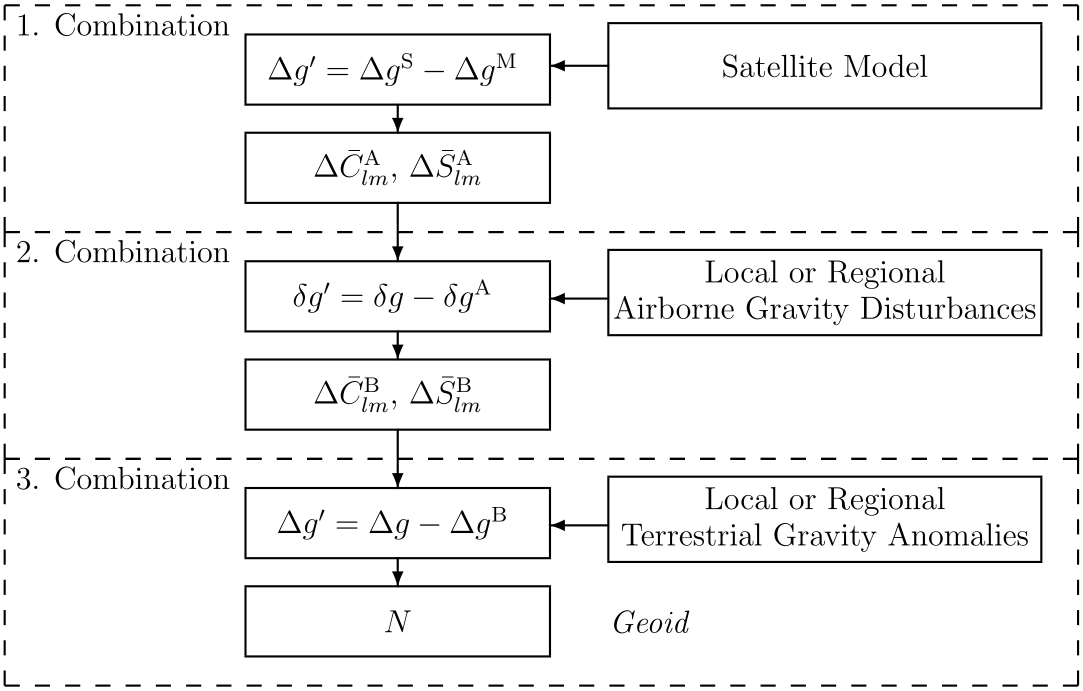

Figure 4.6: Geoid determination using satellite, airborne and terrestrial gravity data

noise of zero mean and 1.5 mGal STD. The gravity anomalies in turn, were computed at varying topographic heights (mean=297.9 m, std=171.8 m). The anomalies were disturbed with noise of 2 mGal STD (independently computed from the noise for the gravity disturbances). The parameters for the local data were selected with the actual data in mind, which will be described in Section 5.2. The statistics of the noisy input data and the reference undulations from GPM98a are provided in Table 4.2.

Table 4.2: Input data statistics for the combination

Type	Min	Max	Mean	Std	Unit
N^{GPM98a}	−36.817	−25.750	−32.054	3.151	m
$\delta g^{\mathrm{GPM98a}} + e$	−65.660	57.853	−18.644	16.362	mGal
$\Delta g^{\mathrm{GPM98a}} + e$	−58.603	69.754	−8.827	16.130	mGal

The computational flow of the first test is shown in Eq. (4.14). Essentially, it represents the combination strategy shown in Figure 4.4. The GPM98a was used as an initial model in the iteration process. The local gravity disturbances were used in the first iteration yielding the model SM1. SM1 is a tailored, high-degree model developed up to degree and order 900. In the second step, the SM1 was used as initial model for the combination with noisy gravity anomalies. The high-degree model SM2 was obtained. Comparisons were made to the GPM98a, where GPM98a is considered to be the true solution. The differences indicate how sensitive the combination strategy is to noisy data. Furthermore, the magnitude of aliasing effects can roughly be estimated. Aliasing may occur since SM1 and SM2 are truncated models and the input gravity data contain higher frequencies.

$$\begin{tikzcd}
\text{GPM98a} \arrow[r] & \delta g^{\text{GPM98a}} + e \arrow[r] & \text{SM1} \arrow[d, leftrightarrow] \arrow[r] & \Delta g^{\text{GPM98a}} + e \arrow[r] & \text{SM2} \arrow[d, leftrightarrow] \\
 & & \text{GPM98a} & & \text{GPM98a}
\end{tikzcd} \tag{4.14}$$

Undulations were computed of SM1 and SM2 for a smaller output area of $2^\circ \times 1^\circ$ in order to avoid edge effects. The results of the first test are shown in Figure 4.7 where the first bar stands for the mean difference and the second bar for the standard deviation in each case. The remaining differences to the true solution are at the cm-level. Hence, the iteration scheme alleviates the effect of aliasing and data noise.

The second test was based on the combination strategy presented in Figure 4.6. The combination output is a combined local geoid based on three data sets. Eqn. (4.15) shows the computational flow.

$$\begin{tikzcd}
\text{GPM98a} \arrow[r] & \delta g^{\text{GPM98a}} + e \arrow[r] & \text{SM1} \arrow[d, leftrightarrow] \arrow[r] & \Delta g^{\text{GPM98a}} + e \arrow[r] & \hat{N} \arrow[d, leftrightarrow] \\
 & & \text{GPM98a} & & \text{GPM98a}
\end{tikzcd} \tag{4.15}$$

The first combination is identical to the previous test, see Eqn. (4.14). Yet, the second combination transforms the local gravity data directly into geoidal undulations by the Stokes integral. Since the gravity anomalies were simulated at varying topographic heights, the data are downward continued first using the Abel-Poisson integral. While the Poisson integration kernel was modified by the VK modification, the Stokes kernel function was modified using the FEO modification ($L_{\mathrm{S}} = 180$, $L_{\mathrm{MD}} = 180$). The undulations were then compared to the undulations from GPM98a. The results, shown in Figure 4.7, are indicated by the last pair of bars. Analogous to the first test, the local data noise does not propagate through the computations. It is filtered out by the iteration method in the first combination and by the Stokes integration in the second combination. Thus, the combination strategy can provide reliable solutions even when the local data contain (white) noise.

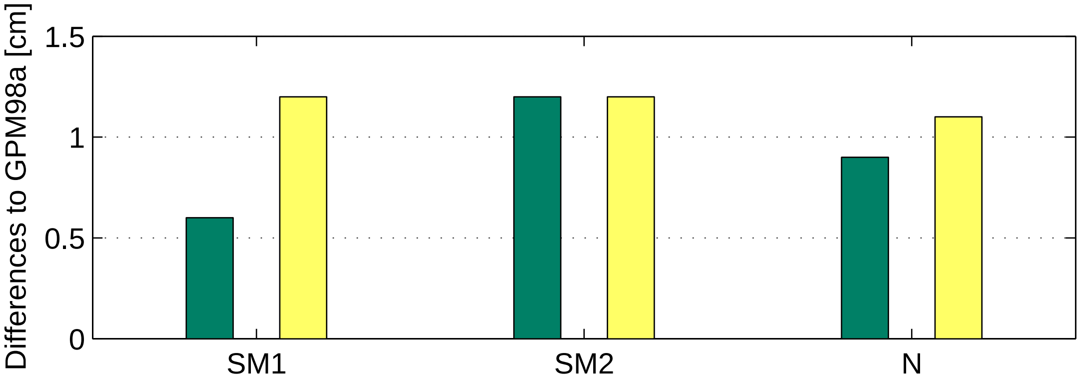

Figure 4.7: Undulation differences compared to GPM98a [cm]; first bar stands for mean difference, second bar is standard deviation

In conclusion, both combination strategies can be used for the combination of real satellite, airborne and terrestrial gravity data. Numerica results will be presented in Chapter 6.

4.5 Combining a Satellite Model with a Geopotential Model

A satellite-only model was combined with a geopotential model using the combination strategy presented in Figure 4.3. The most recent satellite model EIGEN-2 from the satellite mission CHAMP and the geopotential model EGM96 were used. It can be safely assumed that the two models are independent. Three tests were performed that reveal advantages of the combination approach as well as some of its limitations.

The first combination was done for an area enclosing most of Canada ($30° \leq \varphi \leq 80°$ and $240° \leq \lambda \leq 310°$). Mean gravity anomalies were computed from the EIGEN-2 model on a $0.5° \times 0.5°$ grid on the reference sphere R. The summation in Eqn. (4.7) was performed for $l = 2 - 120$, i.e. the gravity anomalies have a resolution down to spatial scales of 167 km. The EGM96 was used as an initial model in the iteration. After 10 iteration steps, the new model has a rms difference of less than 0.5 mGal compared to the EIGEN-2 gravity anomalies. It will be called CSM360, short for Canadian Spherical harmonic Model up to degree and order 360.

Figure 4.8 provides more information on the model. Figure 4.8 (a) shows the differences of the CSM360 and the EGM96 in terms of anomaly degree variances. Differences are visible in all frequencies with a peak at degree $l = 120$. This is the maximum frequency of the EIGEN-2 gravity data. The iteration extends the satellite information to higher degrees; the iteration provides a smooth continuation up to degree 360. The coefficient differences between CSM360 and EGM96 are plotted in logarithmic scales in Figure 4.8 (c). Up to degree $l = 120$, differences in zonal ($m = 0$), sectorial ($l = m$) and tesseral ($l \neq m,\ m \neq 0$) harmonics are visible. Beyond this degree, the magnitudes of the coefficients differences are much smaller indicating that the satellite model does not significantly contribute to these frequencies. Finally, Figure 4.8 (d) compares geoidal undulations computed from the EGM96 and the CSM360. The differences range from -7.850 m up to 7.303 m over the area shown (mean=-0.022 m, std=1.443 m).

In the second test, mean gravity anomalies from EIGEN-2 were computed for a much smaller area, namely $43° \leq \varphi \leq 48°$ and $280° \leq \lambda \leq 290°$. The chosen grid size was $5' \times 5'$. The first 30 degrees of the initial model were unchanged in order to avoid possible leakage problems. After 5 iterations, the rms variations between the newly computed anomalies and the input anomalies were insignificant and remained at a constant level of 1.3 mGal. The model tailored to the local area will be referred to as EGM96e. Differences to the EGM96 are shown in Figure 4.9. Due to the smaller data

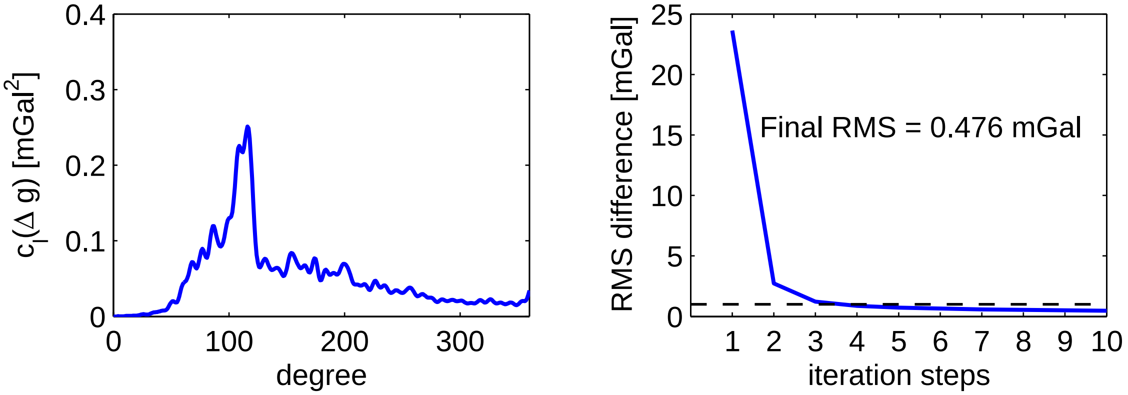

(a) Differences in terms of anomaly degree variances (mGal^2)

(b) RMS differences per iteration (mGal)

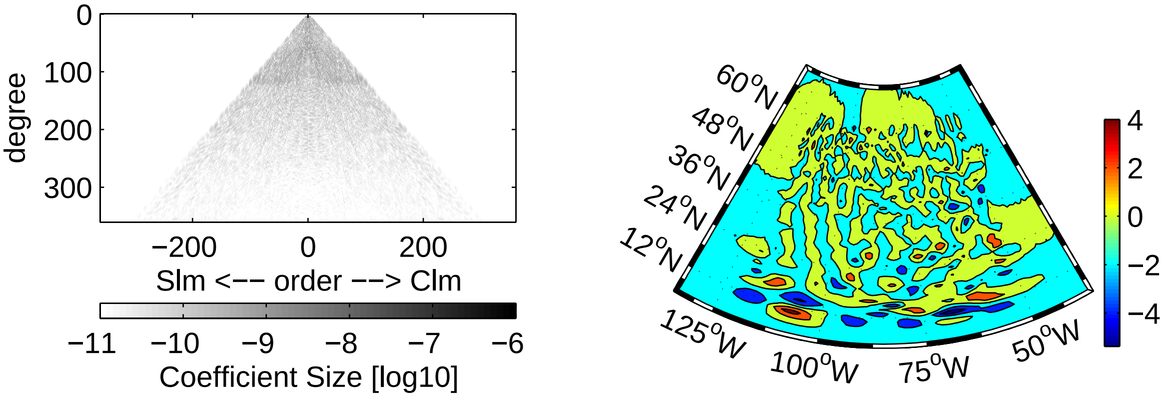

(c) Coefficient differences

(d) Undulation differences (m)

Figure 4.8: Differences between the EGM96 and CSM360

area, the differences of the EGM96e compared to the initial model EGM96 are much smaller than in the previous test. The differences in terms of anomaly degree variances, for instance, are always less than 0.0025 mGal^2 with an expected peak at degree $l = 120$. Figure 4.9(b) shows that the differences to the EGM96 are smaller than in the previous test. Beyond degree 120, the differences are mainly in the sectorial harmonics ($l = m$). As expected, local changes affect the entire set of spherical harmonics since spherical harmonics are globally supported. Hence, EGM96e is invalid outside the data area. This

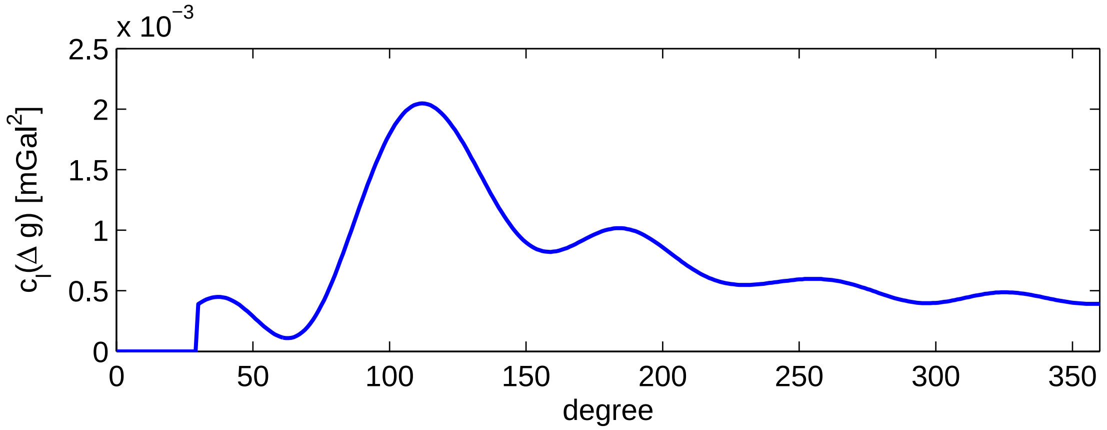

(a) Differences in terms of anomaly degree variances (mGal)

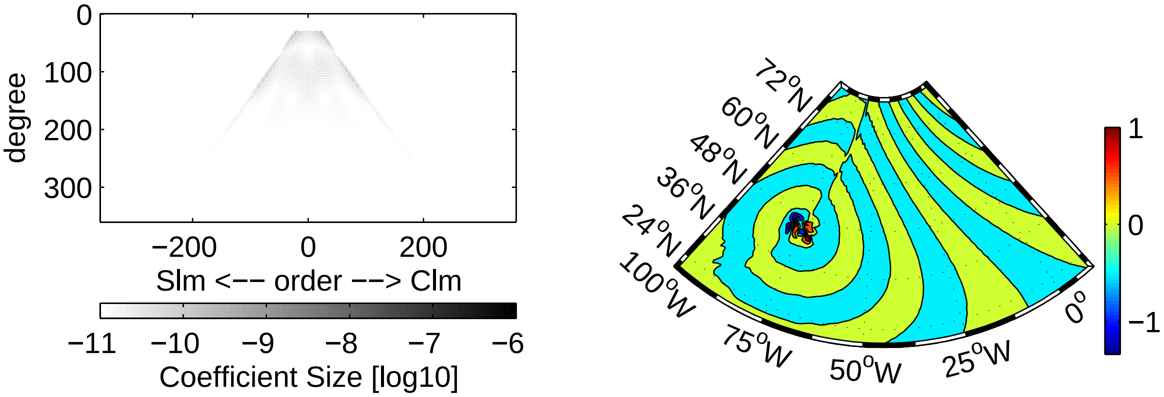

(b) Coefficient differences

(c) Undulation differences (m)

Figure 4.9: Differences between the EGM96 and EGM96e

can be easily seen in Figure 4.9(c). EGM96 and EGM96e undulations are computed for a larger area than the data area. The differences show a typical pattern of the Pellinen smoothing function and emphasize that the computed model EGM96e cannot be used outside the original data area.

A third combination was performed in the area of the first test ($30° \leq \varphi \leq 80°$ and $240° \leq \lambda \leq 310°$). Gravity anomalies from EIGEN-2 were predicted to a $0.5° \times 0.5°$ grid for the frequency band between $l = 2 - 140$. In this case, however, the contributions

$\delta\Delta\bar{C}_{lm}$ and $\delta\Delta\bar{S}_{lm}$ were weighted using spectral weights. Since error measures are available from EIGEN-2 and EGM96, the spectral weights can be obtained from least-squares collocation as, see Table 4.1,

$$p_l = \begin{cases} \dfrac{(\varepsilon_l^{\mathrm{EIGEN2}})^{-1}}{(c_l^{\mathrm{EIGEN2}})^{-1} + (\varepsilon_l^{\mathrm{EIGEN2}})^{-1} + (\varepsilon_l^{\mathrm{EGM96}})^{-1}} & \text{for } l \leq L_{\mathrm{S}} = 140 \\ 0 & \text{for } l > L_{\mathrm{S}} \end{cases} \tag{4.16}$$

where $\varepsilon_l^{\mathrm{EIGEN2}}$ and $\varepsilon_l^{\mathrm{EGM96}}$ are the error-degree variances of the satellite data and the model, respectively. c_l^{EIGEN2} are the signal degree variances from the satellite data. Alternatively, the signal degree variances from EGM96 (c_l^{EGM96}) could be used. The spectral weights are shown in Figure 4.10 (a). The satellite data obtain full weight in the lower degrees. Yet, the weights decrease rapidly with increasing degree since the satellite error degree variances are increasing. Clearly visible is a jump at around degree 70, which is caused by the EGM96 error degree variances. Beyond this degree, the satellite data gain more weight up to degree 140, which is the maximum degree of the model. The weights are forced to be zero beyond degree 140 since there is no additional satellite information. The actual computation by iteration was equivalent to the first combination (except that the weights are used). The iteration seemed to converge after about 9 iterations. However, the final rms difference remained at a high level of 16.9 mGal compared to the gravity anomalies from EIGEN-2 (14000 data points). This may be due to the fact that the weights were set to zero beyond degree 140 and the iteration could not adjust higher degrees.

Figures 4.10 (b-d) show the differences between the tailored model CSM360w and EGM96 after the combination. Figure 4.10 (b) are the anomaly degree variance differences between the new model and the EGM96. The changes are of the same magnitude as for the first combination, see Figure 4.8 (a). However, the differences are limited up to degree 140. This is also visible in Figure 4.10 (c), which shows the coefficient differences between the two models CSM360w and EGM96. As a result, the CSM360w spectrum has a small discontinuity at degree 140 which may have adverse effects. Finally, the undulation differences between the tailored model CSM360w and EGM96 are

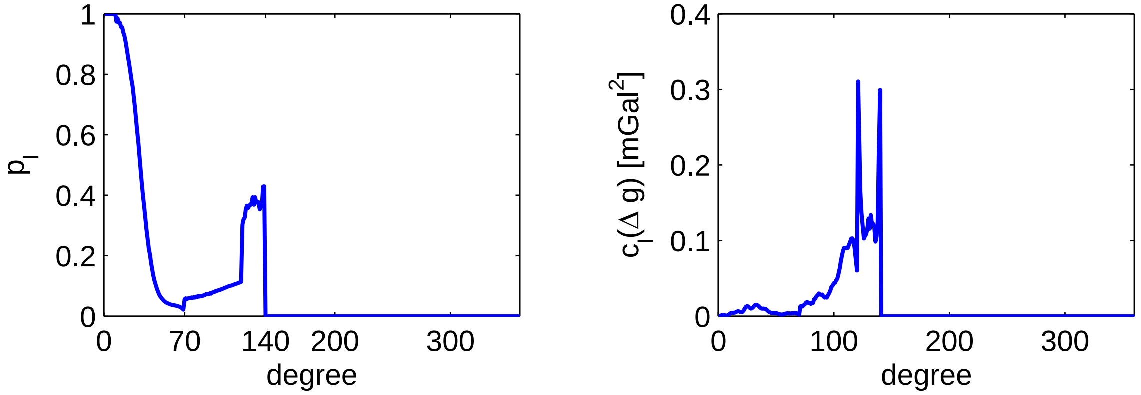

(a) Spectral weights for the satellite data obtained by LSC

(b) Differences in terms of anomaly degree variances (mGal^2)

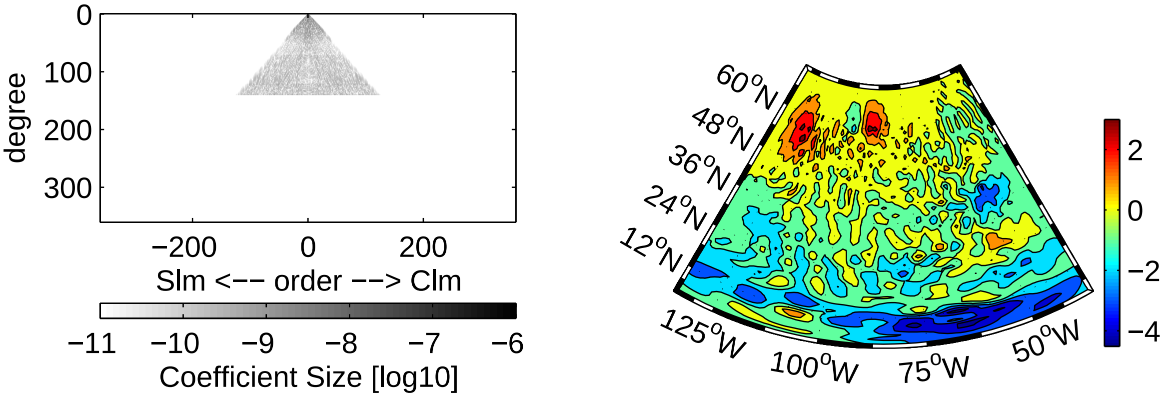

(c) Coefficient differences

(d) Undulation differences (m)

Figure 4.10: Differences between the EGM96 and CSM360w

shown in Figure 4.10 (d). The differences (std=1.104 m) are slightly smaller than in the first combination since the degrees 141-360 in CSM360w are unchanged EGM96 coefficients. However, the CSM360w is biased (mean=-0.219 m) compared to EGM96.

5 From Theory to Application

This chapter analyzes gravity data from a conceptual point of view. Following Schwarz (1984) in the main points, further studies on the upward and downward continuation as well as remarks on the temporal variability of the gravity field will be made. In addition, the gravity data to be used in Chapter 6 will be analyzed.

5.1 General Considerations

Four gravity data characteristics are investigated:

i) Spectral sensitivity
ii) Resolution
iii) Height
iv) Temporal variability.

Both deterministic and stochastic parts of gravity data can be described by the above criteria.

Spectral Sensitivity

Schwarz (1984) coined the term *spectral sensitivity*, i.e., different gravity functionals have the main power in different parts of the spectrum. Although the functionals theoretically resolve all frequencies, the measuring process limits the actual spectral range (bandlimitation). The spectral sensitivity of different gravity functionals is demonstrated in Table 5.1. It compares the power of some functionals computed from model degree variances. The Tscherning-Rapp degree variance model is used, see Tscherning & Rapp (1974) or Appendix A.2.

The following conclusions can be made: Geoidal undulations N are clearly low-frequency in nature. Thus, gravity measurements that have power in the lower frequencies will have a large impact on the geoid. Gravity anomalies and gravity disturbances mainly cover the low to medium frequency range, while the second-order derivatives of the potential obtained from gravity gradiometry may resolve higher frequencies. These measurement types may be advantageous for resource exploration purposes where higher frequencies are decisive. In conclusion, the higher the order of the derivative (of the potential), the higher the sensitivity to the higher frequencies. Additional measures for the spectral sensitivity are collected in Table 5.2. The measures can be derived for every (isotropic) functional of the disturbing potential (Haagmans & van Gelderen M., 1991; Sneeuw, 2000).

Table 5.1: Spectral sensitivity

Functional	$2 \leq l \leq 36$	$37 \leq l \leq 360$	$361 \leq l \leq 3600$	$3601 \leq l \leq 36000$
N	99.2%	0.8%	0.0%	0.0%
Δg	22.5%	41.9%	32.7%	2.8%
δg	32.2%	37.3%	28.1%	2.4%
T_{rr}	0.0%	0.8%	39.0%	60.2%

Resolution

Closely related to the term spectral sensitivity is the *resolution*. Eqn. (5.1) summarizes the main components and indicates connections.

$$\text{Resolution} \left\{ \begin{array}{rccc} \text{spatial}: & \text{coverage} & \longleftrightarrow & \text{density} \\ & \updownarrow & & \updownarrow \\ \text{spectral}: & \text{leakage} & \longleftrightarrow & \text{aliasing} \end{array} \right. \tag{5.1}$$

Table 5.2: Measures for spectral sensitivity

measure	abbreviation	one-dimensional	two-dimensional
signal degree variance	c_l	$\sum_{m=-l}^{l} c_{lm}$	c_{lm}
error degree variance	ε_l	$\sum_{m=-l}^{l} \varepsilon_{lm}$	ε_{lm}
root-mean-square	RMS_l	$\sqrt{\frac{1}{2l+1}\varepsilon_l}$	
signal-to-noise ratio	SNR_l	$\sqrt{\frac{c_l}{\varepsilon_l}}$	$\frac{\lvert c_{lm}\rvert}{\varepsilon_{lm}}$
gain	GAIN_l	$\frac{\varepsilon_l^{\mathrm{old}}}{\varepsilon_l^{\mathrm{new}}}$	$\frac{\varepsilon_{lm}^{\mathrm{old}}}{\varepsilon_{lm}^{\mathrm{new}}}$
power	POW_l	$\frac{\varepsilon_l}{\sum_{l=2}^{\infty}\varepsilon_l}$	
commission variance	$\varepsilon_l^{\mathrm{c}}$	$\sum_{l=2}^{\eta_{\mathrm{res}}} \varepsilon_l$	
omission variance	$\varepsilon_l^{\mathrm{o}}$	$\sum_{l=\eta_{\mathrm{res}}+1}^{\infty} \varepsilon_l$	

* η_{res} is the *degree-of-resolution*, i.e., the maximum degree with signal-to-noise ratio smaller than 1
** RMS_l, GAIN_l, POW_l, $\varepsilon_l^{\mathrm{c}}$ and $\varepsilon_l^{\mathrm{o}}$ can be also calculated for signal degree variances c_l

While the data coverage (global, regional, local) limits the low frequency part of the spectrum, the data density (low, medium, high) represents the upper limit that can be resolved from a data set. Spectral leakage and aliasing can be considered as the spectral equivalents of the data coverage and data density. For further explanations and discussions, Schwarz (1984) should be consulted. The mathematical link between spatial and spectral resolution is provided in Table 5.3. Hence, the terms can be used synonymously; they are different in unit and/or scale. Note that spatial resolution is often expressed in half-wavelengths.

Example. For degree $l = 2160$, aircraft speed $v = 50\,{}^{\mathrm{m}}/_{\mathrm{s}}$ and a geocentric radius given as $r = R + H = 6371000\,\mathrm{m} + 4000\,\mathrm{m}$, the spectral resolution is given as $f = \frac{lv}{2\pi r} \doteq 0.0027\,\mathrm{Hz}$ (corresponds to a spatial resolution down to $x = \pi r / l = 9.272\,\mathrm{km}$). Typical low-pass filters in airborne applications have cut-off frequencies between $f_c = 0.0050$ (=200 s filter) and $f_c = 0.0166\,\mathrm{Hz}$ (=60 s filter).

Table 5.3: Link between spatial and spectral resolution

v [m/s] – speed, r [m] – radius	f [Hz]	l [-]	θ [°]	x [m]
Spectral resolution f	1	$\frac{lv}{2\pi r}$	$\frac{180v}{2\pi r\theta}$	$\frac{v}{2x}$
Spherical harmonic degree l	$\frac{2\pi rf}{v}$	1	$\frac{180}{\theta}$	$\frac{\pi r}{x}$
Block size θ	$\frac{180v}{2\pi rf}$	$\frac{180}{l}$	1	$\frac{180x}{\pi r}$
Spatial resolution x	$\frac{v}{2f}$	$\frac{\pi r}{l}$	$\frac{\pi r\theta}{180}$	1

Height – Attenuation/Amplification

The measurement height plays a significant role when combining gravity data. The gravity field tapers off with approximately $1/l^3$ (Kaula, 1966). At altitude $r = R + H$, this attenuation effect is expressed by $(R/r)^{l+1}$. Figure 5.1(a) shows this attenuation process using geoidal undulations of 1 cm at all frequencies. When the geoidal undulation is upward continued to heights of 1 km, 5 km, 10 km or even 100 km, the attentuation effect is clearly visible. For instance, 1 cm upward continued to a height of 5 km will result in a geoidal undulation of only 0.5 cm at degree 1000. Thus, the main goal in a high-resolution gravity field determination is to counteract this attenuation effect by collecting measurements as low as possible. In addition, measuring a functional of the potential that is sensitive to the desired frequencies will improve the situation (ESA, 1999).

Remark 5.1 *Figures 5.1 (a) and (b) are of qualitative nature and possibly too optimistic for real data.*

When measurements are collected at a certain height, the downward continuation to the surface of the Earth or the geoid leads to an amplification of the high frequencies of the data. The amplification process is shown in Figure 5.1(b). Gravity disturbances of 1 mGal magnitude at all frequencies are downward continued from different heights. The conversion into undulations is simultaneously done by $\frac{r}{l+1}(\frac{r}{R})^{l+1}$. For instance, the above figure indicates that 1 mGal at 5 km height at 5 arcmin spacing results in an effect of approximately 5 cm in terms of geoidal undulations.

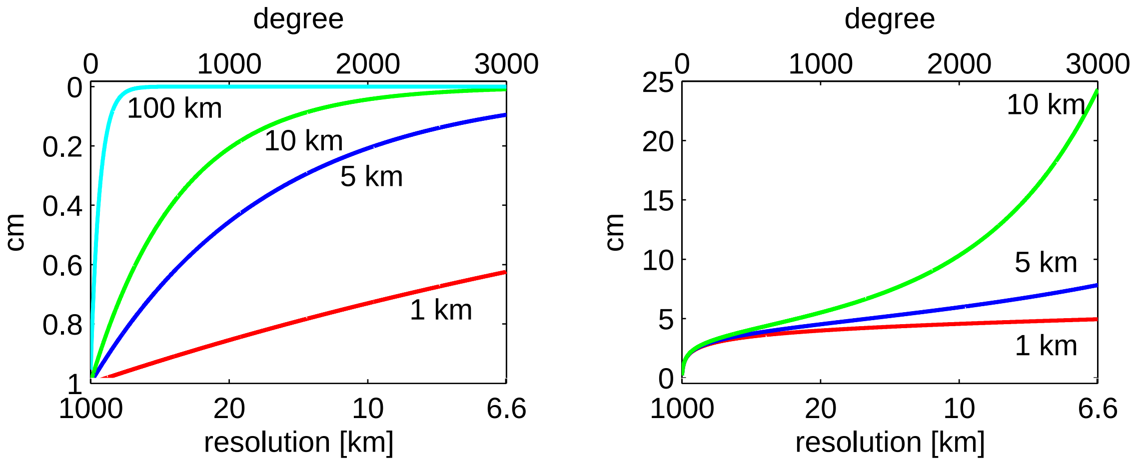

(a) Upward continuation of 1 cm geoidal undulation to flight heights of 1 km, 5 km, 10 km and 100 km

(b) Error in downward continuation of 1 mGal gravity disturbance from flight heights 10 km, 5 km and 1 km

Figure 5.1: Attenuation and amplification

Temporal Variability

The gravity field can be decomposed into a static part and a smaller time-variable part. The time-variable part is on the order of a few millimeters to centimeters when expressed in geoidal heights (NRC, 1997). It is caused by several (superposed) geophysical effects. The most prominent causes, their peroids, wavelengths and approximate magnitude ($g \approx 9.8\ ^{m}/_{s^2}$) are shown in Figure 5.2. Not shown are the tidal effects (magnitude of about $10^{-7}g$ (Torge, 2001)) that would spread over a wide range of periods.

Gravity changes in time can be detected when gravity measurements are collected or derived at different times over the same area with comparable quality. This is expected for the satellite mission GRACE. Assuming a successful mission, it will provide spherical harmonic coefficients with an unprecedented accuracy every few weeks. Global changes can be detected down to spatial scales of a few hundred kilometers. According to Wahr et al. (1998), GRACE will be able to detect monthly changes in water storage to accuracies better than 1 cm. One principal challenge is to isolate individual effects/causes from other effects or measurement errors. Sensitivity analyses and combination of GRACE data with previous models may differentiate individual effects. Notwithstanding the fact that the gravity data at hand may vary in time, this characteristic will be neglected in the following.

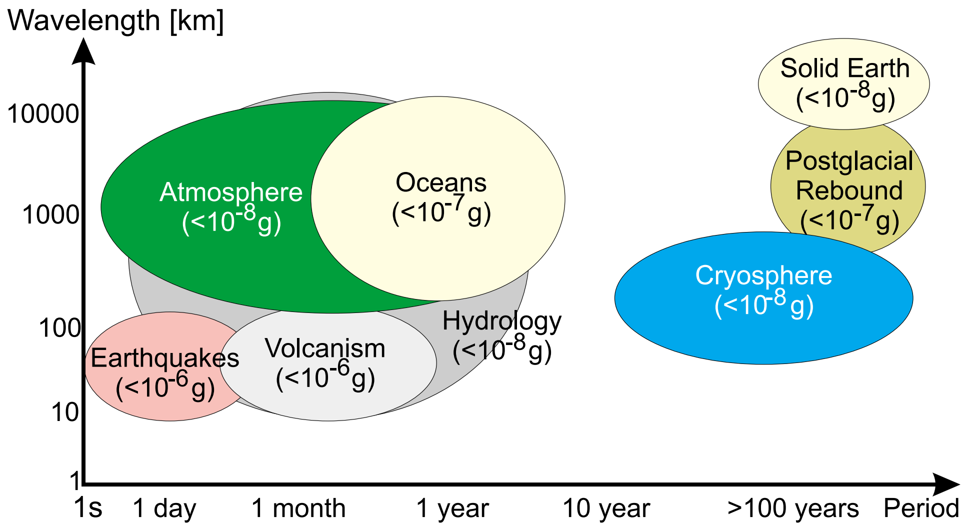

Figure 5.2: Geophysical effects in periods, wavelengths and magnitude (from Verhagen (2000); NRC (1997))

5.2 Specific Considerations

Global Gravity Data

Global gravity data are typically provided in spherical harmonics. They are either calibrated satellite models or combined geopotential models (resulting from a combination of different gravity data sources). The main characteristics of current satellite models are their limited resolution (band-limited spectrum) and high quality in the low-frequencies. The low resolution (an expected maximum 100 km using GOCE) is mainly due to the attenuation effect at satellite altitude and, thus, the downward continuation problem. Yet, the quality at the lowest scales is unmatched.

The combined geopotential models are usually unencumbered by specific satellite mission goals. They aim at providing high-resolution global gravity solutions for a maximum number of applications. Due to the use of heterogeneous gravity data, the models represent an optimally weighted solution that enjoys higher quality and resolution. However, they may have been created using the same terrestrial gravity data that will also be used in the application at hand. Hence, to make the combined solution immune to the inevitable error correlations, satellite data are favoured. Combined geopotential models only come into play for the computation of truncation errors and to increase the limited resolution of the satellite data.

A comparison of different global models is presented in Table 5.4. More information on these models, including their data sources, can be found in Bouman (1997). Most of the models are obtained from Wenzel (1998a). Note that some of the models are not complete in degree and order. The commission error is computed whenever the standard deviations of the coefficients are provided. The formula used is shown in Table 5.2 (η_{res} is set to the maximum degree of the model). To obtain the commission error for the two functionals (geoidal undulations and gravity anomalies) the singular values from the Meissl scheme are employed. The omission error is computed using the Tscherning-Rapp degree variances starting from the maximum degree of the model (plus 1) up to degree 25000. GRS80 is used as a reference ellipsoid.

Example. The models GPM98a,b,c are complete to degree and order 1800, which corresponds to a spatial resolution of about 12 km half-wavelength. Since standard deviations of the coefficients are unavailable, only the omission error is computed from degree 1801 to 25000. The error is about 3 cm in terms of geoidal undulations and about 13 mGal for gravity anomalies. The errors are cumulative errors.

Three of the global models, shown in Figure 5.3, are used in this study. They include

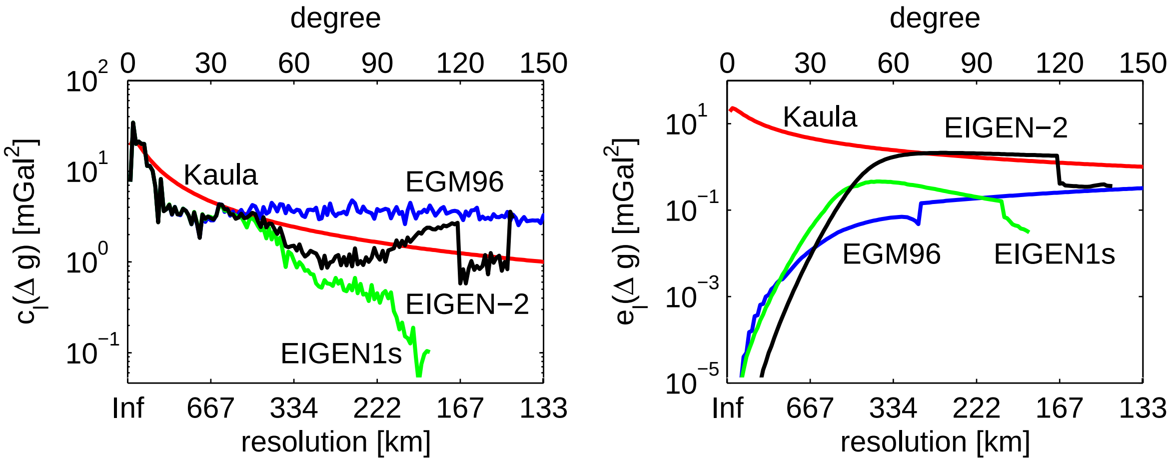

(a) Signal degree variances (b) Error degree variances

Figure 5.3: Signal and error anomaly degree variances of some global models [mGal^2]

the Earth Geopotential Model (EGM96) (Lemoine et al., 1998) and two satellite models from the CHAMP satellite mission (EIGEN1S, EIGEN-2). For details on the CHAMP mission, its objectives and further results refer to Reigber et al. (2002a,b). The anomaly degree variances of the three models $c_l(\Delta g)$, shown in Figure 5.3 (a), are similar up to degree and order 50. The error degree variances in Figure 5.3 (b) underscore the quality of the satellite solutions. Beyond degree 50, the satellite data seem to have less power than EGM96. The EIGEN-2 is most likely correlated with the Kaula rule since it closely follows it. The Kaula rule may have been used to stabilize the normal equation system.

Local Gravity Data

The test area for this study is located close to Ottawa (Ontario, Canada); see Figure 5.4 for the general situation. The location was selected due to its large variations in the gravity field (mean=-9.6 mGal, std=21.7 mGal), yet relatively small topographic height variations (mean=297.9 m, std=171.8 m). Furthermore, the location was conveniently located for one of the major Canadian airborne gravimetry companies, Sander Geophysics Ltd. It supplied the necessary airplane for the airborne test and provided further facilities. The airborne campaign took place in April and May 2000 and included the following participants:

- Sander Geophysics Ltd. (SGL)
- Intermap Technologies Corporation (INTERMAP)
- Geodetic Survey Division Canada (GSD)
- The University of Calgary (UOFC)

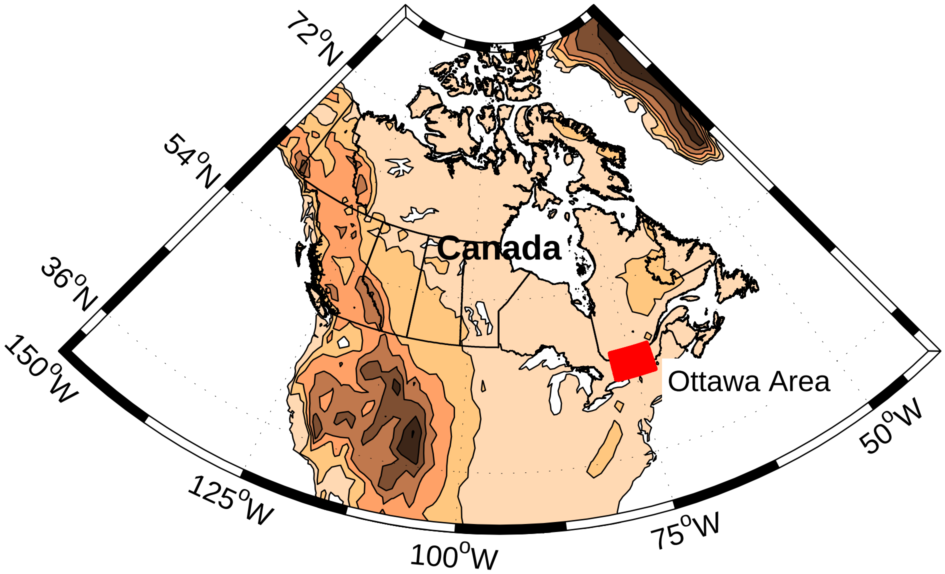

Figure 5.4: Location of the test area

The main purpose of the test was to compare the performance of three different airborne system types. Bruton et al. (2002) and Bruton (2000) should be consulted for further details of the flight campaign. The principal conclusion was that airborne gravity data, although measured with different devices, can provide accurate and reliable estimates of the gravity field. Comparing the airborne data from the different airborne systems to ground gravity anomalies showed only minor accuracy differences (between 0.7 mGal and 1.5 mGal). Since methodology and technology enhancements have gone hand in hand over the years, the quality of airborne gravimetry is most likely better than ground gravity measurements in the medium to high-frequency band (Glennie et al., 2000). The remaining differences are, in part, due to the ground gravity data. Further studies on their quality are still needed.

Two of the systems provided very good results – the three-axis stabilized platform system by SGL and the gravimeter based on an off-the-shelf strapdown inertial navigation system (SINS) owned by Intermap and operated jointly by Intermap and UofC. Details on the principles of these gravimeters can be found in Schwarz & Li (1996); Glennie (1999); Czombo & Ferguson (1995). The airborne data sets were cross-over adjusted and were gridded to a $5' \times 5'$ grid using least-squares collocation. The effective data area was $1° \times 1°$. Since geoid determination necessitates a larger data coverage, the airborne data area was artificially extended by gravity disturbances predicted from either EGM96 or GPM98a (depending on the test).

Terrestrial gravity anomalies were provided by the GSD and cover an area of $10° \times 5°$. The free-air anomalies are shown in Figure 5.2. It is worth noting that they are strongly correlated with the topography. The airborne flight path is plotted on top of the anomalies.

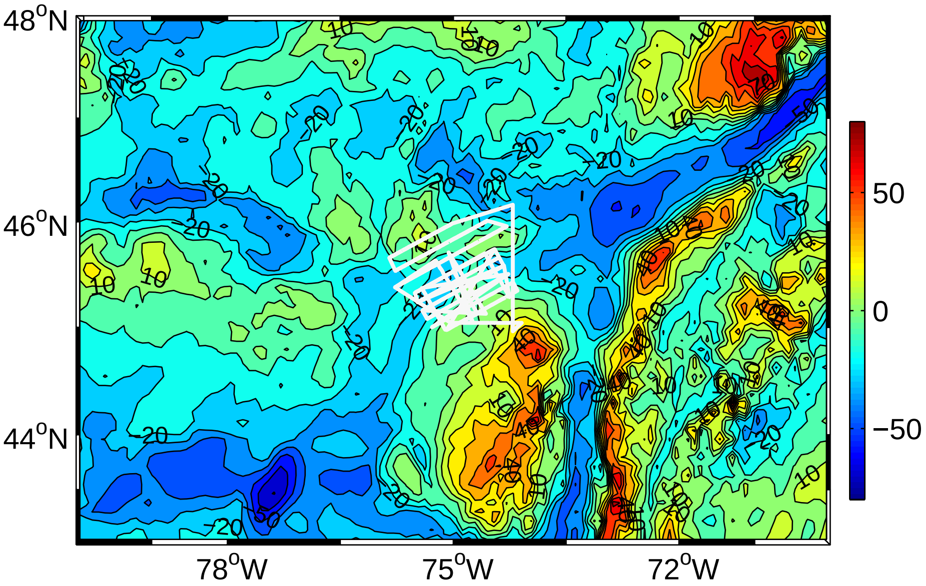

Figure 5.5: Ground gravity anomalies and airborne field test [mGal]

Canadian Gravimetric Geoid (CGG2000)

The Canadian Gravimetric Geoid of 2000 (CGG2000) is used as a reference geoid in this thesis. This description of it closely follows the technical report by Véronneau (2001). The geoid was computed at GSD and was developed in close collaboration with the University of Calgary (Dr. Sideris) and the University of New Brunswick (Dr. Vaníček). The geoid is based on the so-called Stokes-Helmert scheme, which means that residual gravity anomalies were transformed into geoidal undulations using the Stokes integral and that the 2$^{\mathrm{nd}}$ Helmert condensation method was used. The remove-restore technique was applied with EGM96 up to degree $L_{\mathrm{S}} = 30$. The VK Stokes kernel function was used with a spherical cap radius of $\psi_{\mathrm{c}} = 6^{\circ}$ and modification degree $L_{\mathrm{MD}} = 30$. The Stokes integral was evaluated by 1D-FFT to speed up the numerical computations. Indirect effects for the topography and atmosphere were computed (first and second). Also, ellipsoidal corrections were taken into account and the primary indirect effect for the EGM96. The CGG2000 did not include, however, the downward continuation process. The geoid covers most of North America; yet is optimized for Canada. It fits 1090 GPS-levelling benchmarks across Canada with a mean of -0.260 m and 0.179 m STD. The reference ellipsoid is GRS80.

The CGG2000 is used in this thesis since only eight GPS-levelling benchmarks are available in the area under study. As they are very close to each other, no representive surface can be fitted to them. However, since the CGG2000 fits the GPS-levelling points in the area with cm-accuracy (Véronneau, 2001), it was decided that the CGG2000 could be used alternatively. It must be noted that some of the solutions presented in this thesis are based on the same input data as CGG2000 – the same gravity anomaly data and EGM96 were used. Therefore, the results are expected to be close to the CGG2000 with remaining differences mainly due to a smaller integration area, integration cap, the neglected ellipsoidal corrections and the applied downward continuation.

Table 5.4: Satellite and geopotential models

Name	Degree	Resolution	Commission Error		Omission Error		$\sqrt{\varepsilon^{\mathrm{c}}+\varepsilon^{\mathrm{o}}}$	
	l [–]	x [km]	N [m]	Δg [mGal]	N [m]	Δg [mGal]	N [m]	Δg [mGal]
GPM98a,b,c	1800	11.95			0.030	12.676	0.030	12.676
GPM98ar,br,cr	720	27.80			0.103	20.122	0.103	20.122
EGM96	360	55.60	0.421	10.985	0.228	25.210	0.478	27.499
OSU91a	360	55.60	0.314	14.003	0.228	25.210	0.604	28.838
OSU89a	360	55.60	0.403	14.888	0.228	25.210	0.674	29.278
OSU89b	360	55.60	0.404	14.948	0.228	25.210	0.675	29.309
OSU89e,f	360	55.60			0.228	25.210	0.228	25.210
GPM2	200	100.08	0.308	6.869	0.425	29.022	0.526	29.807
OSU81	180	111.19	1.584	20.898	0.474	29.654	1.654	36.278
EIGEN-2	140	142.97	0.992	11.921	0.612	31.095	1.165	33.302
EIGEN1s	119	168.19	0.517	4.560	0.719	31.978	0.885	32.301
JGM3	70	285.93	0.538	4.036	1.201	34.580	1.316	34.815
GRIM4-S2	50	400.30	1.237	5.983	1.641	36.004	2.055	36.497
GRIM4-C2	50	400.30	0.843	4.678	1.641	36.004	1.845	36.306
GEMT2	50	400.30	1.458	6.292	1.641	36.004	2.195	36.549
GRIM3,3b,3-L1,GEM10b	36	555.97			2.206	37.221	2.206	37.221
GEM10	33	606.52	1.608	3.917	2.381	37.515	2.873	37.719
GEM10a	30	667.17			2.588	37.823	2.588	37.823
GEM9	30	667.17	1.924	4.644	2.588	37.823	3.224	38.107
GEML2	30	667.17	1.795	4.445	2.588	37.823	3.149	38.084
GEM8	25	800.60			3.027	38.375	3.027	38.375
GRIM2	23	870.22			3.248	38.610	3.248	38.610
OSU73	20	1000.80	1.556	3.205	3.652	38.982	3.970	39.114
GEM4,6,7	16	1250.90			4.388	39.519	4.388	39.519
OSU68	14	1429.60	3.321	3.964	4.889	39.809	5.910	40.006
GEM3,5	12	1667.90			5.529	40.116	5.529	40.116

6 Real Data Results

Individual and combined solutions over the Ottawa test area are presented. Three test areas are under consideration, namely A0, A1 and A2. A0 is the ground data area with 7200 data points. A1 is the area after the downward continuation process and A2 is the final output area for which most of the comparisons will be made.

$$\boxed{\begin{array}{c}\text{Area A0}\\ 280^\circ \le \lambda \le 290^\circ \\ 43^\circ \le \phi \le 48^\circ \\ \text{7200 points}\end{array}} \longrightarrow \boxed{\begin{array}{c}\text{Area A1}\\ 282^\circ \le \lambda \le 288^\circ \\ 44^\circ \le \phi \le 47^\circ \\ \text{2592 points}\end{array}} \longrightarrow \boxed{\begin{array}{c}\text{Area A2}\\ 284^\circ \le \lambda \le 286^\circ \\ 45^\circ \le \phi \le 46^\circ \\ \text{288 points}\end{array}} \tag{6.1}$$

It should be noted that all analyses presented in this chapter are empirical in nature. Hence, the solutions are affected by the quality of the data.

Geoid Heights and Zero-Degree Term

The quantity under study is the geoid height N. It is computed from Bruns's formula as follows (Heiskanen & Moritz, 1967; Rummel & Teunissen, 1988)

$$N = \frac{T - \Delta W_0}{\gamma} \tag{6.2}$$

where $\Delta W_0 = W_0 - U_0$ is the reference potential anomaly. Geoid heights are derived from a satellite spherical harmonic model or the Stokes integral as

$$N = N_0 + N_1 + \hat{N} \tag{6.3}$$

where N_0 is the zero-degree term, N_1 is the first-order term, i.e. the deviation between the center of mass of the reference ellipsoid and the center of mass of the Earth and $\hat{N}$ is estimated from a satellite model or Stokes' integral. N_1 is neglected in this thesis, i.e. it is assumed that the center of mass of the reference ellipsoid and the center of the actual mass coincide. The zero-order term is computed as

$$N_0 \;=\; -\frac{(W_0 - U_0)}{\gamma} + \frac{GM - GM_0}{R\gamma} = -\frac{\Delta W_0}{\gamma} + \frac{\Delta GM}{R\gamma} \approx -0.422\,\mathrm{m} \tag{6.4}$$

where $R = 6371008.771\,\mathrm{m}$, $\gamma = 9.79764466\,{}^{\mathrm{m}}/_{\mathrm{s}^2}$, $GM_0 = 0.3986005 \cdot 10^{15}\,{}^{\mathrm{m}^3}/_{\mathrm{s}^2}$ and $U_0 = 62636860.85\,{}^{\mathrm{m}^2}/_{\mathrm{s}^2}$ are taken from GRS80, see Moritz (1980a) or Table A.9 in the Appendix. In accordance with the official Canadian Gravimetric Geoid (CGG2000), the geocentric gravitational constant GM of the actual Earth is assumed to be the EGM96 value ($GM = 0.3986004415 \cdot 10^{15}\,{}^{\mathrm{m}^3}/_{\mathrm{s}^2}$). $W_0 = 62636855.8\,{}^{\mathrm{m}^2}/_{\mathrm{s}^2}$ has been adopted as for the CGG2000 (Burša et al., 1997; Véronneau, 2001). Thus, geoid heights or undulations represent the vertical separation between the geocentric reference ellipsoid GRS80 and W_0 along the ellipsoidal normal, see Figure 6.1.

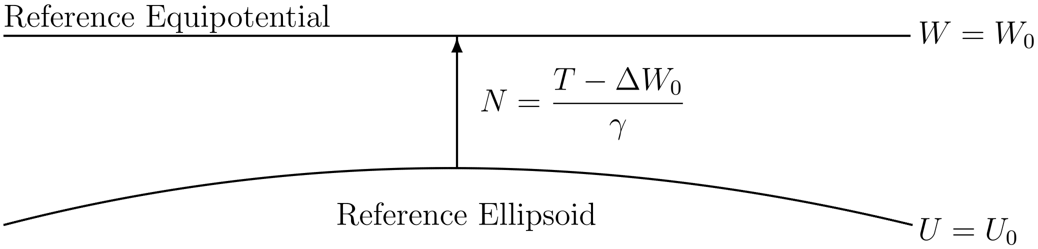

Figure 6.1: Separation between the reference ellipsoid and an adopted reference equipotential

Remark 6.1 *Note that some of the models have a semimajor axis a that is different from the reference ellipsoid* GRS*80. For instance, the semimajor axis of* GRS*80 is* $a_0 = 6378137.0\,\mathrm{m}$*, while the semimajor axis of* EGM*96 is* $a = 6378136.3\,\mathrm{m}$*. The difference of* $\Delta a = 70\,\mathrm{cm}$ *should not be neglected (Véronneau, 2003).*

6.1 Individual Solutions

Individual solutions are presented first, i.e., satellite, airborne and ground data are not combined to a unified solution. This may help to identify problems in the combined solutions and demonstrates the feasibility of the strategies.

Satellite Models and Geopotential Models

Two satellite models and two geopotential models were compared to the current geoid model CGG2000 (Véronneau, 2001). In addition, the tailored models CSM360 and CSM360w were used. The area under study was the output area A2. The statistics of the undulation differences to the CGG2000 are presented in Figure 6.2 or Table B.6 in the Appendix. The first bar in Figure 6.2 stands for the mean difference and the second bar for the standard deviation.

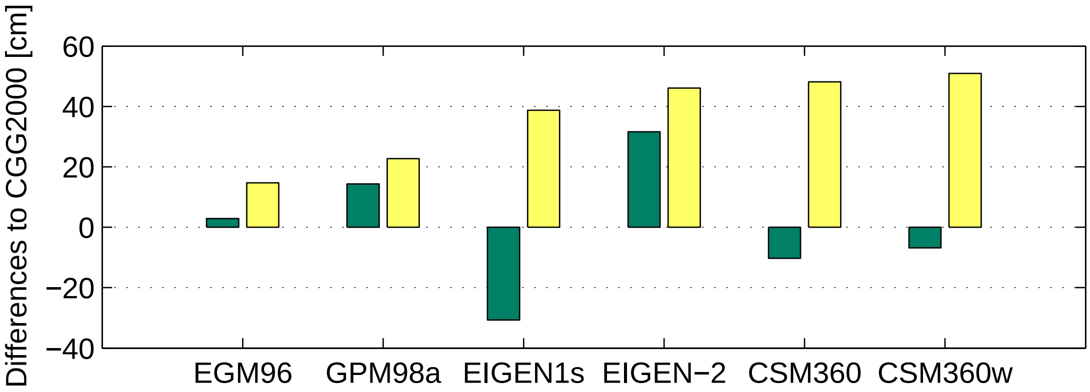

Figure 6.2: Undulation differences between the CGG2000, satellite models and geopotential models [cm]; first bar stands for mean difference, second bar is the standard deviation

The results indicate a relatively good agreement between the models and the official geoid model. Especially the EGM96 and the tailored model CSM360 agree to about 98% with the official geoid (in terms of mean differences). The differences are shown in Figure 6.3. The good fit of the EGM96 is not surprising, though, as the CGG2000 used EGM96 up to degree and order 30 (Véronneau, 2001). The tailored models CSM360 and CSM360w in turn involved EGM96 as the initial model.

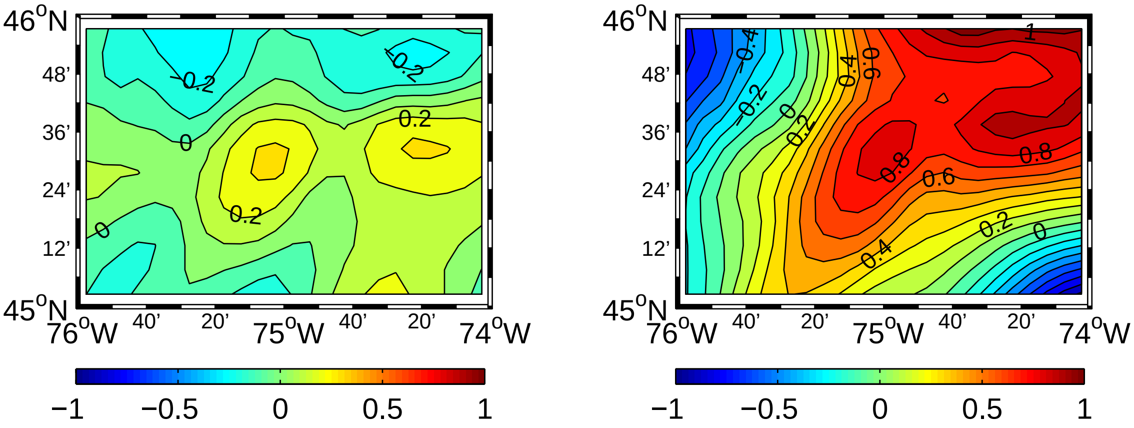

(a) EGM96 -CGG2000 (b) EIGEN-2 -CGG2000

Figure 6.3: Differences between CGG2000 and two models [m]

Geoid Based on Ground Data

A local geoid based on ground gravity data and the EGM96 was computed. All computational steps are summarized in Eqn. (6.5), i.e. the remove-restore technique was used. No surface fitting or bias removal was performed.

$$\begin{aligned} \text{Remove :} \quad & \Delta g'(r) = \Delta g - \Delta g^{\text{EGM96}} + \delta A^{\text{TOP}} + \delta A^{\text{ATM}} \\ \text{Transformation :} \quad & \Delta g'(r) \rightarrow \Delta g'(R) \rightarrow \hat{T}' \\ \text{Restore :} \quad \hat{N} = \ & N_0 + \hat{T}'/\gamma + T^{\text{EGM96}}/\gamma + \delta V^{\text{TOP}}/\gamma + \delta V^{\text{ATM}}/\gamma \end{aligned} \tag{6.5}$$

The EGM96 was used up to degree and order 180 in Δg^{EGM96} and T^{EGM96}. Hence, the far-zone effects can be computed from 181 to 360 when the EGM96 is to be used for the computation of the truncation error. Note that the topographic (δA^{TOP}) and atmospheric (δA^{ATM}) direct effects have to be added (attractions are the positive radial derivative of the potential). Secondary indirect effects as well as far-zone topographic and atmospheric effects were neglected due to their small influence in the specific area, see also Novák et al. (2003b). The downward continuation ($\Delta g'(r) \rightarrow \Delta g'(R)$) did not involve numerical problems due to a spacing of $5' \times 5'$ and a small continuation height (average height=297.870 m). The upward continuation of the Helmert gravity anomalies from the geoid to the Helmert co-geoid was neglected since its effect is less than 0.1 cm (Vaníček et al., 1999). The FEO kernel modification was used in the Stokes integration to ensure a small far-zone effect ($L_{\mathrm{MD}} = 180$) and the VK modification ($L_{\mathrm{MD}} = 180$) in the Poisson integration as recommended in Huang (2002). A spherical cap of 1° was used in both integrations. The statistics of the applied steps are summarized in Table 6.1.

Table 6.1: Statistics of the geoid based on ground gravity data

Data/Effect/Result	Min	Max	Mean	Std	Unit	Area
Δg	−70.390	82.772	−9.566	21.669	mGal	A0
δA^{TOP} (DTE)	−8.086	28.399	0.374	2.344	mGal	A0
δA^{ATM} (DAE)	0.750	0.870	0.840	0.017	mGal	A0
$\Delta g^{\mathrm{EGM96}}$	−39.646	26.579	−8.169	14.834	mGal	A0
$\Delta g'$	−54.637	79.110	−0.183	15.868	mGal	A0
$\Delta g'(R)$	−54.751	85.712	0.020	15.011	mGal	A1
$\hat{T}'/\gamma$	−0.398	0.450	−0.009	0.212	m	A2
$\delta V^{\mathrm{TOP}}/\gamma$ (PTE)	−0.022	0.000	−0.003	0.004	m	A2
$\delta V^{\mathrm{ATM}}/\gamma$ (PAE)	−0.007	−0.006	−0.006	0.000	m	A2
$T^{\mathrm{EGM96}}/\gamma$	−33.898	−30.352	−32.508	0.828	m	A2
$\hat{N}$	−33.996	−29.909	−32.526	0.872	m	A2
$\hat{N}$ - CGG2000	−0.097	0.066	−0.023	0.038	m	A2

Figures 6.4 (a) and (b) show the original (Δg) and the residual gravity anomalies ($\Delta g'$). The residual (Helmert) anomalies are correlated with the topography; yet they are considerably smoother than the original data. The topographic and atmospheric

indirect effects are small due to the small topographic height variations. For a comparison of the 2^{nd} Helmert condensation with the 1^{st} Helmert condensation refer to Appendix B.1.

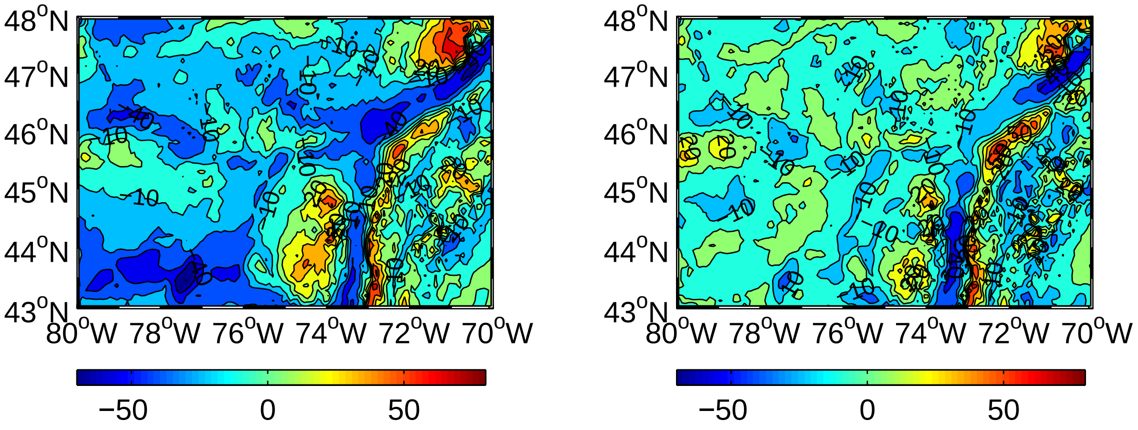

(a) Original gravity anomalies Δg in area A0 (mGal)

(b) Residual gravity anomalies $\Delta g'$ in area A0 (mGal)

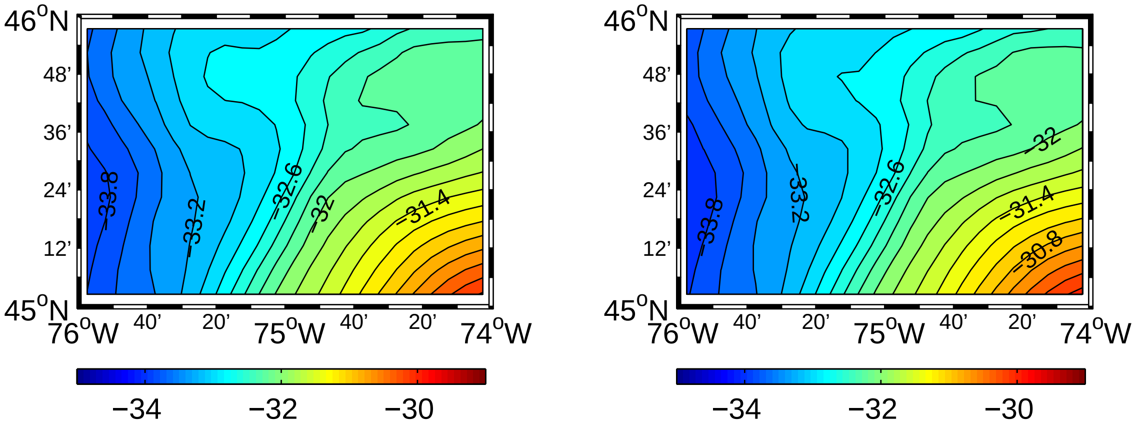

(c) CGG2000 geoid in area A2 (m)

(d) Geoid based on ground gravity data in area A2 (m)

Figure 6.4: Determination of a local geoid based on ground gravity anomalies

As expected, the two solutions are very close, since they essentially use the same data sets. However, the (local) geoid based on ground gravity data is slightly biased with respect to the CGG2000. This is most likely due to the use of EGM96 up to degree 180 vs. degree 30 for CGG2000. In addition, the use of a much smaller spherical cap (1° vs. 6°) and the applied downward continuation may have adversely affected the local geoid determination. However, the local geoid exhibits most of the features of the CGG2000 geoid when comparing figures 6.4 (c) and (d). The quality of the geoid confirms the feasibility of the applied strategy.

The effect of different Stokes kernel modifications on the local geoid is shown in Figure 6.5. The rms undulation differences compared to the FEO kernel are presented. All other steps such as the reductions and the downward continuation process were the same. Clearly, the use of the spherical kernel results in an undulation difference of up to 6 cm compared to the FEO kernel while the MO, M, JK and the VK kernels agree within a cm with the FEO solution. Somewhat surprising is the performance of the HG kernel function with a rms difference of about 4 cm. The reason for the relatively large difference is unclear at this point.

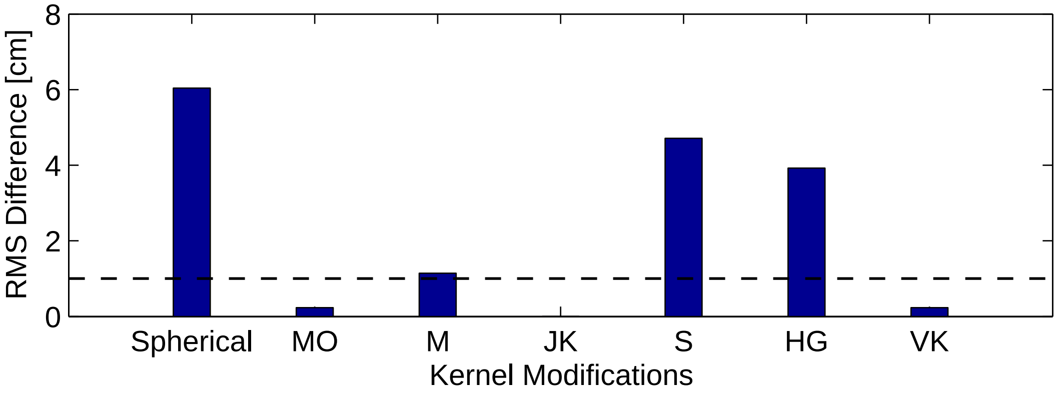

Figure 6.5: Effect of different Stokes kernel modifications

Geoid Based on Airborne Data

Principally, the geoid determination based on airborne data followed the same steps as for the ground data. Additional difficulties arose, however, as the airborne data at hand are limited in their spatial extent; a geoid determined from a 1° × 1° data area would be burdened with large edge effects. Therefore, to preserve the airborne gravity information, gravity disturbances from EGM96 were predicted around the data area, see Figure 6.6 (a). The aforementioned effects were alleviated since the data area was (artificially) extended. The airborne data have a higher frequency content than the EGM96 data and are clearly noticeable in the center of the data area. Alternatively, GPM98a gravity disturbances could be predicted around the airborne data, yet this did not yield better results.

$$\begin{aligned} \text{EGM96}: & \qquad & \delta g = [\delta g^{\text{AIR}}; \delta g^{\text{EGM96}}] \\ \text{Remove}: & \qquad & \delta g'(r) = \delta g - \delta g^{\text{EGM96}} + \delta A^{\text{TOP}} + \delta A^{\text{ATM}} \\ \text{Transformation}: & \qquad & \delta g'(r) \rightarrow \delta g'(R) \rightarrow \hat{T}' \\ \text{Restore}: & \quad \hat{N} = & N_0 + \hat{T}'/\gamma + T^{\text{EGM96}}/\gamma + \delta V^{\text{TOP}}/\gamma + \delta V^{\text{ATM}}/\gamma \end{aligned} \tag{6.6}$$

Eqn. (6.6) summarizes the remove-restore technique for airborne gravity disturbances. Again, no bias removal or surface fitting was performed. Note that the direct effects were computed at flight height and are slightly smaller than for the ground case. Analogous to the previous case, the FEO kernel modification was used in the Hotine integration ($L_{\text{MD}} = 180$). Table 6.2 gives the statistical values for the local geoid based on airborne data. A bias of about 1.2 cm is obtained and a standard deviation of about 15 cm when compared to the CGG2000. Clearly, the geoid based on airborne data suffers from the use of the predicted EGM96 gravity data. This conclusion can be drawn from inspecting Figure 6.6 (c). Although the general direction of the geoid agrees with the ground geoid, the geoid based on airborne data is much smoother than the ground geoid. High-frequency features do not show up in this geoid. Hence, a different combination strategy has to be found for the airborne data.

Remark 6.2 *An additional test was performed with ground data in the same area as the airborne data. Similar to the airborne case,* EGM*96 anomalies were predicted around the limited data area. The obtained ground geoid agreed up to 1.7 cm rms with the geoid based on airborne data and confirmed the quality of the airborne data.*

Table 6.2: Statistics of the geoid based on airborne gravity data

Data/Effect/Result	Min	Max	Mean	Std	Unit	Area
δg	-58.140	62.848	-18.016	19.656	mGal	A0
δA^{TOP} (DTE)	-16.287	33.713	0.339	2.005	mGal	A0
δA^{ATM} (DAE)	0.809	0.809	0.809	0.000	mGal	A0
$\delta g^{\mathrm{EGM96}}$	-50.684	17.627	-17.975	15.561	mGal	A0
$\delta g'$	-33.397	55.032	1.107	10.965	mGal	A0
$\delta g'(R)$	-29.753	51.678	1.241	9.942	mGal	A1
$\hat{T}'/\gamma$	-0.226	0.272	0.026	0.119	m	A2
$\delta V^{\mathrm{TOP}}/\gamma$ (PTE)	-0.022	0.000	-0.003	0.004	m	A2
$\delta V^{\mathrm{ATM}}/\gamma$ (PAE)	-0.007	-0.006	-0.006	0.000	m	A2
$T^{\mathrm{EGM96}}/\gamma$	-33.898	-30.352	-32.508	0.828	m	A2
$\hat{N}$	-33.816	-30.129	-32.492	0.865	m	A2
$\hat{N}$ - CGG2000	-0.354	0.299	0.012	0.143	m	A2

High-Degree Spherical Harmonic Model Based on Ground Data

A high-degree spherical harmonic model (TM900g) based on terrestrial gravity anomalies has been developed. Such a model could be used for calibration or validation purposes of new satellite missions such as GOCE. The high-degree model was tailored to the Ottawa region with GPM98a as an initial model. It was developed up to degree and order 900, i.e. down to spatial scales of about 22 km. A higher development of the model was not deemed to provide more information and is likely to be encumbered with numerical problems. The coefficients of the first 70 degrees were taken over from the GPM98a in order to avoid large leakage effects. To ensure a smooth transition between the global model and the local data, a linear weighting function was applied as follows

$$p_l = \frac{l - l_1}{l_2 - l_1} \quad \text{for} \quad 70 = l_1 > l < l_2 = 140 \quad \text{and} \quad p_l = 1 \quad \forall\, l \geq l_2 \tag{6.7}$$

The input ground data were reduced by the topographic and atmospheric effects. As the downward continuation was not critical for the area under consideration, a simple Taylor series development was used (Wenzel, 1985, pg. 57). The model was obtained after 7 iterations with a final rms difference to the ground data anomalies of 5.882 mGal.

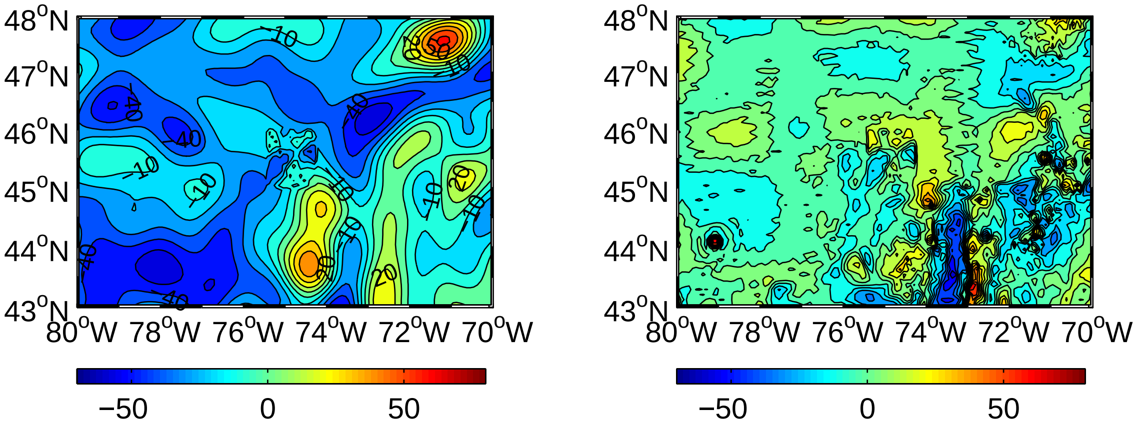

(a) Original gravity disturbances δg in area A0 (mGal)

(b) Residual gravity disturbances $\delta g'$ in area A0 (mGal)

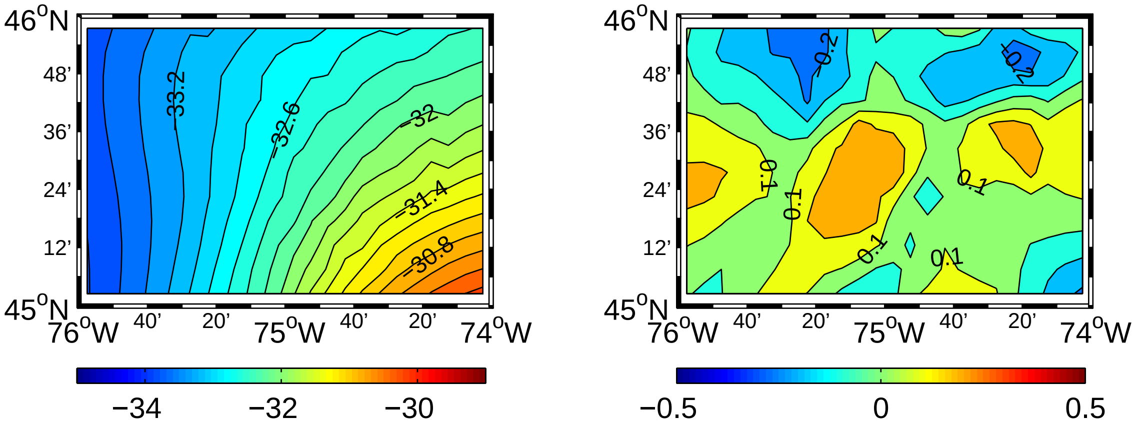

(c) Geoid based on airborne gravity data in area A2 (m)

(d) Difference to ground geoid in area A2 (m)

Figure 6.6: Determination of a local geoid based on airborne gravity disturbances

The statistics of the model and the differences to the reference geoid and the CGG2000 are provided in Table 6.3.

Although the model is band limited, the computed geoidal undulations are of similar quality as the ones from the local ground geoid. However, the high-degree model TM900g is slightly biased compared to the official geoid CGG2000. Furthermore, the

Table 6.3: Statistics of the high-degree model TM900g

Data/Result	Min	Max	Mean	Std	Unit	Area
$\hat{N}$	−33.884	−30.262	−32.539	0.756	m	A2
$\hat{N}$ - $\hat{N}^{\text{Ground}}$	−0.353	0.261	−0.013	0.134	m	A2
$\hat{N}$ - CGG2000	−0.287	0.170	−0.035	0.099	m	A2

standard deviation is larger than for the local ground geoid. This may be due to the fact that the GPM98a was used as an initial model. The undulations of the model are shown in Figure 6.7 (a). Anomaly degree variances of the model are compared to the Tscherning-Rapp anomaly degree variances in Figure 6.7 (b). The model has slightly less power than the Tscherning-Rapp variances beyond degree 200.

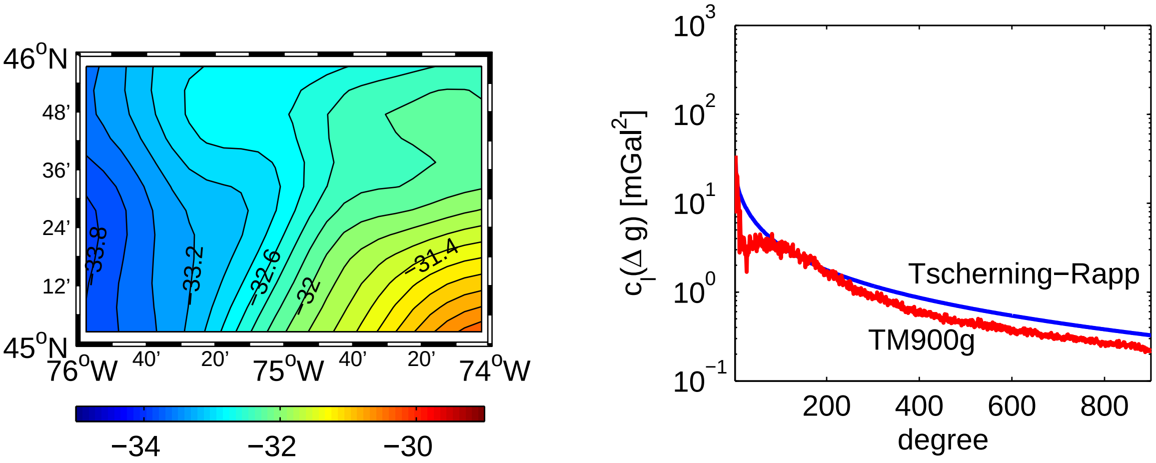

(a) Geoidal undulations from the high-degree model TM900g (m)

(b) Anomaly degree variances of the high-degree model and the Tscherning-Rapp degree variances (mGal^2)

Figure 6.7: High-degree spherical harmonic model based on ground gravity data

High-Degree Spherical Harmonic Model Based on Airborne Data

A spherical harmonic model (GM900sgl) based on airborne data has been developed up to degree and order 900. As the airborne data were provided in a small area, gravity disturbances were predicted from the EGM96 around the airborne data area. This followed the same rationale as described earlier. The gravity disturbances in A0 were reduced by the topographic and atmospheric effects. Otherwise, the computational steps followed the ones for the ground data. The iteration method converged rapidly and the final rms difference between the disturbances predicted from the model and the input disturbances was 6.693 mGal after 7 iteration steps. The results are given in Table 6.4 and Figure 6.8.

Table 6.4: Statistics of the high-degree model GM900sgl

Data/Result	Min	Max	Mean	Std	Unit	Area
$\hat{N}$	-33.971	-30.288	-32.577	0.821	m	A2
$\hat{N}$ - $\hat{N}^{\mathrm{Ground}}$	-0.379	0.194	-0.051	0.095	m	A2
$\hat{N}$ - CGG2000	-0.313	0.137	-0.074	0.083	m	A2

In this combination, the airborne data contributed to the final solution. Especially the medium frequencies were improved by the local data. This can be concluded by inspecting Figure 6.8 (b). Although the bias is slightly larger than for the ground data, the obtained standard deviation is encouraging since it is about 2 cm smaller than for the model based on terrestrial data. Since the airborne data are band-limited, the aliasing effects are most likely smaller. In conclusion, the combination strategy based on tailoring can preserve the information content of the airborne data.

Summary. Four individual solutions have been computed – two local geoids and two high-degree models. All of them are of relatively good quality and the comparison to the official Canadian Gravimetric Geoid CGG2000 may be considered as proof-of-concept. It should be noted once again that no bias removal, surface fitting or additional data filtering was aplied. The remaining differences to the CGG2000 are most likely due to the use of a much smaller integration area and integration cap, the applied downward continuation, the neglect of ellipsoidal corrections and other approximation errors. Nevertheless, the differences are minor for the local geoid based on ground gravity data with a bias of -2.3 cm and standard deviation of about 4 cm, see Figure 6.9. For the airborne geoid, the mean is slightly smaller than for the ground data (1.2 cm). However, the use of predicted EGM96 gravity disturbances around the data

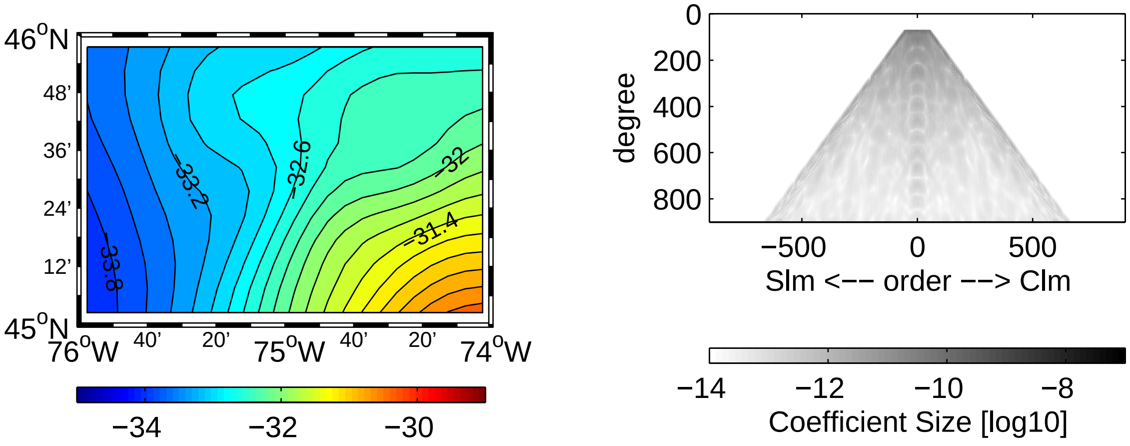

(a) Geoidal undulations from the high-degree model GM900sgl (m)

(b) Coefficient differences of GPM98a and GM900sgl

Figure 6.8: High-degree spherical harmonic model based on airborne data

area adversely affected the solution and the information content of the airborne data was not preserved.

Quite interesting is the performance of the computed high-degree models. To the best of the author's knowledge, these models are by far the highest developed models that have been computed from a local data area (the models from H.-G. Wenzel are based on global data). They provide information down to spatial scales of 22 km. Comparing their performance to the local geoids one can conclude that the high-degree models are of almost the same quality as the local geoids. The high-degree model based on ground data is about 4 cm biased compared to the CGG2000 and has a standard deviation of almost 10 cm. The high-degree model based on airborne data in turn preserves more information from the local data area than the local airborne geoid. A bias of -7 cm and a standard deviation of 8 cm were obtained. Hence, tailored high-degree spherical harmonic models can be seen as an alternative to geoid modelling by integration. Since other functionals can be computed from the models at every point in the data area and above, the high-degree models may be beneficial for even more application areas than a local geoid. For instance, they could be used for the calibration or validation

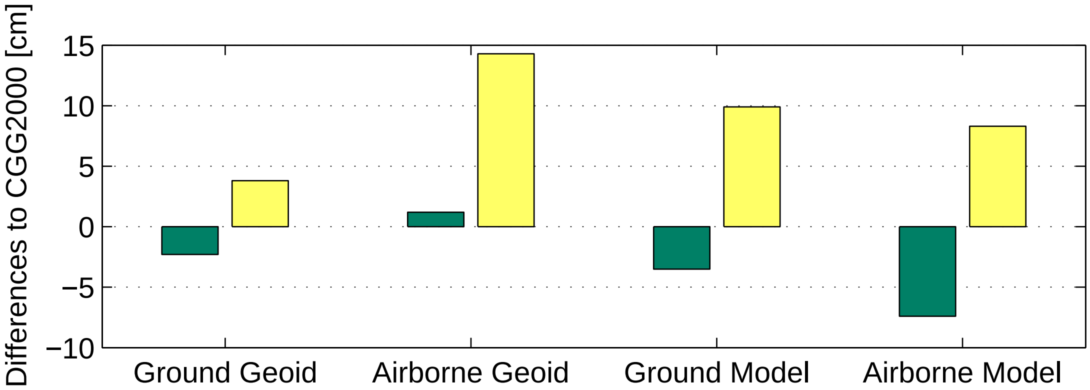

Figure 6.9: Performance of individual solutions. First bar stands for mean difference, second bar is standard deviation

of future satellite missions. With a resolution of about 22 km, they certainly provide more high-frequency information than any current satellite-only model.

6.2 Combined Solutions

Three combination strategies are presented in this section. The first strategy aims at a geoid computed from satellite and terrestrial gravity data. The second combination approach is an attempt to solve for an improved geoid based on a combination of all available gravity data over the Ottawa area, i.e., ground and airborne data. Finally, the third combination uses the global and local gravity information for the development of a tailored high-degree model. It should be noted that the combined solutions provide different solutions than the CGG2000 since additional gravity information is used. Hence, a comparison with the CGG2000 provides differences, which may be due to either methodology or data.

Geoid Determination Based on Satellite and Terrestrial Gravity Data

Terrestrial gravity data and the CSM360 were used in the first combination. An improved local geoid was the main objective. The lowest frequencies that can be resolved from local data in a spherical cap of 1° is about $l = 180$ or a resolution of 111 km.

Hence, combining the local data with the EIGEN-2 ($L_\mathrm{S} = 140$) would result in a gap in the spectrum between $l = 141$ and $l = 179$. To ensure that the geoid contains all frequencies, it was decided to use the CSM360 instead of the EIGEN-2 solution. Thus, the CSM360 is considered to be a high-frequency 'version' of the satellite data EIGEN-2.

The remove-restore technique was applied. The gravity anomalies were first reduced for the direct topographic and atmospheric effects and by the gravity anomalies ($l = 2-180$) computed from CSM360. Downward continuation of the residual gravity anomalies was performed, which was followed by the modified Stokes integration (FEO kernel, $L_\mathrm{MD} = 180$). Restoring the indirect effects and the low-frequency information from the tailored model CSM360 led to a combined local geoid. The statistics of the solution are provided in Table 6.5. The geoid based on a combination of satellite and terrestrial gravity and the CGG2000 differ by about -10 cm. The bias and tilt is likely due to the use of CSM360 rather than EGM96, compare Table B.6. This can also be concluded from Figures 6.10 (a) and (b). The comparison of the CSM360 and CGG2000 in Figure 6.10 (a) shows the same features as Figure 6.3 (b). The differences of the combined model to the CGG2000 are shown in Figure 6.10 (b). The bias and the tilt are clearly visible. It should be noted once again that this difference should not be considered as an error since gravity information was used that is not contained in CGG2000. To evaluate the performance of the combination, a smooth surface was fitted to the geoid which removes the bias and the tilt (Forsberg & Madsen, 1990). The fitted geoid was computed from

$$\hat{\boldsymbol{N}}^{\text{Fitted}} = \hat{\boldsymbol{N}} + \hat{x}(1) + \hat{x}(2)\cos\boldsymbol{\varphi}\cos\boldsymbol{\lambda} + \hat{x}(3)\cos\boldsymbol{\varphi}\sin\boldsymbol{\lambda} + \hat{x}(4)\sin\boldsymbol{\varphi} \tag{6.8}$$

where $\hat{\boldsymbol{x}}_{4\times1}$ is obtained from a least-squares adjustment ($\hat{\boldsymbol{x}} = \left(\boldsymbol{A}^T\boldsymbol{A}\right)^{-1}\boldsymbol{A}^T\boldsymbol{l}$) with the design matrix $\boldsymbol{A}$ computed as

$$\boldsymbol{A}_{m\times 4} = \begin{pmatrix} 1 & \cos\varphi_1\cos\lambda_1 & \cos\varphi_1\sin\lambda_1 & \sin\varphi_1 \\ 1 & \cos\varphi_2\cos\lambda_2 & \cos\varphi_2\sin\lambda_2 & \sin\varphi_2 \\ \multicolumn{4}{c}{\dotfill} \\ 1 & \cos\varphi_m\cos\lambda_m & \cos\varphi_m\sin\lambda_m & \sin\varphi_m \end{pmatrix} \tag{6.9}$$

and $\boldsymbol{l}$ given as $\boldsymbol{l}_{m\times 1} = \hat{\boldsymbol{N}}^{\mathrm{CGG2000}}_{m\times 1} - \hat{\boldsymbol{N}}_{m\times 1}$. The remaining differences are about 5 cm, see Table 6.5. Thus, the quality of the local geoid based on satellite and terrestrial gravity data is comparable to the individual combinations. Equivalent computations were performed for the model CSM360w see Appendix B.4. Since the model CSM360w has more EGM96 components, the fit with CGG2000 is slightly better than with CSM360, see also Table B.7.

Table 6.5: Statistics for the geoid determination of satellite data and a local gravity data set

Data/Effect/Result	Min	Max	Mean	Std	Unit	Area
Δg	−70.390	82.772	−9.566	21.669	mGal	A0
δA^{TOP} (DTE)	−8.086	28.399	0.374	2.344	mGal	A0
δA^{ATM} (DAE)	0.750	0.870	0.840	0.017	mGal	A0
$\Delta g^{\mathrm{CSM360}}$	−29.173	15.180	−9.761	8.808	mGal	A0
$\Delta g'$	−59.482	93.897	1.408	21.639	mGal	A0
$\Delta g'(R)$	−46.250	99.507	−0.125	19.830	mGal	A1
$\hat{T}'/\gamma$	−0.864	0.688	0.004	0.336	m	A2
$\delta V^{\mathrm{TOP}}/\gamma$ (PTE)	−0.022	0.000	−0.003	0.004	m	A2
$\delta V^{\mathrm{ATM}}/\gamma$ (PAE)	−0.007	−0.006	−0.006	0.000	m	A2
$T^{\mathrm{CSM360}}/\gamma$	−34.419	−30.820	−32.598	1.021	m	A2
$\hat{N}$	−34.224	−30.157	−32.603	0.910	m	A2
$\hat{N}$ - CGG2000	−0.281	0.285	−0.100	0.154	m	A2
$\hat{N}^{\mathrm{Fitted}}$ - CGG2000	−0.122	0.177	0.000	0.052	m	A2

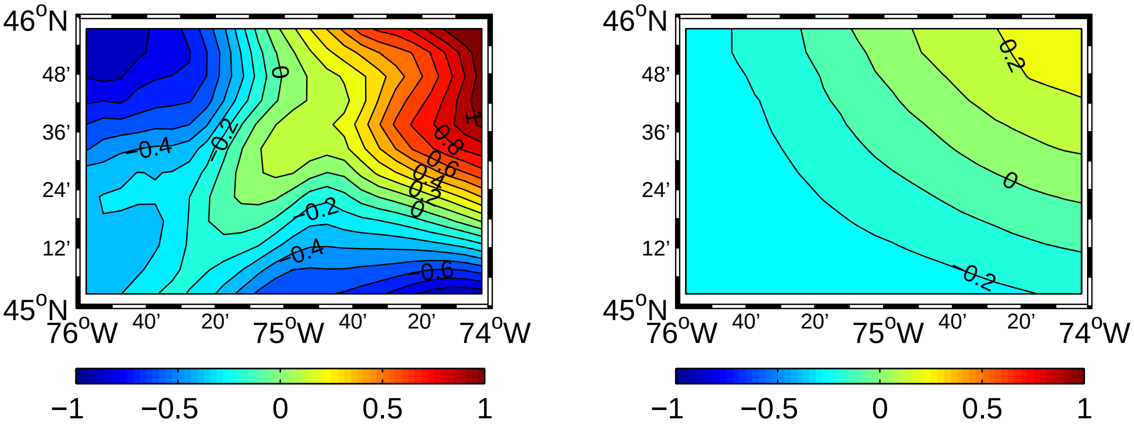

(a) Undulation differences between CSM360 and CGG2000

(b) Undulation differences between a local geoid based on CSM360 and terrestrial gravity data and CGG2000

Figure 6.10: Undulation differences [m]

Geoid Determination Using Satellite, Airborne and Terrestrial Gravity Data

All available gravity information over the Ottawa area was used for geoid determination. The combination strategy presented in Section 4.3 was followed. At first, a high-degree model was developed that combined satellite and airborne data. As in the previous tests, the airborne data area was again extended with predicted GPM98a disturbances to yield a A0 area. The initial model in the iteration was the EIGEN-2 with coefficients up to degree and order 140. The coefficients beyond that degree were set to zero in the initial model. The iteration with residual (topographic and atmospheric reduced) airborne disturbances converged after eight iterations and led to a final rms difference of 6.133 mGal compared to the input disturbances. The new model consisted of the EIGEN-2 coefficients up to degree and order 70 and new coefficients beyond this degree. The semimajor axis a and the geocentric gravitational mass constant GM were adopted from EIGEN-2. The statistics of the tailored model (HM900sgl) are given in Table 6.6. Not surprisingly, the undulations computed from the new model are biased with respect to the CGG2000. Comparing the result with the previous combination result, however, indicates that the bias is slightly larger (-19 cm in Table 6.6 versus -10 cm in Table 6.5).

Yet in this case, the solution has a smaller standard deviation when compared to the CGG2000 (STD = 9 cm).

Table 6.6: Statistics of the first combination – satellite and airborne data

Data/Effect/Result	Min	Max	Mean	Std	Unit	Area
$\hat{N}$	-34.056	-30.298	-32.696	0.851	m	A2
$\hat{N}$ - CGG2000	-0.448	-0.006	-0.192	0.089	m	A2

In the second and final combination step, the new model HM900sgl was used together with terrestrial gravity data. As described in Section 4.3, the remove-restore technique was applied. The HM900sgl was used up to degree and order 180. Note that the truncation error can be computed from 181 up to 900. Since the Poisson and the Stokes integration kernels were modified, the truncation errors were very small and no substantial difference to the truncation errors computed up to degree 360 was found. Adding back the indirect effects and restoring geoidal undulations from HM900sgl up to degree 180 yielded a combined local geoid. All steps applied are documented in Table 6.7. The fitted geoid N^{Fitted} was obtained by removing the systematic trend between $\hat{N}$ and CGG2000, see Eqn. (6.8). Remarkable is the small standard deviation compared to the CGG2000. The solution can be considered as an EIGEN-2 improved geoid.

The geoidal undulations from the first and the second combination are shown in Figure 6.11 (a) and (b). While Figure 6.11 (a) presents undulations computed from the HM900sgl model, Figure 6.11 (b) shows the final result. The first combination using satellite and airborne data provides most of the long and medium frequencies of the solution. Airborne data define the medium and higher frequencies. The terrestrial gravity data in turn, seem to add some high-frequency information to the result, see Figure 6.11 (b). It seems that there is no loss of medium to high-frequency information compared to the CGG2000. Taking the results of the previous combination (satellite+terrestrial gravity data) into account, one could argue that this is due to the use of airborne data. Hence, combining heterogeneous gravity data is beneficial for the final result both in terms of accuracy and resolution.

Table 6.7: Statistics for the geoid determination based on satellite, airborne and terrestrial gravity data

Data/Effect/Result	Min	Max	Mean	Std	Unit	Area
Δg	−70.390	82.772	−9.566	21.669	mGal	A0
δA^{TOP} (DTE)	−8.086	28.399	0.374	2.344	mGal	A0
δA^{ATM} (DAE)	0.750	0.870	0.840	0.017	mGal	A0
$\Delta g^{\text{HM900sgl}}$	−44.770	22.823	−10.893	14.516	mGal	A0
$\Delta g'$	−55.849	77.603	2.541	16.348	mGal	A0
$\Delta g'(R)$	−50.886	85.580	1.680	15.276	mGal	A1
$\hat{T}'/\gamma$	−0.470	0.570	−0.001	0.275	m	A2
$\delta V^{\text{TOP}}/\gamma$ (PTE)	−0.022	0.000	−0.003	0.004	m	A2
$\delta V^{\text{ATM}}/\gamma$ (PAE)	−0.007	−0.006	−0.006	0.000	m	A2
$T^{\text{HM900sgl}}/\gamma$	−34.193	−30.546	−32.715	0.850	m	A2
$\hat{N}$	−34.155	−30.171	−32.726	0.846	m	A2
$\hat{N}$ - CGG2000	−0.312	−0.179	−0.222	0.030	m	A2
$\hat{N}^{\text{Fitted}}$ - CGG2000	−0.026	0.028	0.000	0.007	m	A2

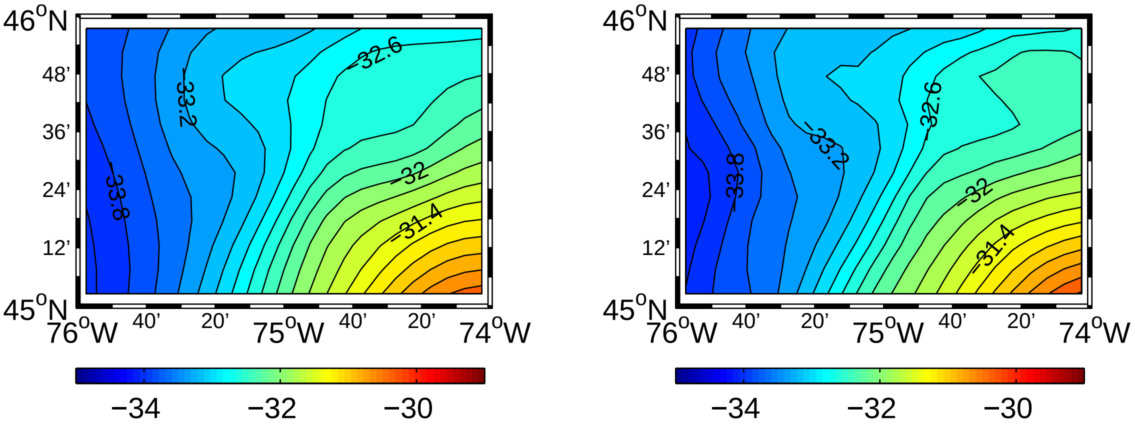

(a) 1.Combination – high-degree model based on satellite and airborne data

(b) 2.Combination – geoid determination based on satellite, airborne and terrestrial gravity data

Figure 6.11: Geoid based on a combination of satellite, airborne and terrestrial gravity data

High-Degree Model Determination

A combined high-degree spherical harmonic model up to degree and order 900 has been developed. It is based on a combination of EIGEN-2 satellite data, airborne gravity disturbances and terrestrial gravity anomalies. In the first combination, the satellite-only model EIGEN-2 and airborne data were combined. Hence, the tailored high-degree model HM900sgl described earlier was obtained.

In the second combination step, the tailored model was used as an initial model. The combination was now performed with terrestrial gravity anomalies. Analogous to the individual combination of a global model and terrestrial data, the first coefficients remained unchanged. The linear weighting function as presented in Eqn. (6.7) was again employed with $l_1 = 70$ and $l_2 = 140$ to ensure a smooth final model. No major variations were obtained after seven iterations (final RMS=6.117 mGal). The tailored model was refined by the information of the ground data. The statistics of the combined model are given in Table 6.8. As in the previous combination yielding a combined geoid, the solution is an improved model. A standard deviation of 3.7 cm compared to CGG2000 demonstrates the quality of the solution. The bias is likely due to the use of EIGEN-2 information. A solution N^{Fitted} without the systematic trend was computed, see Eqn. (6.8).

Table 6.8: Statistics of the high-degree model based on satellite, airborne and terrestial gravity data

Data/Effect/Result	Min	Max	Mean	Std	Unit	Area
$\hat{N}$	−34.362	−30.320	−32.895	0.858	m	A2
$\hat{N}$ - CGG2000	−0.484	−0.309	−0.391	0.037	m	A2
$\hat{N}^{\text{Fitted}}$ - CGG2000	−0.071	0.085	0.000	0.022	m	A2

The second combination resulted in smaller model changes. This can be concluded by inspecting Figure 6.12 (b) which compares the two solution in the spectral domain. Although the terrestrial gravity data contribute to the lower frequencies (beyond degree 70), they do not significantly change the tailored model from the first combination. Hence, the airborne data define the medium to high frequencies of the model with additional high-frequency information from the terrestrial gravity data. The undulations are shown in Figure 6.12 (a). The results are encouraging showing that all available gravity data can contribute to the final solution. The combined model preserves the information content of the global and local gravity data, can filter out measurement errors and noise through the iteration process and provides a high-resolution tailored model that is comparable to local geoid determination by integration.

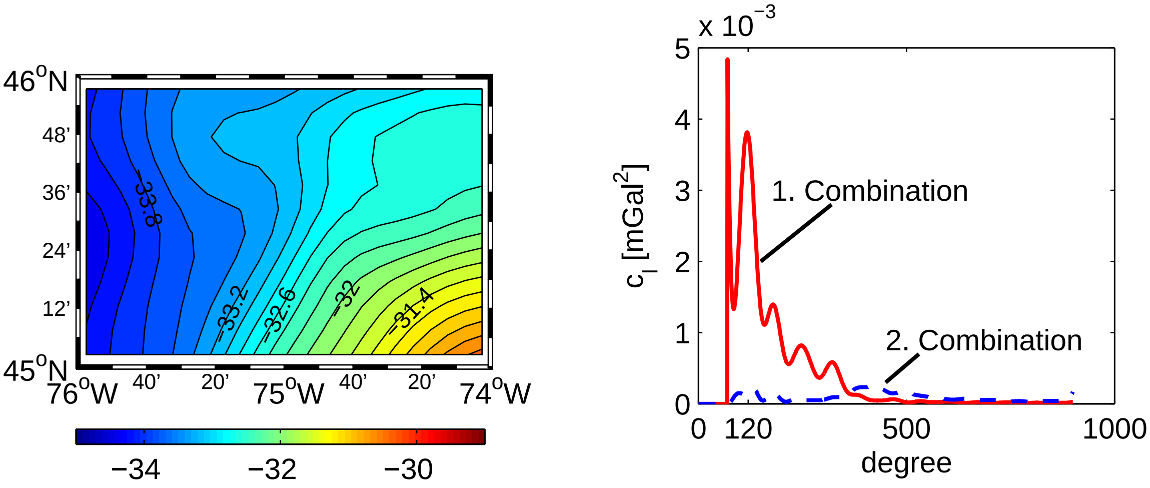

(a) Geoidal undulations from the high-degree model based on satellite, airborne and terrestrial gravity data (m)

(b) Degree variance differences for the first and second combination

Figure 6.12: High-degree spherical harmonic model based on satellite, airborne and terrestrial gravity data

Summary. Three combined solutions were presented. The first solution, a combination of satellite data and terrestrial gravity anomalies, was of similar quality as the individual solutions. Since the satellite data EIGEN-2 are low frequency in nature and could not be directly used in the remove-restore technique, the combination was based on the tailored model CSM360 which was based on EIGEN-2. The second solution in turn, combined gravity information from satellite, airborne and terrestrial gravity data. A local geoid was the desired combination output. The resulting geoid fits the CGG2000 better than all other combinations (after removing a systematic trend). The geoid effectively uses satellite data for the lower frequencies, airborne data for the medium and higher frequencies and terrestrial gravity data for the medium to highest frequencies of the spectrum. Although the airborne data were provided in a small area, they contributed to the solution. A difference of less than 1 cm STD to the CGG2000 was obtained after removing a systematic trend, see Figure 6.13.

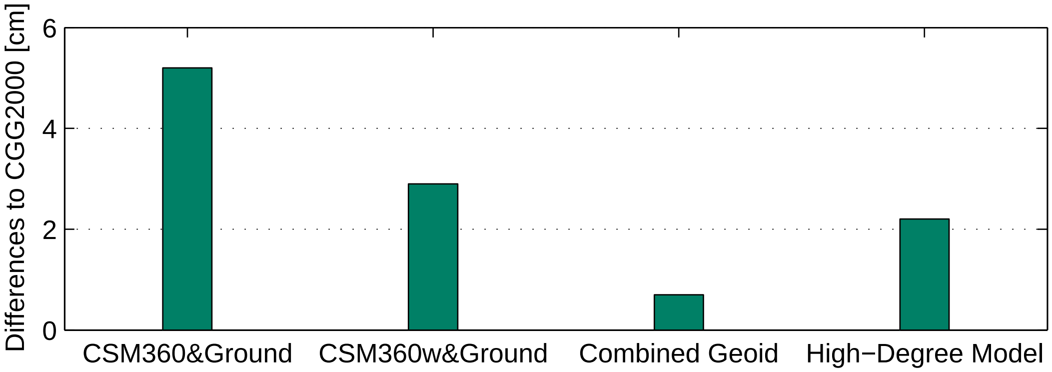

Figure 6.13: Performance of combined solutions. Standard deviation to CGG2000 after removing a systematic trend

Finally, a combined high-degree model was computed. The first combination step was identical to the previous combination (satellite+airborne data) resulting in a high-degree model HM900sgl. The second combination step with terrestrial gravity anomalies changed the model only slightly, underscoring the quality of the airborne data in the medium frequencies of the spectrum. Compared to the CGG2000, a standard deviation of about 2 cm was obtained after removing a systematic trend. Hence, a tailored spherical harmonic model based on satellite, airborne and terrestrial gravity data can achieve cm-accuracy with a resolution down to spatial scales of 22 km.

7 Concluding Remarks

A detailed analysis of the combination and downward continuation of satellite, airborne and terrestrial gravity data was presented. It encompassed theoretical aspects as well as numerical tests.

Conclusions

The following conclusions can be drawn from this study:

- The Helmert scheme, proposed in this thesis, gives insight into the nature of the reduction method and simplifies the comparison of different condensation methods.
- An error analysis of the remove-restore technique led to the conclusion that the far-zone effect has to be considered. It can be minimized by a kernel modification.
- A comparison of deterministic kernel modifications for geoid determination showed that the numerical accuracy of these kernel modifications is at the 1 cm level for noisy gravity anomalies. Taking into account the implementation complexity and overall error, the Heck-Grüninger kernel modification is recommended. When a small far-zone effect is desired and computational efficiency is not a primary concern, the Featherstone-Evans-Olliver kernel should be favoured.
- It is shown that regularization methods for the downward continuation can be considered as filtered least-squares solutions.
- The discrete downward continuation was analyzed as having the characteristics of a discrete ill-posed problem. When applying the Picard condition to analyze the

sensitivity of the problem to noisy input data, it could be shown that for noisy and very densely spaced airborne data, the Picard condition may not be satisfied and regularization has to be applied.

- An alternative approximation, developed in this thesis, showed best performance for the downward continuation of airborne data in terms of accuracy and efficiency.
- Eight different downward continuation methods were numerically compared. Using simulated, noisy, airborne data at 6 km height, the downward continuation error can reach up to 25 mGal for the least-squares solution. Hence, regularization is required to alleviate the effect of noise. The best solutions, the conjugate gradient method and the alternative solution, reduced the error to 5 mGal and 3 mGal, respectively.
- Two strategies for the combination of heterogeneous gravity data – tailoring and the remove-restore technique – were numerically evaluated. Using simulated data, both methods give results at the cm-level.
- Several combination strategies were compared using real gravity data in an area close to Ottawa, Canada. All local solutions were slightly biased compared to the reference used (CGG2000). This is likely due to the fact that CGG2000 is based on different (low-frequency) information and on a different computational strategy. The fit of combined solutions to the CGG2000 was consistently better than the fit of solutions using one data set only. The strategy that provided best results compared to the CGG2000 was the geoid determination based on satellite, airborne and terrestrial data. A standard deviation of less than 1 cm was obtained with respect to CGG2000 after removing a systematic trend. The combined high-degree spherical harmonic model up to degree and order 900 agreed with the CGG2000 up to 2 cm (after removing a systematic trend).

Outlook

An incomplete list of recommendations and future work is given here:

- The gravity data in this thesis are interpolated to a spatial grid of $5' \times 5'$. This interpolation was performed with least-squares collocation and the interpolation error was neglected. Further investigations on the interpolation problem are needed.
- A-priori information about the quality of the local data has not been taken into account in the combination. Future studies may have to include this information in order to improve the combination. Theoretical and numerical comparisons with alternative combination methods such as LSC, MIMO and spectral combination should be performed.
- It has been assumed that the satellite and the local data are calibrated and validated. Studies on data correlations and their effect on the combination result may prove to be useful.
- Synthetic gravity data models that allow for feasibility studies on data combinations are required. These models should also include topographic models.
- The combinations presented in this thesis are not performed at the observation level. Investigations on combining gravity data at the observation or normal equation level of the satellite data could be carried out and compared to the presented combination strategies.
- The feasibility of the downward continuation of satellite data with the alternative approach could be studied. Also, additional gravity data could be used to constrain the downward continuation solution.
- Developing downward continuation methods based on spherical wavelets may be another research direction worthwhile studying. First results in this direction are reported in Schneider (1997).
- Other discretizations of the Fredholm integral of the first kind such as finite element methods or Galerkin methods could be tested.

Bibliography

Albertella A, Sansò F, Sneeuw N (1999) Band-limited functions on a bounded spherical domain: the Slepian problem on the sphere. *Journal of Geodesy* **73**:436–447.

Andritsanos VD, Sideris MG, Tziavos IN (2001) Quasi-stationary sea surface topography estimation by the multiple input/ output method. *Journal of Geodesy* **75**:216–226.

Arnold K (1969) Zur Konvergenz der Kugelfunktionsentwicklung für das Gravitationspotential der Erde im Außenraum der Erde. *Gerland's Beiträge zur Geophysik* **78**:369–372.

Arnold K (1978) Beweis der gleichmäßigen Konvergenz der Kugelfunktionsentwicklung für das Gravitationspotential der Erde im Außenraum. *Vermessungstechnik* **26**:222–226.

Bäschlin CF (1948) *Lehrbuch der Geodäsie.* Verlag Orell Füssli, Zürich.

Bendat JS, Piersol AG (1986) *Random Data – Analysis and measurement procedures.* Second edn., John Wiley & Sons, INC., New York, Chichester, Brisbane, Toronto, Singapore.

Bendat JS, Piersol AG (1993) *Engineering applications of correlation and spectral analysis.* Second edn., John Wiley & Sons, INC., New York, Chichester, Brisbane, Toronto, Singapore.

Björk A (1996) *Numerical Methods for Least-Squares Problems.* SIAM, Philadelphia.

Bouman J (1997) *A survey of global gravity models.* Technical Report 97.1, DEOS TU Delft, Delft University of Technology.

Bouman J (1998) *Quality of regularization methods.* Tech. Rep. 98.2, DEOS, Delft University Press, TU Delft, Delft.

Bouman J (2000) *Quality assessment of satellite-based global gravity field models.* Ph.D. thesis, DEOS, Delft University, TU Delft.

Bruton AM (2000) *Improving the accuracy and resolution of SINS/DGPS airborne gravimetry.* Phd thesis, Department of Geomatics Engineering, The University of Calgary.

URL `http://www.geomatics.ucalgary.ca/Papers/Thesis/KPS/00.20145.AMBruton.pdf`

Bruton AM, Hammada Y, Ferguson S, et al. (2002) A comparison of inertial platform, damped 2-axis platform and strapdown airborne gravimetry. In: G Lachapelle (ed.), *KIS Proceedings*, The University of Calgary, Department of Geomatics Engineering. On CD-Rom.

Burša M, Raděk K, Šima Z, et al. (1997) Determination of the geopotential scale factor from TOPEX/POSEIDON satellite altimetry. *Studia geoph et geod* **41**:203–216.

Chen JY (1981) Formulae for computing ellipsoidal parameters. *Bulletin Géodésique* **55**:170–178.

Colombo OL (1981) *Numerical methods for harmonic analysis on the sphere*. Technical Report 310, Department of Geodetic Science and Surveying, The Ohio State University, Columbus, Ohio.

Czombo J, Ferguson S (1995) Design considerations for a new scalar gravity meter for airborne surveys. In: KP Schwarz (ed.), *IAG Symposium G4 Airborne gravity field determination*, XXI General Assembly of the IUGG, pp. 13–21, Published by The University of Calgary, Boulder Colorado.

Denker H (1988) *Hochauflösende regionale Schwerefeldbestimmung mit gravimetrischen und topographischen Daten*. Ph.D. thesis, Universität Hannover, Hannover.

Dermanis A (1977) Geodetic linear estimation techniques and the norm choice problem. *Manuscripta Geodaetica* **2**:15–97.

Ecker E, Mittermayer E (1969) Gravity corrections for the influence of the atmosphere. *Bolletino di Geofisica Teorica et Applicata* **11**:70–80.

Ekstrom MP, Rhodes RL (1974) On the application of eigenvector expansion to numerical deconvolution. *J Comp Phys* **14**:319–340.

Engl H, Hanke M, Neubauer A (1996) *Regularization of inverse problems*. Kluwer Academic Press.

ESA (1999) *Gravity field and steady-state ocean circulation explorer*. Tech. Rep. Reports for Mission Selection. The Four Candidate Earth Core Missions. ESA SP-1233(1), ESA, Publications Division, ESTEC, Noordwijk.

Evans JD, Featherstone WE (2000) Improved convergence rates for the truncation error in gravimetric geoid determination. *Journal of Geodesy* **74**:239–248.

Featherstone W (2002) Downloadable synthetic gravity fields. International Association of Geodesy's Special Study Group 3.177.
URL `http://www.cage.curtin.edu.au/~will/ssgres.html`

Featherstone WE, Evans JD, Olliver JG (1998) A Meissl-modified Vaníček and Kleusberg kernel to reduce the truncation error in gravimetric geoid computations. *Journal of Geodesy* **72**:154–160.

Forsberg R, Madsen F (1990) High-precision geoid heights for GPS levelling. In: *Proceedings of the 2nd International Symposium on Precise Positioning with the Global Positioning System*, pp. 1060–1074, Ottawa, Canada.

Forsberg R, Tscherning CC (1981) The use of height data in gravity field approximation by collocation. *Journal of Geophysical Research* **86**(B9):7843–7854.

Freeden W, Gervens T, Schreiner M (1994) Tensor spherical harmonics and tensor spherical splines. *Manuscripta Geodaetica* **19**:70–100.

Freeden W, Gervens T, Schreiner M (1998) *Constructive approximation on the sphere.* Clarendon press, Oxford.

Freeden W, Windheuser U (1997) Combined spherical harmonic and wavelet expansion – a future concept in earth's gravitational determination. *Applied and computational harmonic analysis* **4**(960192):1–37.

van Gelderen M, Rummel R (2001) The solution of the general geodetic boundary value problem by least squares. *Journal of Geodesy* **75**:1–11.

Glennie CL (1999) *An analysis of airborne gravity by strapdown INS/GPS*. PhD thesis, Department of Geomatics Engineering, UCGE Report No. 20125, The Unversity of Calgary.

Glennie CL, Schwarz KP, Bruton AM, et al. (2000) A comparison of stable platform and strapdown airborne gravity. *Journal of Geodesy* **74**(5):383–389.

Golub G, Heath M, Wahba G (1979) Generalized cross-validation as a method for choosing a good ridge parameter. *Technometrics* **21**(2):215–223.

Golub G, van Loan C (1996) *Matrix Computations.* Third edn., The John Hopkins University Press, Baltimore, Maryland.

Grafarend EW (2001) The spherical horizontal and spherical vertical boundary value problem - vertical deflections and geoidal undulations - the complete Meissl diagram. *Journal of Geodesy* **75**:363–390.

Grafarend EW, Ardalan AA (1999) World geodetic datum 2000. *Journal of Geodesy* **73**:611–623.

Grafarend EW, Engels J (1994) The convergent series expansion of the gravity field of a starshaped body. *Manuscripta Geodaetica* **19**:18–30.

Grafarend EW, Schaffrin B (1993) *Ausgleichungsrechnung in linearen Modellen.* Wissenschaftsverlag, Mannheim, Leipzig, Wien, Zürich.

Groetsch CW (1984) *The theory of Tikhonov regularization for Fredholm integral equations of the first kind.* Pitman.

Haagmans RHN (2000) A synthetic Earth for use in geodesy. *Journal of Geodesy* **74**:503–511.

Haagmans RHN, van Gelderen M (1991) Error variances-covariances of GEM-T1: Teir characteristics and implications in geoid computation. *Journal of Geophysical Re-*

search **96**(B12):20 011–20 022.

Hadamard J (1923) *Lectures on Cauchy's Problem in Linear Parial Differential Equations*. Yale University Press, New Haven.

Hagiwara Y (1976) A new formula for evaluating the truncation error coefficients. *Bulletin Géodésique* **50**:131–135.

Haines GV (1985) Spherical cap harmonic analysis. *Journal of geophysical research* **90**(B3):2583–2591.

Hammada Y (1996) *A comparison of filtering techniques for airborne gravimetry*. Master thesis, Department of Geomatics Engineering, UCGE Report No. 20089, The Unversity of Calgary.

Hanke M (1995) *Conjugate gradient type methods for ill-posed problems*. Pitman Research Notes in Mathematics Series, Longman Scientific & Technical, Harlow, Essex, UK.

Hansen PC (1990) The discrete Picard condition for discrete ill-posed problems. *BIT* **30**:658–672.

Hansen PC (1994) *Regularization Tools Version 3.1 (for Matlab Version 6.0): A Matlab package for analysis and solution of discrete ill-posed problems*. Department of Mathematical Modelling, Technical University of Denmark, 3.1 edn.
URL `http://www.imm.dtu.dk/~pch/Regutools/index.html`

Hansen PC (1998) *Rank-deficient and discrete ill-posed problems*. SIAM lecture notes, Philadelphia.

Heck B (1979) *Zur lokalen Geoidbestimmung aus terrestrischen Messungen vertikaler Schweregradienten*. Ph.D. thesis, Deutsche Geodätische Kommission, Reihe C, No. 259.

Heck B (1990) An evaluation of some systematic error sources affecting the terrestrial gravity anomalies. *Bulletin Géodésique* **64**:88–108.

Heck B (1992) A revision of Helmert's second method of condensation in the geoid and quasigeoid determination. In: *Proceedings of the 7th Int. Symp. Geodesy and Physics of the Earth, IAG Symposia No. 112*, pp. 246–251, Springer Verlag.

Heck B (2001) On the use and abuse of Helmert's second method of condensation. In: J Adam, KP Schwarz (eds.), *Vistas for Geodesy in the New Millenium*, International Association of Geodesy Symposia. Vol. 125, pp. 144–149, Springer Verlag.

Heck B (2002) On Helmert's methods of condensation. *Accepted by the Journal of Geodesy* .

Heck B, Grüninger W (1987) Modification of Stokes' integral formula by combining two classical approaches. In: *Proceedings of the IAG Symposia on Advances in Gravity Field Modelling, XIX IUGG General Assembly*, pp. 319–337, Vancouver, Canada.

Heiskanen WA, Moritz H (1967) *Physical Geodesy*. Freeman and Company, San Francisco.

Helmert FR (1884) *Die mathematischen und physikalischen Theorien der höheren Geodäsie*. B.G. Teubner, Leipzig.

Hestenes MR, Stiefel E (1952) Methods of conjugate gradients for solving linear systems. *J Res Bur Standards* **49**:409–436.

Hobson EW (1931) *The theory of spherical and ellipsoidal harmonics*. Cambridge University Press, Cambridge, England.

Hoerl A, Kennard R (1970) Ridge regression: biased estimation for nonorthogonal problems. *Technometrics* **12**:55–67.

Hofmann B (1993) *On the ill-posedness of nonlinear problems*. Tech. Rep. Preprint No. A-17, Freie Universität Berlin, Fachbereich Mathematik.

Holmes SA, Featherstone WE (2002) A unified approach to the Clenshaw summation and the recursive computation of very high degree and order normalised associated Legendre functions. *Journal of Geodesy* **76**(5):279–299.

Holota P (1995) Boundary and initial value problems in airborne gravimetry. In: KP Schwarz, JM Brozena, GH Hein (eds.), *Proceedings of the IAG Symposium on Airborne Gravity Field Determination at the IUGG XXI General Assembly*, pp. 67–71, The University of Calgary, Department of Geomatics Engineering, Boulder, Colorado, USA.

Huang J (2002) *Computational methods for the discrete downward continuation of the Earth gravity and effects of lateral topographical mass density variations on gravity and the geoid*. Ph.D. thesis, Department of Geodesy and Geomatics Engineering The University of New Brunswick, Fredericton, New Brunswick.

Hwang C (1993) Spectral analysis using orthonormal functions with a case study on the sea surface topography. *Geophysical Journal International* **115**:1148–1160.

IAG (1967) Geodetic reference system 1967. *Publication Speciale du Bulletin Geodesique* **1**.

Ilk KH (1993) Regularization for high resolution gravity field recovery by future satellite techniques. In: *Inverse Problems: Principles and Applications in Geophysics, Technology and Medicine*, pp. 189–214.

Jekeli C (1978) *An investigation of two models for the degree variances of global covariance funcitons*. Tech. Rep. No. 275, Ohio State University, Department of Geodetic Science, Columbus, Ohio.

Jekeli C (1980) *Reducing the error of geoid undulation computations by modified Stokes' function*. Tech. Rep. No. 301, Ohio State University, Department of Geodetic Science and Surveying, Columbus, Ohio.

Jekeli C (1996) Spherical harmonic analysis, aliasing and filtering. *Journal of Geodesy* **70**:214–223.

Kaula WM (1966) Test and combinations of satellite determinations of the gravity field with gravimetry. *Journal of Geophysical Research* **71**:5303–5314.

Kearsley AHW (1988) Tests on the recovering of precise geoid height differences from gravimetry. *Journal of Geophysical Research* **93**(B6):6559–6570.

Kearsley AHW, Forsberg R (1990) Tailored geopotential models – application and shortcomings. *Manuscipta Geodaetica* **15**:151–158.

Kellogg OD (1929) *Foundations of potential theory*. reprint 1967 edn., Springer, Berlin.

Kern M, Schwarz KP (2001) A comparison of direct and indirect numerical methods for the downward continuation of airborne gravity data. In: J Adam, KP Schwarz (eds.), *Vistas for Geodesy in the New Millenium*, International Association of Geodesy Symposia. Vol. 125, pp. 242–247, Springer Verlag.

Kern M, Schwarz KP, Sneeuw N (2003) A study on the combination of satellite, airborne and terrestrial gravity data. *Accepted by the Journal of Geodesy* .

Kotsakis C (2000) *Multiresolution aspects of linear approximation methods in Hilbert spaces using gridded data*. PhD thesis, UCGE report, Department of Geomatics Engineering. The University of Calgary, Calgary, Alberta, Canada. URL `http://www.geomatics.ucalgary.ca/Papers/Thesis/MGS/00.20138.CKotsakis.pdf`

Krarup T (1969) *A contribution to the mathematical foundation of physical geodesy*. Tech. Rep. Meddelelse No. 44, Geodætisk institut, København, Danemark.

Kress R (1989) *Linear integral equations*. Springer Verlag, Berlin, Heidelberg, New York.

Kuhn M (2000) *Geoidbestimmung unter Verwendung verschiedener Dichtehypothesen*. Ph.D. thesis, Deutsche Geodätische Kommission, Reihe C, No. 520.

Kusche J (2002) Inverse Probleme bei der Gravitationsfeldbestimmung mittels SST- und SGG-Satellitenmissionen. Habilitationsschrift. Deutsche Geodätische Kommission, Reihe C. No. 548.

Kusche J, Klees R (2002) Regularization of gravity field estimation from satellite gravity gradients. *Journal of Geodesy* **76**:359–368.

Lanczos C (1950) An iteration method for the solution of the eigenvalue problem of linear differential and integral equations. *J Res Nat Bur Standards* **45**:255–282.

Lemoine FG, Kenyon SC, Factor JK, et al. (1998) *The development of the joint NASA GSFC and NIMA geopotential model EGM96*. Tech. rep., NASA-TP-1998-206861.

Lense J (1954) *Kugelfunktionen*. Akademische Verlagsgesellschaft, second edn., Geest and Portig K.-G., Leipzig.

Li J, Sideris MG (1997) Marine gravity and geoid determination by optimal combination of satellite altimetry and shipborne gravimetry data. *Journal of Geodesy* **71**(4):209–216.

Li YC, Sideris MG (1994) Minimization and estimation of geoid undulation errors. *Bulletin Géodésique* **68**:201–219.

Louis A (1988) *Inverse und schlecht gestellte Probleme*. Teubner Verlag, Stuttgart.

MacMillan WD (1930) *The theory of the potential*. reprinted 1958 edn., Dover, New York.

Martinec Z (1993) *Effect of lateral density variations of topographical masses in view of improving geoid model accuracy over Canada*. Tech. rep., Contract report for the Geodetic Survey Division, Natural Resources Canada.

Martinec Z (1996) Stability investigations of a discrete downward continuation problem for geoid determination in the Canadian Rocky Mountains. *Journal of Geodesy* **70**:805–828.

Martinec Z (1998) *Boundary-value problems for gravimetric determination of a precise geoid*, vol. 73. Lecture notes in Earth sciences, Springer Verlag, Heidelberg, New York, Berlin.

Martinec Z, Vaníček P (1994a) Direct topographical effect of Helmert's condensation for a spherical approximation of the geoid. *Manuscripta Geodaetica* **19**:257–268.

Martinec Z, Vaníček P (1994b) Indirect effect of topography in the Stokes-Helmert technique for a spherical approximation of the geoid. *Manuscripta Geodaetica* **19**:213–219.

Meissl P (1971a) *Preparation for the numerical evaluation of second order Molodensky-type formulas*. Tech. Rep. No. 163, Ohio State University, Department of Geodetic Science and Surveying, Columbus, Ohio.

Meissl P (1971b) *A study of covariance functions related to the Earth's disturbing potential*. Tech. Rep. No. 151, Ohio State University, Department of Geodetic Science and Surveying, Columbus, Ohio.

de Min EJ (1996) *De geoïde voor Nederland*. Ph.D. thesis, Technische Universiteit Delft.

Molodenskij MS (1958) *Grundbegriffe der geodätischen Gravimetrie*. VEB Verlag Technik, Berlin.

Moritz H (1961) Über die Konvergenz der Kugelfunktionsentwicklung für das Außenraumpotential an der Erdoberfläche. *Zeitschrift für das Vermessungswesen* **49**:11–15.

Moritz H (1966) Methods for downward continuation of gravity. Deutsche Geodätische Kommission. Reihe A. No. 75.

Moritz H (1975) *Integral formulas and collocation*. Tech. Rep. 234, The Ohio State University, Department of Geodetic Science, Columbus, Ohio.

Moritz H (1978) *Statistical foundation of collocation*. Tech. Rep. No. 272, The Ohio State University, Department of Geodetic Science, Columbus, Ohio.

Moritz H (1980a) Geodetic reference system 1980. *Bulletin Géodésique* **54**:395–405.

Moritz H (1980b) Statistical foundations of collocation. *Bollettino di geodesia e scienze* *affini* **XXXIX**(2):131–186.

Moritz H (1989) *Advanced physical geodesy.* Second edn., Wichmann Verlag, Karlsruhe.

Moritz H, Sansò F (1980) A dialogue on collocation. *Bolletino di geodesia e scienze affini* **XXXIX**(2):49–51.

Nahavandchi H, Sjöberg LE (1998) Terrain corrections of the power h^3 in gravimetric geoid determination. *Journal of Geodesy* **72**:124–135.

Novák P (2000) *Evaluation of gravity data for the Stokes-Helmert solution to the geodetic boundary-value problem.* Ph.D. thesis, Department of Geodesy and Geomatics Engineering The University of New Brunswick, Fredericton, New Brunswick.

Novák P, Heck B (2002) Downward continuation and geoid determination based on band-limited airborne gravity data. *Journal of Geodesy* **76**:269–278.

Novák P, Kern M, Schwarz KP (2001a) Numerical studies on the harmonic downward continuation of band-limited airborne gravity. *Studia Geophysica et Geodaetica* **45**:327–345.

Novák P, Kern M, Schwarz KP, Heck B (2001b) *The determination of the geoid from airborne gravity data.* Tech. Rep. UCGE No. 30013, Department of Geomatics Engineering, Calgary.

Novák P, Kern M, Schwarz KP, Heck B (2003a) Evaluation of band-limited topographical effects in airborne gravimetry. *Journal of Geodesy* **76**(11-12):597–604.

Novák P, Kern M, Schwarz KP, et al. (2003b) On geoid determination from airborne gravity. *Journal of Geodesy* **76**(9-10):510–522.

Novák P, Vaníček P, Véronneau M, et al. (2001c) On the accuracy of Stokes's integration in the precise high-frequency geoid determination. *Journal of Geodesy* **74**:644–654.

NRC (1997) *Satellite gravity and the geosphere – contributions to the study of the solid Earth and its fluid envelope.* Tech. rep., National Academic Press, Committee on Earth Gravity from Space, U.S. Geodynamics Committee, Board on Earth Sciences and Resources, Commission on Geosciences, Environment and Resources, Washington, D. C.
URL `http://books.nap.edu/books/0309057922/html/R1.html#pagetop`

Oppenheim AV, Schafer RW, Buck JR (1999) *Discrete-time signal processing.* Second edn., Prentice Hall, New Jersey.

Pail R (2000) *Synthetic global gravity model for planetary bodies and applications in satellite gravity gradiometry.* Dissertation, Mitteilungen der geodätischen Institute der Technischen Universität Graz, Graz, Austria.
URL `http://www.cis.tugraz.at/mggi/pail_diss.html`

Paul M (1973) A method of evaluation the truncation errors coefficients for geoidal heights. *Bulletin Géodésique* **110**:413–425.

Pavlis NK (1988) *Modeling and Estimation of a low degree geopotential model from* *terrestrial gravity data*. Phd Thesis no. 386, Department of Geodetic Science and Surveying, The Ohio State University, Columbus, Ohio.

Pellinen LP (1969) Joint adjustment of gravimetric and satellite data in the determination of the Earth's gravitational field. *Byull Sta Opt Nablyudeniya ISkusstv Sputnikov Zemli* **55**:58–68.

Phillips DL (1962) A technique for the numerical solution of certain integral equations of the first kind. *J Assoc Comput Mach* **9**:84–97.

Rapp RH (1967) Analytical and numerical differences between two methods for the combination of gravimetric and satellite data. *Bollettino di Geofisica Teorica ed Applicata* **9**(41-42):108–118.

Rapp RH (1972) *The geopotential coefficient behaviour to high degree and geoid height information by wavelength*. Tech. Rep. No. 180, The Ohio State University, Department of Geodetic Science, Ohio, Columbus.

Rapp RH (1979) *Potential Coefficient and Anomaly Degree Variance Modelling Revisited*. Tech. Rep. No. 293, The Ohio State University, Department of Geodetic Science, Columbus, Ohio.

Rapp RH (1983) Report of SSG no. 5.39 of IAG fundamental geodetic constants. Paper presented to the 18th IUGG General Assembly, Hamburg.

Rapp RH, Rummel R (1975) *Methods for the computation of the detailed geoids and their accuracy*. Tech. Rep. No. 233, The Ohio State University, Department of Geodetic Science, Columbus, Ohio.

Rauhut A (1992) *Regularization methods for the solution of the inverse Stokes problem*. Ph.D. thesis, Department of Geomatics Engineering, The University of Calgary.

Reigber C, Balmino G, Schwintzer P, et al. (2002a) A high quality global gravity field model from CHAMP GPS tracking data and accelerometry (EIGEN-1S). *Geophysical Research Letters* **29**(14):10.1029/2002GL015 064.

Reigber C, Schwintzer P, Neumayer KH, et al. (2002b) The CHAMP-only EIGEN-2 earth gravity field model. *submitted to Advances in Space Research* .

Rummel R, van Gelderen M (1992) Spetral analysis of the full gravity tensor. *Geophysical Journal International* **111**:159–169.

Rummel R, van Gelderen M (1995) Meissl scheme – spectral characteristics of physical geodesy. *Manuscripta Geodaetica* **20**:379–385.

Rummel R, Rapp RH, Sünkel H, Tscherning CC (1988) *Comparisons of global topographic/isostatic models to the Earth's observed gravity field*. Technical Report 388, Department of Geodetic Science and Surveying, The Ohio State University, Columbus, Ohio.

Rummel R, Schwarz KP, Gerstl M (1979) Least squares collocation and regularization. *Bulletin Géodésique* **53**:343–361.

Rummel R, Teunissen P (1988) Height datum definition, height datum connection and the role the geodetic boundary value problem. *Bulletin Géodésique* **62**(4):477–498.

Sacerdote F, Sansò F (1987) New developments of boundary value problems in physical geodesy. In: *Proceedings of the IAG Symposia on Advances in Gravity Field Modelling, XIX IUGG General Assembly*, pp. 369–390, Vancouver, Canada.

Sansò F (1980) The minimum mean square estimation error principle in physical geodesy (stochastic and non-stochastic interpretation). *Bolletino di geodesia e scienze affini* **2**:112–129.

Sansò F, Sideris MG (1997) On the similarities and differences between system theory and least-square collocation in physical geodesy. *Bolletino di geodesia e scienze affini* **2**:173–205.

Sansò F, Tscherning CC (1980) Notes on convergence in collocation theory. *Bolletino di geodesia e scienze affini* **39**:221–252.

de Santis A (1991) Translated origin spherical cap harmonic analysis. *Geophysical Journal International* **106**:253–263.

de Santis A (1992) Conventional spherical harmonic analysis for regional modelling of the geomagnetic field. *Geophysical Research Letters* **19**(10):1065–1067.

Schneider F (1997) *Inverse problems in satellite geodesy and their approximate solution by splines and wavelets.* PhD Thesis, University of Kaiserslautern, Fachbereich Mathematik, No. D386, Shaker Verlag, Kaiserslautern, Germany.

Schuh WD (1996) *Tailored numerical solution strategies for the global determination of the earth's gravity field.* Tech. Rep. 81, Technische Universität Graz, Graz, Austria.

Schwarz KP (1971) *Numerische Untersuchungen zur Schwerefortsetzung.* Ph.D. thesis, Deutsche Geodätische Kommission, Reihe C, No. 171, München.

Schwarz KP (1973) *Investigations on the downward continuation of aerial gravity data.* Technical Report 204, The Ohio State University, Department of Geodetic Science, Columbus, Ohio.

Schwarz KP (1979) Geodetic improperly posed problems and their regularization. *Bolletino di geodesia e scienze affini* **38**:389–416.

Schwarz KP (1984) Data types and their spectral properties. In: KP Schwarz (ed.), *Proceedings of the Beijing International summer school on local gravity field approximation*, pp. 1–66, China.

Schwarz KP (1986) Problems in estimating the anomalous gravity potential of the earth from discrete spatial data. *Contemporary Mathematics* **59**:77–96.

Schwarz KP, Lachapelle G (1980) Local characteristics of the gravity anomaly covariance function. *Bulletin Géodésique* **54**:21–36.

Schwarz KP, Li YC (1996) What can airborne gravimetry contribute to geoid determination? *Journal of Geophysical Research* **101**(B8):17 873–17 881.

Schwarz KP, Li Z (1997) An introduction to airborne gravimetry and its boundary value problems. In: F Sansò, R Rummel (eds.), *Geodetic boundary value problems in view of the one centimeter geoid*, pp. 312–358, Springer-Verlag.

Schwarz KP, Sideris MG, Forsberg R (1990) The use of FFT techniques in physical geodesy. *Journal of Geophysical Research* **100**:485–514.

Seeber G (1993) *Satellite Geodesy*. Walter de Gruyter, Berlin, New York.

Sideris MG (1987) *Spectral methods for the numerical solution of Molodensky's problem*. Ph.D. thesis, Department of Geomatics Engineering, The University of Calgary.

Sideris MG (1996) On the use of heterogeneous noisy data in spectral gravity field modeling methods. *Journal of Geodesy* **70**:470–479.

Sideris MG, Forsberg R (1991) Review of geoid prediction methods in mountainous regions. In: RH Rapp, F Sansò (eds.), *IAG Symposium No. 106 "Determination of the geoid: present and future"*, pp. 51–62.

Sjöberg LE (1980) A recurrence relation for the β_n function. *Bulletin Géodésique* **54**:69–72.

Sjöberg LE (1986) Comparison of some methods of modifying Stokes' formula. In: *Proceedings of the International Symposium on the Definition of the Geoid*, vol. 2, pp. 577–597, IAG, Florence, Italy.

Sjöberg LE (2000) Topographic effects by the Stokes-Helmert method of geoid and quasi-geoid determinations. *Journal of Geodesy* **74**:255–268.

Sjöberg LE, Hunegnaw A (2000) Some modifications of Stokes' formula that account for truncation and potential coefficient errors. *Journal of Geodesy* **74**:232–238.

Smeets I (1994) An error analysis for the height anomaly determined by combination of mean terrestrial gravity anomalies and a geopotential model. *Bolletino di geodesia e scienze affini* **III**(1):84–96.

Sneeuw N (1994) Global spherical harmonic analysis by least-squares and numerical quadrature methods in historical perspective. *Geophysical Journal International* **118**:707–716.

Sneeuw N (2000) *A semi-analytical approach to gravity field analysis from satellite observations*. Ph.D. thesis, TU München, Deutsche Geodätische Kommission, Reihe C, No. 527.

Strand ON (1974) Theory and methods related to the singular-function expansion and Landweber's iteration for integral equations of the first kind. *SIAM J Numer Anal* **11**:798–825.

Sünkel H (1978) *Approximation of covariance functions by non-positive definite functions*. Tech. Rep. No.271, The Ohio State University, Department of Geodetic Science, Columbus, Ohio.

Sünkel H (1979) *A covariance approximation procedure*. Tech. Rep. No.286, The Ohio

State University, Department of Geodetic Science, Columbus, Ohio.

Sünkel H (1985) *An isostatic Earth model.* Technical Report No. 367, The Ohio State University, Department of Geodetic Science and Surveying, Columbus, Ohio.

Sünkel H (1986) Global topographic-isostatic models. In: H Sünkel (ed.), *Mathematical and numerical techniques in physical geodesy*, pp. 417–462, Springer Verlag, Berlin, Heidelberg, New York.

Svensson SL (1983) Solution of the alimetry-gravimetry problem. *Bulletin Géodésique* **57**:332–353.

Tikhonov AN (1963) Solution for incorrectly formulated problems and the regularization method. *Soviet Math Dokl* **4**:1035–1038.

Tikhonov AN, Arsenin VY (1977) *Solutions of ill-posed problems.* V. H. Winston and Sons; A Halsted Press Book, New York, Toronto, London, Syndey.

Torge W (2001) *Geodesy.* Wolfgang de Gruyter, Berlin, New York.

Tscherning CC, Rapp R (1974) *Closed covariance expressions for gravity anomalies, geoid undulations, and deflections of the vertical implied by anomaly degree variance models.* Tech. Rep. No. 208, The Ohio State University, Department of Geodetic Science, Columbus, Ohio.

Tsoulis D (2001) A comparison between the Airy/Heiskanen and the Pratt/Hayford isostatic models for the computation of potential harmonic coefficients. *Journal of Geodesy* **74**:637–643.

Vaníček P, Featherstone WE (1998) Performance of three types of Stokes's kernel in the combined solution for the geoid. *Journal of Geodesy* **72**:684–697.

Vaníček P, Huang J, Novák P, et al. (1999) Determination of the boundary values for the Stokes-Helmert problem. *Journal of Geodesy* **73**:180–192.

Vaníček P, Kleusberg A (1987) The Canadian geoid – Stokesian approach. *Manuscripta Geodaetica* **12**:86–98.

Vaníček P, Najafi M, Martinec Z, et al. (1995) Higher-degree reference field in the generalized Stokes-Helmert scheme for geoid determination. *Journal of Geodesy* **70**:176–182.

Vaníček P, Sjöberg LE (1991) Reformulation of Stokes's theory for higher than second-degree reference field and a modification of integration kernels. *Journal of Geophysical Research* **96(B4)**:6529–6539.

Vaníček P, Sun W, Martinec Z, et al. (1996) Downward continuation of Helmert's gravity. *Journal of Geodesy* **71**:21–34.

Vassiliou AA (1986) *Numerical techniques for processing airborne gradiometer data.* Ph.D. thesis, Department of Geomatics Engineering, The University of Calgary.

Verhagen S (2000) Time variations in the gravity field – the effect of the atmosphere. Diploma thesis at the TU Delft (unreleased).

Véronneau M (2001) *The Canadian Gravimetric Geoid Model of 2000 (CGG2000)*. Technical report, Natural Resources Canada, Geodetic Survey Division Natural Resources Canada, Ottawa, Ontario.
URL `www.geod.emr.ca/index_e/products_e/publications_e/papers_e/CGG2000a.pdf`

Véronneau M (2003) Email communication.

Vinod HD, Ullah A (1981) *Recent advances in regression methods*. Dekker, New York.

Wahba G (1977) Practical approximate solutions to linear operator equations when the data are noisy. *SIAM Journal of Numerical Analysis* **14**(9):651–667.

Wahba G (1990) *Spline models for observational data*. SIAM, Philadelphia.

Wahr J, Molenaar M, Bryan F (1998) Time variability of the Earth's gravity field: Hydological and oceanic effects and their possible detection using GRACE. *Journal of Geophysical Research* **103**(B12):30 205–30 229.

Wang YM, Rapp RH (1990) Terrain effects on geoid undulation computations. *Manuscripta Geodaetica* **15**:23–29.

Weber G, Zomorrodian H (1988) Regional geopotential model improvement for the Iranian geoid determination. *Bulletin Géodésique* **62**:125–141.

Wei M (1986) *Statistische Probleme bei der Kollokation*. Ph.D. thesis, Technische Universität Graz, Austria.

Wenzel HG (1981) Zur Geoidbestimmung durch Kombination von Schwereanomalien und einem Kugelfunktionsmodell mit Hilfe von Integralformeln. *Zeitschrift für Vermessungswesen* **3**:102–111.

Wenzel HG (1982) Geoid computation by least-squares spectral combination using integral kernels. In: *Proceedings of the general IAG meeting*, pp. 438–453, Tokyo.

Wenzel HG (1985) Hochauflösende Kugelfunktionsmodelle für das Gravitationspotential der Erde. Habilitationsschrift. Wissenschaftliche Arbeiten der Fachrichtung Vermessungswesen der Universität Hannover. No. 137.

Wenzel HG (1998a) Collection of geopotential models, including ultra high degree geopotential models GPM98A, GPM98B and GPM98C to degree 1800.
URL `http://www.gik.uni-karlsruhe.de/~wenzel/geopmods.htm`

Wenzel HG (1998b) Ultra high degree geopotential models GPM98A, GPM98B and GPM98C to degree 1800.
URL `http://www.gik.uni-karlsruhe.de/~wenzel/gpm98abc/gpm98abc.htm`

Wichiencharoen C (1982) *The indirect effect on the computation of geoidal undulations*. Tech. Rep. No. 336, The Ohio State University, Department of Geodetic Science, Ohio, Columbus.

Wichiencharoen C (1984) A comparison of gravimetric undulations computed by the modified Molodenskij truncation method and the method of least squares spectral combination by optimal integral kernels. *Bulletin Géodésique* **58**:494–509.

Wong JCF (2000) On Picard criterion and the well-posed nature of harmonic downward continuation. Masterthesis, Department of Geodesy and Geomatics Engineering, The University of New Brunswick.

Wong L, Gore R (1969) Accuracy of geoid heights from modified Stokes kernels. *Geophys Journ R astr Society* **18**:81–91.

Xu P, Rummel R (1994) Generalized ridge regression with applications in determination of potential fields. *Manuscripta Geodaetica* **20**:8–20.

A Tables and Properties

Table A.1: Quality measures for $x \in \mathbb{R}^n$

Name	Formula	Remark/Abbreviation
L_1 norm	$\sum_{i=1}^{n} \lvert x_i \rvert = \lvert x_1 \rvert + \cdots + \lvert x_n \rvert$	$\lVert \boldsymbol{x} \rVert_1$
L_2 norm	$\sqrt{\sum_{i=1}^{n} x_i^2} = \left(\lvert x_1 \rvert^2 + \cdots + \lvert x_n \rvert^2 \right)^{\frac{1}{2}}$	Euclidian norm $\lVert \boldsymbol{x} \rVert_2$
L_∞ norm	$\max_{i=1}^{n} \lvert x_i \rvert$	$\lVert \boldsymbol{x} \rVert_\infty$
Absolute error	$\lVert \hat{\boldsymbol{x}} - \boldsymbol{x} \rVert$	$\hat{\boldsymbol{x}}$ = estimate
Relative error	$\frac{\lVert \hat{\boldsymbol{x}} - \boldsymbol{x} \rVert}{\lVert \boldsymbol{x} \rVert}$	$\boldsymbol{x} \neq 0$
Mean	$\frac{1}{n} \sum_{i=1}^{n} x_i$	$\bar{x}$
Standard Deviation	$\sqrt{\frac{1}{n-1} \sum_{i=1}^{n} (x_i - \bar{x})^2}$	STD
Root mean square	$\sqrt{\frac{1}{n} \sum_{i=1}^{n} x_i^2} = \frac{\lVert \boldsymbol{x} \rVert_2}{\sqrt{n}}$	RMS

A.1 Filter Window Functions

Low-pass filters are often used in gravity field modeling. For convenience, some of the most common filter window functions are given in Table A.2, see also Hammada (1996). The input data $\boldsymbol{x}$ is filtered with the linear, non-recursive, algorithm

$$y_i = \sum_{k=-M}^{M} w_k h_k x_{i-k}$$

where y_i is the Finite Impulse Response (FIR) filtered output data at the i-th epoch and h_k are the filter impulse response coefficients given as (Oppenheim et al., 1999)

$$\begin{aligned} h_k &= \frac{T}{\pi} \int_0^{\frac{\pi}{T}} H(j\omega) \cos(k\omega T)\ d\omega \\ &= \frac{\omega_\mathrm{c} T}{\pi} \frac{\sin(k\omega_\mathrm{c})T}{k\omega_\mathrm{c} T} \end{aligned}$$

where ω_c is the cut-off frequency [rad/s] and T is the sampling period [s]. $H(\omega)$ is the Fourier transform of the low-pass filter response. M is a selected integer, e.g. $M = 25$.

Table A.2: Filter window functions

Name	Formula for w_k
Bartlett	$\begin{cases} 1 - \frac{\lvert k\rvert}{M} & \lvert k\rvert \le M \\ 0 & else \end{cases}$
Blackman	$\begin{cases} 0.42 + 0.5\cos(\frac{\pi k}{M}) + 0.8\cos(\frac{2\pi k}{M}) & \lvert k\rvert \le M \\ 0 & else \end{cases}$
Hamming	$\begin{cases} 0.54 + 0.46\cos(\frac{\pi k}{M}) & \lvert k\rvert \le M \\ 0 & else \end{cases}$
Hanning	$\begin{cases} 0.5\left(1 + \cos(\frac{\pi k}{M})\right) & \lvert k\rvert \le M \\ 0 & else \end{cases}$
Rectangular	$\begin{cases} 1 & \lvert k\rvert \le M \\ 0 & else \end{cases}$

A.2 Degree Variance Models

Table A.3: Degree variance models (Wenzel, 1985, pg. 147)

Source	Anomaly degree variances [mGal^2]
Kaula (1966)	$(9.7983 \cdot 10^5)^2 (l-1)^2 \frac{1.6 \cdot 10^{-10}}{l^3}$
Rapp (1972)	$\frac{251.6468(l-1)}{(l-2)(l+12.9287+0.000715 l^2)}$
Tscherning & Rapp (1974)	$\frac{425.28(l-1)}{(l-2)(l+24)} 0.999617^{l+2}$
Jekeli (1978)	$\frac{18.3906(l-1)}{l+100} 0.9943667^{l+2} + \frac{658.6132(l-1)}{(l-2)(l+20)} 0.9048949^{l+2}$
Rapp (1979)	$\frac{3.404(l-1)}{l+1} 0.998006^{l+2} + \frac{140.03(l-1)}{(l-2)(l+2)} 0.914232^{l+2}$

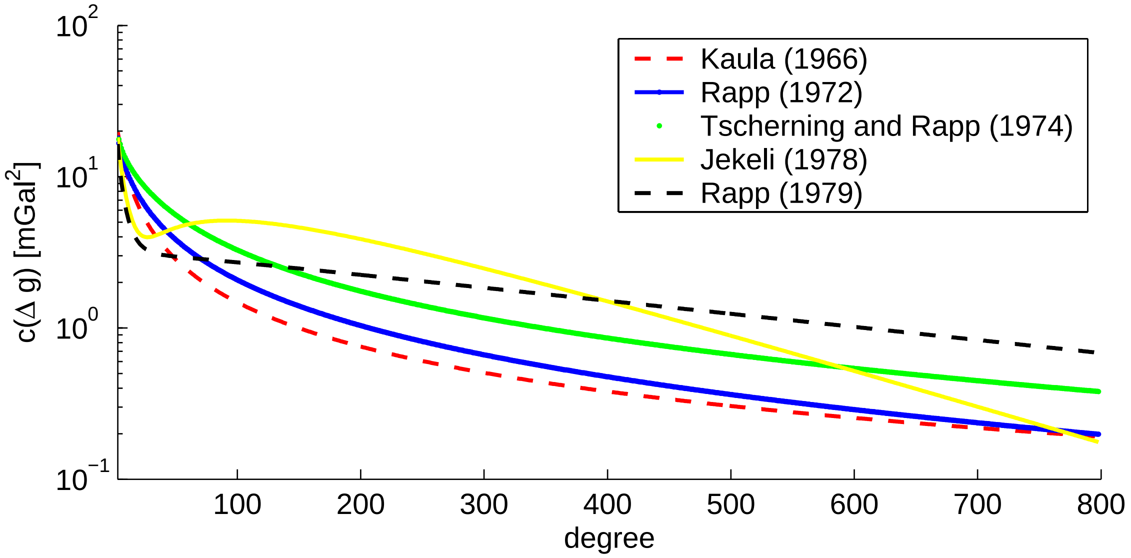

Figure A.1: Degree variance models

A.3 Removing the Singularity from the Stokes Kernel

The Stokes kernel function is singular for $\psi = 0$. This is mainly due to the term $\frac{1}{\sin(\psi/2)}$ in the spherical Stokes kernel. Molodenskij proposed to remove the singularity by adding and subtracting the gravity anomalies at the same point. The integration for the near-zone is then given as

$$\begin{aligned} N_{\omega_c}(\varphi,\lambda) &= \frac{R}{4\pi\gamma}\int\limits_{\omega_c} S(\psi)\Delta g'(\varphi,\lambda) + S(\psi)\big[\Delta g'(\varphi',\lambda') - \Delta g(\varphi,\lambda)\big]\; d\omega' \\ &= \frac{R\Delta g(\varphi,\lambda)}{2\gamma}\int\limits_{\psi=0}^{\psi_c} S(\psi)\sin\psi\; d\psi + \frac{R}{4\pi\gamma}\int\limits_{\omega_c} S(\psi)\big[\Delta g(\varphi',\lambda') - \Delta g(\varphi,\lambda)\big]\; d\omega' \end{aligned}$$

The singularity is removed because the second integration equals zero for $\psi = 0$, see also Martinec (1993). The second integration is then discretized using the mean-value theorem, i.e. the gravity data are mean values corresponding to N cells $\Delta\omega_k$ (Novák et al., 2001c)

$$\frac{R}{4\pi\gamma}\int\limits_{\omega_c} S(\psi)\big[\Delta g(\varphi',\lambda') - \Delta g(\varphi,\lambda)\big]\; d\omega' \approx \frac{R}{4\pi\gamma}\sum_{k=1}^{N} S(\psi_k)\big[\Delta g(\varphi_k,\lambda_k) - \Delta g(\varphi,\lambda)\big]\; \Delta\omega_k$$

The integration over the Stokes kernel is analytically calculated. Table A.4 summarizes the integration terms for the kernel functions discussed. The following abbreviation is used in Table A.4, see Paul (1973) and Hagiwara (1976)

$$R_{l,0} = -\int\limits_{\psi=0}^{\psi_c} P_l(\cos\psi)\sin\psi\; d\psi = \frac{P_{l+1}(\cos\psi_c) - P_{l-1}(\cos\psi_c)}{2l+1} \tag{A.1}$$

Also, the term Q_0 is used (Heiskanen & Moritz, 1967, pg. 263)

$$Q_0 = -4t + 5t^2 + 6t^3 - 7t^4 + (6t^2 - 6t^4)\ln t(1+t), \qquad t = \sin\frac{\psi_c}{2} \tag{A.2}$$

Table A.4: Stokes kernel functions ($L_{\mathrm{MD}} \leq L_{\mathrm{S}}$)

Kernel	$S(\psi) =$	$\int_{\psi=0}^{\psi_{\mathrm{c}}} S(\psi) \sin\psi \; d\psi =$
Spherical	$\frac{1}{\sin(\psi/2)} - 6\sin\frac{\psi}{2} + 1 - \cos\psi\left(5 + 3\ln(\sin\frac{\psi}{2} + \sin^2\frac{\psi}{2})\right)$	$-Q_0$
MO	$S_{\mathrm{spherical}}(\psi) - \sum_{n=0}^{L_{\mathrm{MD}}} \frac{2n+1}{2} r_n P_n(\cos\psi)$	$-Q_0 + \sum_{n=0}^{L_{\mathrm{MD}}} \frac{2n+1}{2} r_n R_{n,0}$
WG	$S_{\mathrm{spherical}}(\psi) - \sum_{n=2}^{L_{\mathrm{MD}}} \frac{2n+1}{n-1} P_n(\cos\psi)$	$-Q_0 + \sum_{n=2}^{L_{\mathrm{MD}}} \frac{2n+1}{n-1} R_{n,0}$
M	$S_{\mathrm{spherical}}(\psi) - S_{\mathrm{spherical}}(\psi_{\mathrm{c}})$	$-Q_0 + S_{\mathrm{spherical}}(\psi_{\mathrm{c}})(\cos\psi_{\mathrm{c}} - 1)$
JK	$S_{\mathrm{MO}}(\psi) - S_{\mathrm{MO}}(\psi_{\mathrm{c}})$	$-Q_0 + \sum_{n=0}^{L_{\mathrm{MD}}} \frac{2n+1}{2} r_n R_{n,0} + S_{\mathrm{MO}}(\psi_{\mathrm{c}})(\cos\psi_{\mathrm{c}} - 1)$
S	$S_{\mathrm{spherical}}(\psi) - \sum_{l=2}^{L_{\mathrm{S}}} \frac{2l+1}{l-1} P_l(\cos\psi)$	$-Q_0 + \sum_{l=2}^{L_{\mathrm{S}}} \frac{2l+1}{l-1} R_{l,0}$
HG	$S_{\mathrm{S}}(\psi) - S_{\mathrm{S}}(\psi_{\mathrm{c}})$	$-Q_0 + \sum_{l=2}^{L_{\mathrm{S}}} \frac{2l+1}{l-1} R_{l,0} + S_{\mathrm{S}}(\psi_{\mathrm{c}})(\cos\psi_{\mathrm{c}} - 1)$
VK	$S_{\mathrm{S}}(\psi) - \sum_{n=0}^{L_{\mathrm{MD}}} \frac{2n+1}{2} r_n P_n(\cos\psi)$	$-Q_0 + \sum_{l=2}^{L_{\mathrm{S}}} \frac{2l+1}{l-1} R_{l,0} + \sum_{n=0}^{L_{\mathrm{MD}}} \frac{2n+1}{2} r_n R_{n,0}$
FEO	$S_{\mathrm{VK}}(\psi) - S_{\mathrm{VK}}(\psi_{\mathrm{c}})$	$-Q_0 + \sum_{l=2}^{L_{\mathrm{S}}} \frac{2l+1}{l-1} R_{l,0} + \sum_{n=0}^{L_{\mathrm{MD}}} \frac{2n+1}{2} r_n R_{n,0} +$ $+ S_{\mathrm{VK}}(\psi_{\mathrm{c}})(\cos\psi_{\mathrm{c}} - 1)$

A.4 Abel-Poisson Kernel Modifications

Analogous to the Stokes integral, the (Abel-)Poisson integral can be modified. The integration is split into a near-zone and a far-zone. Furthermore, the near-zone is split again into the contribution of the computation point and the contribution of the rest of the cap. The respective formulas are derived in Martinec (1996). The Abel-Poisson kernel can be again modified by the modification principles described in Section 2.4. In this case, however, the modification coefficients r_n are dependent on the height. They are computed from minimizing the norm

$$\min_{r_n} \left\{ \int_{\psi_c}^{\pi} \left[K(r,\psi,\psi_{\mathrm{c}},R)\right]^2 \sin\psi \; d\psi \right\} \tag{A.3}$$

which becomes

$$\frac{\partial}{\partial r_n} \left\{ \int_{\psi_c}^{\pi} \left[K(r,\psi,\psi_{\mathrm{c}},R)\right] \right\} = 0 \qquad r_n \in \mathbb{R}^n \tag{A.4}$$

or $(m \leq l)$

$$\sum_{n=0}^{L_{\mathrm{MD}}} \frac{2n+1}{2} r_n(H,\psi_c) R_{n,m}(\psi_{\mathrm{c}}) = \int_{\psi_{\mathrm{c}}}^{\pi} K(r,\psi,R) P_m(\cos\psi) \sin\psi \; d\psi \tag{A.5}$$

All kernel modifications discussed are listed in Table A.5. Note that a substitution is made in Table A.5:

$$P_0 = \int_{\psi=0}^{\psi_{\mathrm{c}}} R\frac{r^2-R^2}{L^3} \sin\psi d\psi = \frac{(r^2-R^2)}{r} \left. \frac{1}{\sqrt{r^2+R^2-2rRx}} \right|_{x=\cos\psi_{\mathrm{c}}}^{1} = \frac{r+R}{r}\left(1-\frac{r-R}{L}\right)$$

This is the primitive function to the indefinite Abel-Poisson integral over ψ (Martinec, 1996). Also, the spatial distance L is given as

$$L = \sqrt{r^2+R^2-2Rr\cos\psi} \tag{A.6}$$

Table A.5: Abel-Poisson kernel functions ($L_{\mathrm{MD}} \leq L_{\mathrm{S}}$)

Kernel	$K(r,\psi,R) =$	$\int_{\psi=0}^{\psi_{\mathrm{c}}} K(r,\psi,R)\sin\psi \; d\psi =$
Spherical	$R\frac{r^2-R^2}{L^3} = \sum_{l=0}^{\infty}(2l+1)\left(\frac{R}{r}\right)^{l+1} P_l(\cos\psi)$	$\frac{r+R}{r}\left(1-\frac{r-R}{L}\right)$
MO	$K_{\mathrm{spherical}}(r,\psi,R) - \sum_{n=0}^{L_{\mathrm{MD}}}\frac{2n+1}{2}r_n(H,\psi_c)P_n(\cos\psi)$	$P_0 + \sum_{n=0}^{L_{\mathrm{MD}}}\frac{2n+1}{2}r_n(H,\psi_c)R_{n,0}$
WG	$K_{\mathrm{spherical}}(r,\psi,R) - \sum_{n=0}^{L_{\mathrm{MD}}}(2n+1)\left(\frac{R}{r}\right)^{n+1} P_n(\cos\psi)$	$P_0 + \sum_{n=0}^{L_{\mathrm{MD}}}(2n+1)\left(\frac{R}{r}\right)^{n+1} R_{n,0}$
M	$K_{\mathrm{spherical}}(r,\psi,R) - K_{\mathrm{spherical}}(r,\psi_{\mathrm{c}},R)$	$P_0 + K_{\mathrm{spherical}}(r,\psi_{\mathrm{c}},R)(\cos\psi_{\mathrm{c}}-1)$
JK	$K_{\mathrm{MO}}(r,\psi,R) - K_{\mathrm{MO}}(r,\psi_{\mathrm{c}},R)$	$P_0 + \sum_{n=0}^{L_{\mathrm{MD}}}\frac{2n+1}{2}r_n(H,\psi_c)R_{n,0} + K_{\mathrm{MO}}(r,\psi_{\mathrm{c}},R)(\cos\psi_{\mathrm{c}}-1)$
S	$K_{\mathrm{spherical}}(r,\psi,R) - \sum_{l=0}^{L_{\mathrm{S}}}(2l+1)\left(\frac{R}{r}\right)^{l+1} P_l(\cos\psi)$	$P_0 + \sum_{l=0}^{L_{\mathrm{S}}}(2l+1)\left(\frac{R}{r}\right)^{l+1} R_{l,0}$
HG	$K_{\mathrm{S}}(r,\psi,R) - K_{\mathrm{S}}(r,\psi_{\mathrm{c}},R)$	$P_0 + \sum_{l=0}^{L_{\mathrm{S}}}(2l+1)\left(\frac{R}{r}\right)^{l+1} R_{l,0} + K_{\mathrm{S}}(r,\psi_{\mathrm{c}},R)(\cos\psi_{\mathrm{c}}-1)$
VK	$K_{\mathrm{S}}(r,\psi,R) - \sum_{n=0}^{L_{\mathrm{MD}}}\frac{2n+1}{2}r_n(H,\psi_{\mathrm{c}})P_n(\cos\psi)$	$P_0 + \sum_{l=0}^{L_{\mathrm{S}}}(2l+1)\left(\frac{R}{r}\right)^{l+1} R_{l,0} + \sum_{n=0}^{L_{\mathrm{MD}}}\frac{2n+1}{2}r_n(H,\psi_{\mathrm{c}})R_{n,0}$
FEO	$K_{\mathrm{VK}}(r,\psi,R) - K_{\mathrm{VK}}(r,\psi_{\mathrm{c}},R)$	$P_0 + \sum_{l=0}^{L_{\mathrm{S}}}(2l+1)\left(\frac{R}{r}\right)^{l+1} R_{l,0} + \sum_{n=0}^{L_{\mathrm{MD}}}\frac{2n+1}{2}r_n(H,\psi_{\mathrm{c}})R_{n,0}$ $+K_{\mathrm{VK}}(r,\psi_{\mathrm{c}},R)(\cos\psi_{\mathrm{c}}-1)$

A.5 Pellinen Mean

The Pellinen mean is the weighted mean of gravity data $\bar{g}$ over a spherical cap, i.e.

$$\bar{g} = \frac{1}{2\pi(1-\cos\psi_{\mathrm{c}})} \int\limits_{\omega_{\mathrm{c}}} g \, d\omega \quad \text{or} \quad \bar{g}_l = \beta_l g_l \tag{A.7}$$

where $2\pi(1-\cos\psi_{\mathrm{c}})$ is the area of a spherical cap ψ_{c}. Table A.6 lists different Pellinen definitions; only the recursion formula derived in Sjöberg (1980) is stable for $\psi_{\mathrm{c}} = 0$ and $l \to \infty$.

Table A.6: Pellinen mean formulas

Source	Formulas for β_l
Pellinen (1969)	$\beta_l = \cot\frac{\psi_{\mathrm{c}}}{2} \frac{P_{l,1}(\cos\psi_{\mathrm{c}})}{l(l+1)}$
Meissl (1971b)	$\beta_l = \frac{1}{1-\cos\psi_{\mathrm{c}}} \frac{1}{2l+1} \left[P_{l-1}(\cos\psi_{\mathrm{c}}) - P_{l+1}(\cos\psi_{\mathrm{c}})\right]$
Sjöberg (1980)	$\beta_l = \frac{2l+1}{l+1}\beta_{l-1}\cos\psi_{\mathrm{c}} - \frac{l-2}{l+1}\beta_{l-2}$ initial values: $\beta_l = 1,\ \beta_l = \frac{1+\cos\psi_{\mathrm{c}}}{2}$ $\psi_{\mathrm{c}} = \arccos(1-\frac{\Delta\omega}{2\pi})$ with $\Delta\omega = \Delta\lambda(\cos\theta_{\mathrm{N}} - \cos\theta_{\mathrm{S}})$

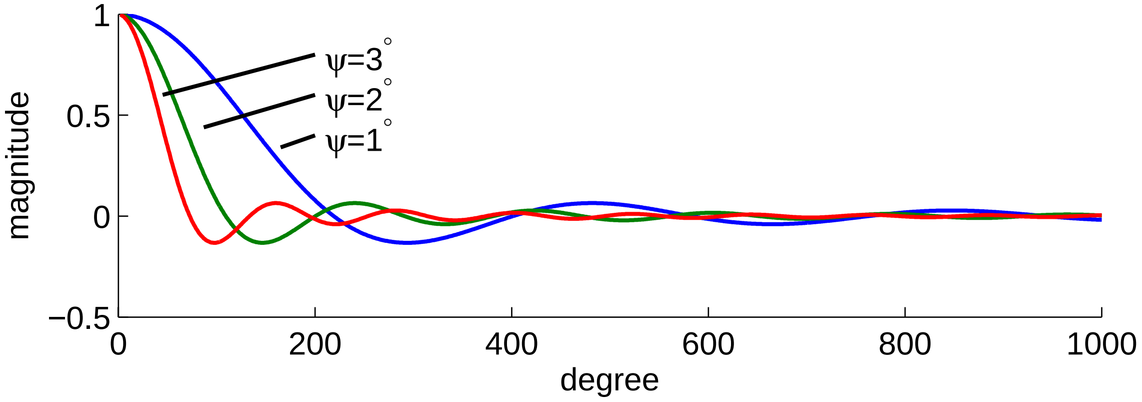

Figure A.2: Pellinen curves β_l for $\psi_{\mathrm{c}} = 1^\circ,\ 2^\circ,\ 3^\circ$

A.6 Covariance Functions and Least-Squares Collocation

Table A.7 lists some of the most commonly used (positive definite) covariance functions (GM stands for Gauss-Markov). All of them are dependent on the spherical distance ψ, i.e. they are homogeneous (origin independent) and isotropic (azimuth independent) (Moritz, 1989, pg. 82). The first seven covariance functions can also be used in the planar case. Then, ψ is replaced by the distance $s = \sqrt{x^2 + y^2}$. The covariance function attributed to Moritz is the usual covariance function used in LSC. c_l are the degree variances and R_{B} is the Bjerhammar sphere radius that is usually chosen slightly smaller than R. C_0 is the variance (scale factor for interpolation errors) and $C_0/2$ the correlation length (describes the behaviour of the covariance function as a function of ψ), see Schwarz & Lachapelle (1980) for further interpretations. Other covariance functions or procedures are described in Sünkel (1978, 1979). Table A.8 summarizes the main components of least-squares collocation as described in Moritz (1989).

The covariance function introduced by Sjöberg is particularly interesting. It allows for an analytical derivation of degree variances as (Sjöberg, 1986)

$$c_l = k(1-\mu)\mu^l \qquad 0 < \mu < 1 \tag{A.8}$$

Example. Selecting a variance of $C(0) = C_0 = 10$ mGal^2 and a correlation length of $C(0)/2 \approx 0.1°$, the parameters $\mu = 0.999$ and $k = 10$ are found. Figure A.3 shows the corresponding covariance function and degree variances computed with Eqn. (A.8). The degree variances are decreasing with degree.

Table A.7: Covariance functions

Name	Formulas for $C(\psi)$	Parameters
Gaussian	$C_0 e^{-A^2\psi^2}$	$C_0,\ A$
Hirvonen	$\frac{C_0}{(1+B^2\psi^2)^m}$	$C_0,\ B,\ m$
Inverse distance	$\frac{C_0 B}{\sqrt{\psi^2+[z_i+z_j+B]^2}}$	$C_0,\ B,\ z_i,\ z_j$
Poisson	$\frac{C_0 B^2[z_i+z_j+B]}{(\psi^2+[z_i+z_j+B]^2)^{3/2}}$	$C_0,\ B,\ m$
first order GM	$C_0 e^{-\frac{\psi}{D}}$	$C_0,\ D$
second order GM	$C_0(1+\frac{\psi}{D})e^{-\frac{\psi}{D}}$	$C_0,\ D$
third order GM	$C_0(1+\frac{\psi}{D}+\frac{\psi^2}{3D^2})e^{-\frac{\psi}{D}}$	$C_0,\ D$
Moritz	$\sum_l c_l \left(\frac{R_{\mathrm{B}}}{r_{\mathrm{P}} r_{\mathrm{Q}}}\right)^{l+1} P_l(\cos\psi)$	$c_l,\ R_{\mathrm{B}}$
Sjöberg	$k(1-\mu)\left(\frac{1}{\sqrt{1-2\mu\cos\psi+\mu^2}}-1-\mu\cos\psi\right)$	$k,\ \mu$

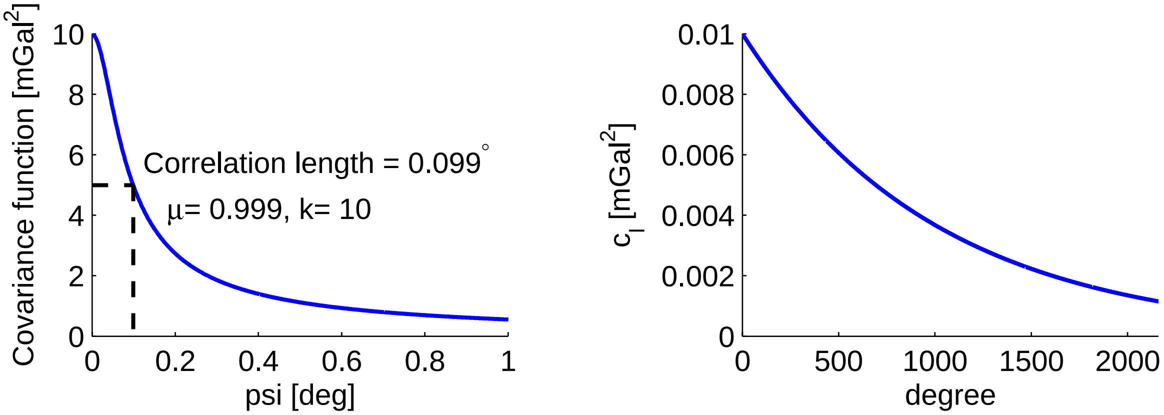

(a) Covariance function

(b) Degree variances

Figure A.3: Covariance function and degree variances

Table A.8: Summary of least-squares collocation (Moritz, 1989)

Name	Formulas		
Model	$\boldsymbol{l}$	$=$	$\boldsymbol{Ax} + \boldsymbol{s} + \boldsymbol{n}$
	$\boldsymbol{l}$		observation vector
	$\boldsymbol{A}$		design matrix
	$\boldsymbol{x}$		parameter vector
	$\boldsymbol{s}$		signal vector
	$\boldsymbol{s'}$		signals to be predicted
	$\boldsymbol{n}$		noise vector
	$\boldsymbol{t}$	$=$	$(\boldsymbol{s},\ \boldsymbol{s'})^T$
Covariance functions	$\boldsymbol{C}_{ss}$	$=$	$\bar{\boldsymbol{E}}(\boldsymbol{ss}^T)$
	$\boldsymbol{C}_{nn}$	$=$	$\bar{\boldsymbol{E}}(\boldsymbol{nn}^T)$
	$\boldsymbol{C}_{ls}$	$=$	$\boldsymbol{C}_{sl}^T = \bar{\boldsymbol{E}}(\boldsymbol{ls}^T)$
	$\boldsymbol{C}_{ll}$	$=$	$\bar{\boldsymbol{E}}(\boldsymbol{ll}^T) = \boldsymbol{C}_{ss} + \boldsymbol{C}_{nn}$
Assumptions	$\bar{\boldsymbol{E}}(\boldsymbol{s})$	$=$	$\bar{\boldsymbol{E}}(\boldsymbol{n}) = \bar{\boldsymbol{E}}(\boldsymbol{sn}^T) = \bar{\boldsymbol{E}}(\boldsymbol{tn}^T) = \boldsymbol{0}$
	$\bar{\boldsymbol{E}}(\boldsymbol{l})$	$=$	$\boldsymbol{Ax}$
Minimum principle	$\boldsymbol{t}^T\boldsymbol{C}_{tt}^{-1}\boldsymbol{t} + \boldsymbol{n}^T\boldsymbol{C}_{nn}^{-1}\boldsymbol{n} = \min$		
Solutions	$\hat{\boldsymbol{x}}$	$=$	$\left(\boldsymbol{A}^T\boldsymbol{C}_{ll}^{-1}\boldsymbol{A}\right)^{-1}\boldsymbol{A}^T\boldsymbol{C}_{ll}^{-1}\boldsymbol{l}$
	$\hat{\boldsymbol{s}}$	$=$	$\boldsymbol{C}_{ss}\boldsymbol{C}_{ll}^{-1}(\boldsymbol{l} - \boldsymbol{A}\hat{\boldsymbol{x}})$
	$\hat{\boldsymbol{s}}'$	$=$	$\boldsymbol{C}_{s's}\boldsymbol{C}_{ll}^{-1}(\boldsymbol{l} - \boldsymbol{A}\hat{\boldsymbol{x}})$
	$\hat{\boldsymbol{n}}$	$=$	$\boldsymbol{C}_{nn}\boldsymbol{C}_{ll}^{-1}(\boldsymbol{l} - \boldsymbol{A}\hat{\boldsymbol{x}})$
Error covariances	$\boldsymbol{E}_{\hat{x}\hat{x}}$	$=$	$\left(\boldsymbol{A}^T\boldsymbol{C}_{ll}^{-1}\boldsymbol{A}\right)^{-1}$
	$\boldsymbol{E}_{\hat{s}\hat{s}}$	$=$	$\boldsymbol{C}_{ss} - \boldsymbol{C}_{ss}\boldsymbol{C}_{ll}^{-1}\left(\boldsymbol{I} - \boldsymbol{A}(\boldsymbol{A}^T\boldsymbol{C}_{ll}^{-1}\boldsymbol{A})^{-1}\boldsymbol{A}^T\boldsymbol{C}_{ll}^{-1}\right)\boldsymbol{C}_{ss}$
	$\boldsymbol{E}_{\hat{s}'\hat{s}'}$	$=$	$\boldsymbol{C}_{s's'} - \boldsymbol{C}_{s's}\boldsymbol{C}_{ll}^{-1}\left(\boldsymbol{I} - \boldsymbol{A}(\boldsymbol{A}^T\boldsymbol{C}_{ll}^{-1}\boldsymbol{A})^{-1}\boldsymbol{A}^T\boldsymbol{C}_{ll}^{-1}\right)\boldsymbol{C}_{ss'}$

Table A.9: Geodetic reference systems

Name	GRS67	GRS80	IAG83	WGD2000
Source	IAG (1967)	Moritz (1980a)	Rapp (1983)	Grafarend & Ardalan (1999)
a	$6378160\,\mathrm{m}$	$6378137\,\mathrm{m}$	$6378136\,\mathrm{m}$	$6378136.572\,\mathrm{m}$
GM	$398603.0 \cdot 10^9\,\mathrm{m^3/s^2}$	$398600.5 \cdot 10^9\,\mathrm{m^3/s^2}$	$398600.44 \cdot 10^9\,\mathrm{m^3/s^2}$	$398600.4418 \cdot 10^9\,\mathrm{m^3/s^2}$
J_2	$1082.7 \cdot 10^{-6}$	$1082.63 \cdot 10^{-6}$	$1082.629 \cdot 10^{-6}$	$1082.6267 \cdot 10^{-6}$
ω	$7.2921151467 \cdot 10^{-5}\,\mathrm{rad/s}$	$7.292115 \cdot 10^{-5}\,\mathrm{rad/s}$	$7.292115 \cdot 10^{-5}\,\mathrm{rad/s}$	$7.292115 \cdot 10^{-5}\,\mathrm{rad/s}$
b	$6356774.5161\,\mathrm{m}$	$6356752.3141\,\mathrm{m}$	$6356751.3306\,\mathrm{m}$	$6356751.9200\,\mathrm{m}$
e^2	0.00669460532877	0.00669438002286	0.00669437592954	0.00669436989500
e'^2	0.00673972512853	0.00673949677544	0.00673949262676	0.00673948651061
$1/f$	298.2471674179	298.2572221028	298.2574047807	298.2576740928
q_0	0.00007334997193	0.00007334625841	0.00007334619094	0.00007334609148
$R = R_1$	$6371031.505\,\mathrm{m}$	$6371008.771\,\mathrm{m}$	$6371007.777\,\mathrm{m}$	$6371008.355\,\mathrm{m}$
R_2	$6371029.915\,\mathrm{m}$	$6371007.181\,\mathrm{m}$	$6371006.186\,\mathrm{m}$	$6371006.764\,\mathrm{m}$
m	$0.00344980143430\,\mathrm{rad}^2$	$0.00344978600308\,\mathrm{rad}^2$	$0.00344978490684\,\mathrm{rad}^2$	$0.00344978582989\,\mathrm{rad}^2$
$\bar{\gamma}$	$9.79763608\,\mathrm{m/s^2}$	$9.79764466\,\mathrm{m/s^2}$	$9.79764625\,\mathrm{m/s^2}$	$9.79764451\,\mathrm{m/s^2}$
γ_e	$9.78031846\,\mathrm{m/s^2}$	$9.78032677\,\mathrm{m/s^2}$	$9.78032836\,\mathrm{m/s^2}$	$9.78032661\,\mathrm{m/s^2}$
γ_p	$9.83217728\,\mathrm{m/s^2}$	$9.83218637\,\mathrm{m/s^2}$	$9.83218796\,\mathrm{m/s^2}$	$9.83218625\,\mathrm{m/s^2}$
U_0	$62637030.523\,\mathrm{m^2/s^2}$	$62636860.850\,\mathrm{m^2/s^2}$	$62636861.176\,\mathrm{m^2/s^2}$	$62636855.797\,\mathrm{m^2/s^2}$
$\bar{U}_{2,0}$	$-0.484198159895 \cdot 10^{-3}$	$-0.484166854895 \cdot 10^{-3}$	$-0.484166407660 \cdot 10^{-3}$	$-0.484165370168 \cdot 10^{-3}$
$\bar{U}_{4,0}$	$0.7904214684 \cdot 10^{-6}$	$0.7903040729 \cdot 10^{-6}$	$0.7903024598 \cdot 10^{-6}$	$0.7902984644 \cdot 10^{-6}$
$\bar{U}_{6,0}$	$-0.16877196 \cdot 10^{-8}$	$-0.16872512 \cdot 10^{-8}$	$-0.16872451 \cdot 10^{-8}$	$-0.16872285 \cdot 10^{-8}$
$\bar{U}_{8,0}$	$0.34625 \cdot 10^{-11}$	$0.34605 \cdot 10^{-11}$	$0.34605 \cdot 10^{-11}$	$0.34604 \cdot 10^{-11}$
$\bar{U}_{10,0}$	$-0.265 \cdot 10^{-14}$	$-0.265 \cdot 10^{-14}$	$-0.265 \cdot 10^{-14}$	$-0.265 \cdot 10^{-14}$

Table A.10: Legendre polynomials and Legendre functions

Description	Legendre Polynomials	Associated Legendre Functions (first kind)
Differential Eqn.	$(1-t^2)P_l^{''}(t) - 2tP_l^{'}(t) + l(l+1)P_l(t) = 0$	$(1-t^2)P_{lm}^{''}(t) - 2tP_{lm}^{'}(t) +$ $+ \left(l(l+1) - \frac{m^2}{1-t^2}\right) P_{lm}(t) = 0$
Rodriguez	$P_l(t) = \frac{1}{2^l l!} \frac{d^l}{dt^l}(t^2-1)^l$	$P_{lm}(t) = (1-t^2)^{m/2} \frac{1}{2^l l!} \frac{d^{l+m}}{dt^{l+m}}(t^2-1)^l =$ $= (1-t^2)^{m/2} \frac{d^m P_l(t)}{dt^m}$
Orthogonality	$\int\limits_{-1}^{+1} P_l(t)P_n(t)dt = \frac{2}{2l+1}\delta_{ln}$	$\int\limits_{-1}^{+1} P_{lm}(t)P_{nm}(t)\ dt = \frac{2}{2l+1}\frac{(l+m)!}{(l-m)!}\delta_{ln}$
Recursion	$P_l(t) = \frac{2l-1}{l} tP_{l-1}(t) - \frac{l-1}{l} P_{l-2}(t),\ \forall\ l \geq 2$ starting values $P_0(t) = 1,\ P_1(t) = t,\ t = \cos\psi$	$P_{l,m}(t) = \frac{2l-1}{l-m} tP_{l-1,m}(t) - \frac{l+m-1}{l-m} P_{l-2,m}(t)$ $P_{l,l}(t) = (2l-1)\sin\theta P_{l-1,l-1}(t)$ $P_{l,l-1}(t) = (2l-1)tP_{l-1,l-1}(t)$ starting values $P_{0,0}(t) = 1,\ t = \cos\theta$ where θ – co-latitude
Special Values or Symmetry	$P_l(-t) = (-1)^l P_l(t),\ t \in [-1,1]$ $P_l(1) = 1,\ P_l(-1) = (-1)^l$	$P_{l0}(t) = P_l(t),\ P_{lm}(-t) = (-1)^{l+m} P_{lm}(t)$ $P_{lm}(t) = 0$ for $m > l$

B Additional Results

B.1 First Helmert versus Second Helmert Condensation Method

An additional test was performed for the topographic effects in the Ottawa area – the first Helmert condensation method was tested against the second Helmert condensation method. The formulas are explicitly derived in (Heck, 2002; Kuhn, 2000). The results indicate that the first Helmert condensation produces a smoother residual field. In effect, the RMS of the indirect effect is almost five times larger than the one of the second Helmert effect.

Table B.1: First Helmert versus second Helmert condensation method

Name		Min	Max	Mean	Std	RMS	Unit
1. Helmert	DTE	−55.185	28.712	0.381	6.277	6.288	mGal
2. Helmert	DTE	−8.086	28.399	0.374	2.344	2.373	mGal
1. Helmert	PTE	−1.273	0.438	−0.013	0.109	0.110	m
2. Helmert	PTE	−0.174	0.000	−0.014	0.015	0.020	m

B.2 Stokes Integration and Continuation Results

Table B.2: Stokes integration – noise-free data

Name		Min	Max	Mean	Std	RMS	Remarks
Spherical	Near-zone	−3.209	1.520	−1.060	1.209	1.605	
	Far-zone	−0.047	0.086	0.016	0.030	0.033	
	Error	−0.053	0.043	0.008	0.021	0.022	
MO	Near-zone	−1.582	0.750	−0.523	0.596	0.791	$L_{\mathrm{MD}} = 120$
	Far-zone	−0.040	0.020	−0.007	0.016	0.018	
	Error	−0.007	0.007	0.001	0.003	0.003	
WG	Near-zone	−2.564	1.215	−0.847	0.966	1.282	$L_{\mathrm{MD}} = 20$
	Far-zone	−0.027	0.044	0.011	0.018	0.021	
	Error	−0.035	0.026	0.003	0.012	0.013	
M	Near-zone	−1.547	0.733	−0.511	0.583	0.774	
	Far-zone	−0.043	0.027	−0.000	0.018	0.018	
	Error	−0.008	0.005	−0.001	0.003	0.003	
JK	Near-zone	−1.394	0.660	−0.460	0.525	0.697	$L_{\mathrm{MD}} = 120$
	Far-zone	−0.049	0.021	−0.009	0.019	0.021	
	Error	−0.005	0.003	−0.000	0.002	0.002	
S	Near-zone	−0.371	0.176	−0.123	0.140	0.185	$L_{\mathrm{S}} = 120$
	Far-zone	−0.104	0.053	−0.034	0.041	0.053	
	Error	−0.020	0.022	−0.003	0.009	0.010	
HG	Near-zone	−1.049	0.497	−0.347	0.395	0.525	$L_{\mathrm{S}} = 120$
	Far-zone	−0.073	0.030	−0.027	0.026	0.038	
	Error	−0.009	0.004	−0.003	0.004	0.005	
VK	Near-zone	−1.582	0.750	−0.523	0.596	0.791	$L_{\mathrm{MD}} = 120$
	Far-zone	−0.040	0.020	−0.007	0.016	0.018	
	Error	−0.007	0.007	0.001	0.003	0.003	
FEO	Near-zone	−1.394	0.660	−0.460	0.525	0.697	$L_{\mathrm{MD}} = 120$
	Far-zone	−0.049	0.021	−0.009	0.019	0.021	
	Error	−0.005	0.003	−0.000	0.002	0.002	

Table B.3: Stokes integration – noisy data

Name		Min	Max	Mean	Std	RMS	Remarks
Spherical	Near-zone	−3.361	1.602	−1.075	1.241	1.638	
	Far-zone	−0.047	0.086	0.016	0.030	0.033	
	Error	−0.048	0.065	0.019	0.023	0.030	
MO	Near-zone	−1.657	0.790	−0.530	0.612	0.808	
	Far-zone	−0.040	0.020	−0.007	0.016	0.018	
	Error	−0.014	0.025	0.008	0.008	0.011	
WG	Near-zone	−2.686	1.280	−0.859	0.992	1.309	
	Far-zone	−0.027	0.044	0.011	0.018	0.021	
	Error	−0.032	0.045	0.013	0.015	0.020	
M	Near-zone	−1.620	0.772	−0.518	0.598	0.790	
	Far-zone	−0.043	0.027	−0.000	0.018	0.018	
	Error	−0.016	0.025	0.007	0.009	0.011	
JK	Near-zone	−1.459	0.696	−0.467	0.539	0.711	
	Far-zone	−0.049	0.021	−0.009	0.019	0.021	
	Error	−0.016	0.023	0.006	0.008	0.010	
S	Near-zone	−0.388	0.185	−0.124	0.143	0.189	
	Far-zone	−0.104	0.053	−0.034	0.041	0.053	
	Error	−0.027	0.027	0.000	0.011	0.011	
HG	Near-zone	−1.099	0.524	−0.351	0.406	0.536	
	Far-zone	−0.073	0.030	−0.027	0.026	0.038	
	Error	−0.013	0.020	0.002	0.007	0.007	
VK	Near-zone	−1.657	0.790	−0.530	0.612	0.808	
	Far-zone	−0.040	0.020	−0.007	0.016	0.018	
	Error	−0.014	0.025	0.008	0.008	0.011	
FEO	Near-zone	−1.459	0.696	−0.467	0.539	0.711	
	Far-zone	−0.049	0.021	−0.009	0.019	0.021	
	Error	−0.016	0.023	0.006	0.008	0.010	

Table B.4: Continuation results [mGal]

Height	Method	Min	Max	Mean	Std	RMS	Remark
2 km	INV	−7.638	11.679	0.150	2.604	2.608	
	LAI	−7.637	11.678	0.150	2.603	2.607	11 steps
	LSQ	−7.440	11.622	0.104	2.680	2.682	
	TIK	−10.280	10.577	1.029	4.104	4.231	$\alpha = 0.575$
	DSVD	−13.144	11.648	1.426	5.266	5.456	$\alpha = 0.575$
	TSVD	−7.440	11.628	0.093	2.682	2.683	$k = 863$
	CG	−7.170	11.355	0.059	2.654	2.655	$k = 3$
	A	−3.546	2.991	0.024	1.213	1.213	
	DA	−0.023	0.031	−0.001	0.011	0.011	[m]
3 km	INV	−10.852	16.113	0.207	3.622	3.628	
	LAI	−10.851	16.111	0.206	3.622	3.628	21 steps
	LSQ	−11.239	16.837	0.121	4.122	4.124	
	TIK	−8.794	12.204	0.563	3.357	3.404	$\alpha = 0.360$
	DSVD	−12.382	13.232	1.091	4.545	4.675	$\alpha = 0.360$
	TSVD	−11.207	16.855	0.109	4.126	4.128	$k = 863$
	CG	−10.950	15.947	−0.029	3.724	3.724	$k = 3$
	A	−4.596	3.560	0.020	1.513	1.513	
	DA	−0.024	0.030	−0.001	0.010	0.010	[m]
4 km	INV	−15.879	23.007	0.266	5.195	5.202	
	LAI	−15.878	23.003	0.265	5.194	5.201	37 steps
	LSQ	−18.433	27.564	0.134	6.395	6.396	
	TIK	−12.322	18.220	0.306	4.550	4.560	$\alpha = 0.212$
	DSVD	−13.898	16.671	0.789	4.753	4.818	$\alpha = 0.212$
	TSVD	−18.410	27.554	0.123	6.394	6.395	$k = 863$
	CG	−14.667	21.037	−0.110	4.488	4.490	$k = 3$
	A	−5.967	4.300	0.016	1.924	1.924	
	DA	−0.027	0.028	−0.001	0.011	0.011	[m]

Table B.5: Continuation results [mGal] – cont.

Height	Method	Min	Max	Mean	Std	RMS	Remark
5 km	INV	−23.919	33.824	0.330	7.750	7.757	
	LAI	−23.917	33.820	0.328	7.749	7.756	68 steps
	LSQ	−28.161	41.147	0.143	9.883	9.884	
	TIK	−22.325	32.587	0.196	7.276	7.279	$\alpha = 0.122$
	DSVD	−19.419	24.265	.555	6.531	6.555	$\alpha = 0.122$
	TSVD	−28.113	41.158	0.128	9.893	9.894	$k = 862$
	CG	−16.155	22.892	−0.131	4.822	4.824	$k = 3$
	A	−7.760	5.498	0.013	2.481	2.481	
	DA	−0.031	0.028	−0.001	0.012	0.012	[m]
6 km	INV	−57.393	77.000	0.381	18.928	18.932	
	LAI	−57.393	76.985	0.380	18.926	18.930	224 steps
	LSQ	−72.707	83.350	0.055	24.096	24.096	
	TIK	−62.619	78.605	0.049	20.220	20.220	$\alpha = 0.037$
	DSVD	−52.768	67.383	0.172	17.267	17.268	$\alpha = 0.037$
	TSVD	−72.831	83.546	0.042	24.049	24.049	$k = 862$
	CG	−17.410	24.639	−0.168	5.083	5.086	$k = 3$
	A	−10.113	7.380	0.020	3.236	3.236	
	DA	−0.037	0.030	0.001	0.014	0.014	[m]

B.3 Satellite Models and Geopotential Models

Table B.6: Undulation differences between the CGG2000, satellite and geopotential models [m]

Model	Min	Max	Mean	Std	Area
EGM96	−0.280	0.323	0.029	0.147	A2
GPM98a	−0.276	0.780	0.143	0.227	A2
EIGEN1s	−1.534	0.628	−0.307	0.387	A2
EIGEN-2	−0.923	1.059	0.316	0.461	A2
CSM360	−0.880	1.184	−0.103	0.481	A2
CSM360w	−0.957	1.028	−0.068	0.509	A2

B.4 Geoid Determination Based on Satellite and Terrestrial Gravity Data

Table B.7: Statistics for the geoid determination of satellite data and a local gravity data set

Data/Effect/Result	Min	Max	Mean	Std	Unit	Area
Δg	−70.390	82.772	−9.566	21.669	mGal	A0
δA^{TOP} (DTE)	−8.086	28.399	0.374	2.344	mGal	A0
δA^{ATM} (DAE)	0.750	0.870	0.840	0.017	mGal	A0
$\Delta g^{\mathrm{CSM360}w}$	−37.071	20.249	−9.232	10.581	mGal	A0
$\Delta g'$	−55.723	90.519	0.879	18.092	mGal	A0
$\Delta g'(R)$	−44.036	98.807	0.153	17.690	mGal	A1
$\hat{T}'/\gamma$	−0.733	0.725	0.042	0.331	m	A2
$\delta V^{\mathrm{TOP}}/\gamma$ (PTE)	−0.022	0.000	−0.003	0.004	m	A2
$\delta V^{\mathrm{ATM}}/\gamma$ (PAE)	−0.007	−0.006	−0.006	0.000	m	A2
$T^{\mathrm{CSM360}w}/\gamma$	−34.467	−30.838	−32.605	1.007	m	A2
$\hat{N}$	−34.152	−30.128	−32.572	0.882	m	A2
$\hat{N}$ - CGG2000	−0.240	0.211	−0.069	0.124	m	A2
$\hat{N}^{\mathrm{Fitted}}$ - CGG2000	−0.063	0.116	0.000	0.029	m	A2

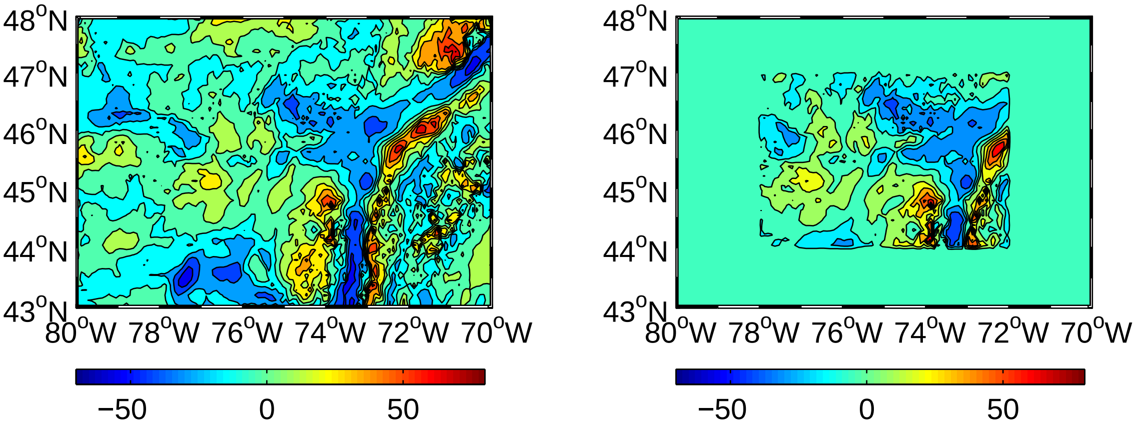

(a) Residual gravity anomalies $\Delta g'(r)$

(b) Residual gravity anomalies after downward continuation $\Delta g'(R)$

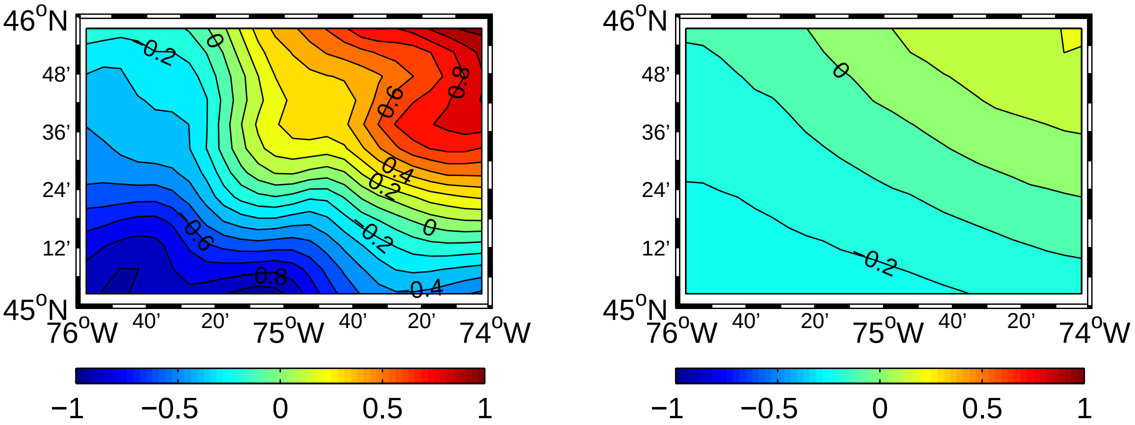

(c) Undulation differences between CSM360w and CGG2000

(d) Undulation differences between a local geoid based on CSM360w and terrestrial gravity data and CGG2000

Figure B.1: Geoid determination based on satellite and terrestrial gravity data

Index

Abel-Poisson
  design matrix, 48
  integration, 95, 158
  kernel function, 47
  kernel modification, 158
Airy-Heiskanen model, 13
Alternative numerical solution, 67
Anomalous quantities, 9, 24
Atmospheric
  effect, 7
  indirect effect, 7

Bouguer shell, 14, 15
Brillouin sphere, 11, 15

CHAMP, 2
Condensation
  comparison of schemes, 21
  density model, 14
  scheme, 17
Condensed topographic effect, 17
Condition number, 64
Conjugate gradient method, 59, 62
Conservation scheme
  mass, 17
  mass-centre, 17, 22
  mean density, 17
Contribution
  far-zone, 27
  near-zone, 27
Covariance functions, 161

Damped singular value decomposition, 57
Data frequency division, 27
Degree, 8
Degree variance models, 155
Degree variances, 104
Direct topographic effect, 14, 21
Disturbing
  potential, 7, 11, 24, 25, 46, 47, 84, 85, 103
  quantities, 9

Eigenvalue analysis, 8
Eigenvalues, 8
Ellipsoidal corrections, 6

Filter window functions, 154
Fredholm integral of the first kind, 51
Free boundary value problem, 24

Generalized cross-validation, 75
Geodetic reference systems, 164
Geoid determination, 3, 112, 117, 121, 127, 130
Global stationary field, 2
GOCE, 2
GRACE, 2
Gravity Disturbance, 12
GRS80, 12, 164

Hadamard conditions, 62
Harmonic field, 12

Height-to-spacing ratio, 64
Helmert
  direct effect, 19
  first condensation method, 166
  indirect effect, 14, 19, 21
  scheme, 12, 19
  scheme for other functionals, 20
  second condensation method, 13, 166
  values, 19, 22

Identity operator, 9, 65
Ill-posedness, 51
  discrete, 63
  mild, 64
  moderate, 64
  severe, 64
Improperly posed, 3
Integral representation, 25, 26
Integration domain division, 27
Inverse
  generalized, 51
  regularized, 53
Isostatic model, 13

Krylov space, 60

L-curve, 75
Landweber iteration method, 58
Laplace equation, 12
Laplace harmonics of the topographical heights, 20, 22
Least-squares collocation, 62, 81, 163
Legendre
  functions, 11, 165
  polynomials, 14, 29, 72, 86, 91, 165

Mapping, 24
Meissl scheme, 8
Model, 113
  geopotential, 1, 33, 48, 69, 86, 89, 96, 108, 116
  satellite, 7, 12, 34, 89, 96, 109, 116, 171
Multiple-input/multiple-output method, 82

Newtonian integration kernel, 14

One-step approach, 24
Operator
  adjoint, 8
  bijective, 52
  bounded, 52
  compact, 51
  continuous, 51
  injective, 52
  self-adjoint, 8
  surjective, 52
  unbounded, 52
Orthogonality, 10

Pellinen mean, 160
Picard
  condition, 65
  ratio, 66
  regularized ratio, 67
Pratt-Hayford model, 13

Regularization, 52
  error, 54
  parameter, 53
  scheme, 53
Remove-restore technique, 7, 27
Residual disturbing potential, 7
Residual gravitational potential, 13, 18
Resource exploration, 3
Ridge regression, 57
Runge's theorem, 11

Satellite geodesy, 1

Scalar product, 8
Singular
  systems, 8
  value, 8, 12, 22, 25
  value decomposition, 8, 53
Singular function
  left, 8
  right, 8
Somigliana-Pizzetti field, 12
Space
  domain, 8
  localization, 10
Spectral combination, 83
Spectral domain, 8, 28
Spherical
  approximation, 5
  cap, 27, 28
  distance, 15
  harmonic models, 5
  harmonics scalar, 9, 10
  harmonics tensor, 9
  harmonics vector, 9
Stokes
  -Helmert scheme, 112
  Featherstone et al. kernel, 157
  Heck-Grüninger kernel, 157
  integration, 26, 112, 115, 118, 156, 167, 168
  kernel function, 26, 96, 120, 131, 156, 157
  Meissl kernel, 157
  Molodenskij kernel, 157
  spherical kernel, 30, 157
  spheroidal kernel, 157
  Vaníček-Kleusberg kernel, 157
  Wong-Gore kernel, 157

Tailoring, 4, 86, 125
Terrain, 15
Tikhonov regularization, 56, 62
Time-variable field, 2, 106
Topographic
  effect, 7, 13
  indirect effect, 7
Topography, 15, 109
Transformation step, 7, 24
Truncated singular value decomposition, 57

Well-conditioned, 65
Well-posed, 52, 62